BEST-ESTIMATE PLUS UNCERTAINTY ANALYSIS OF 37-ELEMENT CANDU FUEL RELIABILITY

ANALYSE PAR MEILLEURE ESTIMATION ET PAR DÉTERMINATION DE L'INCERTITUDE DE LA FIABILITÉ DU COMBUSTIBLE CANDU À 37 ÉLÉMENTS

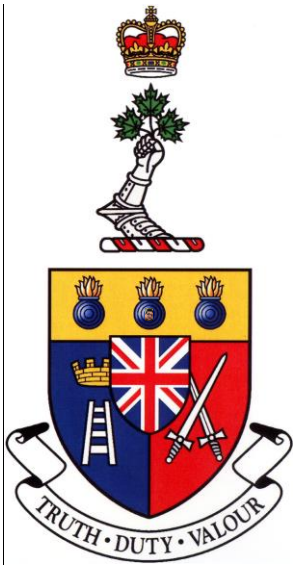

A Thesis Submitted

to the Division of Graduate Studies of the Royal Military College of Canada

by

Jason Jaeho Song, B.Eng, M.A.Sc, rmc
Lieutenant Navy

In Partial Fulfillment of the Requirements for the Degree of

Doctor of Philosophy of Applied Science in Nuclear Engineering

April 2021

Acknowledgements

First and foremost, I express my greatest appreciation for my supervisors, Dr. Paul K. Chan, Dr. Hugues W. Bonin and Dr. M. Pandey, for their excellent guidance and mentorship throughout the course of this research. Their profound knowledge and mentorship were instrumental in ensuring the success of this work.

I extend my gratitude to Dr. Benjamin Rouben, Dr. Zlatko Catovic, Dr. Wei Shen, and Dr. Andrew Prudil for their sincere and helpful assistance in utilizing and adapting the industry standard toolset codes and other relevant codes for the methodology used in my research. I greatly appreciate their guidance as it has significantly accelerated the progress of my research. I also give my thanks to my fellow graduate students at RMCC who provided the best of company both in and outside the office, and was always willing to help me refine the contents of my thesis and its defence.

I would like to personally thank the CANDU Owners Group Inc. (COG), the Natural Sciences and Engineering Research Council of Canada (NSERC), and the Department of National Defense for their provision of funds and resources that greatly helped propel this project forward. Their support is very much appreciated.

Finally, I am deeply grateful to the Ontario Power Generation corporation and Cameco Fuel Manufacturing corporation for providing the RMC Fuel Group with their proprietary data. This novel and interesting research would not have been possible without their help, so they have my utmost appreciation.

Abstract

Song, Jason (Chemical Engineering). Royal Military College of Canada. April 2021. Best Estimate Plus Uncertainty Analysis of 37-Element CANDU Fuel Reliability. Supervisors: Drs. Paul K. Chan, Hugues W. Bonin, and M. Pandey.

A novel method for assessing the reliability of the 37-element CANDU [Canada Deuterium Uranium (reactor)] fuel was developed. The approach follows the principle of "best estimate plus uncertainty" where reliability or probability of failure to meet fuel performance criteria is predicted via a best-estimate code with probabilistic treatment of both manufacturing and operating conditions. This method can be implemented where there is availability of an accurate best-estimate code for a fuel type, as well as sufficient manufacturing and operating data to be adapted for probabilistic treatment of code input. Furthermore, this method can be used for various applications within the nuclear industry, including safety design and analysis of novel fuels, as well as changes to existing fuel designs, identification of limiting failure criteria, and performance sensitivities to changes in manufacturing and operating conditions. In this study, the methodology is developed and implemented for the CANDU fuel type, with fuel performance predicted using the Canadian industry standard codes, ELESTRES and ELOCA. The two codes respectively model fuel behaviour during normal operation and transient conditions. The probability distributions of input variables pertaining to the fuel properties were adapted from real manufacturing data supplied by the Cameco Fuel Manufacturing Inc. The inputs for fuel element operating data were simulated from core-following data generated using a 3D diffusion code, the Reactor Fuelling Simulation Program. The reactor model used for the study is the Darlington Nuclear Generating Station core type. Random sampling was used to obtain input parameter values for the codes, and the outputs were compared against failure criteria derived from industry norms to determine the probability of failure.

The results of the study yielded probability distributions of fuel output response functions which predict zero probability of failure against limit conditions during normal operation of the fuel. A loss of coolant accident scenario with an 80% reactor outlet header break was also assessed, which predicts a zero probability of fuel failure. The output distributions were also compared to a deterministic “limit of envelope” benchmark, which is a generic adaptation of current safety benchmarking practices used within the industry. The output response functions predicted by the current study exhibited significantly larger safety margins to limit conditions in comparison to the benchmark case. This finding provides a novel demonstration of additional safety margin that is not accounted for by the current, conventional safety benchmarks. A global sensitivity analysis was also conducted, which provided a novel confirmation of the hierarchy of sensitivities of the output fuel response functions to the variance of individual input parameters.

Keywords: Best Estimate Plus Uncertainty, CANDU Fuel, Fuel Management, Fuel Performance, Reactor Safety Licensing, Fuel Safety Analysis, Reactor Aging.

Résumé

Song, Jason (Génie Chimique). Collège Militaire Royal du Canada. Avril 2021. Meilleure estimation plus analyse d'incertitude de la fiabilité du combustible CANDU à 37 éléments. Superviseurs: Dr. Paul K. Chan, Dr. Hugues W. Bonin, et Dr. M. Pandey.

Une nouvelle méthode d'évaluation de la fiabilité du combustible CANDU [Canada – deutérium - uranium (réacteur)] à 37 éléments a été mise au point. L'approche conceptuelle suit le principe de «meilleure estimation plus incertitude» lorsque la fiabilité ou la probabilité de transgression d'un critère de performance du combustible est prédite grâce à un code de «meilleure estimation» qui effectue un traitement probabiliste des conditions de fabrication et d'exploitation. Cette méthode peut être mise en œuvre lorsque l'on peut disposer d'un code précis de meilleure estimation pour un type de combustible et d'un ensemble suffisant de données de fabrication et d'exploitation qui peuvent être adaptées pour un traitement probabiliste de l'ensemble des données d'entrée du code. Cette méthode peut être utilisée pour diverses applications dans l'industrie nucléaire, incluant des études de sûreté pour le design et l'analyse de nouveaux combustibles, les modifications des designs actuels, l'identification des limites pour les critères de défaillance, et de la sensibilité de la performance aux changements des conditions de fabrication et d'exploitation.

Dans cette étude, les performances du combustible CANDU ont été prédites à l'aide des codes standard de l'industrie nucléaire canadienne, ELESTRES et ELOCA, qui, respectivement, modélisent le comportement du combustible en régime normal d'exploitation et dans des conditions de régime transitoire. Des distributions de probabilités pour les variables d'entrée pertinentes au combustible ont été adaptées en utilisant les données réelles de fabrication fournies par Cameco Fuel Manufacturing Inc. Les données d'entrée pour l'exploitation des éléments de combustible ont été obtenues par la simulation à partir d'un ensemble de données de suivi du cœur du réacteur générées par un code de diffusion en 3-D appelé « Reactor Fuelling Simulation Program

» (RFSP). Le modèle de réacteur utilisé pour l'étude est le type de cœur de la Centrale Nucléaire de Darlington. On a utilisé un échantillonnage aléatoire pour obtenir les valeurs des paramètres d'entrée pour les codes, et les valeurs de sortie ont été comparées aux critères de défaillance.

Les distributions des probabilités des variations des données de sortie pour la performance du combustible ont été obtenues par la méthode qui prédit une probabilité zéro d'atteindre les conditions limites de défaillance durant l'exploitation normale du combustible. Un scénario d'accident de perte de liquide de refroidissement avec une rupture de tête de réacteur à 80% a également été évalué, qui prédisent également une probabilité nulle de défaillance avant l'arrêt. Les distributions des valeurs de sortie ont été aussi comparées à celles obtenues d'un repère déterministe « limite d'enveloppe », qui est une adaptation générique des pratiques courantes de référence en sûreté utilisées dans l'industrie. L'analyse de référence a prédit des valeurs des paramètres de sortie nettement plus près des conditions-limites que les valeurs déterminées dans la présente étude, ce qui indique que la marge de sûreté disponible est supérieure à celle prédite par les résultats de sûreté de référence courants.

Mots-clefs : « Meilleure estimation plus incertitude », Combustible CANDU, Gestion du combustible, Performance du combustible, Homologation de la sûreté des réacteurs, Analyse de la sûreté du combustible, Vieillissement du réacteur.

Table of Contents

List of Tables

List of Figures

Glossary

Aging:	Time and environmental stress driven process by which the safe function of reactor systems, structures and components degrade
Best Estimate Plus Uncertainty:	An approach for simulation method where best-estimate codes along with realistic boundary conditions, assumptions on system availability, as well as treatment of inputs are used to predict the response of a system, plus its associated uncertainties
Bundle Power	The power produced by a single fuel bundle
Bundle Shift	This term describes the axial relocation of fuel bundles within a fuel channel as a consequence of the push-through-type refuelling. The size of the "bundle shift" of old fuels within the channel is equal to the number of fuels inserted, which also equals the number of fuels pushed out of (removed) the channel
Bi-directional Fuelling:	A refuelling strategy which involves fuelling adjacent pairs of fuel channels in opposing directions to induce an axially symmetrical neutron flux as a blended average between the two channels, which helps prevent axially uneven generation of power
Channel Power	The total power of a fuel channel. The sum of the powers of all fuel bundles within a fuel channel
Channel Power Peaking Factor:	Ratio of the highest channel power to average channel power in the reactor core

Derating:	The act of reducing a reactor's total power output by engaging its neutron absorbing devices
Differential Fuelling:	Differentiating the rate of refuelling between the inner (high-power) and peripheral (low-power) regions of the core to allocate high-burnup fuels into the high-power region and low-burnup fuels into the low-power region, which assists in flattening the inherent radial power differential between the inner and peripheral regions of the core
Dryout:	The condition where a region of the fuel channel loses a significant portion of its liquid coolant inventory such that the fuel bundle(s) in the region experience a complete loss of contact with the liquid coolant. This leaves vapours or gas remaining within the channel to carry out the thermal energy and results in a much less efficient cooling of the fuel
Fuel Burnup:	A measure of energy produced by the fuel, usually given in Megawatt-hours per kilogram of uranium
Fuelling Outage:	A necessary reactor shutdown which occurs in the process of bulk refuelling operation for reactors that cannot be refuelled on-line
Fuelling Transient:	A phenomenon which occurs during the first 2-3 full power operating days, following a refuelling, when a transient peak in power occurs in the vicinity of freshly loaded fuel bundles
Full Power Day:	Operation of a reactor at full power for 24 hours

Irradiation:	Measure of exposure to neutron flux during a given time. It is given by the time integral of the flux and is expressed in units of cm^{-2} or "neutrons per kilo-barn."
Limit of Envelope	The condition where a variable parameter is near the limit of its allowable range, or the envelope, of values. As an approach for defining the input variables for a simulation, the "limit of envelope" assumption refers to a situation where all input parameters are simultaneously near the limits of their envelopes
Liquid Zone Controller	A reactivity device consisting of a chamber that is variably filled up with (or drained of) light water. The water acts as a source of negative reactivity to decrease the power density of its surrounding region, and its fill level is controlled as a function of the region's power differential from the core average
Moment (mathematics)	Quantitative measures related to the graphical shape of a function. For probability distribution functions, the zeroth moment is the total probability sum equal to one, the first moment is the mean, the second moment is the variance, the third moment is the skewness, and the fourth moment is the kurtosis
Neutron Absorber:	Generalized term for indicating materials possessing high neutron absorption cross-sections
Operating Margin:	The margin between the instantaneous value of an operating parameter and its licensed operating limit.

Plutonium Peak:	A phenomenon which occurs for natural uranium fuels at approximately 40-50 full power operating days of in-core irradiation, when a transient peak in power occurs in the vicinity of affected fuels due to the accumulation of fissile plutonium isotopes
Power Density:	Ratio of the local power level to the volume of the part of the reactor considered
Radial Form Factor:	The ratio between the value of the highest-powered channel in the core to the average value of channel powers in the core. It is used as an indicator of how flat the distribution of power is in the core
Reactivity:	The measure of a nuclear reactor's fractional departure from criticality
Reactivity Bank:	The excess reactivity available within the core, which may be used to operate the reactor without refuelling for a period of time
Reactivity Device:	A device used to introduce positive or negative reactivity into the reactor core for means of control. Positive reactivity can be inserted by using neutron producing material. Negative reactivity can be inserted using neutron-absorbing materials
Reference Fuelling Scheme	The normal allocation of refuelling modes used for each of the fuel channels of the model core used in the study. The allocation consists of 8-bundle-shift fuelling mode in the outer core and 4-bundle-shift fuelling mode in the inner core

Refuelling Ripple:	A phenomenon which occurs in CANDU reactors as the consequence of daily refuelling. On-power refuelling perpetually perturbs the distribution of power density within the core due to the effects of the fuelling transient and the plutonium peak
Regionalized Fuel Grouping	Organization of fuels (operating data) within the core into groups that experience similar operating power conditions. Fuels may be grouped per radial regions (channel groups) or axial (position groups) regions. This is done to highlight the difference in operating power histories between regions, improve the fit of power operating data to statistical distributions, and to determine the region of highest overpower risk
Safety Margin:	An additional margin adopted beyond the extent of the reactor's operating margin. The safety margin exists as a buffer to ensure safety and maintain control of the reactor in the event that the operating margin should be exceeded. The safety margin is not a region in which the reactor may be operated.
Sobol Indices	A method of global sensitivity analysis using a decomposition of the variance of the model/system output into fractional indices that can be attributed to the variance of the input parameters. The method provides the advantage of measuring sensitivity across the whole input space, and can deal with non-linear responses, as well as measuring the effect of interactions in non-additive systems

Voiding:	Formation of air pockets (bubbles) or slugs in the coolant
4-Bundle Shift:	A fuelling mode which involves pushing four fresh fuel bundles into a given channel and withdrawing four irradiated fuel bundles at the other end of the same channel
8-Bundle Shift:	A fuelling mode which involves pushing eight fresh fuel bundles into a given channel and withdrawing eight irradiated fuel bundles at the other end of the same channel

List of Acronyms

AECL	Atomic Energy Canada Limited
BEPU	Best Estimate Plus Uncertainty
BNA	Burnable Neutron Absorber
CANDU™	CANada Deuterium Uranium
CCP	Critical Channel Power
CDF	Cumulative Distribution Function
CHF	Critical Heat Flux
CNL	Canadian Nuclear Laboratories (Formerly Chalk River Nuclear Laboratories of Atomic Energy of Canada Limited)
CPPF	Channel Power Peaking Factor
DBA	Design Basis Accident
DBE	Design Basis Event
FPD	Full Power Day
HF	Heat Flux
IST	Industrial Standard Toolset
LLOCA	Large Loss Of Cooling Accident
LOCA	Loss Of Cooling Accident
LOE	Limit Of Envelope
LZC	Liquid Zone Controllers
MW_{th}	MegaWatt (thermal): Power of a reactor before conversion to electrical power by multiplying by the efficiency coefficient
N/A	Not Applicable
NOC	Normal Operating Condition
NOP	Neutron Overpower Protection
NGS	Nuclear Generating Station
NU	Natural Uranium
OBPL	Operating Bundle Power Limit
OCPL	Operating Channel Power Limit

PDF	Probability Distribution Function
PHTS	Primary Heat Transport System
RFF	Radial Form Factor
RFSP	Reactor Fuelling Simulation Program
ROH	Reactor Outlet Header
RTD	Resistance Temperature Detector
SDS	ShutDown System
SLOCA	Small Loss of Cooling Accident

List of Symbols

k_{eff}	Effective neutron multiplication factor
k_{inf}	Infinite neutron multiplication factor
ρ	Reactivity
β^-	Beta (negative) decay
P_r	Pellet Radius
P_L	Pellet Length
D_d	Dish Depth
D_r	Dish Radius
R_c	Radial Chamfer
A_c	Axial Chamfer
L_w	Land Width
P_p	Initial Pellet-to-Pellet Gap
D_{gap}	Initial Pellet-to-Sheath Gap
S_T	Sheath Thickness

Chapter 1: Introduction

The operational licensing of a nuclear reactor follows a rigorous process that must satisfy highly conservative safety standards, which includes safety confirmation via predictive modelling. Historically, the norm for predictive safety modelling has largely relied on benchmark calculations obtained using conservative, typically Limit-Of-Envelope (LOE) assumptions and boundary conditions [1]. The reason for this practice was due to a lack of adequate means to predict behaviours of safety-significant components and processes using probabilistic methods with sufficient detail and confidence. During the early developmental stages of nuclear technology, large quantities of reliable data, both experimental and operational, and predictive models were limited in their availability and detail. These restrictions posed significant challenges in the way of implementing statistical studies of reliability for the purpose of safety decision-making. Moreover, such studies required large quantities of computational resources that were quite limited and expensive at the time. However, with significant advancements in information technology, it is now feasible to conduct statistical studies involving significantly better-detailed models with reasonable cost and time.

Since the commercial operation of the first full-scale CANDU reactor at the Douglas Point Nuclear Generating Station in 1968, the cost of computational resources as a commodity has decreased by a magnitude of approximately 10^8 times by 2004 [2]. **Figure 1** shown below illustrates the progression in the cost of computational resources between the years 1890 to 2004 [2]. In addition to lower computing costs, the accumulation of extensive experimental, operating, and manufacturing experience over time has also contributed significantly to the development of improved models and the availability of reliable data. These developments have enabled the conditions to now conduct detailed studies incorporating a Probabilistic Safety Analysis (PSA) approach. A wide-spread and an in-depth implementation of such an approach for safety decision-making is desirable, because deterministic methods generally require conservative assumptions in order to account for their lack of data-driven accuracy.

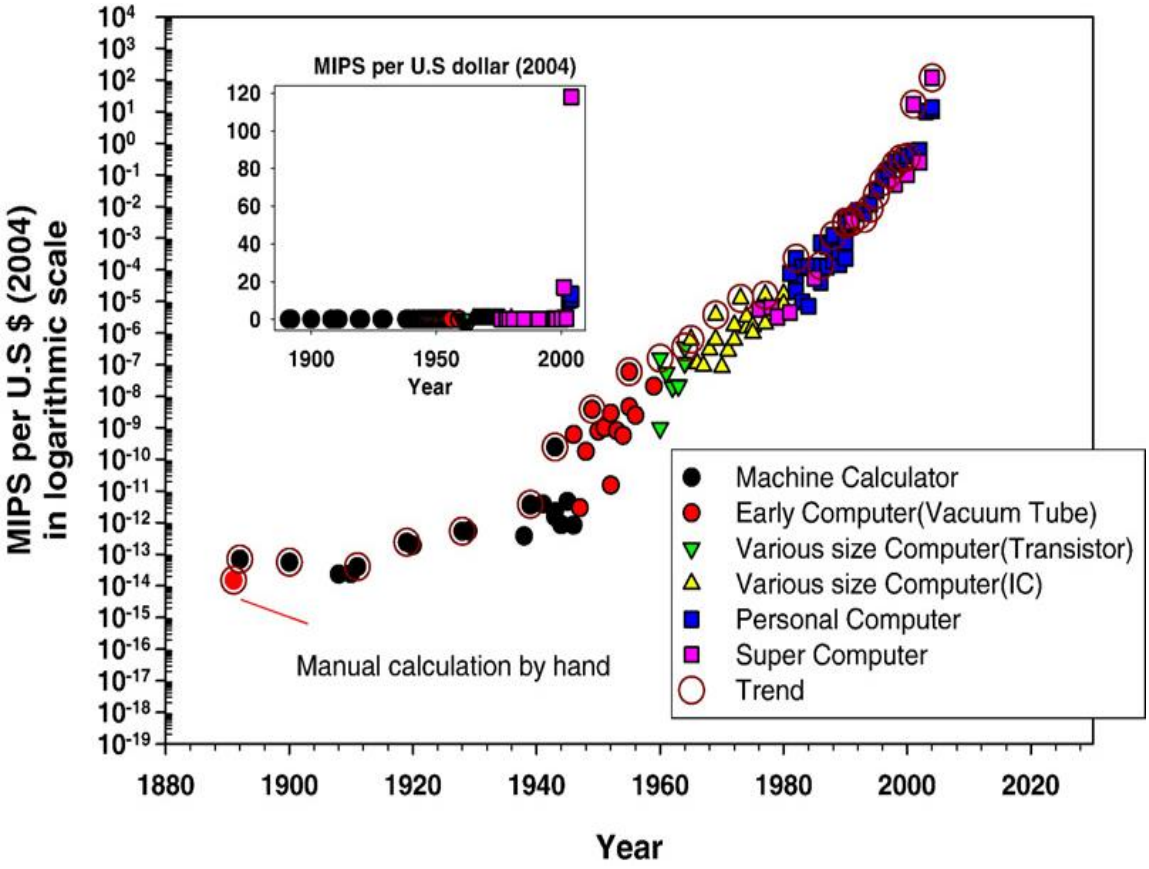

Figure 1. Progress in computing resource versus cost, in million instructions per second (MIPS) per US dollars (2004) [2].

Currently, there are a total of 31 active CANDU reactors in service around the world, with 19 of them being located within Canada. The average age of these reactors stands at approximately 35 years with respect to the start of their commercial operation. Consequently, many of these reactors are at, or close to the end of their design life, and their operating margins are already reduced to account for the effects of aging. Nevertheless, commercial operation and licensing efforts continue onwards, and refurbishments for life extension of several stations have been committed, or are being actively pursued with a few reactors already back in service [3,4,5,6]. Opportunities of significant value therefore exist in accurately determining the reliability of safety-significant components and their associated margins of failure for these aged reactors. **Table 1** below outlines the current list of active CANDU reactors in Canada.

Table 1. Current list of active CANDU reactors in Canada [3,4,5,6].

Unit Name	Commercial Ops. Date	Life Ext. Projects	Current License End
Bruce-A1	Sept 1977	1995-2012	Sept 2028
Bruce-A2	Sept 1977	1995-2012	
Bruce-A3	Feb 1978	2023-2028	
Bruce-A4	Jan 1979	2023-2028	
Bruce-A5	Mar 1985	2026-2033	
Bruce-A6	Sept 1984	2020-2024	
Bruce-A7	April 1986	2026-2033	
Bruce-A8	May 1987	2026-2033	
Darlington-1	Nov 1992	2022-2025	Nov 2025
Darlington-2	Oct 1990	2016-2020	
Darlington-3	Feb 1993	2020-2024	
Darlington-4	June 1993	2023-2026	
Pickering-A1	July 1971	Plan to shut-down	Aug 2028
Pickering-A4	June 1973	Plan to shut-down	
Pickering-B5	May 1983	Plan to shut-down	
Pickering-B6	Feb 1984	Plan to shut-down	
Pickering-B7	Jan 1985	Plan to shut-down	
Pickering-B8	Feb 1986	Plan to shut-down	
Pt. Lepreau	Feb 1983	2008-2012	June 2022

In consideration of this current industry landscape, there certainly is significant value to be captured in further developing the limited, conventional safety analysis framework and further advancing the envelope of its accuracy. This endeavour would in turn significantly improve the strategic planning and qualification of safety decisions of the future, whether it be refurbishment and licensing of aged reactors, or construction and licensing of new projects. In light of this consideration, the current study aims to develop and demonstrate a novel PSA framework by implementing the *Best-Estimate Plus Uncertainty* (BEPU) approach within the scope of CANDU fuel operational safety analysis. This novel approach is yet to be implemented by the industry in the framework of PSA for CANDU fuel safety analysis, and will advance the current state-of-the-art in improving the accuracy of identifying the real, probabilistic limits of the CANDU fuel in both normal operating and accident conditions. Furthermore, the novel method aims to establish a computer experiment framework to provide the means of flexibly conducting multitudes of safety studies including but not limited to: impact of fuel design changes, manufacturing processes, and operating practices.

In the subsequent chapters two to four, a general background of the CANDU reactor and its fuel design, as well as the current state-of-the-art of the safety analysis framework, followed by the objectives and the scope of this study, are presented. These chapters are then followed by the theories of CANDU fuel design and its failure mechanisms, as well as the probabilistic safety analysis method, and a description of the novel, *best-estimate plus uncertainty* approach in chapter five. Next, the method development of the study is discussed in chapter six. This chapter outlines the computer simulation framework, which integrates multiple physics codes, models, and statistical toolset to predict the probabilistic output response of the model CANDU fuel. The results of the study are then presented in chapter seven, firstly in the form of an in-depth analysis of the behaviour of a randomly sampled fuel as a detailed example, and secondly as the general, statistical properties of the probability distributions of the output response functions. The results also include probabilities associated with the critical response levels of each response function tied to their respective limit conditions, and a global sensitivity analysis of the response functions in relation to the input parameters. In chapter eight, the results of the study are discussed in detail with respect to their implications for the operating and manufacturing standards, plus practices of the CANDU fuel. This is followed by the conclusions of the study in relation to its scope and objectives in chapter nine. In closing, the recommendations for future research are provided in chapter ten.

Chapter 2: Background

Among many of the safety-critical components within a nuclear power generating station, the nuclear fuel itself is a component of fundamental importance to safety. This is because the structural integrity of the fuel represents the primary barrier against a release of radioactive fission products. The nuclear fuel is therefore designed to endure prolonged periods of exposure to the harsh conditions present within a nuclear reactor core without defect. The 37-element CANDU fuel is designed with this same principle in mind, but with considerations for the unique circumstances under which CANDU reactors are operated.

The CANDU reactors, like many other nuclear reactors, are employed as the primary heat sources of nuclear power generating stations, and features many of the same system characteristics and sub-system features that are present in other conventional nuclear reactor systems. Generic diagrams illustrating a CANDU-based nuclear power generating station are shown below in **Figure 2**, **3** and **4**.

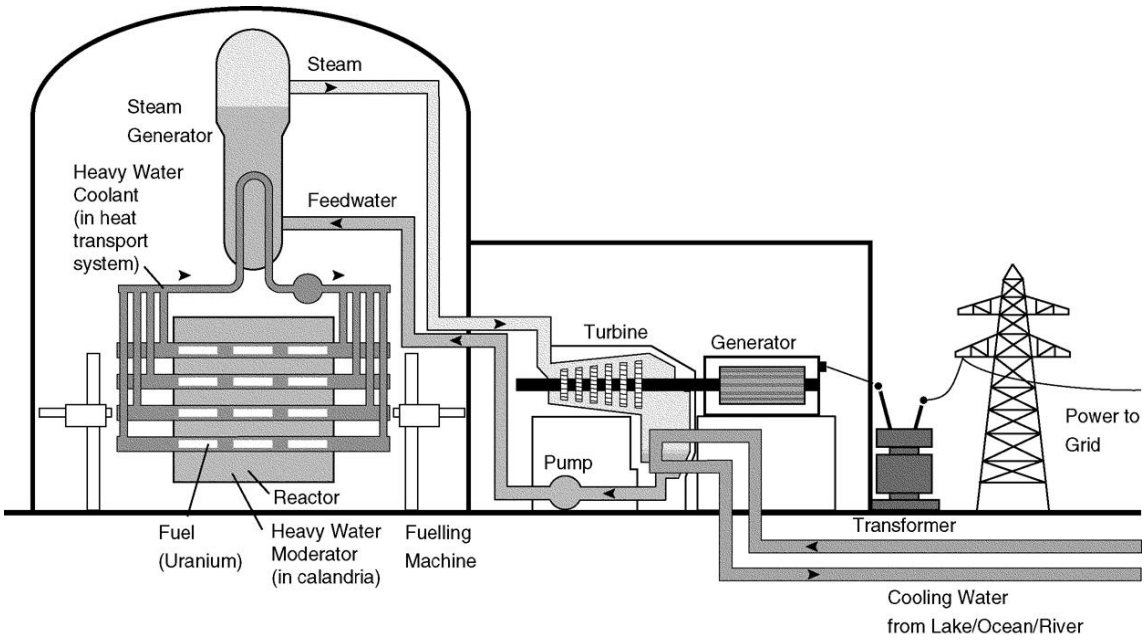

Figure 2. A concept diagram of the overall CANDU nuclear plant [7].

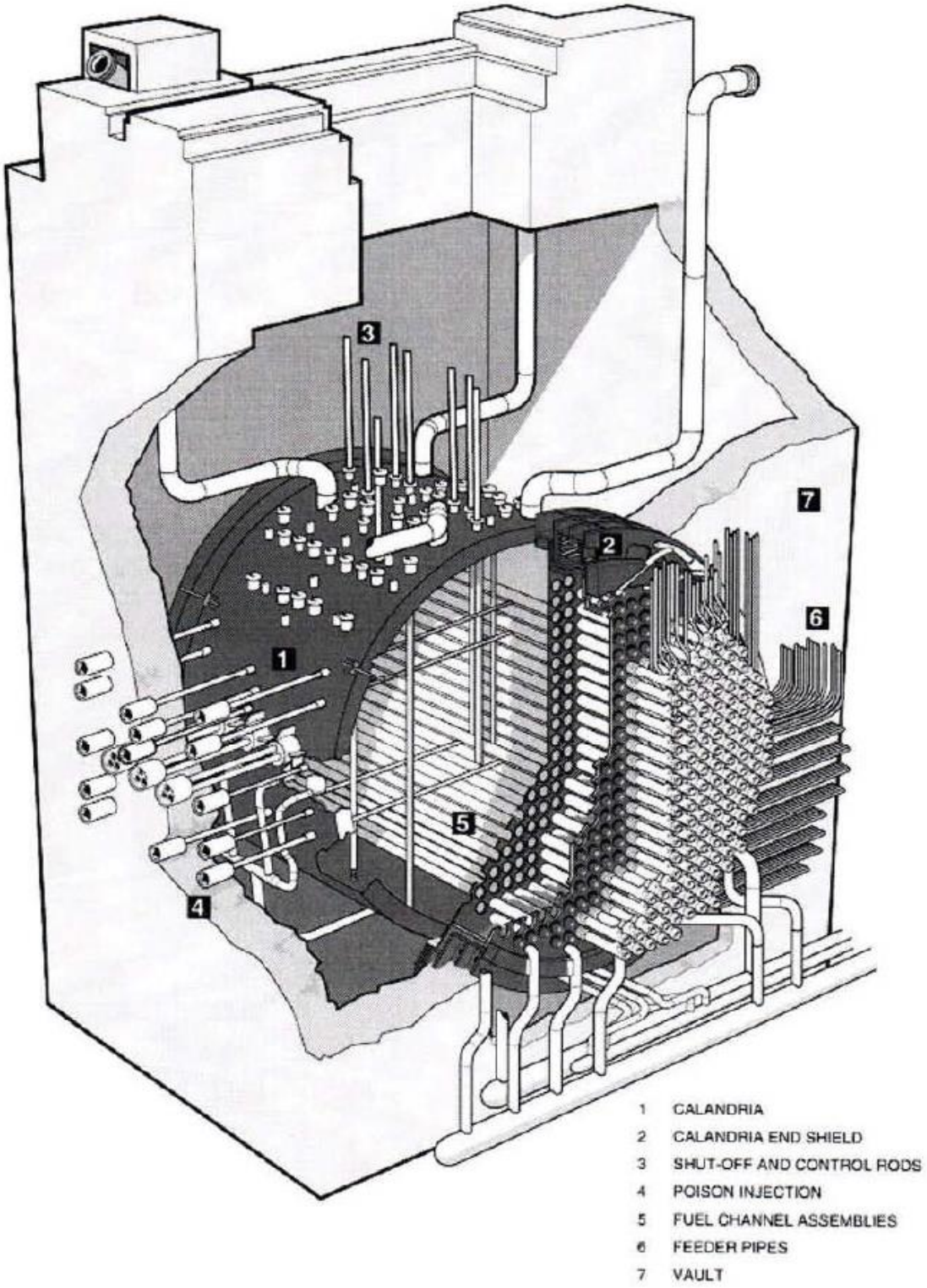

Figure 3. CANDU reactor vault and assembly, showing the guide-tubes and the reactivity devices penetrating the core [8].

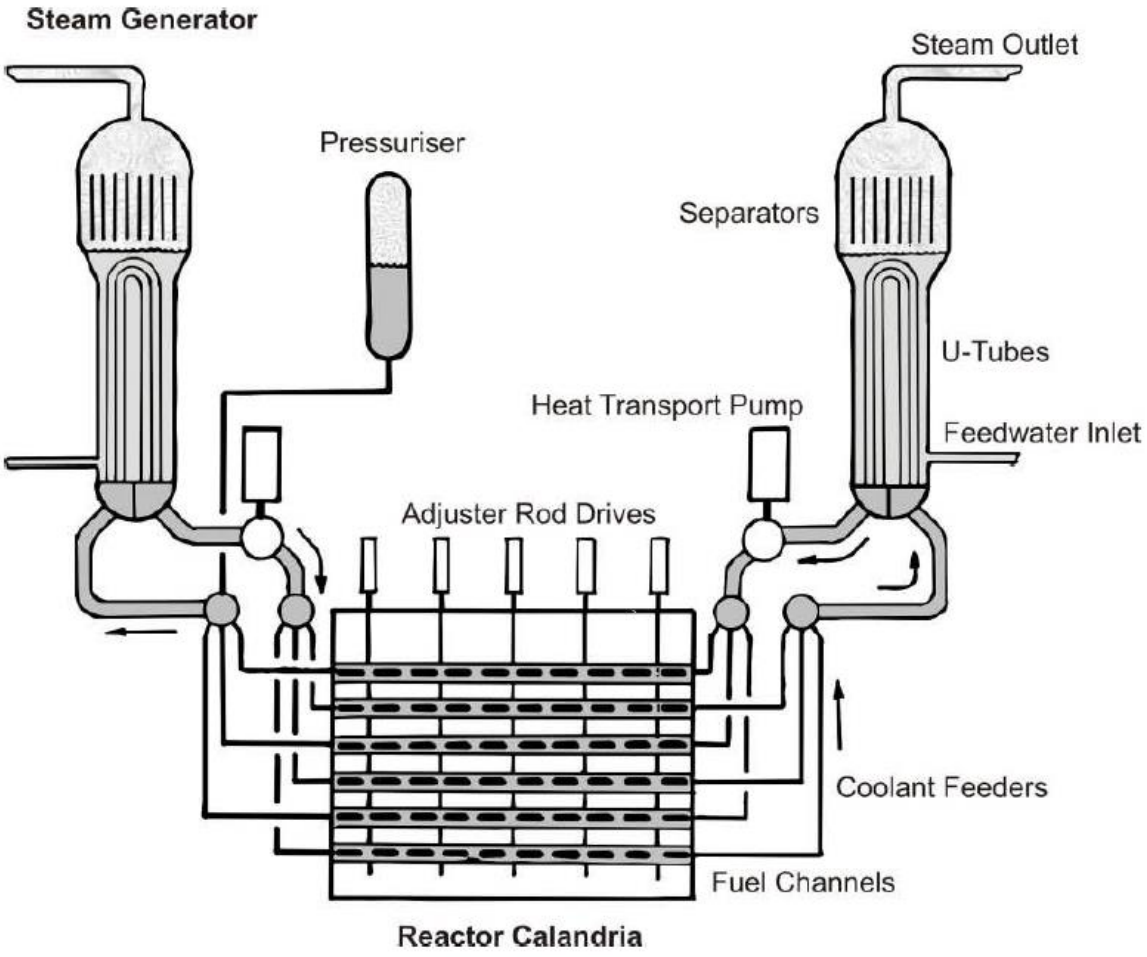

Figure 4. Cross-section of a CANDU core and the coolant system, as well as vertically inserted adjuster rods [8].

The CANDU plant system incorporates three coolant loop systems. The primary and secondary cooling loops, which are used to cool the reactor core and generate steam, interface via the steam generator, whereas the tertiary loop consists of the heat sink, which interfaces with the secondary loop via the condenser. Many auxiliary and safety systems are also incorporated into the reactor, which include but are not limited to: the generator-turbine assembly, the reactor control system, the shutdown systems, as well as various instrumentations for remote monitoring and diagnostics. Unlike many other top-loaded, batch-fuelled, Pressurized Water Reactors (PWR) or Boiling Water Reactors (BWR), a CANDU core is fuelled horizontally while on-power. Moreover, CANDU

reactors utilize heavy water (D_2O) instead of light water (H_2O) in the core, which allows the use of non-enriched, Natural Uranium (NU) fuel. This is because heavy water provides a much greater economy of neutrons than light water, while maintaining a similar level of moderating and cooling capabilities. The above advantage occurs due to the relatively lower neutron absorption cross section of heavy water compared to light water. As a result of the use of natural uranium fuel, CANDU fuels are typically irradiated to lower values of burnup than those values achieved in common PWR designs.

The contemporary CANDU fuel consists of 37 rod-elements fabricated from zircaloy-4, which is an alloy of zirconium. Each of the 37 fuel elements contains stacks of NU fuel pellets, and are assembled together in the form of fuel bundles. A diagram of the 37-element fuel bundle is shown in **Figure 5**. Each element is approximately 50 cm long, and when they are assembled together in a bundle, the diameter is approximately 10 cm. The elements are fixed together using end-plates and are spaced apart via spacer pads to maintain the shape of the bundle assembly. The coolant flows around, as well as through the spaces between the elements to remove the heat generated by the fuel.

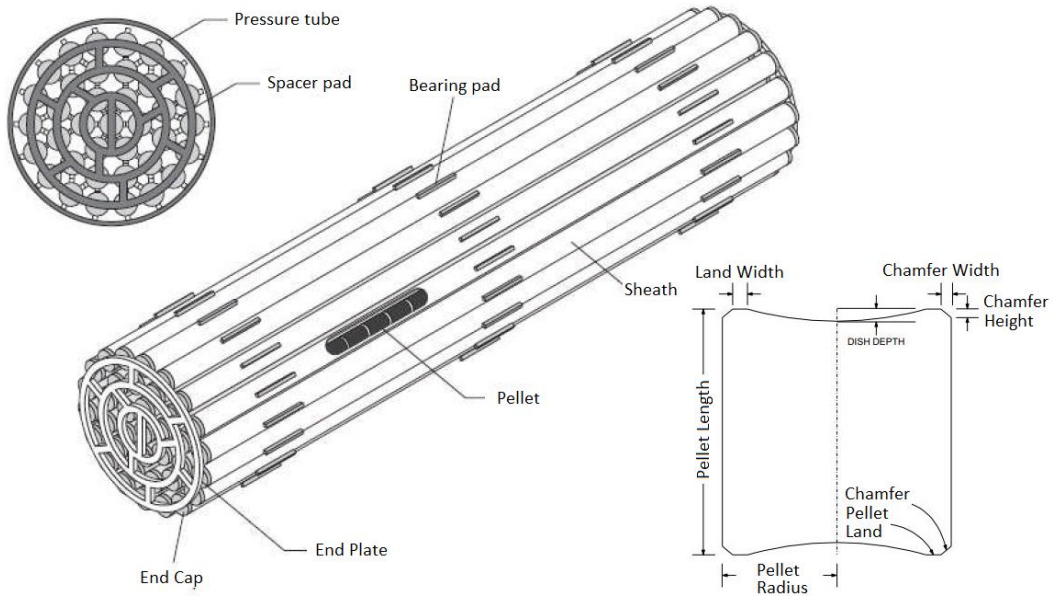

Figure 5. A diagram of the 37-element CANDU fuel and its sub-components, including a detailed image of the fuel pellet [9].

The fuel pellets used within the CANDU fuel elements are cylinder types that have been adapted with an axial dish on the two flat ends. This feature is implemented by stamping the pellet ends in the shape of a concave scoop, typically before the sintering phase. This feature is desirable, as it provides some allowance for thermal expansion at the hot, central regions of the pellet [10]. A chamfer is also implemented along the edges of the pellet such that chipping caused by pellet-to-pellet contact during fuel loading and subsequent handling, as well as sheath strain at pellet interfaces can be mitigated [10]. A depiction of the chamfer-to-chamfer contact interface is provided in **Figure 6** below.

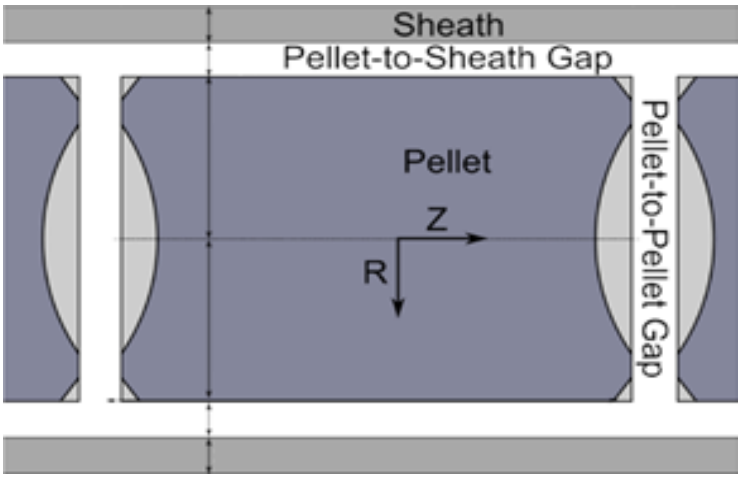

Figure 6. A diagram depicting the chamfer-to-chamfer contact interface between adjacent fuel pellets within a CANDU fuel element [11].

Chapter 3: State of the Art

The International Atomic Energy Agency's (IAEA) safety series 52 describes the principle of *best-estimate plus uncertainty* as "the biggest effort for a proper use of best estimate models in order to minimize unnecessary conservatism while accounting for uncertainties associated to simulation results [12]." The idea to combine the best-estimate codes and assumptions with their uncertainties is a widely desired goal in practices not limited to engineering. In fact, a literature search on the use of BEPU yields numerous references in the field of finance and mathematics [13]. The ideal approach to safety analyses would involve best estimate codes and realistic inputs with uncertainty that are used in conjunction with probabilistic assumptions for boundary conditions. However, the current safety licensing practice for nuclear reactors in most countries still mainly rely on conservative inputs and boundary conditions, although best-estimate or realistic codes are now widely used [14]. The current state-of-the-art for the safety analyses of nuclear reactors is therefore still largely deterministic. Nevertheless, the current international regulatory trends have begun to require the incorporation of the PSA approach in the assessment of safety margins to support and supplement the conservative predictions imparted by deterministic analyses, technical judgment and experiences. In the case of Canada, the regulatory framework for the licensing of CANDU reactors is also evolving, with increased emphasis on the PSA approach. The Canadian Nuclear Safety Commission (CNSC) regulatory document 2.4.2, "Probabilistic Safety Assessment (PSA) for Nuclear Power Plants (NPP)," first published in 2005, outlines the PSA requirements for the licensing basis [15]. The above CNSC document largely adopts the IAEA guidelines published under the specific safety guide documents for the probabilistic safety assessments of nuclear power plants [16,17].

Chapter 4: Goals and Scope of Work

The objective of this study is to develop and conduct a novel reliability analysis of the 37-element CANDU fuel during both Normal Operating Conditions (NOC), as well as during a postulated transient, using the BEPU approach. The NOC state is chosen as the primary basis for analysis because from the perspective of fuel management, it represents approximately 95% of the lifetime of a CANDU reactor [18]. The representative transient used in the study is a Loss Of Coolant Accident (LOCA) condition. The methodology of the study follows the novel BEPU approach, and it is intended that the development of this approach will provide a more accurate method that will improve the operating margins of the 37-element fuel. Furthermore, it is also intended that this effort will support the advancement of the World Association of Nuclear Operators' (WANO) zero fuel defect criterion [19].

The BEPU approach implemented in this study places an emphasis on improving the accuracy of the safety analysis by replacing assumptions embedded within simulation inputs, with inputs that are statistically commensurate with real, or simulated data. In [20], a reliability assessment of the 37-element fuel was conducted using the ELESTRES and ELOCA codes that were provided with fuel manufacturing data obtained from the Cameco Fuel Manufacturing (CFM) Inc. The previous study, however, was limited by its use of fixed linear element rating against burnup, which was assumed to be at a limit-of-envelope value of 55.0 kWm^{-1}. The current study extends the methodology by incorporating fuel operating data derived from core-following histories for a realistic treatment of operating inputs to the fuel performance simulations. Moreover, the methodology incorporates a large-sample global sensitivity analysis implemented without simplification via surrogate modelling or dimensional reduction, in contrast to [20]. Finally, in addition to the regular 37-element CANDU fuel, the safety impact of a fuel design change in the form of adding Burnable Neutron Absorbers (BNA) to the fuel is also investigated using the method framework. The reference BNA fuel used for this

study is the 150 mg GdO_2 and 300 mg EuO_2 which was recommended by [21] for optimal flattening of the reactivity versus burnup curve.

Chapter 5: Theory

Assessing the reliability of a nuclear fuel via computer simulation requires not only a detailed multiphysics approach to the model simulation, but also a realistic definition of the model inputs and boundary conditions. To produce an accurate prediction, these variables must be commensurate with real-life manufacturing quality control, as well as the conditions under which the fuels are operated. In the following subsections of this chapter, the theories and considerations incorporated within the methodology of this study, for the modelling and simulation of fuel failures, are described in detail.

5.1 CANDU Fuel Defects

A defective fuel bundle is defined as a fuel unit where one or more sheath penetrations have formed, through which fission products can escape [22]. An illustrative diagram of a defective CANDU fuel (on a single element) is shown below in **Figure 7**. When fission products escape from the containment of the sheath element into the coolant, it can induce radioactivity within the coolant system that poses health risks to station personnel who are exposed to the proximity of the coolant circuit.

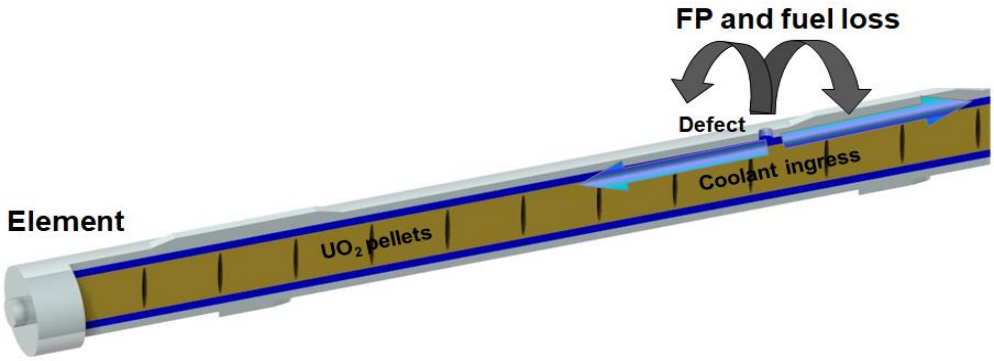

Figure 7. A defective fuel element where a crack has penetrated the sheath element [22].

Historically, fuel performance has been recognized as a strong attribute of CANDU reactors, with less than 0.1% of fuel units out of more than 1,300,000 fuel bundles that were irradiated prior to 1996 in Canada having developed defects [10]. Furthermore,

among defects that were observed, the most severe examples were limited to single-element failures [10]. This corresponds to an approximate failure rate of 1 in 10^5 fuel bundles irradiated in the core [10]. A graph of causes for defects with their proportional rates of occurrence is shown in **Figure 8**. Recently, the overall defect rate is reported to have further decreased as the result of fuel element and bundle design improvements, tighter quality control for manufacturing processes, in addition to much improved operating procedures and greater restrictions on the licensed operating envelopes [23].

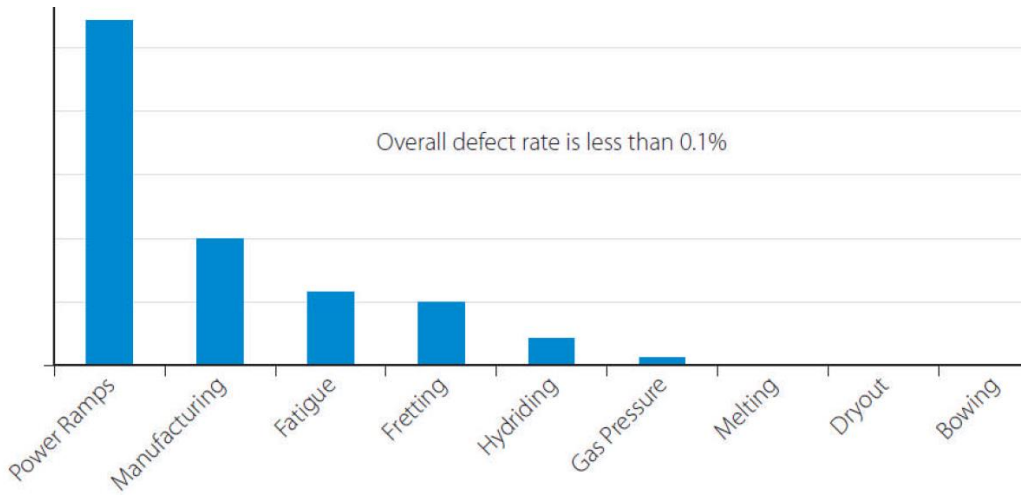

Figure 8. Causes of defects in CANDU fuel from years 1967 to 1996, excluding failures due to debris damage [9].

5.1.1 Defect Categorization

Generally, the causes for fuel defects are categorized between manufacturing, operational, or design defects. Design defects are faults that occur due to the degradation of design features that are vulnerable to the harsh loads that act upon a fuel during its in-core life. Design defects therefore include inherent degradation mechanisms such as the stress-corrosion-cracking of the zircaloy sheath due to the effect of corrosive fission products, as well as internal overpressure of the element due to fission gas buildup [22]. Typically, design defects tend to occur when the fuel is near the end of its engineered life where material degradation can begin to encroach onto failure limits. Examples of stress corrosion cracking and fission-gas overpressure are shown below in **Figure 9**.

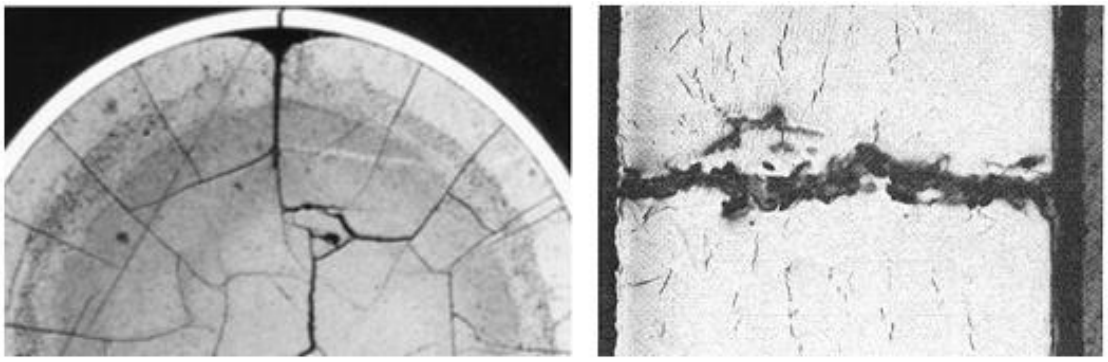

Figure 9. Diagrams depicting a formation of stress corrosion crack penetration on the inner surface of zircaloy sheath (left) and fission-gas overpressure break of sheath (right) [22,24].

Manufacturing defects, on the other hand, relate to faulty instances of manufacturing execution, typically observed in processes where the reliability of the resulting product is more vulnerable to lower quality control, such as welding. An example of an incomplete weld on a CANDU fuel element is shown below in **Figure 10**.

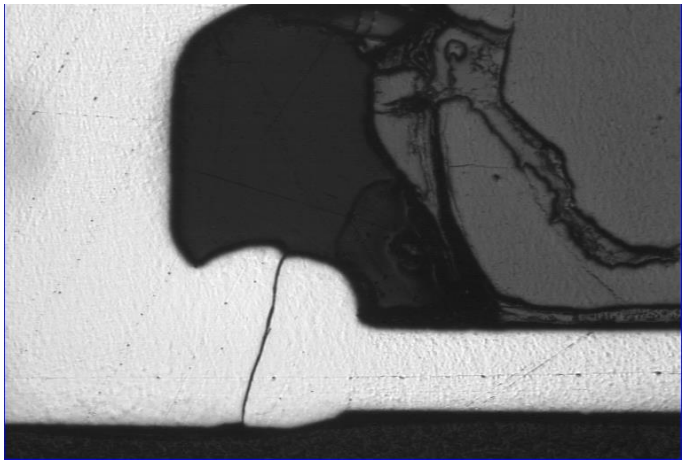

Figure 10. Incomplete end-closure weld on a CANDU fuel element [22].

Finally, operational defects relate to potentially damaging operational scenarios such as mechanical damage during fuel handling (typically during refuelling), as well as debris fretting or damages caused by acoustic resonance of standing waves in the coolant [22]. A photograph showing an example of fuel damage from debris fretting is presented below in **Figure 11**.

Figure 11. Fuel damage from debris fretting on a CANDU fuel element [22].

5.1.2 Detection and Removal of Fuel Defects

The CANDU industry has significantly improved the reliability of its fuel design, manufacturing techniques and operating methods, and has achieved fuel defect probabilities close to the WANO zero fuel defect criterion. However, fuel defects do still occur at a very infrequent rate. Therefore, utility operators require reliable detection, location and response mechanisms to mitigate their adverse consequences. The most commonly employed detection method consists of spatial coolant sampling where coolant samples are collected at various locations throughout the primary coolant loop, while at power [22]. The samples are then transported to an inspection laboratory where they are analyzed and screened for radioactivity as well as for concentrations of dissolved radioisotopes. This method provides the advantage of accuracy, however, it is limited by its extensive requirement for human resources, with its inevitable risk of occupational exposure during sample collection, transportation and handling, as well as disposal. An alternative and also commonly employed detection method is the Gaseous Fission Product (GFP) monitoring system, which is an automated, high-resolution gamma spectrometer that is integrated into the primary coolant loop. The GFP system, by the virtue of its integration into the coolant loop, can continuously monitor the coolant system for elevated radioactivity [22]. Generally, utility operators employ both methods in tandem for defect detection, such that the information gathered by one method may be

confirmed by the other, or be used in the absence of the other whenever one of the systems becomes unavailable.

When a defective fuel bundle is detected, its location must be determined to the level of its host fuel channel, such that the defective fuel may be removed by the on-power refuelling system from the affected channel at the earliest opportunity. This is a unique advantage of the CANDU reactor, as further spread of the fuel bundle damage and radioactive contaminants can be minimized. Two methods are typically used to this end, which are: the Feeder Scanning System (FSS) and the Delayed Neutron Scanning (DNS) system [22,25]. FSS consists of Geiger-Mueller detectors transported through guide tubes that run between the fuel channel lattices within the calandria. The FSS is utilized with the reactor at shut-down state, and its detectors can traverse across the outlet feeder tubes and measure the presence of elevated radioactivity emanating from coolant exiting the fuel channel containing the defective fuel. As the Geiger-Mueller detectors would become saturated if the reactor was on-power, the FSS method is disadvantaged by its requirement for reactor shutdown, and is generally only capable of detecting larger defects that can cause a substantial release of radioisotopes into the coolant.

The DNS method, on the other hand, is deployed with the reactor on-power, and is used to scan each of the fuel channels for delayed neutrons. The DNS system is integrated into the coolant system via coolant sampling lines, which are connected to each of the outlet feeders of fuel channels. This allows the representative coolant samples to be directly collected and examined from a centralized neutron scanning equipment room [22,25]. A schematic diagram of the DNS system is shown below in **Figure 12**. The target isotopes for the DNS system consist of neutron-emitting fission products such as Iodine-137 [22]. The DNS system provides significantly improved reliability over the FSS, as the monitoring can be conducted while on-power, and is capable of locating defects with an improved spatial resolution, sometimes down to the specific bundle position within the fuel channel.

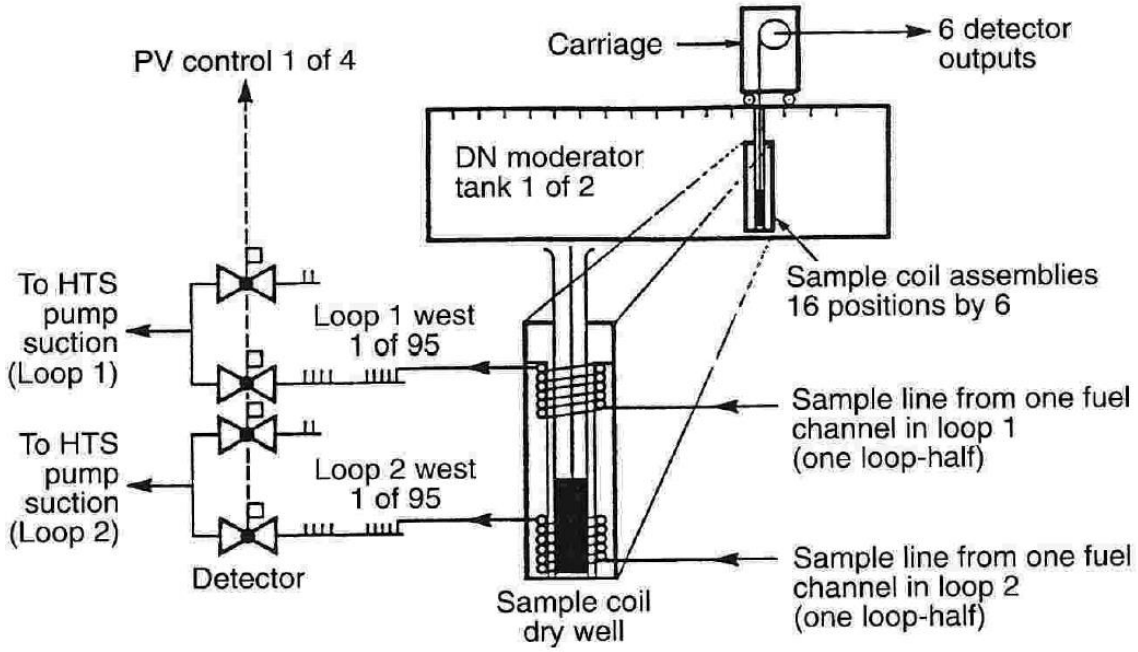

Figure 12. Schematic diagram of a delayed neutron monitoring system in a CANDU 6 reactor [23].

5.1.3 Sheath Failure Mechanisms

Fuel sheath failures result from a complex, inter-related combination of thermal-mechanical loads that cause deformations of the zircaloy sheath beyond the limit of its material strength. This phenomenon is aided by multiple mechanisms that cause changes to the sheath's physical material properties, as well loss of material strength due to corrosive chemical interactions driven by fission reactions and the formation of hydrides in the coolant. Some of these mechanisms relate directly to the formation of defects on the fuel sheath, whereas some create the conditions that significantly increase the probabilities of defect formation. In this study, the defect mechanisms of interest are limited to those of which are available in the fuel performance model that is incorporated within the ELESTRES and ELOCA codes [26,27]. The full list of known defect mechanisms for CANDU fuels, with indication of which mechanisms are tracked by ELESTRES and ELOCA, are shown below in **Table 2**.

Table 2. Defect mechanisms considered for CANDU fuels, excluding damages caused by accidents or dimensional incompatibilities during fuel handling/refuelling [9,26,27].

Mechanism	Description / Impact	Tracking by ELESTRES	Tracking by ELOCA
Pellet melting	• Molten UO_2 may flow into contact with the sheath and cause it to melt	Tracked	Tracked
Sheath melting	• Insufficient cooling may melt the zircaloy sheath, thereby resulting in fission product release	Tracked	Tracked
Contact overheating	• Reduced cooling due to coolant flow stagnation between sheath and neighbouring surface that can cause overheat failure	Not Tracked	Not Tracked
Crevice corrosion	• Restricted coolant flow in crevices can cause voiding during near-stagnant conditions. • Concentration of LiOH (coolant pH buffer) in the crevice can increase and accelerate sheath corrosion	Not Tracked	Not Tracked
Deformation via creep / thermal-expansion	• Deformations caused by thermal expansion and/or creep can cause the fuel to become larger than the available space within the channel • This incompatibility can lead to large stresses and fuel damage	Tracked	Tracked
Stress Corrosion Cracking (SCC)	• Corrosive fission products release to pellet-to-clad boundary • Stress-Corrosion-Cracking (SCC)	Indirectly Tracked[1]	Not Tracked
Fatigue	• Alternating stress caused by vibration, power manoeuvring and load following can cause fuel to fail through fatigue	Not Tracked	Not Tracked
High Strain-Rate Sheath Failure	• At high strain/creep rates, the fuel sheath can fail before the local sheath failure criterion is reached	Not Tracked	Tracked
Low-Ductility Sheath Failure	• Reduced strain failure limit at lower temperatures can cause athermal overstrain sheath failure at low strain values	Not Tracked	Tracked

[1] ELESTRES tracks pellet deformation at circumferential ridge and the fission-gas concentration, which is stored in TAPE26 and can be used by the post-processing codes, FEAST, INTEGRITY and SHEATH, to predict the probability of a defect formation due to stress-corrosion-cracking [26].

Table 2 (Continued).

Mechanism	Description / Impact	Tracking by ELESTRES	Tracking by ELOCA
Overstrain from Internal Gas and Coolant Pressures	• Stress & strain on sheath element induced by coolant pressure • Element pressurization due to release & build-up of fission gas • Sheath stress & strain induced by element internal pressure • Sheath creep	Tracked	Tracked
Primary hydride failure	• Congregation of hydrogen and deuterium at cooler locations or at locations of relatively higher stress causes reduced ductility of zircaloy	Indirectly Tracked[2]	Not Tracked
Oxide spalling and hydride lens formation	• When sufficiently thick oxide surface forms on the sheath, it may spall away and create a local temperature gradation, which can form local hydride/deuteride deposits which embrittle zircaloy	Not Tracked	Not Tracked
Overstrain with Oxide Cracks	• Oxidation of zircaloy sheath in water • Increased probability of crack formation and penetration against oxide layer on the outer surface of zircaloy sheath at low strain levels • Overstrain failure due to localized stress & strain at crack due to reduced sheath thickness	Not Tracked	Tracked
Oxygen Embrittlement & Hydraulic Shock Failure following LOCA	• Enhanced oxidation of zircaloy sheath via steam at high temperatures • Oxidative sheath embrittlement • Increased probability of embrittled sheath failure via impulsive hydraulic loading during re-wet	Not Tracked	Tracked
Beryllium—Assisted Crack Penetration	• Beryllium crack penetration of the sheath via liquid metal embrittlement in high-temperature conditions (transients)	Not Tracked	Tracked

[2] The FEAT code, which may be used to post-process ELESTRES outputs is capable of modelling temperature and solid mechanics effects caused by pellet-to-end-cap interactions and end-flux peaking. The FEAT code in turn, can be paired with the FEED code in order to model hydriding of the fuel sheath [26].

As indicated by **Table 2**, the primary mechanism by which a zircaloy fuel sheath may fail is by thermal-mechanical stress and strains. This mechanism includes a chain of thermal effects caused by volumetric heating and heat transfer, such as thermal expansion and creep, as well as mechanical loads induced by fuel-to-sheath contact and the balance between coolant and element internal pressures. Generally, the specific failure criterion tracked for this mechanism is the occurrence of sheath strain values beyond the zircaloy's material limit. However, the overall mechanism tracked by ELESTRES and ELOCA includes many assisting processes that are relevant to the net sum of stress and strain interactions. This includes the pellet densification and swelling phenomena for their effects on heat transfer and linear power, pellet-to-sheath contact, as well as fission gas migration from the pellet to the pellet-sheath gap [26,27].

The ELOCA code also tracks failure mechanisms that are more prevalent during transient conditions which include brittle, low-strain failure pathways such as impulsive, high strain-rate failure which may exist during sudden and large power ramps, as well as athermal overstrain failure at low temperatures. In addition, the oxide and crack-assisted failure mechanisms are also tracked by ELOCA, which include overstrain failure with sheath degradation via oxide cracks, embrittlement failure via steam oxidation and impulsive re-pressurization following a LOCA, and beryllium-assisted crack penetration at high temperatures [27]. The stress corrosion cracking phenomenon may also be indirectly tracked via post-processing the results of ELESTRES using the FEAST, INTEGRITY and SHEATH codes, but is not included as part of this study [26]. Similarly, primary hydriding may also be tracked indirectly via post-processing the results of ELESTRES using FEAT and FEED codes, but is not included as part of this study [26].

5.2 Fuel Manufacturing

A CANDU fuel is designed and manufactured under critical consideration for its safety performance against all failure mechanisms, in addition to the economic considerations. Due to the stringent safety regulations that govern the industry, as well as the complicated bundle design that is implemented, the manufacturing process for CANDU fuel requires a high degree of precision and accuracy. Strict quality control and assurance programs are therefore implemented to ensure that deviations from the target design parameters are minimized to stay within tight tolerance limits.

5.2.1 Fuel Pellet Manufacturing

The manufacturing of the UO_2 pellet starts with the receipt of the UO_2 powder, which is typically pre-processed physically to improve its "compactability" characteristics when forced into pellet pressing dies. This pre-processing involves the compaction followed by a granulation of the powder, as well as addition of a lubricant which helps to reduce the tendency of UO_2 powders to agglomerate and impede the consistent filling of the pellet pressing dies. Next the UO_2 powder is pressed into its designed shape, after which it is sintered. This process requires temperatures in excess of 1600℃ for at least one hour in order to achieve densities greater than 90% of theoretical, all the while carefully avoiding excessively high firing rates [28]. Within the hierarchy of importance for the pellet manufacturing process, the sintering step is critical due to its significant impact on the distribution of pellet density, as well as preventing the formation of cracking or chipping. Therefore, the sintering process requires a precise control of temperature, time as well as the atmosphere that the pellet is subjected to during the sintering cycle. The cross-section of a UO_2 pellet, which has been distorted by an excessively high firing rate and failed to properly densify, is presented below in **Figure 13** to illustrate the impact of sub-optimal sintering.

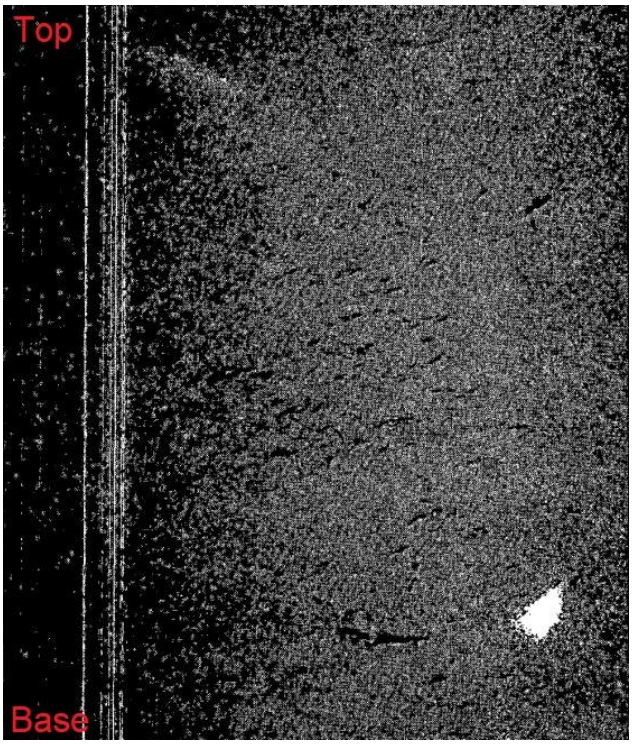

Figure 13. Cross-section of a UO_2 pellet showing high porosity at base caused by high firing rate in excess of 200°C per hour, sintered between 1200 and 1650°C (10X magnification) [28].

The pressing and sintering of the UO_2 powder produce an hourglass shaped pellet that must be ground down to remove the hourglass shape and produce the desired cylinder-shaped pellet. The hourglassing effect of sintering is caused by the as-pressed densities of the UO_2 powder being higher near the pellet ends than at the centre, prior to sintering [9]. This is because the pellet pressing process involves contact-pressures that are driven and counteracted at the end-faces of the pellet. Consequently, the sintering process causes greater densification at the midplane than ends that are already at a higher initial density. The ground pellets are then sorted by diameter such that they can be matched for precise diametric clearances as they are placed into stacks within fuel rod elements. This is necessary because end pellets may require reduced diameter to account for weld-induced shrinkage of the tube element, or to account for requirements pertinent to differing designs of CANDU fuels that employ differing tube element diameters.

Finally, the pellets are placed into stacks and sorted in relation to the tube-element lengths in order to ensure a precise control of the axial clearance between the pellet stack and the tube element end fittings. This sorting process is critical to ensuring a precise adherence to the diametric clearance requirement and the prevention of "over-stuffed" fuel elements. The above process has an important impact on defect formation as it can significantly affect the end-flux peaking phenomenon, the volumetric margin of the element plenum to account for fission gas release, as well as the pellet-to-pellet and pellet-to-sheath clearances to account for pellet swelling.

5.2.2 Production of Sheath Sub-assemblies

The CANDU fuel sheath is manufactured using zircaloy-4, which is an alloy of zirconium, tin, iron and chromium. Zircaloy-4 is an excellent material for nuclear fuel sheath as it is a metal alloy that has highly desirable corrosion-resistance properties, as well as a low thermal neutron absorption cross-section, good heat resistance and suitable mechanical properties [9]. For CANDU fuels, zircaloy-4 is manufactured in tube forms. This is a highly precise process with very tight quality control and assurance steps that are built-in to minimize the occurrence of manufacturing defects. The fabrication of CANDU fuel sub-assemblies first starts with the receipt of zircaloy-4 tubes that have been produced to the required diametral specification and then cut to the specified length requirements from the material manufacturer. In parallel to the receipt of the zircaloy tubes, auxiliary material such as zircaloy sheet, strip, bar, and rods are received for their use in the fabrication of appendage components such as spacers, bearing pads and end-caps [9]. In addition to the zircaloy, graphite slurry for use in CANLUB coating, and beryllium for brazing [9] are also received.

The appendage components vary in production techniques depending on initial material used. For example, if the zircaloy sheet is used, the sheet is first coated with beryllium, then punched and coined into the final desired shape. When manufactured

from wire, the appendages are cut to length, coined, then coated with beryllium. The produced appendages are then attached to the tube elements using spot welding and are brazed, where heat is applied until the beryllium coating forms an alloy with the zircaloy metal in the appendage and the tube [9]. The above processes are tightly controlled in order to ensure the appendage dimensions, the shape of coined surfaces, as well as the thickness of brazing material and their locations of attachment are consistent with design specifications, as they are critical in ensuring a seamless assembly and dimensional compatibility.

The CANLUB coating is created using the graphite slurry, which is first diluted with an industrial-grade alcohol, then is applied to the inside surface of the tube sub-assembly. The tube sub-assembly is then heat-dried in a desiccating oven, which cures the coating mixture. This results in the graphite coating that is conventionally referred to as the CANLUB coating, which helps mitigate the occurrence of stress-corrosion-cracking by providing a protective layer for the fuel sheath element from interfacing with corrosive fission products. This process is also precisely controlled in order to ensure an exact thickness and hydrogen content, as it can affect the diametral clearance of the pellet-to-clad interface, as well as the potential hydriding of the sheath element under high-temperature conditions during irradiation [9].

5.2.3 Fuel Element Assembly

Following the CANLUB coating process, the ends of the sheath assemblies are machined to a precise length to produce the end-surface profile required for end-cap welding. Additionally, any residual CANLUB and other debris may be removed from the sub-assemblies. It is at this point; the pellet stacks are inserted into the sub-assemblies and the end-caps are welded onto the tubes using electro-thermal resistance welding. During this process, the tube element is purged and then blanketed with inert helium fill gas to ensure the air trapped within the element is removed while the welds

are closed. The end-caps are machined from the zircaloy bars and rods to exactly match the sheath sub-assembly weld-prepping, as well as their interface to the end-plate for the final element assembly. As mentioned previously for the sorting of ground UO_2 pellets, the end-caps experience a diametral shrinkage during welding due to the combination of heating and cooling processes involved with the weld cycle and the restraint provided by the collet that is used to affix the tube element in place during welding. For this reason, the end pieces of the UO_2 pellet stacks are sorted to ensure they have a reduced diameter that is commensurate with the diametral shrinkage caused by the welding of the end-caps. The end-cap welding process is a critically important step in the manufacturing of CANDU fuels, as it has an important impact on the overall structural integrity of the fuel. For this reason, although very few fuel defects have been experienced in the long operating history of CANDU reactors, among the ones that have been identified to be caused by manufacturing faults, more than 90% have been attributed to faulty or incomplete end-cap welding [9]. Finally, following the end-cap welding, the fuel elements are inserted into an assembly affixture jig and the elements are resistance-welded to end-plates to form the final bundle assembly. The end plates are fabricated from zircaloy sheets.

5.2.4 Description of Design Parameters

The CANDU fuel design parameters are largely grouped into three categories: pellet, element (or rod), and the bundle. The full list of design parameters considered during the manufacturing process is provided below in **Table 3**, **4** and **5**. Each of the parameters are quality controlled to be kept rigorously within manufacturing tolerance limits that reside within a narrow acceptance envelope around the design value of the parameter. This is because each of the parameters may have a significant impact on the safety performance of the fuel, especially during exasperated stress conditions such as during an accident scenario (transient).

Table 3. Summary of CANDU fuel bundle design parameters [9,22].

Bundle Design Parameters	Impact on Fuel Safety Performance
Bundle Diameter	• Dimensional compatibility • Impact on fuel volume, both fissile content as well as free volume • Coolant by-pass-flow characteristics
Bundle Length	• Dimensional compatibility • Impact on fuel volume, both fissile content as well as free volume
End Plate Thickness	• Impact on neutron flux shape in the vicinity of the end-plate region • Effect on end-flux-peaking • Structural strength of end-plate (which may be affected by alternating stress from fuel element deflections)
Latch-Mating Bundle Surface Profile	• Dimensional compatibility
Element to Element Clearance	• Affect coolant flow
Element Orientation / Match-up	• Dimensional compatibility • Affect alternating stress from fuel element deflections
End Plate Waviness	• Dimensional compatibility
End Plate Squareness	• Dimensional compatibility
End Plate Metallographic Homogeneity	• Impacts consistency of material property • Differential rate of thermal expansion
End Plate Web Widths	• Structural strength of end-plate • Impact on neutron flux shape in the vicinity of the end-plate region • Effect on end-flux-peaking • Affect coolant flow
End Plate Tensile Strength	• Structural strength
End Cap to End Plate Weld Strength	• Structural strength
Surface Conditions / Contamination	• Impact on quality of manufacturing processes • Impact on surface corrosion • Impact on coolant flow characteristics against surface

Table 4. Summary of CANDU fuel element design parameters [9,22].

Element Design Parameters	Impact on Fuel Safety Performance
Bearing Pad Height	• Dimensional compatibility • Affect bearing-pad fretting, sliding wear, and crevice corrosion in pressure tubes
Sheath Diameter (ID/OD)	• Affects collapsibility of the sheath • Structural strength
Bearing Pad Surface Condition	• Impact on quality of manufacturing processes • Impact on surface corrosion • Impact on coolant flow characteristics against surface
Minimum Spacer Height	• Dimensional compatibility • Affect element-to-element clearance and coolant flow • Affect spacer-pad wear and vibrational fretting
End Cap / Sheath Weld Interface	• Structural strength
End Cap Weld Steps	• Structural strength
Bearing Pad Parallelism	• Dimensional compatibility • May affect coolant flow • May cause uneven load sharing between bearing pads
Bearing Pad Edge Radius	• Dimensional compatibility • May cause uneven load sharing between bearing pads
Minimum End Cap Thickness	• Impact on neutron flux shape in the vicinity of the end-cap region • Effect on end-flux-peaking • Structural strength
End Cap / Sheath Weld Strength	• Structural strength
Braze Heat Affected Zone Grain Structure	• Affect material property • Structural strength
Hydrogen Content of Fill Gas	• Affect hydrogen embrittlement of zircaloy
Sheath Mechanical and Chemical Composition	• Affect material property
Minimum Sheath Thickness	• Affect structural strength • Affect neutron flux
Pellet / Sheath Diametric Clearance	• Affect free volume in the element • Affect collapsibility of sheath • Affect sheath-to-pellet contact
Pellet Stack / End Cap Axial Clearance	• Affect free volume in the element • Affect pellet-to-endcap contact • Affect end-flux-peaking
CANLUB coverage, thickness, adhesion, and curing	• Affect corrosive/oxidative degradation of sheath clad
Surface Condition / Contamination	• Impact on quality of manufacturing processes • Impact on surface corrosion • Impact on coolant flow characteristics against surface

Table 5. Summary of CANDU fuel pellet design parameters [9,22].

Pellet Design Parameters	Impact on Fuel Safety Performance
Pellet Shape / Dimensions	• Affect free volume in the element • Affect collapsibility of sheath • Affect sheath-to-pellet contact
Pellet Microstructure	• Affect grain growth & fuel restructuring • Affect pellet density & heat transfer properties • Affect fission gas release (coarser grain release less) • Fracture resistance (better resistance in fine grain)
Pellet Impurities / Equivalent Boron Content (EBC)	• Affect economy of neutrons via parasitic absorption of thermal neutrons
Pellet Surface Roughness	• Affect pellet-to-sheath contact area, which affects gap thermal conductivity and therefore gap heat transfer
Pellet Density	• Affect thermal conductivity in the pellet
Surface Condition / Contamination	• Impact on quality of manufacturing processes • Impact on pellet-to-sheath contact • Impact on economy of thermal neutrons

The generic design values for the 37-element CANDU fuel geometry, adapted from [9], are shown below in **Table 6** and **7**.

Table 6. Summary of generic CANDU fuel geometry parameter targets [9,22].

Design Parameters	Design Value
Overall bundle length	495 mm
Overall maximum bundle diameter	102 mm
Element length	493 mm
Element outer diameter	13 mm
Sheath clad thickness	0.4 mm
Pellet outer diameter	12 mm
Pellet length	16 mm
Endplate width, outer ring	4.9 mm
Endplate thickness	1.6 mm
Diameter of assembly weld	4 mm

Table 7. Summary of CANDU fuel material parameter targets [9,22].

Pellet Design Parameters	Design Value
Uranium weight per bundle	19.2 kg
Pellet density (design theoretical)	10.97 g cm^{-3}
Pellet density (as fabricated)	10.75 g cm^{-3}
Pellet thermal conductivity at 1000 ℃	2.8 W (m K) $^{-1}$
Pellet specific heat capacity at 1000 ℃	328 J (kg K) $^{-1}$
Pellet melting point at zero burnup	2840 ℃
Pellet-to-endcap heat transfer coefficient (at high power, hard contact, low burnup)	1 kW $(m^2 K)^{-1}$
Pellet-to-sheath heat transfer coefficient (at high power, hard contact, low burnup)	80 kW $(m^2 K)^{-1}$
Pellet Young's modulus at 1000 ℃ (at 98% theoretical density)	190 GPa
Pellet Poisson's ratio	0.316
Pellet yield strength at 1000 ℃ (for 25 micron grain size)	180 MPa
Pellet coefficient of linear thermal expansion at 1000 ℃	12.5 μm (m K) $^{-1}$
Zr-4 weight per bundle	2.2 kg
Zr-4 sheath density	6.56 g cm^{-3}
Zr-4 thermal conductivity at 300 ℃	16.4 W (m K) $^{-1}$
Zr-4 specific heat capacity at 300 ℃	327 J (kg K) $^{-1}$
Zr-4 melting point	1850 ℃
Zr-4 sheath-to-coolant heat transfer coefficient	50 kW $(m^2 K)^{-1}$
Zr-4 Young's modulus	80 GPa
Zr-4 shear modulus	27 GPa
Zr-4 Poisson's ratio	0.37
Zr-4 yield strength at 300 ℃ (78% cold-worked and stress relieved at 510 ℃)	274 MPa
Zr-4 coefficient of linear thermal expansion	6.72 μm (m K) $^{-1}$

5.3 Fuel Management

As shown previously in **Figure 8**, the major cause for CANDU fuel defects is due to rapid power ramps. These power ramps can be caused by many aspects of reactor operation, such as the effects of refuelling ripples, movement of adjuster rods and zone controllers, as well as movement of control rods used to control the overall power rating of the reactor. The practice of operational fuel management is therefore a very important aspect of preventing fuel defects by preventing or minimizing the occurrence of rapid power variations or manoeuvres that are conducive to fuel failures.

5.3.1 On-power Refuelling

In nuclear reactor physics, the maintenance of the state of "criticality" is of great importance to the control of the reactor. A nuclear reactor is considered "critical" when the balance of neutrons generated at an instance in the overall, continuous cycle of fission chain reaction is equal to the net quantity of neutrons lost and consumed in the previous instance in the cycle. This ensures that the continuous process of generation of neutrons within the reactor core iterates in a stable manner without a runaway expansion in the net number of neutrons produced, which is a state referred to as "super-critical." Furthermore, this also avoids the situation where the net balance of neutrons at each instance within the cycle is less than that of the previous cycle, which is a state referred to as "sub-critical," and it causes the net number of neutrons produced to decline over time until the fission chain reaction ceases altogether. The concept of criticality is expressed in terms of the effective multiplication factor, k_{eff}, which is the neutron balance ratio between the current generation to the previous generation in the cycle, with consideration for losses by leakage. An important measure relating to the effective multiplication factor of the core is the reactivity of the core. The reactivity of the core is defined as the measure of its fractional departure from the state of core criticality equal to unity, which is the ideal state when the reactor is exactly critical [18]. Expressed in terms of the k_{eff}, the reactivity is a unitless quantity commonly measured in "pseudo units" such as "milli-k" or "mk," which is the unit used within the Canadian nuclear industry. The equation for reactivity, ρ, where 1 mk is when ρ is equal to 0.001, is as follows:

$$\rho = \frac{k_{eff}-1}{k_{eff}} \tag{5.1}$$

The reactivity of a nuclear reactor core therefore governs the rate of change of the neutron population in the current generation in comparison to the previous generation, within its finite boundaries. For an exactly critical reactor, accounting for the neutron leakage outside the core, k_{eff} is equal to 1 and ρ is equal to 0. Thus, the ideal value of

reactivity for a nuclear reactor is equal to 0, but in practice this value will fluctuate by a very small amount above and below 0. To maintain and replenish the decline in core reactivity due to fuel burnup, a nuclear reactor must be refuelled, where spent fuel bundles are replaced with fresh ones. In batch (or bulk) fuelled reactors, large quantities of irradiated fuel assemblies are replaced at each instance of refuelling, up to a quarter or even a third of the core load [18]. Bulk fuelled reactors therefore require refuelling only at low frequencies, as each instance of refuelling inserts a large sum of excess positive reactivity that must be suppressed. In CANDU reactors, refuelling operations replace small, discrete quantities of irradiated fuel bundles with fresh fuel bundles on a daily basis [18], with upwards of 3 fuel channels refuelled in a 24-hour period. This type of discrete, routine refuelling allows CANDU reactors to operate at essentially constant criticality by refuelling at a rate that is proportional to the rate of reactivity decline within the core [18]. This rate is approximately 0.42 mill-k per each Full Power Day (FPD) operation of a 480-channel, 2650 MW (thermal) model of CANDU core, which typically can be met via the refuelling of two different fuel channels in a day.

The refuelling operation for CANDU reactors uses a push-through methodology, which involves fresh fuel bundles being inserted into the fuel channel at the one end while the spent fuel bundles are pushed out of the core at the opposite end of the channel. This procedure is conducted while maintaining the reactor at full power and the positive pressurization (approximately 10 MPa) of the fuel channel by means of the reactor's pressurizer in conjunction with the pressurizers of the refuelling machines which lock onto both ends of the fuel channel that is being refuelled. A drawing of a typical fuelling machine is shown below in **Figure 14**, with an illustration of the push-through refuelling methodology in **Figure 15**, and a picture of the fuelling machine used at the Darlington Nuclear Generating Station (DNGS) is shown in **Figure 16**. Each refuelling typically results in either four or eight fuel bundles being replaced within the channel. The peripheral channels which produce lower powers are typically refuelled using an 8-bundle-shift refuelling mode, whereas the central, high-powered channels are preferably refuelled using a 4-bundle-shift refuelling mode.

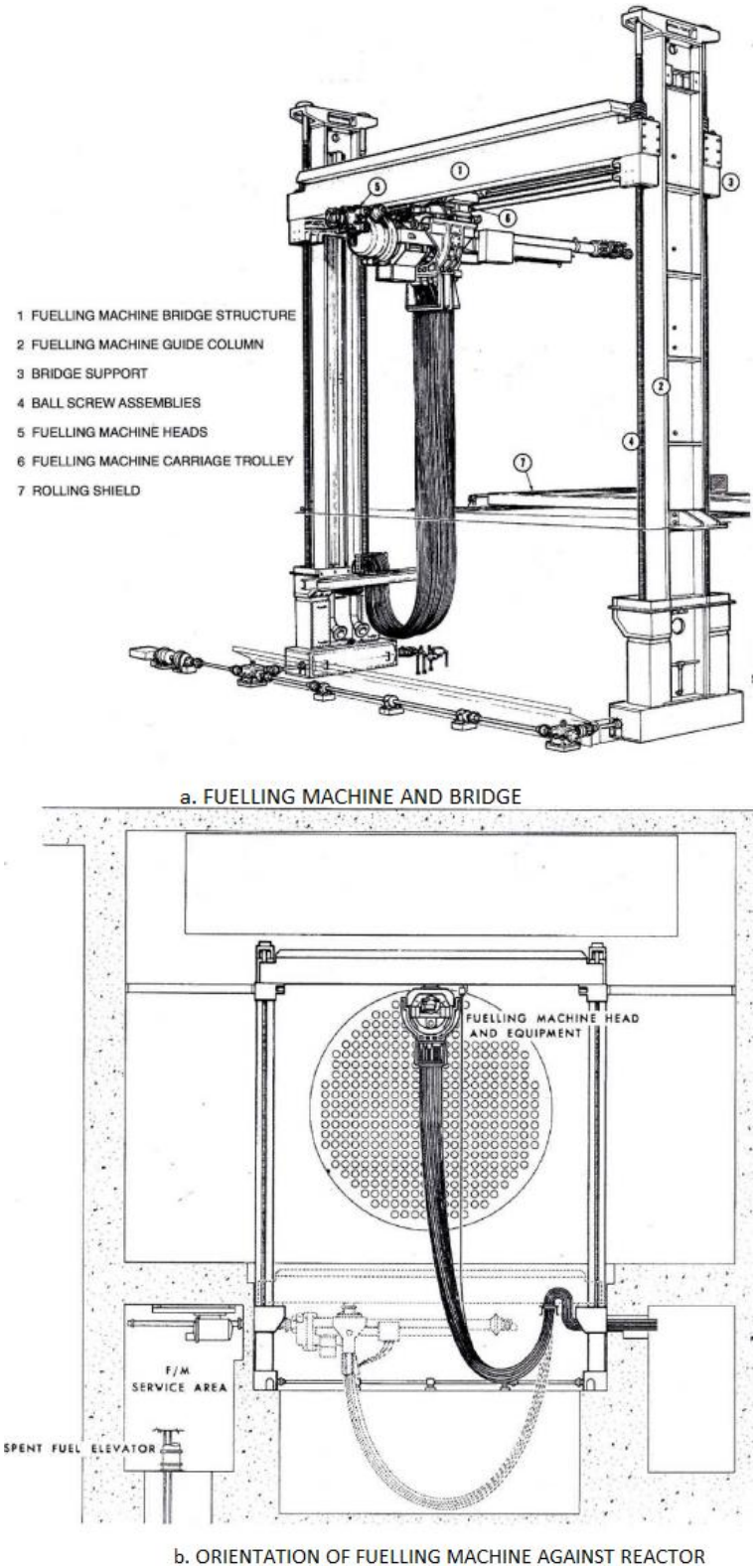

Figure 14. Typical refuelling machine design used for CANDU reactors [8].

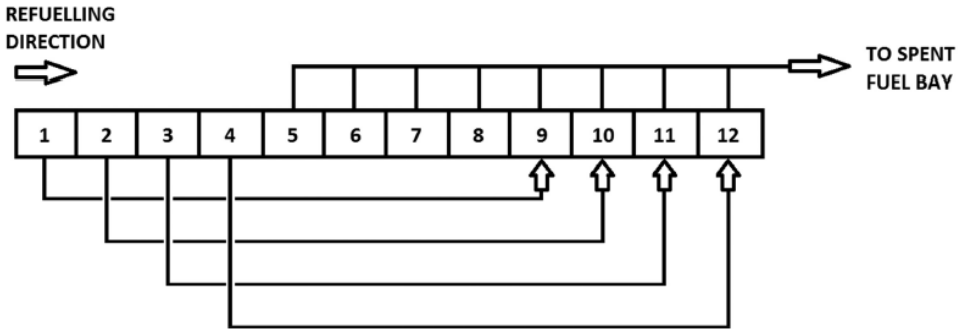

Figure 15. Push-through refuelling method used in CANDU reactors. An 8-bundle-shift refuelling mode is depicted [21].

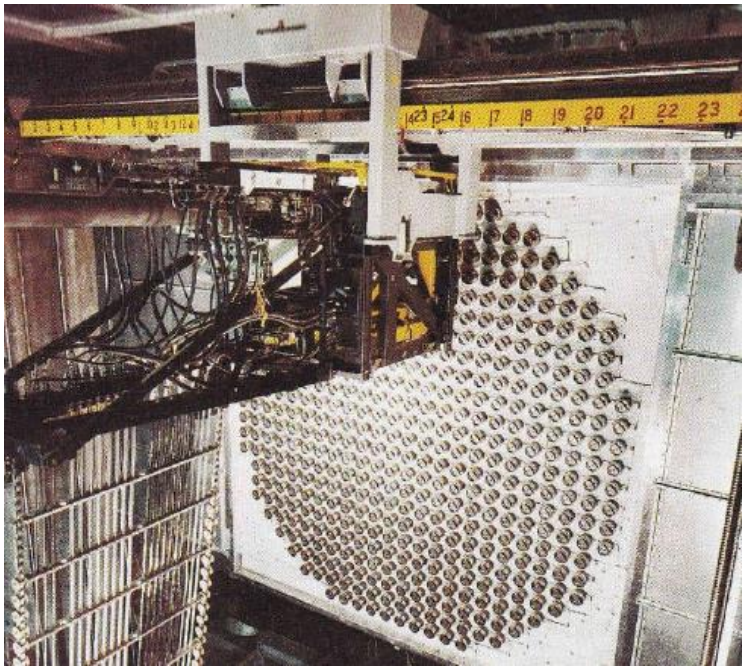

Figure 16. The radial face of a Darlington reactor core with a fuelling machine [8].

5.3.2 Refuelling Ripples

Due to their characteristic of on-power refuelling, the distribution of power density across a CANDU core is in constant perturbation. These perturbations, also known as refuelling ripples, are fundamentally caused by the routine insertion of fresh fuels in place of highly irradiated ones, and it occurs as a combination of two separate phenomena: The Fuelling Transient (FT), and the Plutonium Peak (PP). The fuelling

transient is a term used to describe the instantaneous increase in local flux and power density which occurs in the vicinity of a freshly inserted fuel unit when it replaces an old, spent fuel unit in its place. This is a phenomenon which occurs in all types of nuclear reactors which refuel by discretely replacing spent fuels units with fresh ones, and it causes localised power density perturbations whenever the refuelling takes place. For bulk-fuelled reactors, however, this phenomenon is minimized and does not result in continuous instances of localized power density perturbations following each refuelling. This is because for bulk-fuelled reactors, the fresh fuel assemblies are designed according to their intended position in the reactor core, and initially provided with graded fuel enrichments and neutron absorbers. Some of the fresh fuel assemblies are designed to contain control rod channels in the case of PWRs. For BWRs, some assemblies are intended to be positioned against the cruciform control blades and are designed differently than other assemblies. Due to this design, bulk-fuelled reactors discharge some of its assemblies from the core, shuffle some into to new positions, and load fresh fuel assemblies into the core at each refuelling outage, which in turn minimizes the refuelling reactivity transients by maintaining a relatively constant distribution of fuel reactivity. By contrast, in CANDU reactors, the increase in power density due to the fuelling transient occurs in small part due to the replenishment of fissile isotope content within the lattice, but mostly due to the removal of fission products within the old fuels [21]. Many fission products possess large neutron absorption cross-sections that induce a significant net negative reactivity within the affected fuel lattice. These fission products may be categorized into two types: saturating and non-saturating.

The saturating fission products are generated quickly in the early stages of fuel burnup, then rapidly reach equilibrium concentrations due to decay processes that counterbalance their generation [21]. The decay processes of the saturating fission products consist of neutron absorption followed by the transmutation of the target nucleus into a radionuclide, which subsequently results in radioactive decay. The rate of radioactive decay depends on both the decay constant, or the half-life of the radioisotope,

and the value of its concentration at an instance. In the case of saturating fission products, their concentration values are relatively quick to reach saturation because of their very large neutron absorption cross-sections, which promote their transmutation and thus inhibit their accumulation. The equilibrium concentration at the point of saturation depends on the ambient neutron flux, as it affects the rates of generation and conversion.

Non-saturating fission products, in contrast to saturating, accumulate over time without reaching an equilibrium. Non-saturating fission products therefore eventually cause the fuel lattice to become subcritical, thereby imparting a net-negative effect on the reactivity of the core [21]. The accumulation of non-saturating fission products and the eventual fuel sub-criticality is a relatively slow and linear processes, with lattice sub-criticality typically occurring at a burnup value of approximately 170 MWh(kg·U)$^{-1}$ for CANDU fuels [9]. The production of saturating fission products up to their equilibrium concentrations, however, is a significantly faster process, which typically occurs within the first two to three FPDs of irradiating the newly inserted fuels [21]. This is because saturating fission products with the largest neutron cross-sections such as Xe-135, Sm-149, Sm-151 and Rh-103 reach their equilibrium concentrations during this relatively short period of time [21]. The local reactivity of fresh fuels during the first two to three FPDs of in-core irradiation therefore follows the shape of a sharp peak, which is also mirrored by its local flux and power density.

The second component of the refuelling ripple is the plutonium peak, and it is a characteristic unique to natural uranium fuels, such as the fuels used for CANDU reactors. NU fuels contain approximately 0.71% U-235, and 99.28% U-238, and a trace amount of U-234. The plutonium peak occurs due to the high U-238 isotope content within NU fuels. U-238 is transmuted into Pu-239, a fissile isotope, via the capture of a neutron followed by a double beta decay. This process can be represented as follows:

$$^{238}_{92}U + ^{1}_{0}n \rightarrow \ ^{239}_{92}U \xrightarrow{\beta^-} {}^{239}_{92}Np \xrightarrow{\beta^-} {}^{239}_{92}Pu \tag{5.2}$$

As the fresh fuel is irradiated, the concentration of Pu-239 accumulates over time, resulting in an increase in the net reactivity of the fuel lattice, which is accompanied by an increase in the local neutron flux and power density. This increase occurs until a peak value is reached, after which the reactivity declines in a linear shape. Although there is little change to the inventory of U-238 to be converted within the fuel, this peak-and-decline effect of the reactivity occurs due the accumulation of non-saturating fission products that overcomes the accumulation of Pu-239 [21]. Typically, the plutonium peak occurs between forty to fifty FPDs of in-core irradiation in contrast to the fuelling transient. The evolution of the overall fuel lattice reactivity for the 37-element CANDU fuel, as a function of burnup, is shown below in **Figure 17**. The initial peak in the neutron multiplication factor of the lattice corresponds to the fuelling transient, and the second, smaller peak corresponds to the plutonium peak.

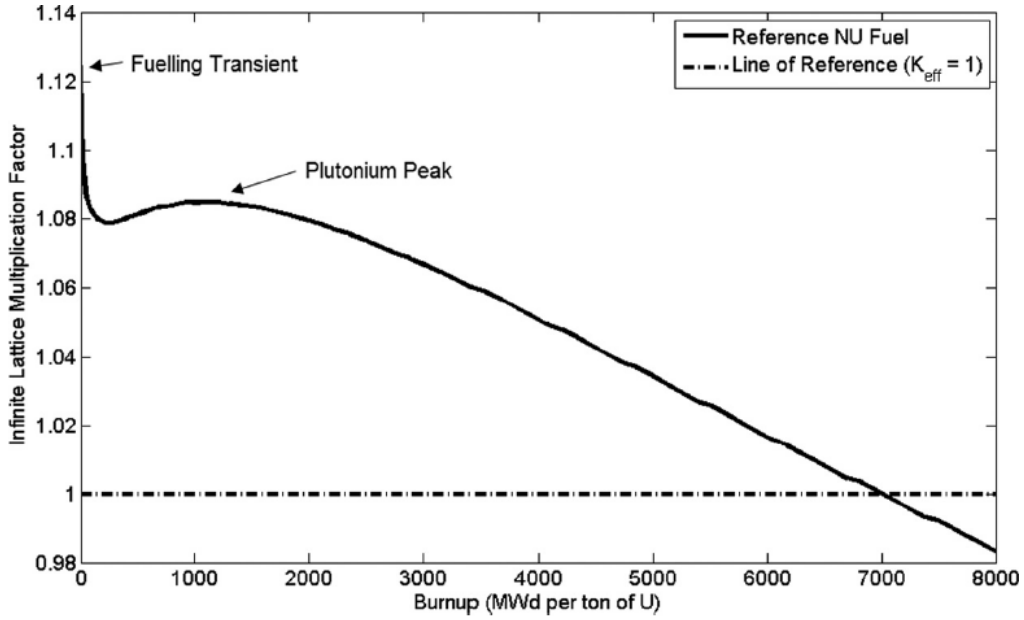

Figure 17. Evolution of lattice reactivity (k_{inf}) against burnup for a typical CANDU fuel [21].

The fuelling transient and the plutonium peak, which are propagated by the routine refuelling operations that is characteristic of CANDU reactors, result in constant perturbations of localized neutron flux and density that resemble “ripples” when

examining the radial power distribution (channel powers) of the core. A diagram depicting the channel power distribution of a CANDU core (radial face of the core) is shown below in **Figure 18**.

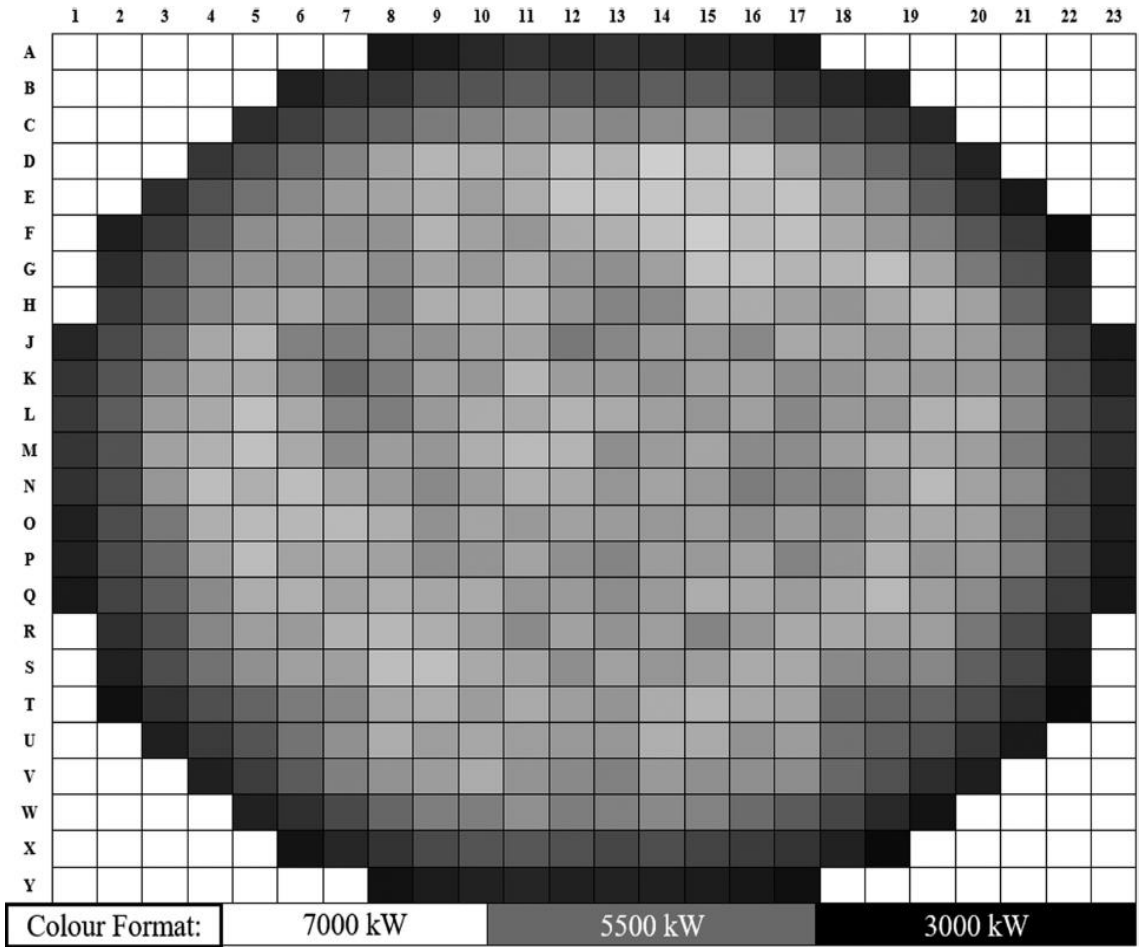

Figure 18. Radial (channel) power distribution of a 480-channel, 2650 MW (thermal) CANDU core [21].

5.3.3 Reactivity Control

From the perspective of fuel management, refuelling power ripples pose a challenge to maintaining the target operating power envelope of fuel channels due to the spatial instability that they pose. CANDU fuel engineers must therefore take into account the impact of refuelling ripples on the overall effort for reactivity control. A

well-established control of the reactivity within the core is an important requirement for the safe and steady operation of all nuclear reactor types. This involves ensuring that the "bulk" reactivity of the core, which is the net reactivity of the core, is maintained consistently at a small excess from the critical state. Simultaneously, the "spatial" distribution of reactivity, which affects the power density distribution within the core, must also remain evenly balanced without excessive, localized peaking.

For CANDU reactors, reactivity control is primarily accomplished via refuelling management. This involves strategically choosing the rate at which refuelling takes place, the location of the channel to be refuelled next, as well as how many fuel bundles are inserted and replaced at each time. The above considerations directly affect the positions of localized positive reactivity insertions into the core, and when utilized correctly, it can practically and effectively control the net balance and distribution of reactivity within the core at a steady equilibrium across time. This is the key advantage of the on-line refuelling feature that is available in CANDU reactors. However, the CANDU reactor still incorporates a series of reactivity devices to assist with the overall effort for controlling the bulk and spatial reactivity within the core. The types of reactivity devices, including safety devices, used within CANDU reactors are listed below in **Table 8**. An overall schematic of reactivity devices distribution within the CANDU core is shown below in **Figure 19** and **20**.

Table 8. Reactivity devices' worth, for a 380-channel, 2064 MW (thermal) CANDU 6 reactor model [29].

Device	Function	Total Reactivity Worth (milli-k)	Maximum Reactivity Rate (mk s^{-1})
14 Liquid Zone Controllers	Control	7	± 0.14
21 Adjusters Rods	Control	15	± 0.10
4 Mechanical Control Absorbers	Control	10	± 0.075 (driving) - 3.5 (dropping)
Moderator Poison	Control	N/A	- 0.01 (extracting)
28 Shut-off Rods	Safety	80	- 50
6 Shut-off Poison-Injection Nozzles and associated tanks and plumbing	Safety	> 300	- 50

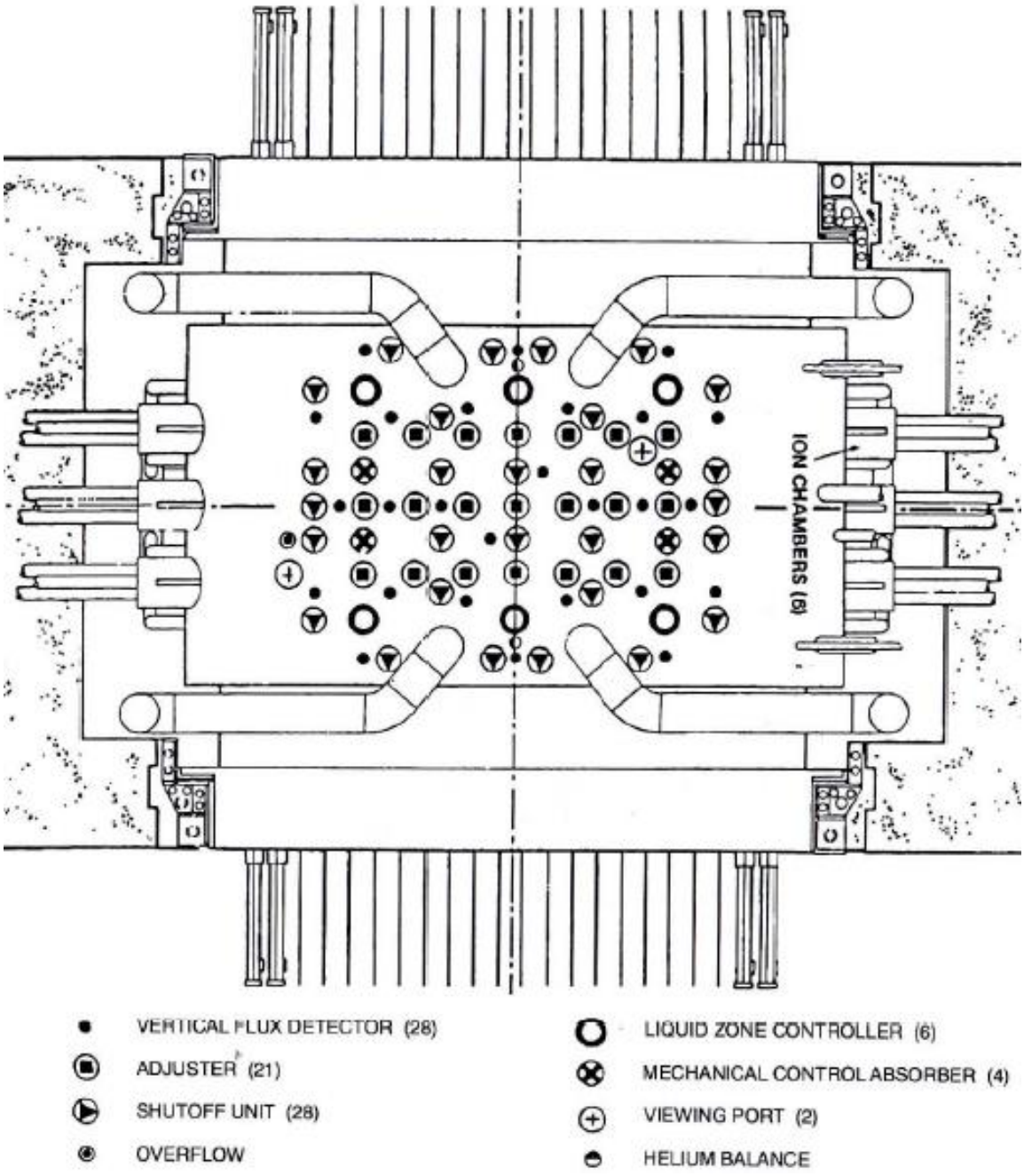

Figure 19. Bird's eye view of the 380-channel, 2064 MW_{th} CANDU 6 reactor core, with guide-tube insertion points for each of the rod-type reactivity devices and instrumentations [8].

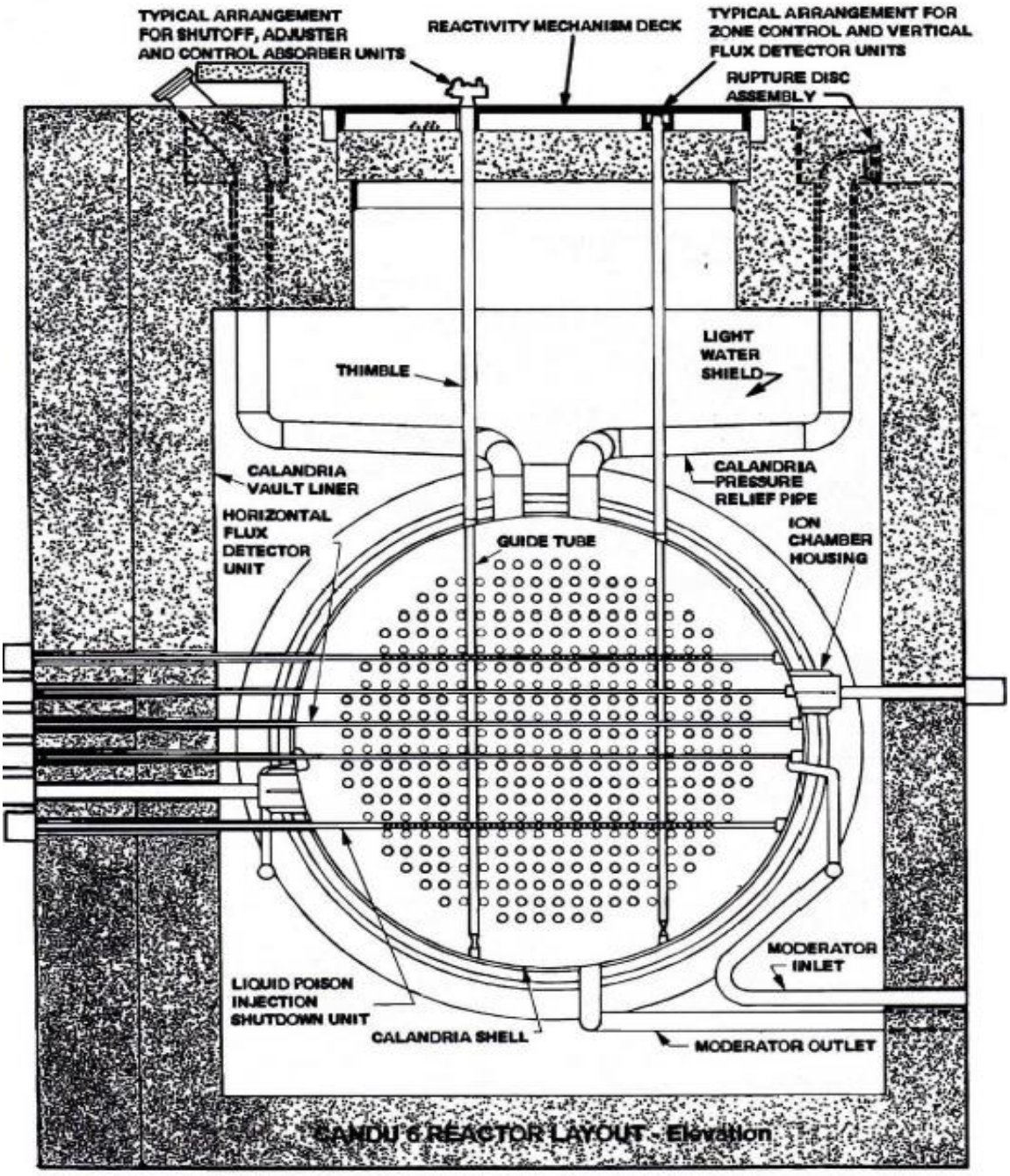

Figure 20. Radial face view of the 380-channel, 2064 MW_{th} CANDU 6 reactor core, with depiction of guide tubes traversing the reactor core vertically, and liquid poison injection units traversing the reactor core horizontally [8].

The bulk reactivity control for CANDU reactors is primarily provided via controlling the rate of refuelling of the core. This is a significant contrast against batch-fuelled reactors, for which the bulk reactivity control, as well as the spatial, are primarily implemented via the slow and spatially varied withdrawal of control rods from the core. This method is necessary for batch-fuelled reactors in order to suppress then slowly release the initially large excess reactivity that varies with incremental fuel burnup. For CANDU reactors, however, due to the unique feature of on-line refuelling, a large excessive reactivity is not required to maintain the core critical for extended periods of time without refuelling. This is one of the main safety-related advantages of the feature, in addition to the use of a heavy water moderator, that allows the use of natural uranium fuels within CANDU cores. A CANDU reactor at all times, maintains a relatively small quantity of net-positive reactivity. This reactivity is typically suppressed to a small margin above criticality via the continuous, dynamic engagement of its 14 Liquid Zone Controllers (LZCs) and the 4 mechanical control rods, as well as the 21 (for the CANDU 6 design) adjuster rods that are permanently engaged within the core.

For optimal power production, it is necessary to flatten the neutron flux shape of the CANDU core in both the radial and axial directions, because this optimizes the distribution of power. An evenly distributed neutron flux within the core allows the power density distribution within the core to be leveled out in proportion to the flux shape. A level distribution of power is desirable, because it allows the core to operate without excessive localized power concentration, which is a part of the essential effort to ensure fuel channels and bundles operate within their licensed power envelope [21]. If the distribution of heat and flux within the core is not uniform, there is significantly greater risk of the central region of the core, where there is lower leakage loss of neutrons, experiencing peaked powers that may exceed the licensed limits. For this reason, the control of reactivity distribution within the core, which is commonly referred to as the spatial reactivity control, is an important consideration for the daily operation of a CANDU reactor.

The long-term spatial reactivity control of CANDU reactors is largely managed via selectively scheduling the order and the time between which fuel channels are refuelled. This strategy is a unique feature of CANDU reactors that allows the operator to control the placement of high-burnup and low-burnup fuels within the core without the need of a refuelling shutdown. When an ideal distribution of spent and fresh fuels across the core is established, the distribution of the power density within the core can be flattened significantly without the assistance of reactivity devices, thus improving the neutron economy. However, it should be noted that the above refuelling strategy is not sufficient to completely overcome the large power concentration that naturally occurs at the central region of the core.

In order to further flatten the concentration of neutron flux at the central region of the core, CANDU reactors are equipped with 21 (for CANDU 6 design) adjuster rods. The adjuster rods are spread across the central region of the core, in three rows extending along the axis of the reactor, as shown in **Figure 19** above. The adjuster rods are typically fully inserted during normal operation to suppress neutron flux across the high-powered, central region of the reactor core in order to reduce its power differential in comparison to the peripheral region and establish a more even power distribution. Additionally, the mechanical adjusters may also be used for bulk reactivity control if necessary, as their withdrawal from the core can be used as a source of positive reactivity in situations where an exertion of additional positive excess reactivity is required to overcome the Xe-135 surges following a significant power reduction or an emergency reactor shut-down. In contrast, the short-term spatial reactivity control, which largely involves the management of routine perturbations caused by refuelling ripples, is effectively managed via the use of LZCs and mechanical control rods. LZCs consist of compartments containing a variable fill level of light water, which are individually placed within each of the 14 divided control zones within the reactor. A diagram demonstrating a simplified design of an LZC is shown below in **Figure 21**.

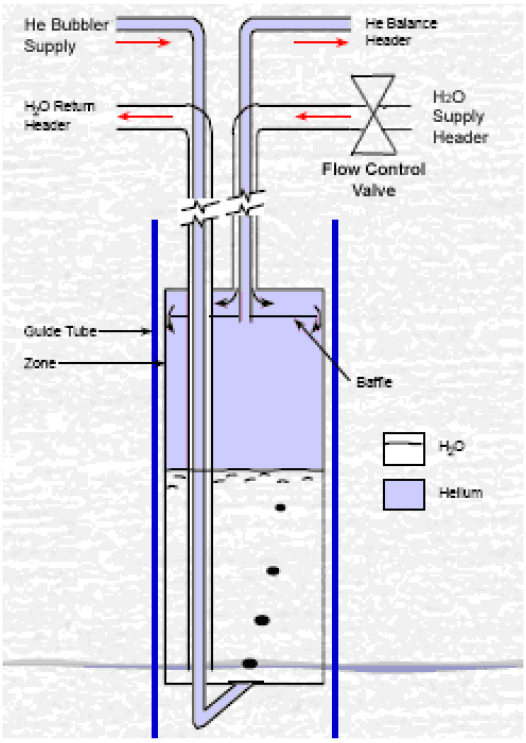

Figure 21. A simplified diagram of a liquid zone control compartment [30].

The LZC compartments rest between fuel channel lattices, and are automatically controlled via a mechanism that is triggered by zonal neutron flux detectors which determine the overall power differential of the individual zones against the average of the all 14 zones. Depending on the direction and magnitude of the power differential, the control valve will adjust the rate of inflow of light water into the LZC compartment, while the rate of outflow is kept constant. Therefore, when there is a positive power differential for a zone, the rate of inflow of light water will exceed the outflow for the zone's LZC in proportion to the magnitude of the differential, whereas the opposite is true when there is a negative power differential. This results in either an increase or a decrease in the fill level of the LZC depending on the direction of the power differential, at a rate that depends on the magnitude of the differential. Once the power differential is mitigated and becomes zero as a consequence of the fill level change, the rate of inflow will become equal to the rate of outflow and the fill level will stabilize until the next

power perturbation. A diagram illustrating the 14 control zones for a typical CANDU core is shown below in **Figure 22**.

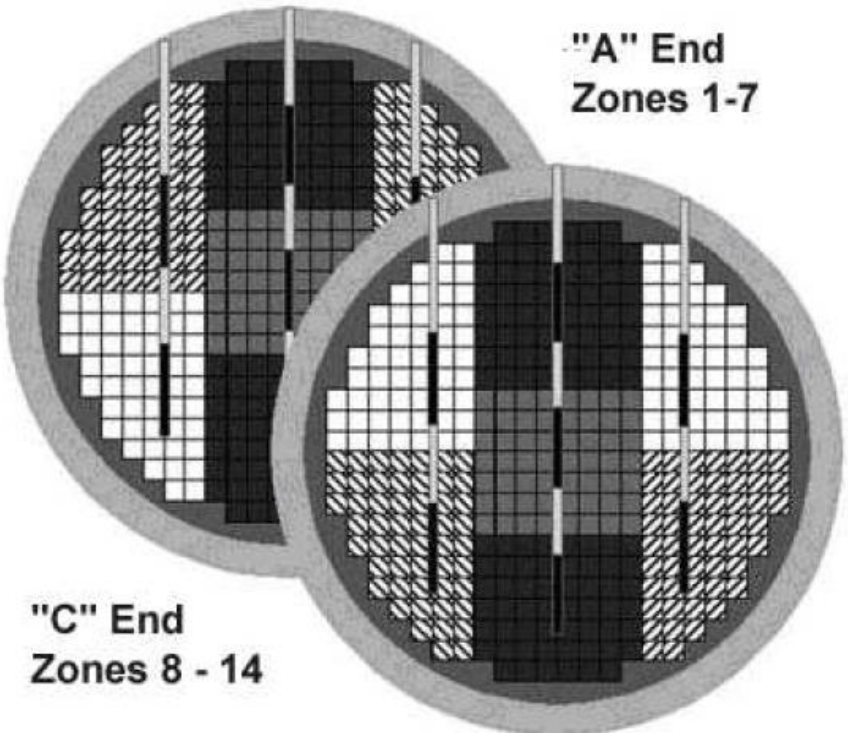

Figure 22. Arrangement of the 14 control zones of a typical CANDU reactor [30].

However, in situations when an excessively high localized power ramp occurs, the four control absorber rods are inserted into the core to conduct a rapid power step-back, thereby derating the overall power of the core. The LZCs and mechanical control rods are a working solution that effectively mitigates perturbations in local power densities. However, they derate power in a relatively larger volume of the core compared to the volume that is actually affected by the fuels experiencing transient powers. Therefore, the spatial control via LZCs and mechanical controllers is detrimental to the reactor's neutron economy. This is particularly evident in the case of mechanical control rods, which cause a much cruder power step-back for a larger volume of the core than the relatively finer, localized control that LZCs provide. Therefore, the use of long-term, strategic refuelling strategy to achieve a naturally balanced distribution of the power

density across the core with small, controlled refuelling ripples is the preferred, primary method of spatial reactivity control for CANDU reactors. The LZCs further provide a secondary layer of short-term control to mitigate larger power density perturbations, and the presence of mechanical controllers provides further protection against more significant over-power conditions which may occur due to significant, sub-optimal refuelling decisions or irregular operations of the core. A suboptimal refuelling may occur due to various reasons including but not limited to an operator mistake or an emergency fuelling to remove a defective fuel bundle.

5.3.4 Licensed Operating Limits

As indicated previously with regards to spatial reactivity control, each fuel channel within a CANDU core has specific safe operating power limits depending on its cooling capacity [21]. The licensing of the safety limits requires a safety analysis, via which the limitations of the fuel channels are calculated or estimated [21]. In practice, however, the actual channel power limits are set at significantly lower values than the Critical Channel Powers (CCP) at which the Critical Heat Flux (CHF) occurs, which is the rate of heat generation required for coolant voids to form and the onset of fuel channel dryout begins [21]. The actual Operating Channel Power Limits (OCPL), furthermore, are licensed with additional margins of safety beyond the safety analysis power limits, which were already estimated using conservative assumptions. As mentioned previously in **Table 8**, CANDU reactors are equipped with two independent shut down systems, one in the form of several solid absorber rods, and the other in the form of a liquid absorber injection system. The automatic engagement of these shutdown systems in response to regionalized power concentrations in excess of the operating envelope constitutes the Neutron Overpower Protection (NOP) feature of CANDU reactors, which is also referred to as the Regional Overpower Protection (ROP) [18]. In the event that the power density of a designated NOP safety channel reaches or exceeds the trip set point (set at a

margin below the safety power limits), the NOP detectors detect the threshold power density and engage the two independent shutdown systems to shut down the reactor [18].

During normal operation, each fuel channel within a CANDU core must be operated within an envelope below the licensed OCPL. As described previously, this is primarily achieved via optimal refuelling schedules and the assistance of LZCs and control rods which together provide spatial reactivity control by temporarily derating regions of high power densities within the core. In practice, however, to minimize occurrences of such power reductions, utility operators typically operate fuel channels at optimal reference or "target" powers, which are significantly below the licensed operating power limit. The differences between the target operating powers of fuel channels and their licensed operating power limits constitute the operating margins of the channels. In addition to the OCPL, a maximum Operating Bundle Power Limit (OBPL) is also calculated and licensed in the safety analyses. This is because the mechanism of fuel failure depends on a variety of factors in addition to the coolant properties on which the channel power limits are based. The OBPL is imposed on the fuel bundles themselves, because even without occurrences of voiding and dryout conditions, it is possible for fuels to fail due to unforeseen variations in manufacturing and operating practices as previously mentioned in Section 5.1. Hence the licensed OBPL is used to specify the operating power envelope for the fuel bundles themselves, and it is therefore an important parameter for fuel failure analyses. In the case of the 480-channel, 2650 MW (thermal) model CANDU cores used at the Darlington nuclear generating station, the licensed maximum operating power for any fuel channel is 7200 kW, and the licensed bundle power limit is 950 kW [31].

5.4 Effects of Aging on Licensing and Operation

Aging is an important aspect of consideration for the safe operation of nuclear reactors, as it could impart negative effects on the safe function of various safety-

significant Systems, Structures and Components (SSCs). This is of particular concern for CANDU reactors, as the average age of the currently active fleet of 31 CANDU reactors in the world is approximately 35 years from the respective start dates of their commercial operation [3,4,5,6]. For consideration, examples of affected SSCs and the impact of aging on their performances are outlined in detail in **Table 9**. The implications of the aging considerations for safety analyses are highly significant as their effects would reduce the safety margins that were previously available. This of course is because the safety margins tend to decrease in proportion to the reduced capacity of the aged SSCs, which affects the performance of safety-significant systems such as the Primary Heat Transport System (PHTS) that affect the cooling of fuel channels. Changes to such systems will significantly impact the predictions of safety analyses, which generally lead to tighter operating license limits required by the regulators, and therefore a reduction in operating margins for the utility operators. Overall, this results in a demand for increased conservatism in the control of the power density, which further results in tighter constraints on refuelling operations to ensure compliance to power limits.

With the significant average age of CANDU reactors across the world, it is becoming more critical for the CANDU industry to implement aging management strategies to mitigate its negative impacts on the continued licensing and operation of the existing CANDU fleet. The current aging management strategy implemented by the Canadian nuclear industry includes tracking and mitigation strategies such as improved data collection and analyses, servicing components, changing operating conditions and modifying the fuel design, as well as improvements to the safety analysis framework to increase accuracy and eliminate overly conservative predictions wherever possible [32]. The incorporation of the *best-estimate plus uncertainty* approach as part of the safety analysis framework is therefore a useful implementation that complements the industry effort to mitigate margin loss due to aging and supports the continued licensing and operation of the existing CANDU fleet.

Table 9. Summary of aging issues: effect on trip coverage and safety concerns [33].

Aging Issue	Effect	Safety Concern
PHTS pipes' roughness changes	Core flow redistribution (selective Magnetite dissolution & deposition)	Fuel/pressure boundary failures, safety margins
Aging of the pump bowl and impeller	Change in pump run-down curve	Low flow trip may be adversely affected
Steam Generator: Tube fouling, thinning, plugging or crimping, divider plate leak and/or break	Reduced heat transfer to boilers, higher pressure drop on the tube side (fitness requirement	Reduction in PHTS flows, fuel and pressure boundary failures, Reduction in safety margins, Fission products by-pass of containment
Feeder thinning (multiple feeder break is not a DBA)	Increased Channel flow, corrosion products and debris in the PHTS, Feeder Break is a DBE. However, multiple feeders break as the initiating event has not been analyzed. It may be argued that the impact may be somewhere between a SLOCA and LLOCA, both of which have been analyzed	Low flow trip, potential fuel and pressure boundary failures, reduction of safety margins, single or multiple channel flow blockage, multiple channel flow blockage has not been analyzed
Pressure Tube axial & radial creep, and sag	Core volume increases, flow-bypass, decrease in yield strength, falling off channel bearing, CHF Reduction, operating with depleted fuel bundles, (CHF and reactor physics issues), increase positive coolant void reactivity, bundle power increase, radial bundle power peak factor increase; pin power increase, changes to bundle powers uncertainty, changes in burnup, and flux at detector locations; changes in the limiting flux shape in a slow LOR event, SDS1 shut off rod drop reactivity curve may change	Adversely affect trip coverage for all DBEs Overall trip coverage including LLOCA power pulse issues, Fuel/fuel channel integrity
Aging of other structures inside and outside the core	In-Core: Potential elongation and bending of the guide tube due to neutron fluence, temperature, etc., Out-Core: Support structures	Adverse effect on SDS performance (regular interval testing is performed)
Passive or active component aging (valve passing/seating, corrosion etc.)	Valve passing/seating issues, Change in the leakage characteristics of check valves, Thermocouple degradation, etc.	Safety and safety related systems (Surveillance and regular interval testing is done)
Aging of the Instrumentation	Corrosion (RTD wells), Orifice degradation, Changes in the impulse lines, Electronic component degradation	Trip coverage, reactor trip delays, Spurious trips, post-accident reactor monitoring issues.
Operation with empty channels	Empty Channels (BA U3), Operation with depleted fuel bundles at certain channels, heat flux issues	Safety has been re-assessed

5.5 Reliability Theory

Reliability is the measure of the likelihood that an engineered structure, system, or a component will perform its designed task within the acceptable envelope of performance tolerance, for the duration of time that it was designed to last. In the case of nuclear fuel, reliability is the likelihood that a fuel unit will maintain its structural integrity through its expected duration of in-core irradiation without failing. The reliability of an engineered system depends largely on five fields: system design, material selection, manufacturing quality control, operating history, and maintenance. In this study, the design and material selection of fuel is fixed to the specification of the 37-element CANDU fuel. Thus, this analysis focuses on the impact of manufacturing and operating variables, whereas maintenance is not considered because in-core repair of fuels is not possible.

5.5.1 Uncertainty

In reliability prediction, uncertainties can arise from many factors including the inadequate knowledge about system design, the level of system degradation via operational wear, the inherent variability in manufacturing and operating demand, and the inability to know the exact time of a critical component failure. Such uncertainties can be categorized into two major types, which are aleatory uncertainty and epistemic uncertainty [34]. The aleatory uncertainty, which is also referred to as stochastic uncertainty, describes uncertainty that is a function of inherent randomness of the natural world. The aleatory uncertainty is irreducible as there will always be variability in such underlying variables. The epistemic uncertainty, on the other hand, is also referred to as deterministic uncertainty, and describes an uncertainty that is a function of lack of human knowledge regarding a system and its peripherals. This refers to situations where a parameter or a response of fixed value exists, but is unknown because the process is not understood and thus cannot be modelled precisely. To implement an accurate reliability

analysis, it is very important to minimize, or account for the existence of epistemic and aleatory uncertainty. The epistemic uncertainty can be reduced by improving the scientific understanding of the underlying multiphysics phenomena, material engineering, as well as developing superior models. On the other hand, the aleatory uncertainty cannot be reduced, however, may be accounted for via a probabilistic analysis based on a statistical quantification of randomness.

5.5.2 Random Variables

In systems engineering, some of the random variables that describe a system often exhibit the property of aleatory (or random) uncertainty, thereby imparting an uncertainty in determining the performance or reliability of the system. A random variable is defined as the type of variable where its value, which may be ascertained via the outcome of a random experiment, cannot be known *a priori* to the observation of the experiment. An example of this includes the casting of a six-faced dice to determine which face it lands. For these types of variables, only relative probabilistic weights can be assigned to different possible values of the random variable. Random variables such as these are therefore best represented in terms of probabilities. Random variables may be discrete, such as the tossing of a six-faced dice, or continuous, which then follows a Probability Density Function (PDF) that may be represented by $f_x(x)$ as shown below in **Figure 23**.

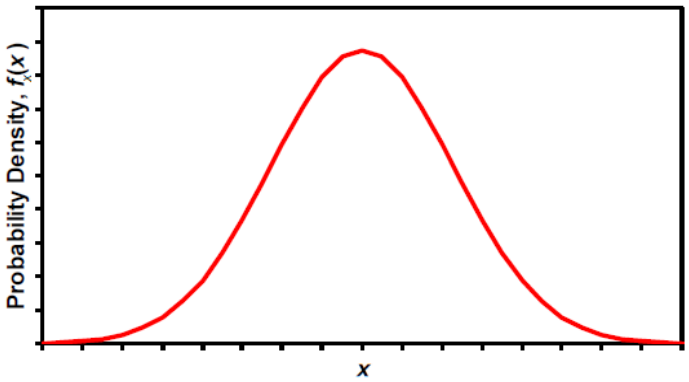

Figure 23. An example of a probability density function (the normal distribution is depicted here) [34].

The probability associated with a continuous random variable in a given range of values is represented by the area under the PDF, between the given ranges of values. Hence the integration of the PDF, over the specified range, yields the cumulative probability that the value of random variable X will reside within the range. The total area under the PDF, on the other hand, represents the cumulative probability of all possible values of the random variable X, which is by definition, equal to 1.0. The integration can be represented by the following equation:

$$P(x_1 < X \leq x_2) = \int_{x_1}^{x_2} f_x(x)dx \tag{5.3}$$

Alternatively, to avoid having to carry out an integration every time a cumulative probability is calculated, the integrated form of the PDF, which is known as the Cumulative Distribution Function (CDF), is typically utilized instead. The CDF, represented as $F_x(x)$, relates to its PDF as follows:

$$P(x_1 < X \leq x_2) = F_x(x_2) - F_x(x_1) \tag{5.4}$$

where $F_x(x)$ may be represented as:

$$F_x(x) = P(X \leq x) = \int_{-\infty}^{x} f_x(u)du \tag{5.5}$$

The CDF may be used to directly compute the probability of value of X less than or equal to x, and for probability of values between x_1 and x_2, the CDFs of both x_1 and x_2 may be computed and the difference used to determine the probability, as shown in equation 5.5. **Figure 24** below shows an example plot of the CDF of a Normal distribution.

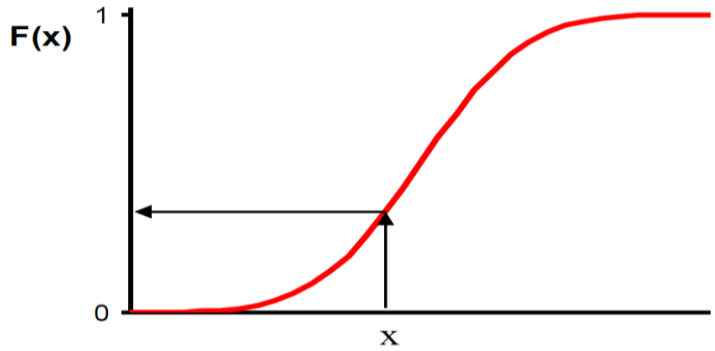

Figure 24. An example plot of CDF of a random variable (the normal distribution is depicted here) [34].

5.5.3 Distribution of Random Variables

In mathematics, random variables are categorized into different types of probability distributions which are used to describe the shape of the PDF and CDF of the random variable. Each distribution has a specific and unique mathematical formula which is expressed in terms of one or several parameters. In engineering applications, geometry and material properties of manufactured systems are typically best represented via the "Gaussian," or Normal distribution (shown in **Figure 23** and **24**), and the Log-normal distribution by extension. The major cause for this tendency is described by the Central Limit Theorem (CLT), which is the tendency for normalized sums of variables, themselves resulting as sums of multiple independent variables, to converge towards a Normal distribution even if their constituent variables are not normally distributed [34].

5.5.4 Limit State Problem

The reliability of a system can be very well defined through the concept of probability. The use of statistics to predict the probability of system failure under specified conditions is an integral aspect of modern systems engineering. This is because the statistical analysis allows for a probabilistic derivation of a system's propensity for failure, which may then be made commensurate with the consequence of the failure to produce a quantitative representation of the expected (or probabilistic) damage or loss.

In systems engineering, as well as many other applications where it is used, commonly refer to this process as "risk analysis," and its product value of the expected occurrence of adverse events, such as casualties or material damage, as "risk." The process of risk analysis is highly useful, as it allows decision makers to quantitatively assess the risk, and therefore quantitatively plan and implement mitigation measures that are commensurate with the expectations. The major advantage of this process, in comparison to any qualitative efforts for assessing the expected occurrence of failures, is that it provides decision makers with the opportunity for optimizing the effectiveness and efficiency of the mitigating measures. Statistical analysis of reliability has therefore become an integral part of reliability standards and industry requirements across many engineering disciplines including nuclear.

The principle of failure from a probabilistic perspective can be represented by a limit-state function. Consider a simple system with a random demand and capacity to meet that demand. Where capacity is represented by variable "x_1" and demand by "x_2," the randomness is characterized by their means μ_R and μ_S, standard deviations σ_R and σ_S, and probability density functions $f_R(x_1)$ and $f_S(x_2)$. **Figure 25** below provides an illustration of this principle.

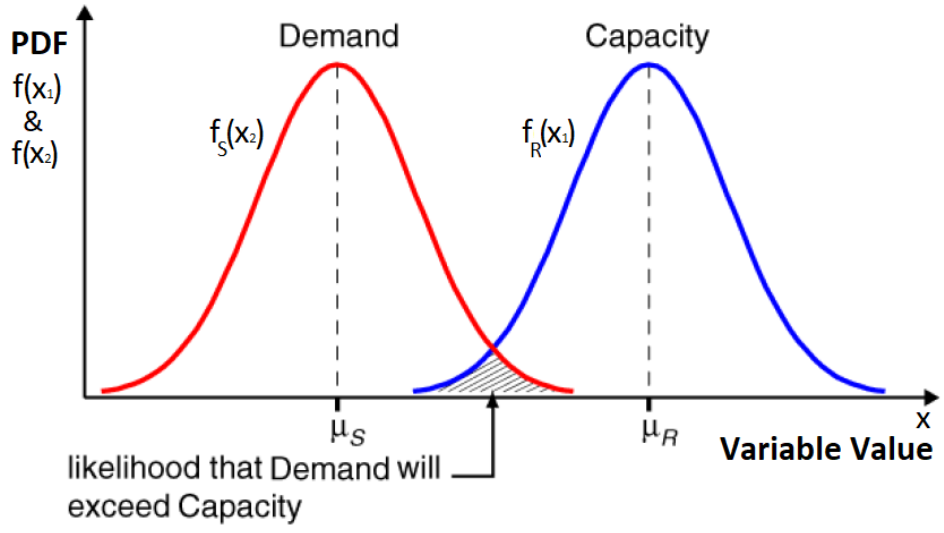

Figure 25. Graphical representation of PDFs $f_R(x_1)$ and $f_S(x_2)$ [34].

The system is considered reliable if the limit state is as follows:

$$DEMAND \leq CAPACITY \tag{5.6}$$

Failure occurs if:

$$DEMAND > CAPACITY \tag{5.7}$$

Or in probabilistic terms:

$$Reliability = P[x_2 \leq x_1] \tag{5.8}$$

Or alternatively, the probability of failure, P_f, is given by:

$$P_f = P\{x_2 > x_1\} = \int_{x_2=-\infty}^{\infty} \int_{x_1=-\infty}^{x_2} f_{x_1,x_2}(x_1, x_2) dx_1 dx_2 \tag{5.9}$$

If variables x_1 and x_2 are independent of one another, their joint PDF, $f_{x_1,x_2}(x_1, x_2)$, is equal to:

$$f_{x_1,x_2}(x_1, x_2) = f_R(x_1) f_S(x_2) \tag{5.10}$$

Using equation 5.10, the probability of failure in equation 5.9 can be written as follows:

$$P_f = \int_{x_2=-\infty}^{\infty} \int_{x_1=-\infty}^{x_2} f_R(x_1) f_S(x_2) dx_1 dx_2 \tag{5.11}$$

This is further simplified into

$$P_f = \int_{x_2=-\infty}^{\infty} f_S(x_2) \left[\int_{x_1=-\infty}^{x_2} f_R(x_1) dx_1 \right] dx_2 \tag{5.12}$$

By using the definition of CDF as being the integral of the PDF, equation 5.12 becomes:

$$P_f = \int_{x_2=-\infty}^{\infty} f_S(x_2) F_R(x_2)\, dx_2 \tag{5.13}$$

where $F_R(x)$ and $F_S(x)$ are the CDFs of variables x_1 and x_2, respectively, such that equation 5.13 can be interpreted as:

$$P_f = \int_{-\infty}^{\infty} PDF_{Load\ Demand} \times \mathrm{CDF}_{\text{Resistance Capacity}} \tag{5.14}$$

which is a convolution integral that expresses the amount of overlap of the load function as it is shifted over the capacity function.

Instead by simplifying equation 5.11 with the CDF for the load, then by taking the complement of the CDF, which is given by $1\text{-}F_S(x_2)$, equation 5.13 can also be equivalently written as:

$$P_f = 1 - P\{x_2 \leq x_1\} = \int_{-\infty}^{\infty} [1 - F_S(x_1)] f_R(x_1) dx_1 \tag{5.15}$$

Furthermore, in the case where the capacity variable, x_1, is fixed to a known, constant limit value (such as a licensed safety limit), then the reliability equation can simply be written as:

$$P_{survival} = P\{Limit > x_2\} = \int_{x_2}^{\infty} f(u) du = 1 - F_s(x_2) \tag{5.16}$$

Equation 5.16 is a complementary CDF of the load, $F_s(x)$, which yields the probability of system survival against the load, and is often referred to as the survival function, $S(x_2)$.

5.5.5 Functions of Random Variables

Many engineering problems, including reliability considerations as illustrated in **Figure 25**, involve the evaluation of functions where there is a relationship between the dependent variable and one or more independent variables. If any of those independent variables are random, the dependent variable will also be random by relation. Moreover, the probability distribution and the moments of the dependent variable will also be functionally related to the independent random variables. In the case of a dependent variable that is a function of a single random variable, the probability distribution of the

dependent variable can be derived through a simple transformation of the independent variable and solved analytically. In a similar manner, functions consisting of two random variables can be derived, as it was shown in equation 5.14 for the capacity and demand problem. However, equation 5.14 is a convolution integral and in many problems, integrating a convolution integral can be very challenging, especially when the involved independent variables are of different distribution types [34]. Moreover, multivariate analysis with an increasingly large number of independent variables quickly becomes too difficult to derive and solve analytically. This is the case for analyzing the reliability of CANDU fuels, as the behaviour of a fuel depends on multiple random variables representing both manufacturing and operating parameters. The fuel performance codes, ELESTRES and ELOCA, compute the response outputs (dependent variables) of the model fuel by numerically solving a combination of functions contained within the overall code. These functions consist of complex arrangements of a large number of independent variables and boundary conditions. The limit state problem of fuel reliability using these performance codes is therefore very difficult to solve analytically, or via numerical methods that require manipulation of the functions contained within the codes. Therefore, a Monte Carlo method, which is a numerical method that can bypass the above challenges, is used in this study.

5.5.6 Monte Carlo Methods

Monte Carlo methods are a broad class of stochastic, numerical methods of determining the statistical moments of a response function of a system using repeated random sampling. In reliability analysis, the performance of a system can be described by a model incorporating multiple parameters that are inputs to the response function. These parameters are often random variables subject to uncertainty, and the distribution of the model output can be derived from the input variables via mathematical methods or numerical methods. As mathematical methods can quickly become very complex with

an increasing number of variables, a numerical method is often pursued to simulate complex systems.

A Monte Carlo method follows the principle that when a random experiment is performed in large enough repetition, the average observed outcome will begin to approach the true average of the outcome variable, which may be otherwise difficult to derive analytically. A Monte Carlo random experiment is driven via random number generation, between 0 and 1.0, which encompass the range of PDF of an independent random variable. The value of the random variable, per each instance of the random experiment, is determined via the randomly generated value of probability in relation to the known probability distribution of the independent random variable, which is known as the inverse CDF method. The value of the random variable that has been generated may then be used to compute the output of the response function, for the specific iteration of the random experiment. When this process is repeated to a sufficiently large magnitude, the moments of the distribution of the system response output will converge to their true values [34].

5.6 Safety Analysis for Licensing

Among many aspects of safety analysis for CANDU reactor licensing, the safety performance of fuels is of critical importance. This is because the structural integrity of the fuel is a fundamental and primary line of defense against the release of radioactive fission products. Generally, the fuel safety analysis process involves conducting predictive modelling of the performance of the fuel using manufacturing, operational and any other boundary condition inputs that attempt to provide a best representation of the typical fuel that will be subject to irradiation within a CANDU core. Such models are typically benchmarked against experimental test data that are available for the fuel design type, or extrapolated from a similar design type. The primary safety analysis is targeted for the normal operating condition, as it is the condition of the CANDU reactor that

represents approximately 95% of its operational lifetime [18]. The transient operating conditions, such as design base accidents, are also considered, but they are typically assessed in conjunction with the effectiveness of the safety systems. Thus, the structural integrity of the fuel must be demonstrated for the duration of the onset of the transient, prior to the full engagement of the safety systems. Furthermore, although the goal of the safety analysis is to capture a best-representation of the performance of an average fuel, the determination of license limits is based on the predicted extremes of fuel behaviour that encroach closest to the limit state of the fuel and the fuel channel sub-system. This prediction is typically accounted for with a relatively large margin of conservatism in the case of deterministic analyses, where conservative assumptions are incorporated into the prediction input parameters. Alternatively, in the case of probabilistic analysis, the actual probabilistic material limits are calculated using statistical data, after which a significantly smaller margin of conservatism that is commensurate with the confidence level of the prediction may be added. **Figure 26**, shown below and further discussed in the subsequent sections, provides an example of how the failure limit of a CANDU fuel may relate to its predictive performances based on varying degrees of conservatism ranging from the limit-of-envelope to a best-estimate prediction.

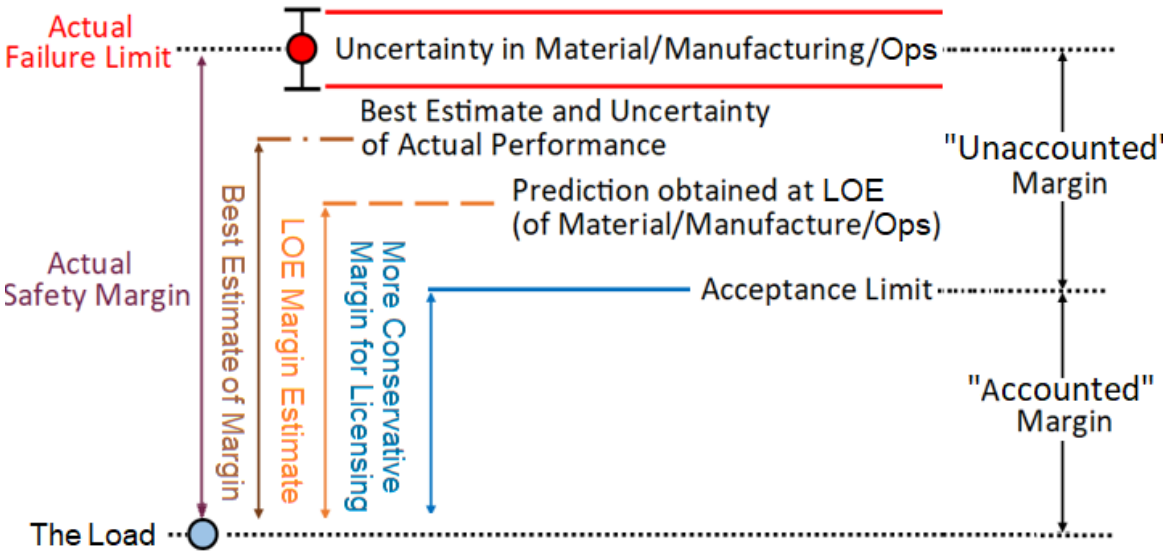

Figure 26. An illustration of how the failure limit relates to performance predictions based on varying degrees of conservatism associated with input parameter treatment [35].

5.6.1 Deterministic Analysis Method

As stated in Chapter 1, the historical practice for safety analysis in the nuclear industry has relied primarily on deterministic analyses. On **Figure 26**, this type of analysis corresponds to the fuel performance prediction represented by the line labeled "Prediction obtained at LOE," as well as the line labeled "Prediction via conservative assumptions." The above two predictions are characterized by their relatively pessimistic estimation of the performance in relation to the actual performance. Consequently, they are placed much closer in proximity to the failure limit than the prediction that is made using a more realistic treatment of input parameters. Deterministic analyses may utilize varying levels of conservative assumptions, with the most extreme example being the limit-of-envelope, where all input parameters including material, manufacturing as well as operational parameters are simultaneously assumed to be at their limits.

The deterministic analysis approach is typically utilized in situations where there is either a difficulty in accurately determining the probability of a negative event occurrence, such as a fuel defect, or there is an important event or a scenario that must be confirmed as a safety benchmark regardless of its probability for occurrence. For CANDU reactors, a fuel unit can possess a range of possible manufactured properties and dimensions. At the same time, a fuel unit can experience a significantly wide range of operating conditions depending on its lattice location, the power history, as well as its in-core residency time and burnup. Therefore, the overall behaviour of a random CANDU fuel bundle can fall anywhere within a significant range of response levels for safety-significant response functions, which may be well below, encroaching on, or exceeding their respective limit conditions.

When sufficient data on manufacturing and operating conditions, as well as sufficiently accurate predictive models and multi-physics codes are not available, the unknown margin of error that is imparted on the confidence of the prediction must be mitigated via a deliberate addition of a conservative margin. This margin is typically

added by tailoring and examining pessimistic scenarios for both manufacturing and operating conditions, as well as any other boundary conditions that the fuel may experience. The fuel response predicted using these assumptions serve as a conservative benchmark of safety confirmation. For a CANDU fuel during normal operation, a safety benchmark scenario may consist of an operator error resulting in a significant power ramp. Simultaneously, the operating condition of the affected fuel may be located in a high-power, high-burnup location, and its manufacturing properties may also be at the limit of their acceptance envelopes. The benchmark conditions typically reflect manufacturing and operating conditions that can occur in real life within the reasonable limits of the probabilistic envelope. However, they are often compounded by the fact they are assumed to all occur simultaneously, which is unrealistic. Such an assumption is not a good representation of the average conditions that a CANDU fuel may experience, and it typically results in a very conservative prediction for the behaviour of the fuel.

The Canadian regulatory guideline for a deterministic safety analysis of nuclear reactors is governed by REGDOC 2.4.1 [1]. The document provides the standards that must be met for the deterministic safety analysis of nuclear power plants, with a list of specific events or combinations of events that may challenge the reactor's safety and control functions. These individual cases of events, depending on the severity of the scenario, provide a deterministic benchmark for the reactor and its operation. The scenarios may include, but are not limited to: initial approach to reactor criticality, changes in power levels, reactor restart from shutdown to nominal power, as well as various other power ranges and refuelling conditions [1]. The scope of each of these scenarios will typically include components or system malfunctions, as well as operator mistakes and any realistic internal or external events such as a fire or a security alert.

5.6.2 Probabilistic Analysis Method

In contrast to deterministic analyses where a single or a few limited cases of conservative input scenarios are considered as a representation of the actual margins to

failure, the probabilistic analysis requires a statistical treatment of inputs that is commensurate with real life probability conditions. This is a difficult concept to implement in the safety analyses of complex systems such as a nuclear reactor, where there are multiple random variables at play, as well as many factors that are difficult to measure, collect data for, and develop models of probabilistic distribution. The Canadian regulatory procedure for probabilistic safety analysis of nuclear reactors is governed by the REGDOC-2.4.2, which mainly focuses on the probabilistic elements of safety systems [15]. The probabilistic analysis of safety systems, as outlined by the REGDOC-2.4.2 document, takes into consideration the probabilities associated with the sequences of events that are associated with postulated accidents. The analysis consists firstly of level 1 analysis, which is the assessment of probability of occurrence for an event that may initiate the chain of events leading to a loss of core structural integrity and fuel failures. The level 2 analysis is the continuation from the level 1, where the containment behaviour is assessed, as well as the extent of the radionuclides released from the failed fuel into the environment. The level 3 analysis, which is the highest level, is a continuation of the level 2 analysis where the distribution of radionuclides in the environment and their effect on public health are assessed.

For this study, the level 1 consideration for the probabilistic safety analysis is of primary relevance, because assessing the reliability of CANDU fuels is synonymous with determining its probability, or the frequency, of failure occurrence that is expected. The frequency of failure is in fact the core input of the level 1 initiating event that is used in the probabilistic safety analysis of CANDU reactors under the guideline of REGDOC-2.4.2. The current norm for deriving the frequency of level 1 initiating events however, is based largely on a Bayesian probability, which is a best guess of the event occurrence frequency that is extrapolated from past experience and limited data that have been interpreted within the concept of probability. This is because the actual probabilities of level 1 initiating events' occurrence are difficult to predict accurately, as they are a multivariate phenomenon involving both operational and manufacturing variability. In

the specific case of the CANDU fuel, there is data available on the past failures of fuels, but the rate of failure has historically been very small, and most of its occurrence has been categorically attributed to power ramps. Thus, the sample size of data pertaining to post-failure defect measurement and its associated operating history are limited in their statistical significance, and do not provide a complete representation of the typical operating conditions. Furthermore, due to the continued significant improvements in fuel design, manufacturing quality control, as well as operating practices, the defect rates of CANDU fuels have declined greatly in comparison to when the majority of past failures were observed [23]. Therefore, the analysis of past failure data is not expected to provide a strong representation of current likelihood of defect formation. Lastly, it should be also noted that some safety limits set by regulatory authority are not directly related to defect formation, but rather associated with other safety considerations such as the controllability of the reactor. An example of this is the effect of fuel clad surface temperature on void formation, for which the actual melting failure limit of the clad is 1850°C, but for practical prevention of the onset of dryout, is normally set closer to 600°C [9]. In this case, as shown in **Figure 8**, past data on fuel clad failure via breach of melting temperature are also very limited, thus it is very difficult to account for the actual probability of its occurrence.

5.6.3 Best Estimate Plus Uncertainty (BEPU)

The *best-estimate plus uncertainty* method proposed within this study attempts to address the current limitations in the probabilistic safety analysis framework outlined above in section 5.6.2. As described in Chapter 3, the current state-of-the-art of safety analyses for nuclear reactors remains largely deterministic with budding elements of probabilistic considerations. The concept of *best-estimate plus uncertainty* is considered as an improved approach for safety analysis in relation to the current approach, because it seeks to incorporate all improved aspects of modern technology, database and methodologies that pertain to modelling and predicting fuel behaviour. In relation to

deterministic and probabilistic analysis, the *best-estimate plus uncertainty* approach is simply the best combination of method implementation that is currently available. The approach may therefore consist partly of probabilistic safety analysis where applicable, while other components of the analysis may still be based on deterministic benchmark assumptions. The *best-estimate plus uncertainty* approach is therefore best described as the reassessment of current conventional practices and the implementation of improvements in models, methods and technology wherever available in order to provide the best-estimate that is currently achievable. This concept can be further explored in relation to the four major considerations of safety analysis, outlined below in **Table 10**.

Table 10. Summary of historical combinations of four major considerations for safety analysis from IAEA TECDOC-1332 [14].

Applied codes	Input & BIC (boundary & initial conditions)	Assumptions on systems availability	Approach
Conservative codes	Conservative input	Conservative assumptions	Deterministic
Best estimate (realistic) codes	Conservative input	Conservative assumptions	Deterministic
Best estimate codes + Uncertainty	Realistic input + Uncertainty	Conservative assumptions	Deterministic
Best estimate codes + Uncertainty	Realistic input + Uncertainty	PSA-based assumptions	Deterministic + probabilistic

The current state-of-the-art remains largely within the second row of **Table 10**. This combination involves the use of best-estimate codes, but the input parameters as well as the boundary and initial conditions plus the assumptions about safety systems availability are still largely based on conservative benchmarks. This is such that the analyses still result in being largely deterministic. The ideal combination of the four considerations, pursued in this study, corresponds to the fourth row where best-estimate codes are used with realistic and probabilistic treatment of all the inputs, as well as the boundary and initial conditions, plus the system availability.

Chapter 6: Methodology

6.1 Statement of Novelty

As previously explained in the first chapters of this thesis, the nuclear industry is currently in transition from the conventional practice of deterministic safety analyses using conservative benchmarks towards a greater implementation of probabilistic approaches. The *best-estimate plus uncertainty* approach, developed in this study, incorporates the latest industry standard toolset codes specific to nuclear engineering, as well as statistical toolsets suited for design and analyses of computer experiments to provide a best estimate of fuel reliability based on both realistic models, codes and treatment of input data. The application of the *best-estimate plus uncertainty* approach within the nuclear industry thus far has been very limited, and have only been pursued within the scope of analyzing accident scenarios from the thermal hydraulic perspective at the pressure tube level, or the management of accident scenarios from the perspective of safety systems, as described by [36]. In the case of the *best-estimate plus uncertainty* method development for fuel defect rate during both NOC and LOCA, the current study is the first of its kind to be applied to CANDU fuels, as well as for the PSA of any nuclear fuel in general.

6.2 Summary of Methodology

The methodology used in this study incorporates the use of five Industry Standard Toolset (IST) codes for modelling CANDU reactors and fuels. The 37-element CANDU fuel is modelled using the WIMS-AECL IST code, the core-reactivity devices are modelled using the DRAGON IST code, the core-following is simulated using the Reactor Fuelling Simulation Program (RFSP) IST code, and the fuel performance outcomes during NOC and transients are simulated using the ELESTRES and ELOCA codes, respectively. This study utilizes the simulated fuel operating data that are generated using the RFSP code with assistance from the WIMS-AECL and DRAGON

codes, which are combined with the manufacturing data that are provided by Cameco Fuel Manufacturing [37]. The combined operating and manufacturing inputs are used to predict the statistical trends in fuel performance outcomes via Monte Carlo simulations. The overall flow of the methodology is summarized below in **Figure 27**.

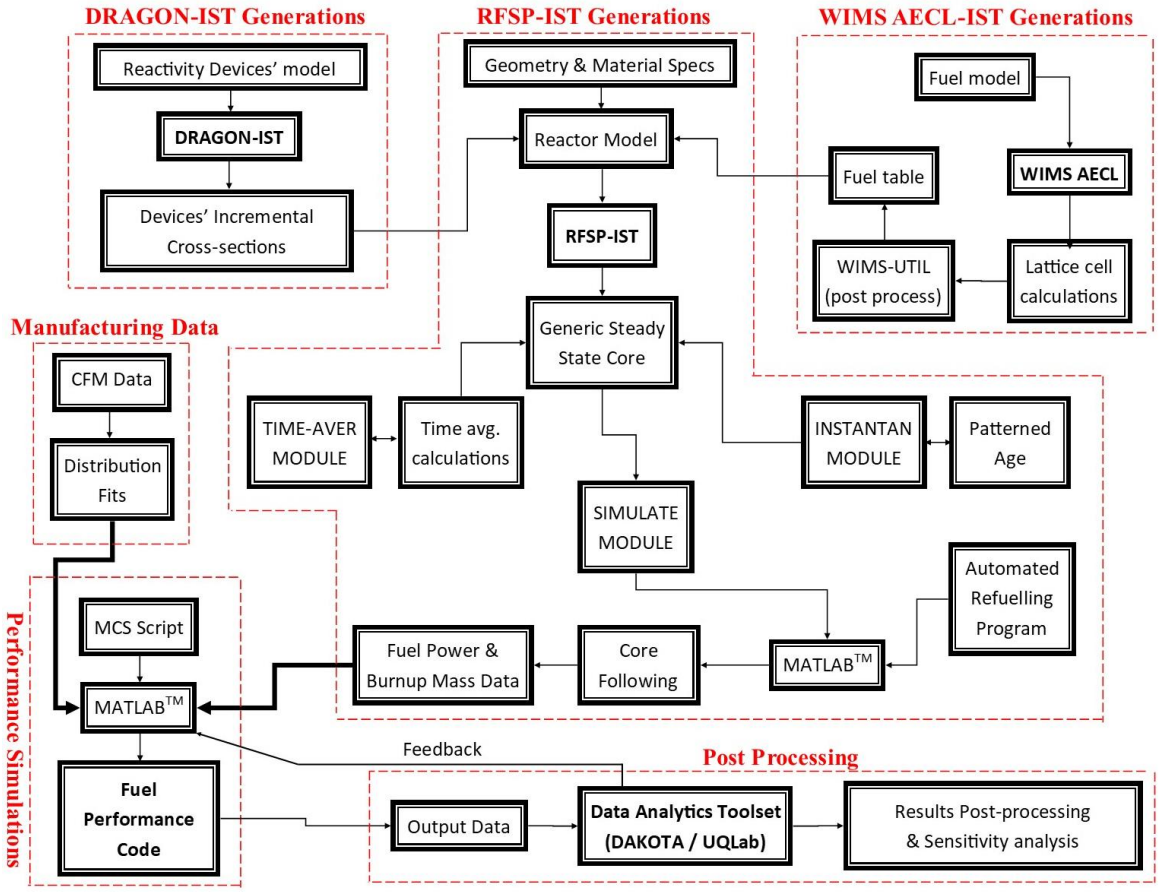

Figure 27. Flow diagram of method framework.

6.3 Generation of Manufacturing Inputs

6.3.1 Distribution Fitting of Raw Data

The manufacturing inputs parameters used in this study were derived from a representative set of fuel manufacturing measurement data obtained from Cameco Fuel

Manufacturing Inc. The measurement data, per each parameter of interest, typically provided sample sizes between 500 to 2000 data points. The measurement data were processed using the MATLAB™ numerical computing environment [38]. The measurement data were first fitted to probability distributions using a regression method to generate the linearized cumulative distribution function. The POLYFIT function in MATLAB™ was used, and the residual sum of squares, as well as the total sum of squares were used to determine the coefficient of determination (R^2 value). The accuracy of the curve fitting was estimated from the determination of the uncertainty on the straight curve-fitted line's slope and the differences between the y-values of the points on the line. The overall results of the distribution fitting provided similar results as [20], with typical R^2 values in the range of 0.77 to 0.99. The best-fit results for each manufacturing parameter of interest are provided below in **Table 11**. An example of a distribution fit for the pellet density measurement data is also shown below in **Figure 28**. The linear regression fit (top), as well as the empirical CDF fit with 95% confidence level plotted alongside theoretical distribution fits (bottom) are presented.

Table 11. Best fits for fuel manufacturing measurement data.

Parameter	Sample Size	Best-fit Distribution	R^2
Pellet Diameter	1920	Log-Normal	0.96
Dish Depth	900	Log-Normal	0.91
Land Width	897	Log-Normal	0.97
Pellet Density	1618	Normal	0.99
Pellet Length	454	Log-Normal	0.77
Pellet Oxygen-to-Uranium Ratio	121	Weibull / Normal	0.98 / 0.97
Sheath Thickness	834	Log-Normal	0.97
Fill Gas Helium fraction	111	Log-Normal	0.98
Pellet Grain Size	362	Log-Normal	0.97
Weld Displacement	400	Weibull / Log-Normal	0.98 / 0.97
Sheath Outer Diameter	834	Log-Normal	0.93
Sheath Inner Diameter	834	Log-Normal	0.98
Sheath Yield Stress	822	Normal	1.00
Burst Test Sheath Hoop Elongation	163	Log-Normal	0.99
Burst Test Sheath Hoop Stress	163	Log-Normal	0.88
Tensile Test Sheath Ultimate Hoop Elongation	315	Normal	0.99
Tensile Test Sheath Ultimate Hoop Stress	315	Normal	1.00

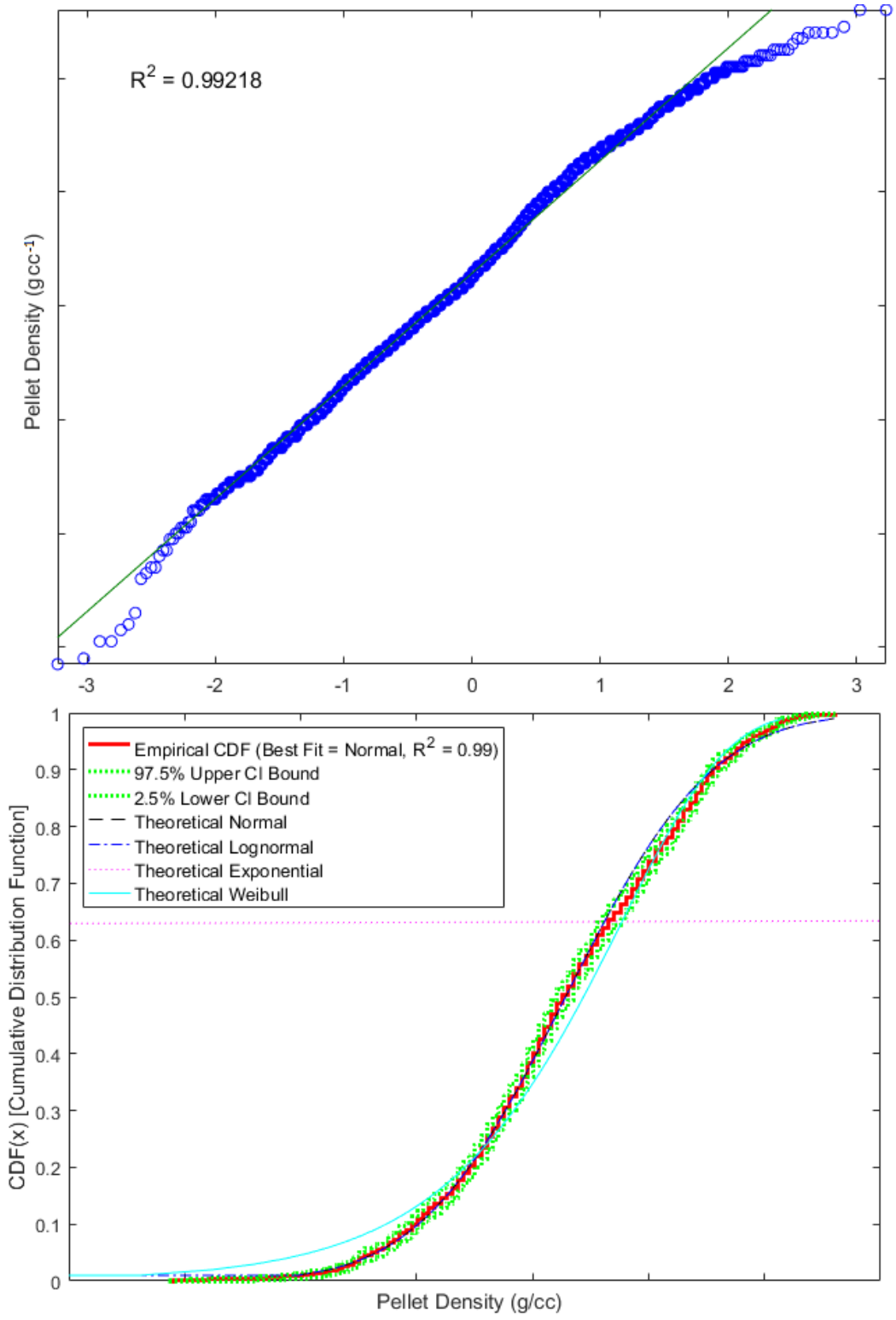

Figure 28. Regression plot of linearized Normal distribution CDF (top) and empirical CDF with 95% confidence level and theoretical fits (bottom) for pellet density data.

As observed on **Table 11**, all parameters except the pellet length exhibit good fit to either Normal, Log-Normal or Weibull distribution types. It should be noted, however, the pellet length was not actually used as a direct input parameter in this study. This is because the actual input parameter required by the fuel performance codes used in this study is the stack length, which is a function of the pellet length, the axial gap and the pellet gap. The raw data provided by Cameco Fuel Manufacturing Corporation did not include the axial gap and pellet gap data that are additionally required to calculate the stack length. Instead, post-processed data for stack length were provided in the form of statistical moments and properties. These included the mean, the standard deviation, the minimum and the maximum values of the stack length, plus indication that the dataset best follows the normal distribution with a centered mean and a min-max range totalling 6 standard deviations. Therefore, instead of fundamental derivation from pellet length and gap values, the statistical moments and descriptions provided by Cameco Fuel Manufacturing Inc. were directly used for this study. Similar to the stack length, the zircaloy sheath tube length was also provided in the form of statistical moments, plus characterization of its best fit distribution. Therefore, the moments of the sheath tube length were also used directly as is for this study.

Four additional parameters also required as input for the fuel performance codes were not included in the dataset provided by the Cameco Fuel Manufacturing Corporation. These parameters include the pellet surface roughness and sheath surface roughness, as well as data for radial and axial chamfers. A literature review was conducted to obtain the statistical moments and the best-fit statistical distribution of these parameters where available. In the case of pellet surface roughness, an average of the measurement data for the three Romanian CANDU-6 fuel samples obtained from [39] (sample names 3, 9.3 and 9.4) was used as the mean and the standard deviation. For the sheath surface roughness, the target roughness value for polished tubes from [40], as stated in the US Patent No. 7738620B2 for zircaloy-4 nuclear fuel clads, was used as the mean whereas the standard deviation value was approximated via extrapolation using

zircaloy-4 tube samples measurement data from [41]. For the radial and axial chamfer depths, no measurement data were available from literature, thus the mid-range of expected chamfer values for the ELESTRES code as described by [42] were adapted as the mean values with an arbitrarily assumed standard deviation value of 0.1 mm. As the literature review did not yield a good indication of the best-fit statistical distribution for the above four parameters, they were assumed to follow a normal distribution with a centered mean. This arbitrary assumption was assessed to be the best available course of action given the lack of availability of real data, as most random variability in the physical properties of manufactured goods tend to follow, or can be reasonably modelled using a variation of the normal distribution [34]. In the field of statistical mathematics, this phenomenon is often described using the Central Limit Theorem, which was previously discussed in section 5.5.3. An upper bound was also set for both the radial and axial chamfer parameters, because the mean and standard deviation pair for these parameters sometimes yielded chamfer values that exceed the geometry input limits for ELESTRES. The parameters for which some arbitrary assumptions were made, are listed below in **Table 12**. It should be noted that when further measurement data become available, the assumed values in **Table 12** may be seamlessly replaced by distribution fits derived from actual measurement data to improve the quality of the best estimation approach.

Table 12. Assumed distribution fits for parameters lacking measurement data.

Parameter	Mean	Standard Deviation	Bounds	Assumed Distribution
Sheath Surface Roughness	0.40 µm	0.033	N/A	Normal
Pellet Surface Roughness	0.78 µm	0.130	N/A	Normal
Radial Chamfer Depth	0.825 mm	0.100	Upper bound: 1.00 mm	Normal
Axial Chamfer Length	0.183 mm	0.100	Upper bound: 0.36 mm	Normal

6.3.2 Calculated Input Parameters

The calculated input parameters relevant to the fuel performance codes used in this study include the diametral clearance, axial gap, pellet gap, and the filling gas volume. The above parameters were derived as follows:

1. The axial gap, which is the total sum of space along the fuel element axis between the pellet stack and the sheath tube ends, is derived as follows:

$$a_g = L_T - L_S - (d_1 + d_2) \tag{6.1}$$

where a_g is the axial gap, L_T and L_S are each the sheath tube and stack lengths, and d_1 and d_2 are the weld-induced shrinkage displacements at the sheath tube ends where the end-caps are fitted.

2. The pellet gap, which is the gap between the individual pellets, is derived as follows:

$$p_g = \frac{a_g}{N_p - 1} \tag{6.2}$$

where p_g is the pellet gap, the axial gap, a_g, is divided by the number of such gaps, which is one less than the total number of pellets, N_p, to determine the averaged gap between the individual pellets.

3. The diametral clearance, which is the clearance between the pellet's radial surface and the inner surface of the fuel sheath:

$$d_g = ID_s - OD_P \tag{6.3}$$

where d_c is the diametral clearance, the ID_S is the inner diameter of the sheath tube, and the OD_P is the outer diameter of the pellet.

4. The fill gas volume, which is the total volume of free space within the fuel element, can be obtained by determining the volume within the sheath that is not occupied by the pellet stack. This is derived by first determining the following volume spaces within the sheath tube:

    a. The stack-to-sheath gap volume, V_S, which is the pocket of volume between the pellet stack and the sheath tube, without accounting for the pellet-to-pellet gaps:

$$V_S = \frac{\pi}{4} L_S (ID_S^2 - OD_P^2) \tag{6.4}$$

    b. The combined gap volume, V_G, which is the volume along the sheath tube where there is no pellet due to gaps between the pellets.

$$V_G = \frac{\pi}{4} a_g (ID_S^2) \tag{6.5}$$

Additional free volumes are provided by the post-processing of the cylindrical pellet where extrusions are made on its edges as well as on the surface. The extrusions made on the edges are referred to as the chamfers, and the extrusions made on the surfaces are referred to as the dishes. An illustration of the typical UO_2 pellet geometry with its extrusions are shown below in **Figure 29**.

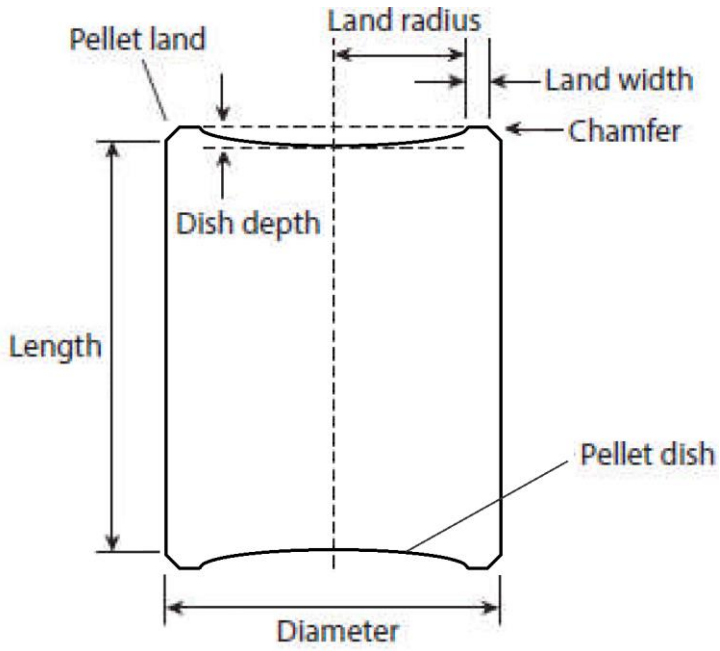

Figure 29. A side view of the UO_2 pellet geometry featuring the chamfer and dish [9].

c. The free volume gained from the chamfer cut, V_C, which is a right-angle triangle-shaped extrusion along the edge of the two circular surfaces of the cylindrical fuel pellet, in the azimuthal direction. The summation of the two extruded volumes from both surfaces' edge takes the shape of an extruded cylinder, which can be expressed as follows:

$$V_C = \frac{\pi}{4} N_P C_a [OD_P^2 - (OD_P - 2C_r)^2] \quad (6.6)$$

where C_a and C_r are each the axial and radial chamfer dimensions.

d. The sum of pellet dish volumes, V_D, which is the total free volume created from the concave extrusion on both sides of the fuel pellet surface. The dish radius of the concave extrusion, D_r, is first determined via the Pythagorean Theorem, using the right-angle triangle formed via the land radius, which is the half of the land diameter, L_D, and the dish depth, D_d.

$$(D_r - D_d)^2 = Dr^2 - \left(\frac{L_D}{2}\right)^2 \quad (6.7)$$

where the land diameter L_D is obtained via:

$$L_D = OD_P - 2c_r - 2l_w \quad (6.8)$$

where l_w is the land width.

Therefore, the dish radius becomes:

$$D_r = \frac{L_D^2}{8D_d} + \frac{D_d}{2} \quad (6.9)$$

The dish volume, V_D, is then obtained via integrating the "slices of circular planes" or "disks" along the dish depth, represented by x:

$$V_D = 2N_P \int_0^{D_d} \pi r(x)^2 dx \quad (6.10)$$

To solve equation 6.10, the radius of the slices of circular planes, r, which is integrated along the dish depth, must be expressed alternately in terms of x. This is once again done via the Pythagorean Theorem, using the right-angle triangle created by the radius, r, of the circular plane, the distance x along the dish depth, and dish radius, D_r, which remains constant.

$$r(x)^2 = D_r^2 - (D_r - x)^2 \quad (6.11)$$

which becomes:

$$r(x)^2 = 2D_r x - x^2 \quad (6.12)$$

Next, equation 6.10, by incorporating 6.12, becomes:

$$V_D = 2N_P\pi \int_0^{D_d} (2D_r x - x^2)dx \tag{6.13}$$

which results in:

$$V_D = 2N_P\pi (D_r D_d^2 - \frac{D_d^3}{3}) \tag{6.14}$$

The final, total fill gas volume, V_G, is given by adding together all of the free volumes computed above.

$$V_G = V_S + V_G + V_C + V_D \tag{6.15}$$

6.3.3 Random Generation by Inverse Transform Sampling

The random generation of manufacturing inputs was achieved via the inverse transform sampling method, which is a basic method for random sampling. The method incorporates a uniform random number generation to obtain a quantile value, and that value is then inputted into the inverse CDF function of the distribution of the manufacturing parameter of interest. In this study, the MATLAB™ computing environment's NORMINV function was used for the inverse of the normal distribution CDF, LOGNINV for the inverse of Log-Normal, EXPINV for the inverse Exponential, and WBLINV for the inverse of the Weibull distribution.

6.4 Generation of Operating Inputs

To capture a realistic and complete representation of the operating conditions of the fuel bundles, large quantities of core-following data at the fuel bundle level, for all fuel channels, at various axial locations and various points in the irradiation cycle are

required. Limited quantities of the Fully INstrumented CHannels (FINCH) data from the Darlington Nuclear Generating Station were made available for this study. The FINCH are fuel channels within the CANDU core that have been fitted with a series of neutron flux detectors for the purpose of measuring the flux of the fuel channel while the reactor is on power. However, due to a lack of sufficient variety, resolution, and the size of data, as well as proprietary restrictions, the FINCH data were not directly used in this study. Instead, a simulated core-following dataset was generated using the RFSP IST code with an automated refuelling and core-following algorithm that is executed via a combination of MATLAB^{TM} script and functions. The simulated dataset was benchmarked against the FINCH data (later discussed in 8.5.2). The methodology of this section largely follows the approach used for automated core-following simulations by [21].

6.4.1 Fuel Lattice Calculations

Before the RFSP code can be used to conduct core-following simulations, the fuel model must first be developed. In the first portion of this study, the WIMS-AECL IST code was used to model the regular 37-element fuel (as opposed to the modified 37-element fuel with a smaller central rod). The WIMS-AECL IST code is a deterministic, two-dimensional, multi-group neutron transport code used routinely for CANDU reactor lattice calculations [43]. Version 3.1 of the WIMS-AECL code was used for this study, with the E70ACR IST nuclides library. The geometry and material properties used for the fuel model are outlined in Appendix A. The benchmarking of the model was obtained from [44], where the Monte Carlo N-particle transport code Version 6 (MCNP6), which is a probabilistic 3D transport code, was used for an equivalent 37-element fuel model. The WIMS-AECL fuel model was used to conduct the burnup calculations for the 37-element CANDU fuel lattice, which were then used to develop a "fuel table." The fuel table is a table of fuel lattice properties such as neutron macroscopic cross-sections and diffusion coefficients listed as functions of the burnup for the modelled fuel, that has been homogenized at the lattice level. The fuel lattice is

defined as a rectangular volume which encompasses a portion of the length of the fuel channel, plus its moderator and the coolant, that houses a single fuel unit. The value of the rectangular volume is determined in accordance to the value of the lattice pitch of the reactor model. An illustration of the CANDU fuel lattice is shown below in **Figure 30**. The fuel table used in this study incorporates the two-group energy separation of neutrons, which is a suitable representation for the CANDU core where neutrons are extensively moderated to thermal energy levels via the use of heavy water moderator.

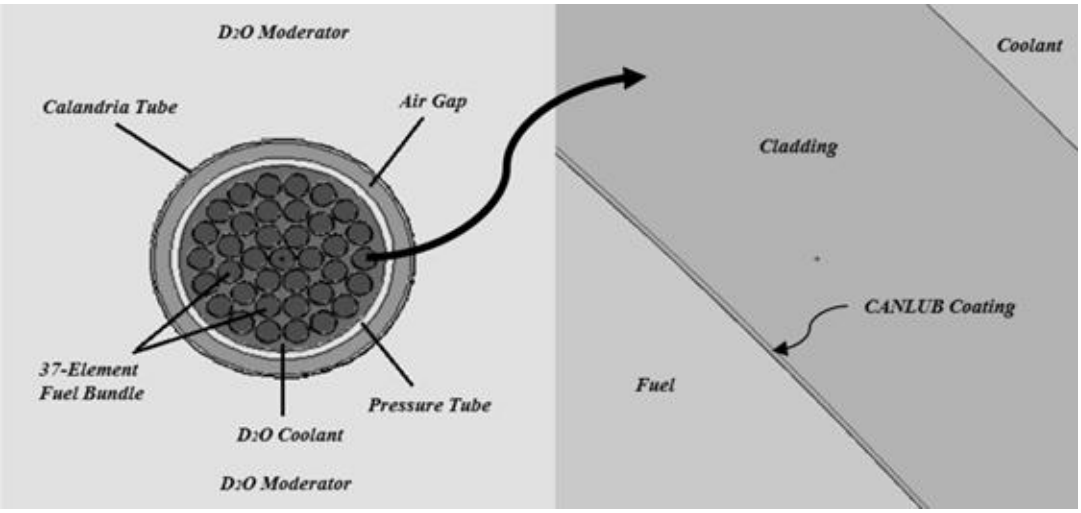

Figure 30. A cross-sectional illustration of the CANDU fuel lattice [21].

6.4.2 Reactivity Devices

The RFSP code incorporates reactivity devices such as control rods, adjuster rods, and liquid zone controllers in the form of incremental cross-sections that are added on top of the neutron cross-section and diffusion coefficients of the affected fuel lattice. As shown before in **Figure 19** and **20**, these devices move in and out of the core via guide tubes that are situated within the calandria, running between fuel channels. This spatial arrangement may be treated such that these reactivity devices co-occupy the volumes constituting the halves of its adjacent fuel lattices. It is for this reason the incremental cross-sections of devices may be blended onto the neutronic properties of the adjacent lattices for the purpose of accounting for the impact of reactivity devices on the diffusion

of neutrons. The incremental cross-sections of these devices, for use by the RFSP code, are calculated using the DRAGON IST code which is a deterministic, three-dimensional, multi-group neutron transport code used to conduct 3D supercell transport calculations [45]. It is capable of utilizing collision probability methods to solve the transport equations in various spatial schemes and multiple energy groups [45]. The reactivity device model would be used to determine the homogenized, additive or subtractive influence of the device cross-section on the overall property of the affected CANDU fuel lattices, as a function of the distance of the insertion or the fill level of the device. For this study, a reference set of incremental cross-sections computed for reactivity devices installed in Darlington station's CANDU cores was used as is for the RFSP model.

6.4.3 Refuelling & Core-Following Simulation

The core-following was performed using the RFSP IST code, which is a multi-modular IST code used as the standard design and safety modelling tool in the CANDU industry [46]. RFSP incorporates the homogenized, two-group macroscopic cross-sections and diffusion coefficients of fuel-cells generated by WIMS-AECL, and incremental cross-sections for reactivity devices generated by DRAGON-IST, to perform multitudes of neutron diffusion calculations for CANDU cores of specified geometries [46]. In particular, RFSP is capable of simulating the effects of the local power transients caused by refuelling ripples. RFSP has been tested and validated against benchmark power-reactor measurements, and is known to give reasonable results when compared with experimental reactor data [47]. The version REL_3-04 of RFSP is used throughout the study. The model core used in this study is a 480 channel CANDU model used at the Darlington Nuclear Generating Station, which has a nominal power rating of 2650MW_{th}. For this CANDU model, each fuel channel contains 13 fuel bundles, with the first and last fuel bundles sitting partially outside of the fuel channel by approximately half the length of the fuel bundle. Three RFSP modules, TIME-AVER, INSTANTAN and SIMULATE, are used in this study to determine the time-averaged performance and generate the core-following data. The TIME-AVER module was first

used to determine the average operating power and burnup values of each fuel bundle as an average over time. This was done so for the total core power rating of 2650MW_{th} and an effective multiplication factor value of 1.000. This yields what is referred to as the time-averaged snapshot of the core, which is used as the reference core snapshot for the initial assessment of the expected power and burnup values of the fuels and fuel channels as an average over time. **Figure 31** below provides an illustrative capture of the time-averaged channel power values of the model core.

	1	2	3	4	5	6	7	8	9	10	11	12	13	14	15	16	17	18	19	20	21	22	23	24
A								3.4	3.7	4.0	4.2	4.2	4.2	4.2	4.0	3.7	3.4							
B						3.4	4.0	4.4	4.8	5.0	5.2	5.2	5.2	5.2	5.0	4.8	4.4	4.0	3.4					
C					3.8	4.3	4.9	5.4	5.7	5.8	5.9	5.9	5.9	5.9	5.8	5.7	5.4	4.9	4.3	3.8				
D				3.9	4.6	5.2	5.7	6.0	6.1	6.2	6.2	6.3	6.3	6.3	6.3	6.2	6.0	5.7	5.2	4.6	3.9			
E			3.8	4.6	5.3	5.8	6.1	6.2	6.3	6.3	6.3	6.3	6.4	6.3	6.4	6.4	6.4	6.1	5.8	5.3	4.6	3.8		
F		3.5	4.4	5.3	5.9	6.3	6.3	6.4	6.4	6.3	6.3	6.2	6.3	6.3	6.4	6.5	6.5	6.3	6.3	5.9	5.3	4.4	3.4	
G		4.0	5.0	5.8	6.3	6.5	6.4	6.5	6.5	6.4	6.3	6.0	6.0	6.3	6.4	6.5	6.5	6.4	6.5	6.3	5.8	5.0	4.0	
H		4.6	5.5	6.1	6.4	6.5	6.4	6.5	6.5	6.4	6.3	6.1	6.1	6.3	6.4	6.4	6.4	6.3	6.4	6.4	6.1	5.5	4.5	
J	3.9	4.9	5.8	6.3	6.3	6.2	6.2	6.3	6.4	6.4	6.4	6.2	6.2	6.3	6.4	6.4	6.3	6.1	6.2	6.4	6.3	5.8	4.9	3.8
K	4.1	5.2	6.0	6.4	6.4	6.2	6.1	6.3	6.4	6.4	6.4	6.3	6.3	6.4	6.4	6.4	6.2	6.0	6.1	6.3	6.4	6.0	5.1	4.0
L	4.3	5.2	6.0	6.4	6.4	6.3	6.2	6.2	6.4	6.4	6.4	6.3	6.3	6.3	6.4	6.3	6.2	6.1	6.2	6.3	6.3	5.9	5.1	4.1
M	4.3	5.2	6.0	6.3	6.4	6.3	6.2	6.2	6.3	6.3	6.2	6.1	6.1	6.2	6.2	6.2	6.2	6.1	6.2	6.3	6.2	5.9	5.1	4.2
N	4.3	5.2	6.0	6.3	6.3	6.3	6.2	6.2	6.2	6.2	6.1	6.0	6.0	6.1	6.1	6.2	6.1	6.1	6.2	6.2	6.1	5.8	5.1	4.2
O	4.2	5.1	5.9	6.2	6.3	6.3	6.2	6.2	6.2	6.1	6.0	5.8	5.8	6.0	6.1	6.1	6.1	6.1	6.2	6.3	6.1	5.8	5.0	4.1
P	4.0	5.0	5.8	6.2	6.2	6.2	6.1	6.1	6.1	6.1	6.0	5.8	5.8	6.0	6.0	6.1	6.1	6.1	6.2	6.2	6.2	5.8	4.9	3.9
Q	3.7	4.7	5.5	6.0	6.2	6.2	6.1	6.0	6.1	6.0	5.9	5.8	5.8	5.9	6.0	6.0	6.0	6.0	6.1	6.1	6.0	5.5	4.6	3.6
R		4.3	5.1	5.7	5.8	5.8	5.7	5.9	6.1	6.1	6.1	6.0	6.0	6.0	6.1	6.0	5.9	5.7	5.7	5.8	5.7	5.1	4.3	
S		3.8	4.6	5.2	5.6	5.5	5.5	5.8	6.0	6.1	6.1	6.0	6.0	6.1	6.1	6.0	5.9	5.6	5.5	5.6	5.2	4.6	3.7	
T		3.2	4.0	4.7	5.2	5.3	5.5	5.8	6.0	6.0	6.0	5.9	5.9	6.0	6.0	6.0	5.8	5.5	5.3	5.2	4.7	4.0	3.2	
U			3.5	4.1	4.7	5.0	5.4	5.8	6.0	6.1	5.9	5.8	5.8	6.0	6.0	6.0	5.8	5.4	5.0	4.7	4.1	3.4		
V				3.5	4.1	4.6	5.1	5.6	5.8	5.9	5.8	5.6	5.6	5.9	5.9	5.9	5.6	5.2	4.7	4.1	3.5			
W					3.4	3.9	4.5	5.0	5.4	5.5	5.5	5.3	5.3	5.5	5.5	5.4	5.0	4.5	3.9	3.4				
X						3.0	3.6	4.1	4.4	4.7	4.7	4.7	4.7	4.7	4.7	4.4	4.1	3.6	3.0					
Y								3.1	3.4	3.7	3.8	3.9	3.9	3.8	3.7	3.4	3.1							

Colour Format: 7000 kW | 5000 kW | 3000 kW

Figure 31. Time-averaged channel power distribution of the model core (in 10^3 kW). The value of k_{eff} is 1.000, the maximum channel power is 6528 kW at channel G-6, the max bundle power is 788 kW at channel G-6, bundle #6, and the radial form factor (peak channel power divided by core average) is 1.18 [21].

In addition to the time-averaged core snapshot, an instantaneous snapshot of the model core at the equilibrium refuelling state was required as the reference starting point of all core-following simulations. The equilibrium refuelling state is defined as the core state where the rate of continuous refuelling that inserts positive reactivity into the core is equal to the rate of decrease in reactivity due to fuel burnup. The equilibrium refuelling state is an important core state for the operation of the reactor, because it is the normal state in which CANDU reactors spend the majority of their operational lifetime, as opposed to temporary, transitory states such as during reactor start-up or significant power perturbations. Furthermore, an instantaneous core snapshot represents the actual operating values of a CANDU core at a particular point in time as opposed to the average value over time that is represented by the time-averaged snapshot.

To create a generic equilibrium-refuelling state core, the INSTANTAN module was used following the same approach used in [21]. This involved the generation of a patterned distribution of "in-core age" for each fuel channel within the core, which is a measure of the combined burnup of the fuel bundles contained within the fuel channel. The distribution of "in-core age" was used in conjunction with the reference shape of the burnup distribution (within each fuel channel) obtained from the time-averaged core to approximate the instantaneous burnup values of individual fuel bundles within each of the 480 channels within the snapshot core. The distribution of the "in-core age" was designed following the principle of the Haling distribution, where the ideal distribution of burnup (which in this case is a function of the "in-core age") is that which maximizes the power margins by avoiding localized power concentrations. This is achieved primarily by evenly distributing the burnup distribution of fuels in an interlocking pattern such that the concentrations of "fresh" fuels in a small localized area are avoided, while also implementing a bias for higher burnup fuels to be located in the central region of the core where there is lower neutron leakage. **Figure 32** below provides an example of the distribution of the "in-core age" used for this study.

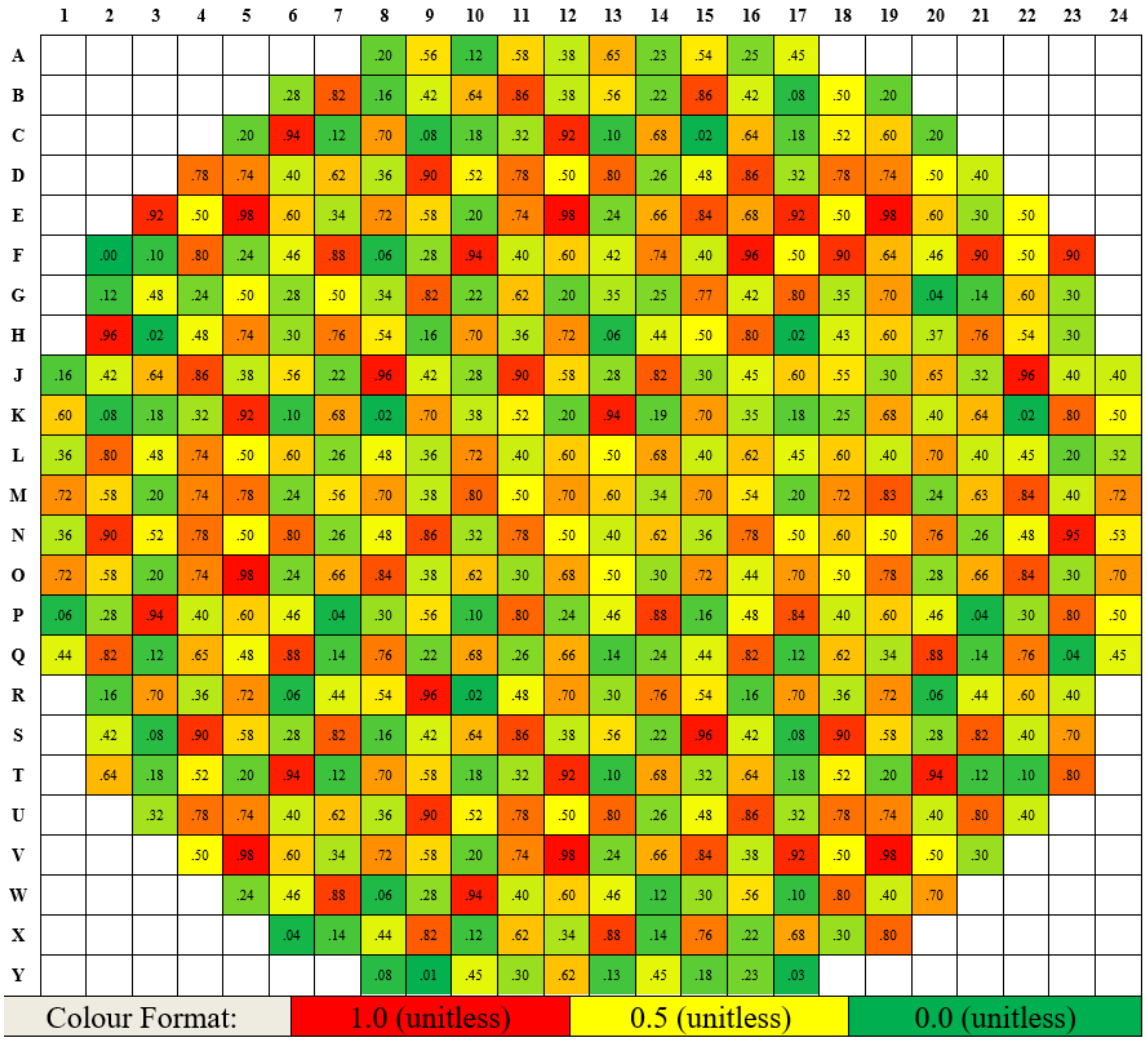

Figure 32. The patterned-age used to generate an instantaneous snapshot of the model core at the equilibrium refuelling state. The value of 0 indicates the channel is freshly refuelled and the value of 1.0 indicates the channel has reached its time-average end-of-cycle irradiation.

The instantaneous core snapshot that was obtained via the INSTANTAN module was further allowed to stabilize to its true equilibrium state by conducting a core-following for 2000 FPDs. This is a significantly long period of time that is much longer than the time a core would need to reach equilibrium from initial start-up. This time is referred to as "approach to refuelling equilibrium." The core-following was conducted using an improved iteration of the refuelling algorithm used in [21], which was developed using the principles of fuel management adapted from [18]. The final

resulting equilibrium core snapshot, which was used as the starting point of core-following data generation for this study, is shown below in **Figure 33**. It can be observed that in comparison to the time-average core in **Figure 31**, which is symmetrical from left to right, the instantaneous core does not exhibit symmetry in any direction. This is because the instantaneous core is always experiencing small, localized power perturbations due to refuelling ripples, which in this case is located in the vicinity of channel D-14.

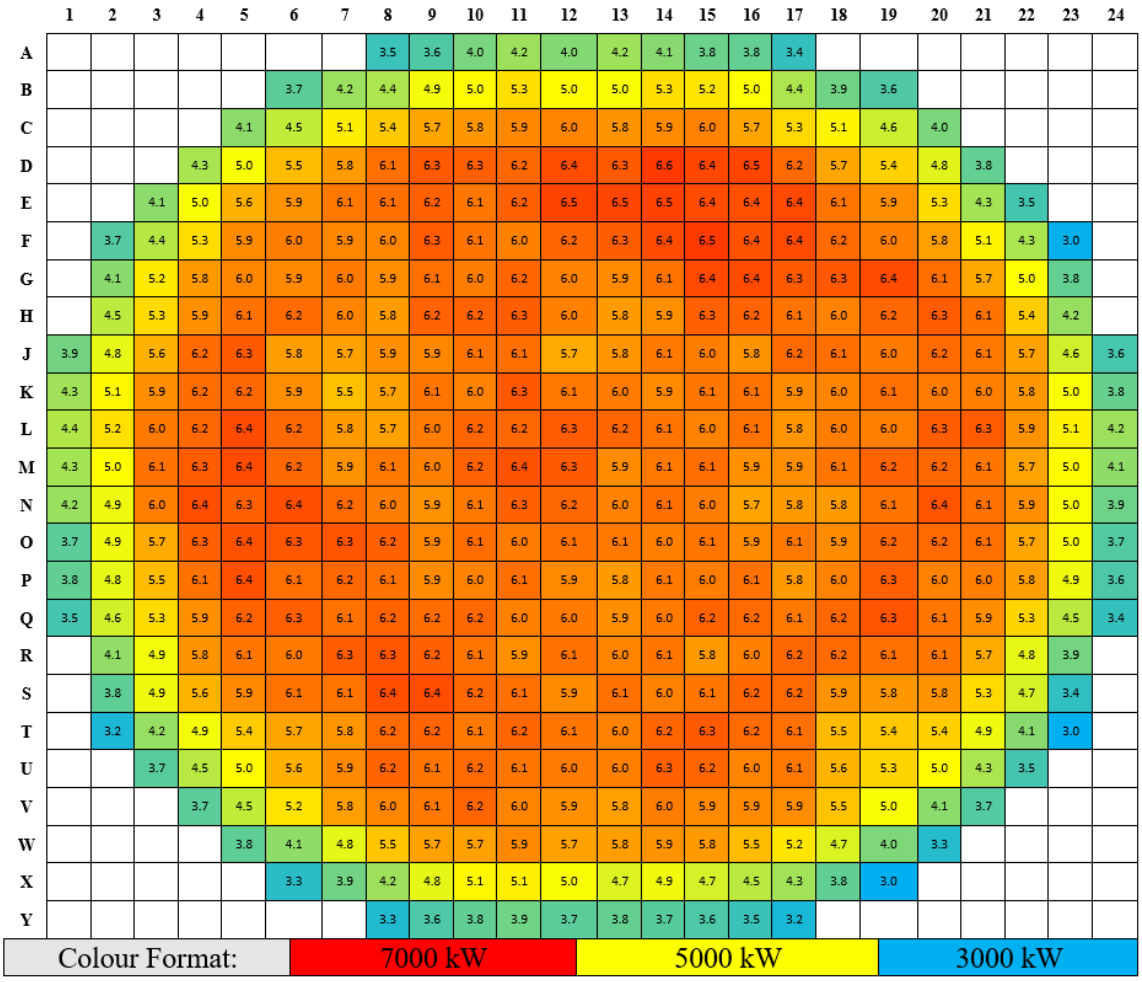

Figure 33. Instantaneous channel power distribution of the generic equilibrium core (in 10^3 kW). The value of keff is 1.000, max channel power is 6554 kW at D-14, max bundle power is 799 kW at D-14, the radial form factor is 1.19, and the rate of reactivity decline is -0.4167 milli-k FPD-1.

Prior to the generation of actual operating data that would be input into fuel performance codes, a refuelling history was first generated using the automated refuelling algorithm. This involved the running of the refuelling algorithm adapted from [21] with all liquid zone controllers fixed at 42.5% fill level, which disables variable spatial power dampening. This fill value is not an accurate representation of individual fill levels for all liquid cone controllers at an instance, but it represents the typical time-averaged fill level across LZCs during normal operation for the model core [21]. The liquid zone controllers were affixed to this value in this case for the purpose of allowing the refuelling algorithm to maintain an ideal distribution of power densities across the core without the assistive spatial power dampening provided by the zone controllers. This is necessary because spatial power dampening is an automatic function built into the RFSP code, and cannot be controlled or be accounted for by the refuelling algorithm's decision-making process. This approach ensures that the dampening effect that zone controllers have on power ripples would not inhibit the refuelling algorithm from making optimal decisions that mitigate the refuelling ripples. As an improvement to the method used in [21], multiple iterations of core-following simulations were executed using adjusted weighting factors for refuelling criteria derived from fuel management principles found in [18]. Adjusted criteria include critical refuelling considerations such as discharge burnup, power compliance and maintenance of criticality at full power. **Table 13** below lists the weighing factors considered for optimization.

Table 13. Weighing factors considered for core-following optimization.

Refuelling Criteria
Channel Power Limit Compliance
Bundle Power Limit Compliance
Maintenance of Criticality
Radial Power Flattening
Axial Power Flattening
Avoidance of Consecutive, Localized Refuelling
Maintenance of Target Burnup Values
Maintenance of Target Channel Power Values
Avoidance of Current Maximum Power Location

This approach was used to iteratively optimize the ideal combination of weighing factors to be used for each refuelling criterion for the generation of the refuelling history. However, the number of iterations used at this time is limited to a small sample size of ten iterations due to the prohibitively long computing hours required to process multiple core-following histories of significant durations. The resulting core-following outcomes pertinent to ideal core behaviour, such as power, burnup and power peaking factors were scored as a function of its average deviation from ideal values, such as the value of 1.0 for the Channel Power Peaking Factors (CPPF), which is the deviation of the channel power from its target value. Each iteration was scored per each criterion, and the scores for each criterion were normalized, summed, and ranked in order to determine the best refuelling history.

Using the best refuelling history obtained via the above approach, a very large quantity of core-following data was generated from the equilibrium core model. The generation consists of 10,000 FPDs (~27 years) of core-tracking which includes a total of 40,000 refuelling events and results in a total of 2.496×10^{8} unique, individual fuel histories. The linear element power rating, which is the particular input required by the fuel performance codes used in this study, was adapted from the fuel-bundle averaged power value obtained from the individual fuel histories. For this study, the highest-powered fuel element position within the bundle, which is typically in the outermost annulus due to the self-shielding effect of neutrons, was chosen as the representative fuel element for the bundle. This is a conservative representation, but it is necessary because the computational resource required to process all four annuli of the fuel bundle for each iteration of fuel performance simulations would necessitate a significantly larger resource requirement. Specifically, it would increase the resource demand by a factor of 4 on what is already a demanding and a large computational endeavour. The radial power peaking ratio between the outer annulus elements to the bundle average used in this study is a value of 1.14, which is the value obtained from [48]. The fuel elements' operating power data obtained from the core-following were grouped into radial zones, in order to

account for the significant variation in power and burnup characteristics between fuels irradiated near the centre of the core versus those irradiated within the peripheral regions where there is significant neutron leakage. The core was therefore divided into 12 radial regions, with zone #1 starting at the outermost fuel channels from the center. **Figure 34** below provides an illustration of the zonal separation schematic. It should be noted radial zones #1 and #2 are refuelled using the 8-bundle-shift refuelling mode, and the remainder are refuelled using the 4-bundle-shift refuelling mode for the model core used in this study (discussed in section 5.3.1).

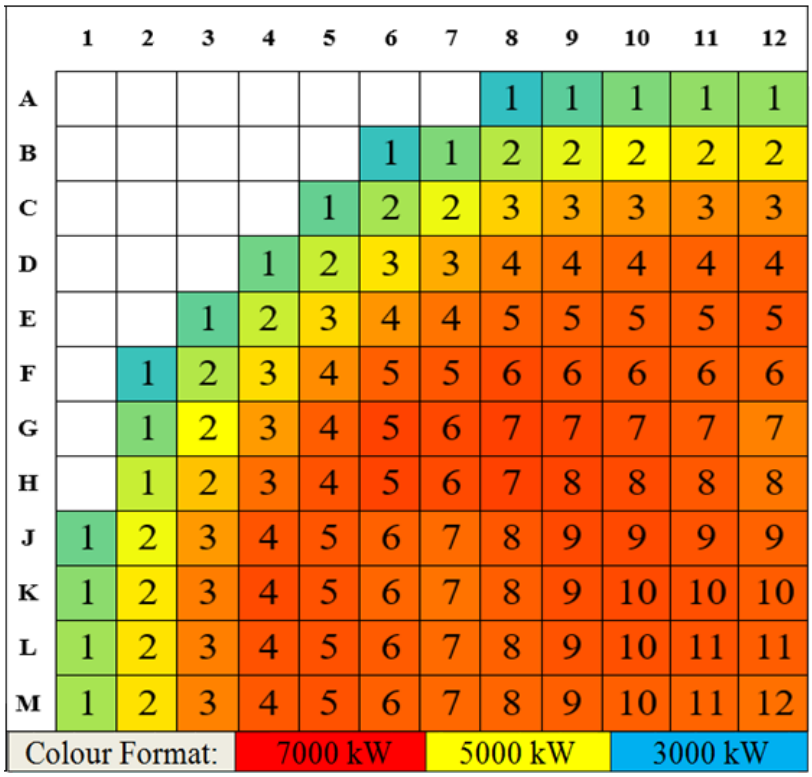

Figure 34. A quadrant view of the 12-zone, radial division schematic used to organize the fuel element operating data.

The average discharge burnup of fuels within each zone were also calculated, because they directly impact many of the output fuel performance parameters such as fission gas build-up. Moreover, the extent of the fuel burnup range used for the NOC simulations will influence the burnup value at which the transient simulations are

initiated, which has a significant impact on the transient simulations. The resulting trends in both average peak linear element rating and average discharge burnup of fuels for each zone are shown below in **Figure 35** and **36**, respectively. The distribution of the peak fuel power density across the model core indicates that on average, the largest occurrences of fuel power densities are likely to occur in the vicinity of zones #3, #4 and #5, which is reflected in **Figure 35**. The power rating of the outermost elements for a fuel bundle, if corresponding to the licensed power limit of 950kW for the model core, is approximately 59 kWm^{-1} [31]. Thus, the predicted maximum linear element rating values shown in **Figure 35** indicate that the large majority of fuel elements irradiated within the model core operate at power densities significantly below their licensed limit.

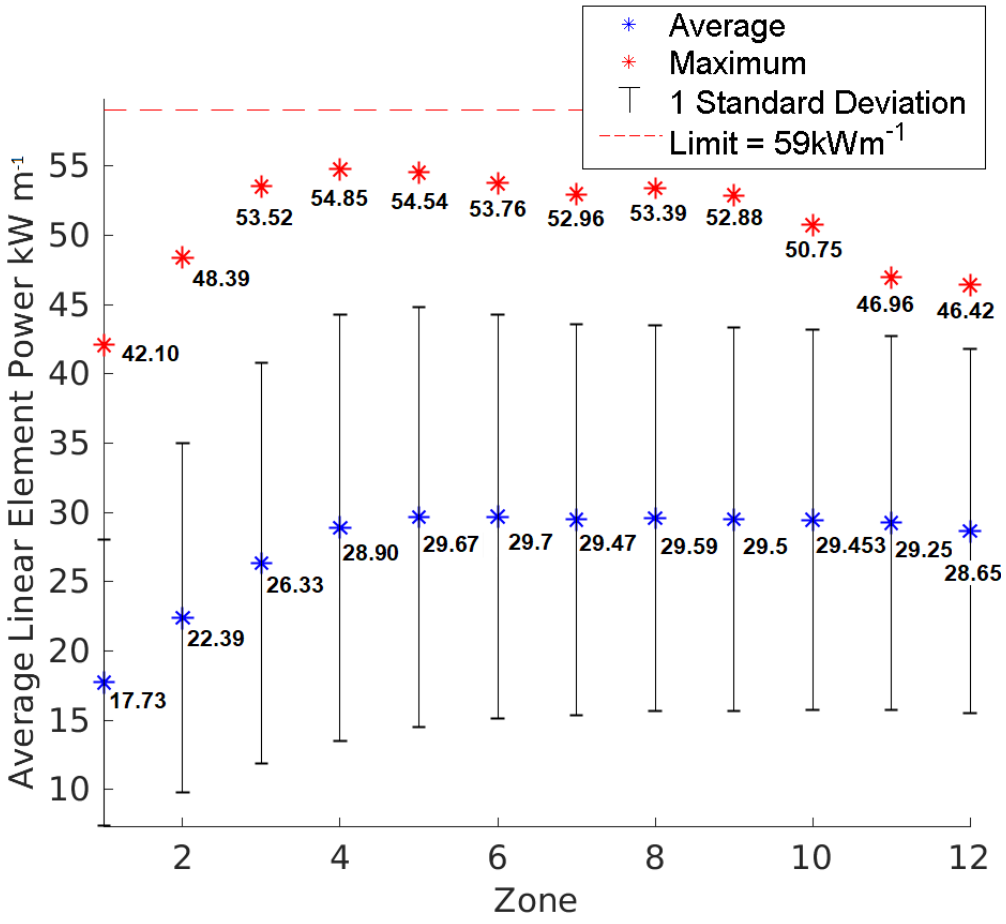

Figure 35. Average peak linear element power rating of each radial zone.

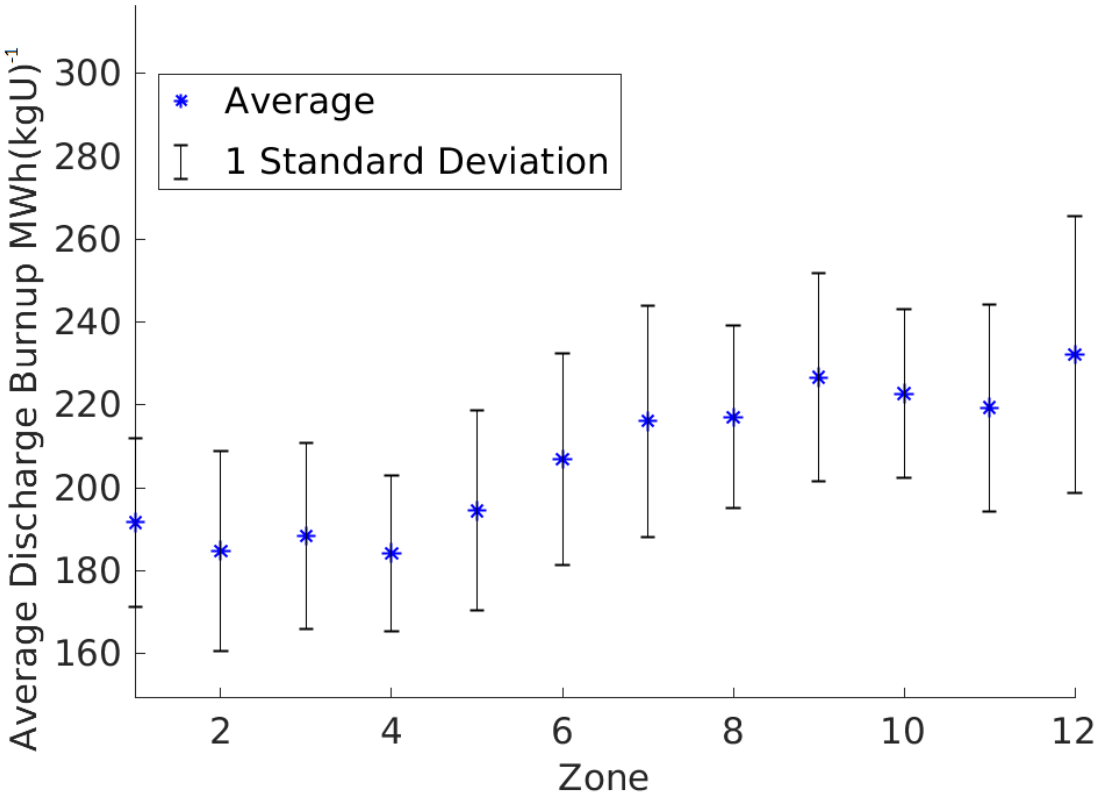

Figure 36. Average discharge burnup of each radial zone.

6.4.4 Random Selection of Operating Data

The random generation of linear element rating and burnup values to be used as operating input for the fuel performance code was difficult to implement via the inverse transform sampling method from a fitted distribution. This is because each individual fuel operating data consists of a paired series of burnup and fuel power values, as opposed to a single series of data associated with a random variable that can be fitted to a probability distribution. For the operating data to be fitted to a probability distribution, a function would first have to be fitted to each of the unique, individual fuel's history of burnup and power values. The mathematical moment that determines the shape of the fitted functions can then be determined from the fit. The value of the moments of the functions provides an overall representation of the individual fuel histories, and this

value can be fitted to a probability distribution. However, this approach is subject to significant reductions in the resolution of the operating data, as there will be imperfections in the fits of functions that would be used to represent the power and burnup relationship of each fuel. The moments of the functions are an extrapolation from the fit, which would also result in a loss of accuracy from the original core-following dataset. This is further aggravated by the fact the model core implements two different types of push-through refuelling modes; both the 4-bundle-shift and the 8-bundle-shift, as described previously in **Figure 15**.

The function that is needed to describe the relationship between the fuel power and the burnup of a fuel is discrete (not continuous), due to the significant step-up or a step-down in power that occurs when the fuel is shifted from its original axial position to further down the channel due to the push-through refuelling. In the case of the 4-bundle shift refuelling, there are always multiple step-downs and/or step-ups in the history of the fuel, because the fuel always enters at the low-power axial positions #1-4, shifts to #5-8, then shifts for the second time to positions #9-12, then is finally discharged or is shifted once more to axial position #13. This is illustrated below in **Figure 37**, where the power versus burnup relationship is shown for a fuel bundle that was irradiated within a 4-bundle-shift refuelled channel (in zone #11), starting at axial position #3.

Depending on the individual history of the fuel, the descriptive function may be a single step-up, a single step-down, or a double step of up then downward perturbation of power. Also, for the unique situation for a fuel bundle starting at axial position #1 for a 4-bundle-shift fuelled channel, a triple step combination of up and down-ward power perturbations can be experienced. So, there is a total of four degrees of freedom in the shape of the non-continuous functions, and it was therefore assessed that there is an excessive complexity to implement a distribution fit as a means of transform random sampling of operating data. An alternative approach was therefore pursued, where the advantage of the unlimited quantity of operating data that could be generated via the

RFSP code and the refuelling algorithm was utilized. The approach involves the random selection of a fuel operating data generated from core-following via random generation of an identifying marker for each of the unique, individual fuels that were simulated throughout the entire core-following data generation. This was first implemented within the bounds of individual zones, where random numbers were assigned to all fuels that have passed through the specific radial zone during core-following. A uniform distribution function was then used with transform sampling to obtain a random number that would identify a particular fuel. This approach results in discrete random sampling with a very low likelihood of repeat samples due to the large size of individual fuel history data that is well in excess of the number of iterations of fuel performance simulations that must be computed for a statistically significant reliability analysis.

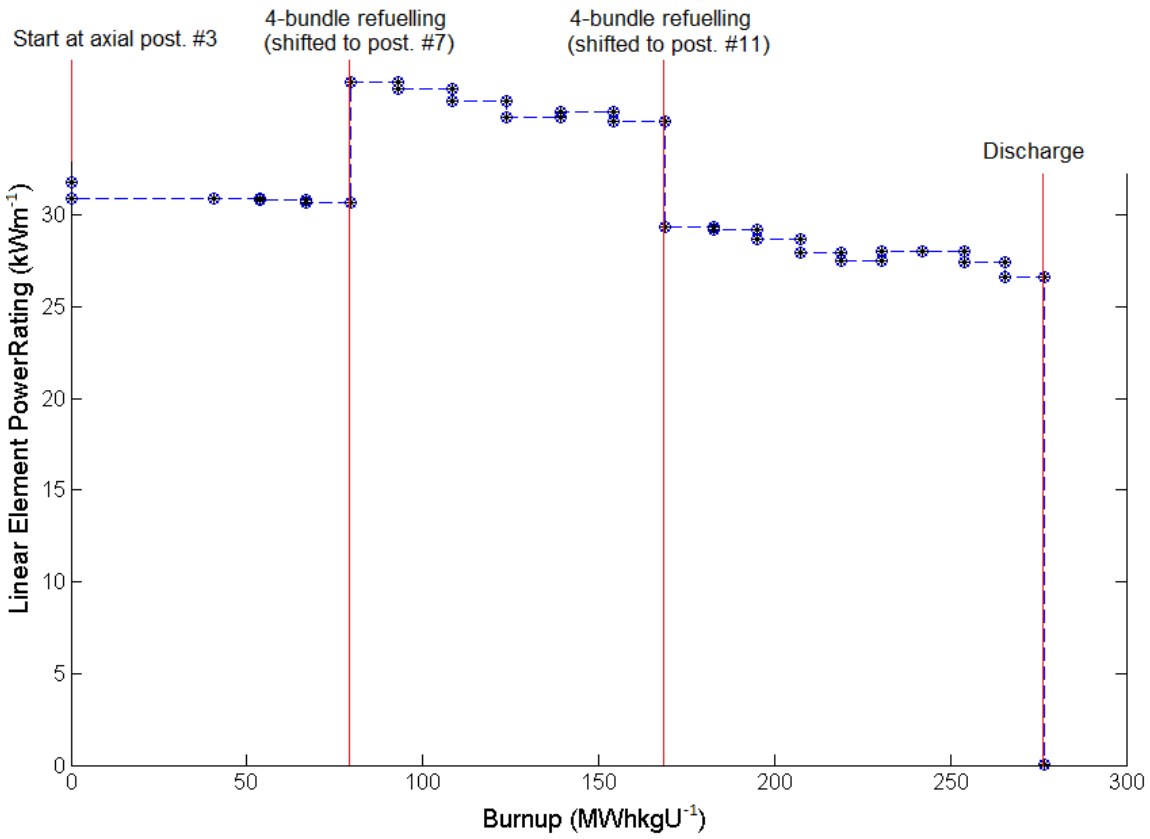

Figure 37. The representative power and burnup relationship of a fuel obtained via core-following simulation from a 4-bundle push-through refuelled channel in zone #11.

The second implementation of this approach was for fuel performance simulations that were conducted for the whole core without a distinction between radial zones. This was achieved by first post-processing the core-following data to determine the frequency at which each of the radial regions were refuelled. The resulting values for each region were then fitted to probability distributions to determine the best fit. The Poisson distribution, and therefore its Normal approximation was found to be the most suitable fit for the distribution of refuelling probability between radial regions, with a R^2 value of 0.96. Plot diagrams are provided below in **Figure 38** which include a histogram of the dataset with the PDF fit of normal distribution (top), plus the empirical CDF with 99% confidence interval that is presented in comparison to other theoretical CDF fits (bottom). It can be seen from the histogram that the lowest power regions are seldom refuelled due to the low rate of burnup, and the central-most regions of the core are also refuelled deliberately at a low rate to maintain a high burnup value. Therefore, the radial regions between zones #3 to #7 are the most frequently refuelled regions of the core. It should also be noted that the distribution that best describes the probability of refuelling between zones is the Poisson distribution, due to the discrete nature of the refuelling density distribution. However, with round-up or round-down post-processing, the Normal approximation may also be used to describe the statistical uncertainty of the refuelling frequency.

With the distribution fit of refuelling rates of zones available, the first marker for the random selection of the fuel, which is the zone that the fuel is from, can be randomly generated using transform sampling. Next, a random channel within the zone is selected via transform sampling using a uniform distribution, as all channels are equally likely to be refuelled within the zone. Finally, the axial position at which the random fuel started its in-core life is randomly generated via transform sampling, once again using a uniform distribution as all axial locations possess an equal chance of being selected. With the above three random markers ascertained via random sampling, a corresponding random fuel that has passed through the core during the core-following is finally identified.

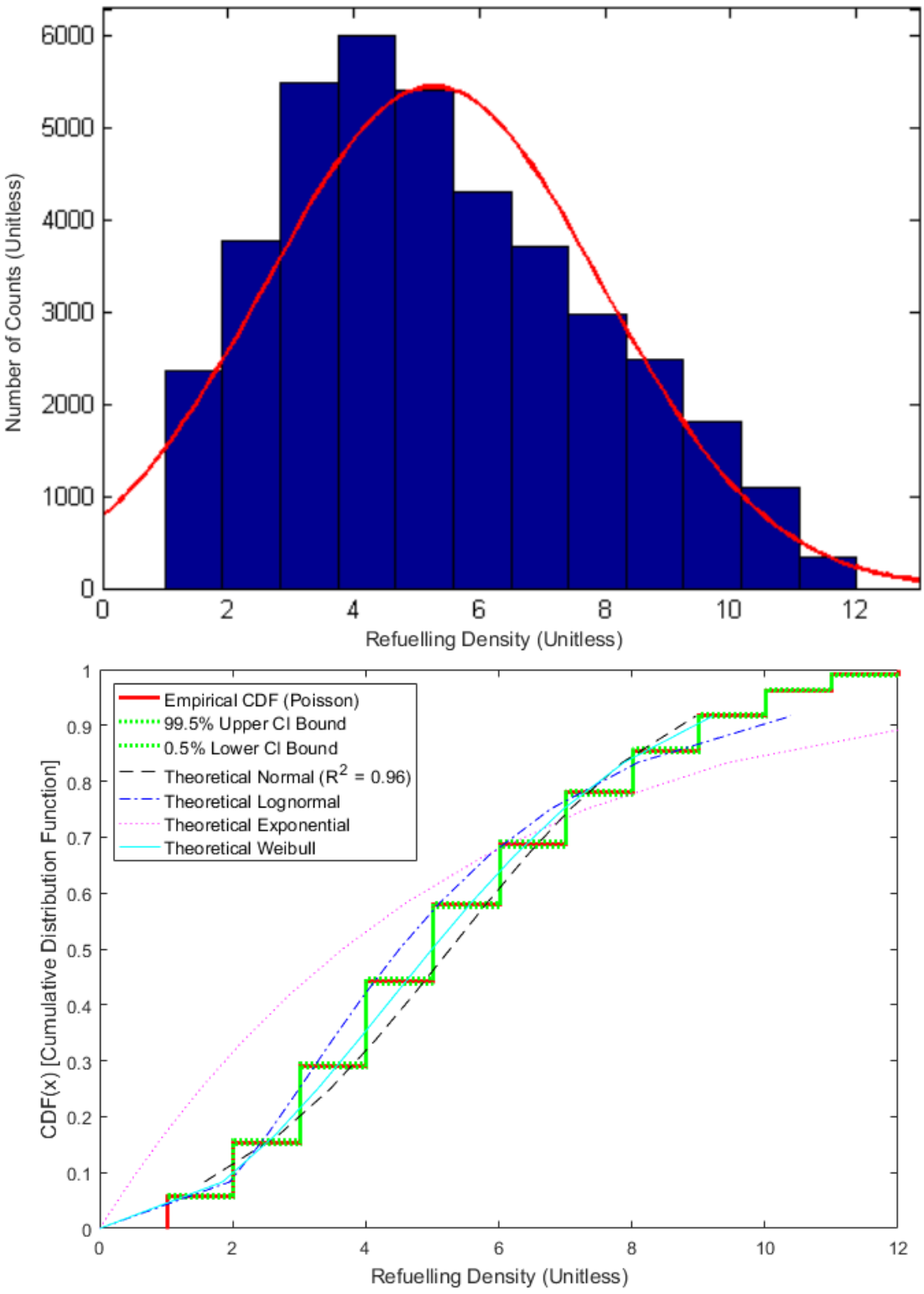

Figure 38. Histogram and Normal distribution fit of refuelling density (top) and empirical CDF fit with 99% confidence interval and theoretical CDF fits (bottom).

6.5 Monte Carlo Simulation of Fuel Performance

6.5.1 Simulation of Normal Operating Condition

Consistent with the two approaches used to generate and randomly sample fuel operating data, the NOC simulation consists of both a series of regionalized simulations where the random simulations were isolated to fuel data that were specific to each of the radial zones, as well as a full-core random simulation where fuel data were randomly sampled from the entire core. The ELESTRES IST code was used in this study to predict the fuel behaviour during NOC. ELESTRES is an axisymmetric thermal-mechanical and micro-structural prediction code designed to simulate the performance of CANDU fuels during NOC [26]. The ELESTRES code was implemented in this study using a combination of iterative script and functions in MATLAB^{TM}. Each iteration of ELESTRES executions within the Monte Carlo experiment were input with randomly generated values of manufacturing and operating parameters from the MATLAB^{TM} computing environment. An example input file to the ELESTRES code with an explanation of its structure is provided in Appendix B. The ELESTRES code outputs multiple fuel response parameters such as fuel and sheath temperatures, sheath strains, as well as the fission gas concentration and the internal gas pressure. An example of the TAPE4 file, which includes all of the outputs of the ELESTRES code, is also provided in Appendix B.

Post-processing of the ELESTRES outputs involve the capture of the most detrimental performance values for each of the output parameters as their representative, "worst moment," value of performance for the fuel during its in-core life. These values were assessed against the limit state criteria to determine if a failure condition was met. In the case of the Fuel Centerline Temperature (FCT) as an example, the "worst-moment" value corresponds to the instance of highest temperature that is predicted for the specific fuel power history. This is because its failure condition is based on a high-temperature

limit. The peak value of temperature typically coincides to when the highest fuel element linear power rating is experienced. This usually occurs after a refuelling shift or an insertion of the fuel into a high-power axial position. It should be noted that oftentimes, the output fuel response values observed at the "worst-moment" in the fuel history, especially for non-cumulative parameters such as temperatures, only occur for a very short period of time. However, in this study, any instantaneous occurrence of the limit state was considered as an implicit fuel failure.

6.5.2 Simulation of Transient Condition

Like the NOC simulations, the transient simulations were also conducted via the two random sampling methods for the operating data, both regionalized and for the whole core. The ELOCA IST code, which is a thermal-mechanical prediction code used to simulate CANDU fuels during transients, was used to simulate an 80% Reactor Outlet Header (ROH) break Loss Of Coolant Accident (LOCA) as a representative transient [27]. **Figure 39** below outlines the characteristics of the transient with respect to coolant pressure and relative power rating versus time, respectively. An example input file to the ELOCA code with an explanation of its structure is provided in Appendix C.

Each iteration of ELOCA executions within the Monte Carlo experiment were triggered immediately following the completion of the ELESTRES execution that preceded it. This is because the ELOCA code utilizes the ELESTRES code output to establish its pre-transient input condition. The ELESTRES outputs provide the reference snapshot of the fuel with specific power, burnup, temperatures, stresses and strains, as well as fission gas buildup that is used as the starting point of the transient simulation. The ELOCA code also outputs multiple fuel response parameters similar to those previously listed for ELESTRES. An example of the ".CSV" file, which includes all of the outputs of the ELOCA code, is also provided in Appendix C. Similar to ELESTRES, the post-processing of the ELOCA outputs also involved the capture of its most

detrimental performance values for each of the output parameters as representatives to be assessed against the limit state criteria.

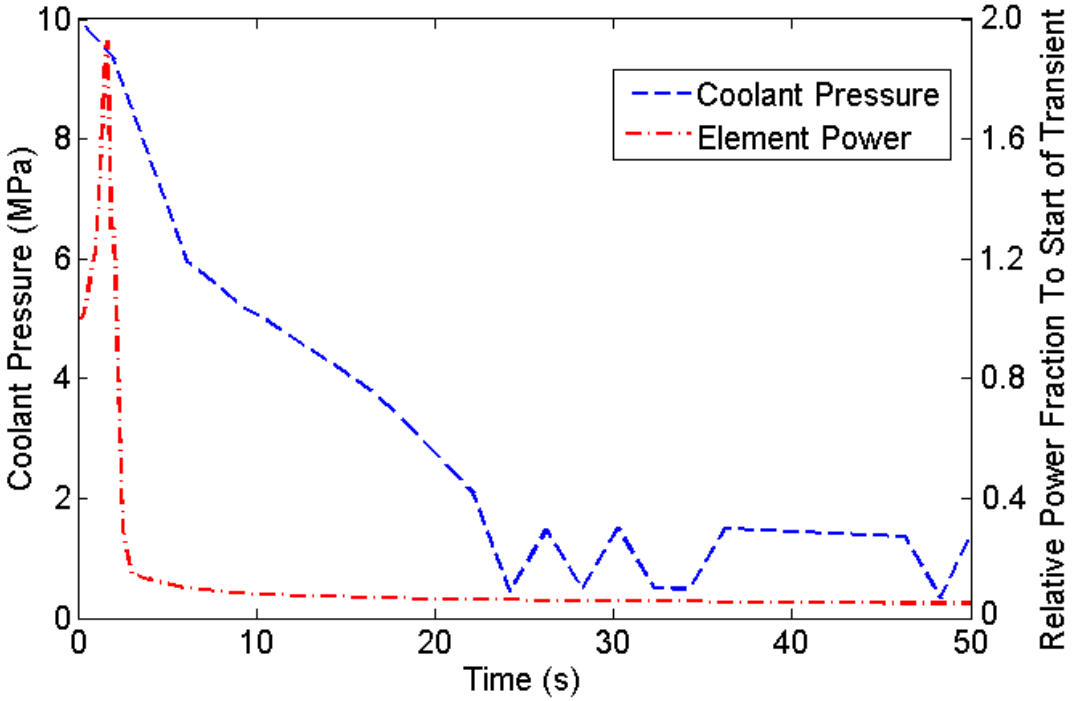

Figure 39. Coolant Pressure and Relative Power Fraction versus time relationship for the 80% ROH break transient.

6.6 Reliability Analysis

6.6.1 Limit State Criteria

The limit state criteria for this study were developed in consultation with industry literature, including the license condition handbook for the model core used in this study [31]. **Table 14** below provides a description of the fuel damage considerations adapted from [9], which was used as the basis to develop the limit state criteria used in this study. The final selection of the limit state criteria was made by taking into consideration the possible types of fuel damage in conjunction with whether their driving mechanisms are tracked by either ELESTRES and ELOCA codes (as outlined in **Table 2**), as well as their implications on limits associated with other safety-significant reactor sub-components.

Table 14. Fuel damage considerations adapted from [9].

Damage Consideration	Acceptance Criterion
Fuel element failure due to fuel melting	T1: Local temperature in all parts of the pellet shall stay below the melting point of the pellet, with a minimum acceptable margin.
Fuel element failure due to sheath melting	T2: Local temperature in all parts of the sheath and the endcap shall stay below the local melting point of the material, with a minimum acceptable margin.
Fuel element failure due to crevice corrosion	T3: Underneath a bearing pad or spacer pad, the temperature at the sheath outer surface shall be less than that required to cause crevice corrosion of the sheath, with a minimum acceptable margin.
Fuel or pressure tube failure due to overheating by contact	T4: Fuel bundle dimensional changes (e.g., due to irradiation, loads, creep, bowing, etc.) shall maintain a minimum acceptable clearance between neighbouring sheaths or endcaps and also between the pressure tube and its sheath/endcap.
Fuel sheath failure due to overpressure	S1: The excess of internal pressure over coolant pressure shall be less than the pressure that causes cracking in the fuel sheath or in the sheath/endcap junction, with a minimum acceptable margin.
Fuel sheath failure due to environmentally assisted cracking due to power ramps	S2: Stresses and strains (or related powers and ramps) during power increases in fuel elements at circumferential ridges and at sheath/endcap junctions shall be less than the appropriate defect thresholds (with a minimum acceptable margin), including the effects of pellet chips, if any.
Fuel failure due to static mechanical overstrain	S3: Local principal strain (elastic plus plastic) shall be less than the available ductility minus the minimum acceptable margin, and local creep strain shall be less than the creep rupture strain, with a minimum acceptable margin.
Fuel failure due to fatigue	S5: Cumulative fatigue damage from repeated cycles of alternating stresses and strains shall be less than the allowable fatigue life, with minimum acceptable factors of safety on the magnitude of cyclic strain and on the number of cycles.
Primary hydride failures	S7: Equivalent concentration of internal hydrogen of an as fabricated fuel element, from all sources excluding the sheath, shall not exceed the minimum acceptable limit.
Formation of a local hydride lens due to oxide and crud	S8: The combined thickness of oxide and crud on the fuel sheath outer surface shall be less than the amount required for spalling from the surface, with a minimum acceptable margin.

The final list of limit state criteria used for this study, presented below in **Table 15**, largely incorporates those which were used in [10] and [20]. The chosen limit state criteria were used as the limit response levels of the fuel performance response functions, to estimate the probability that the limit response level would be exceeded. This was done so using the survival function equation 5.16.

Table 15. Limit criteria for the 37 element CANDU fuel bundle adapted from [9,10,20].

Parameter	Failure Limit	Rationale	Predicted By
Fuel Centerline Temperature	2840°C	Fuel centerline melting temperature	ELESTRES & ELOCA
Sheath Surface Temperature	600°C for NOC 1850°C for LOCA	600°C is temperature for commencement of nucleate boiling 1850°C is zircaloy-4 melting temperature	ELESTRES & ELOCA
Fuel Sheath Strain	5% for Sheath Temps ≤ 1000°C 2% for Sheath Temps > 1000°C	Limits for excessive strain, with differing values for low and high temperature range	ELESTRES & ELOCA
Internal Gas Pressure	10 MPa	Value at which internal pressure will exceed coolant pressure	ELESTRES & ELOCA
Oxide Cracks	≥1 Oxide Cracks	Can result in localized overstrain failure due to sheath thinning and stress/strain concentration	ELOCA

6.6.2 Limit-Of-Envelope Benchmark

The limit-of-envelope benchmark used in this study adopts the same approach used in [20], where all input parameters were maximized or minimized within the reasonable range of their envelopes to the detriment of the fuel performance. The linear element power rating was conservatively affixed to a constant value of 55 kWm^{-1} against the burnup ranging from 0 to 200 $MWh(kg \cdot U)^{-1}$. **Table 16** below provides a description of the treatment of each input parameters for the limit-of-envelope benchmark.

Table 16. Description of treatment of each input parameters for the limit-of-envelope benchmark [20].

Parameter	Action	Substantiation
Pellet Diameter	Maximize	This increases the quantity of fissile material present, resulting in increased fission gas release and internal pressure. It also decreases diametral clearance.
Dish Depth	Minimize	This decreases the available free volume for gas to occupy, increasing the element internal gas pressure.
Land Width	Maximize	This both increases the quantity of fissile material and decreases the available free volume.
Pellet Density	Minimize	This decreases the thermal conductivity of the fuel pellet.
Stack Length	Maximize	This decreases the available free volume.
Axial Gap	Minimize	This decreases the available free volume.
Diametral Clearance	Minimize	This decreases the available free volume and increases the likelihood of pellet-clad interaction.
Sheath Thickness	Minimize	This increases the likelihood of defect formation and crack propagation.
Sheath ID/OD	Minimize	This decreases the available free volume as well as sheath thickness.
Filling Gas Volume	Minimize	By decreasing the gas volume within the fuel element, the internal gas pressure will have to increase, resulting in higher sheath strain.
Helium Fraction of Filling Gas	Minimize	As helium is a much better heat transfer medium than air, this action has a direct impact on the ability of the element to dissipate excess heat to the coolant, resulting in higher fuel temperatures.
Sheath Surface Roughness	No change	This parameter is assumed to be at its limit value during the MCS exercise.
Pellet Surface Roughness	No change	This parameter is assumed to be at its limit value during the MCS exercise.
Pellet Grain Size	Minimize	This will reduce the ability of the pellet to contain fission gas, resulting in higher internal gas pressure.
Pellet Gap	Minimize	This is related to the axial gap.
Axial/Radial Chamfer	Minimize	This decreases the available free volume.
Sheath Yield Stress	Minimize	A weaker sheath increases the likelihood of cracking and defect formation.
End-Cap Weld Displacement	Maximize	Increasing the displacement caused by end cap welds decreases the axial gap, reducing available free volume.
Tube Length	Minimize	This decreases the available free volume.

6.7 Uncertainty Quantification & Sensitivity Analysis

6.7.1 Uncertainty Quantification

The uncertainty quantification of this study was performed using the DAKOTA statistical analysis toolset developed by the Sandia National Laboratories [49]. All the uncertainty quantification methods used in DAKOTA perform a forward uncertainty propagation in which uncertainty characterizations for input parameters are mapped to the probabilities of the output response functions [49]. In this study, a Monte Carlo random sampling method was used to determine the input uncertainties. The uncertainty quantification was conducted for the non-regionalized, full-core simulations only, because this portion of the study best reflects the probability of failure of a random fuel within the CANDU core. The regionalized Monte Carlo simulations, on the other hand, were used to demonstrate the difference in the range of response values observed between radial regions, and to identify the most limiting region. The 95% confidence level for each of the statistical moments for the response functions of the non-regionalized Monte Carlo simulations were computed, and their respective distributions based on the upper and lower bounds of the moments were fitted.

6.7.2 Sensitivity Analysis

A global sensitivity analysis based on a variance-based decomposition method was also conducted using the DAKOTA statistical toolset. This analysis is useful, as it provides a measure of how much the uncertainty in a model output can be attributed to uncertainty associated with individual input variables. The analysis provides an account of the magnitude of the impact of errors associated with individual input variables where the analytical error propagation may be difficult to compute. The method uses two primary measures, the main effect sensitivity index and the total effect index, which are commonly referred to as Sobol indices. The main effect index corresponds to the fraction of the uncertainty in the response function that can be attributed solely to an

input variable, whereas the total effect index also accounts for the interaction between input variables. In this study, as it is assumed there are mechanistic relationships between some of the input variables, the total Sobol index is computed and presented to account for the effects of their correlation. The sensitivity analysis is conducted for the non-zonalized simulations, where operating data were randomly sampled indiscriminately from the entire core, as per the refuelling probability distribution between each zone. Both Monte Carlo random sampling as well as Latin hypercube sampling, which is a statistical method for generating near-random samples of parameter values from a distribution, were used for the analysis. However, there were negligible differences between input parameter values generated by the two sampling methods.

6.8 Case Study: Performance of Fuels Containing Burnable Absorbers

In addition to performing best-estimate analyses of current fuel reliability and safety margins, the methodology used in this study may be used to assess the impact of fuel design changes on its in-core safety performance. In order to demonstrate this useful application, the fuel safety performance simulations were repeated using 37-element fuels that have been doped with trace amounts of BNAs. The fuel design incorporates 150 mg of Gd_2O_3 and 300 mg of Eu_2O_3, which is the design used in [21]. The addition of the BNAs completely eliminates the power peaking observed during the fuelling transient, and also significantly reduces the peak powers observed during the plutonium peak. The resulting benefit of the above effects is a meaningful reduction in the size of the refuelling ripples experienced by the CANDU core on a daily basis. This is significantly effective in reducing the peak element power densities experienced by the fuels. Furthermore, the specific combination of Gd_2O_3 and Eu_2O_3 provides reactivity inhibition that specifically targets the power-peaking regions of fuel burnup. Therefore, there is negligible impact on the useful reactivity and the in-core life of the fuel. The evolution of the lattice reactivity against burnup, for the modified fuel design containing varied quantities of BNAs, is shown below in **Figure 40** and **41**.

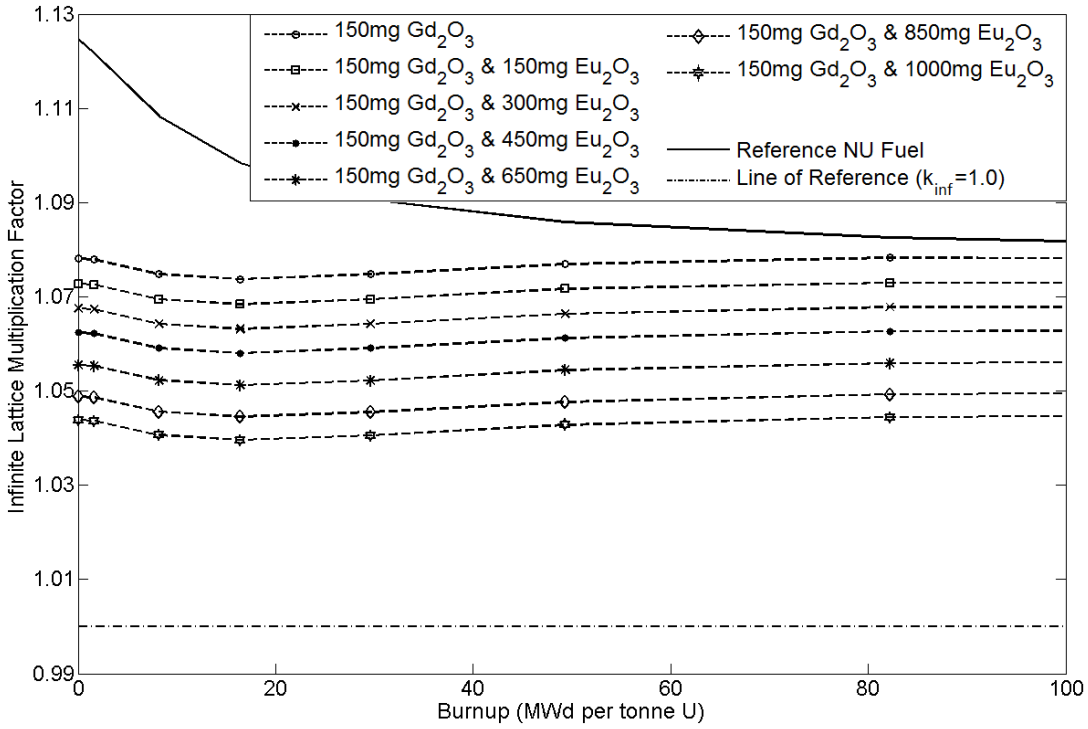

Figure 40. Evolution of the lattice reactivity (k_{inf}) versus burnup between 0 to 100 MWd (tonneU)$^{-1}$ for CANDU fuels containing burnable absorbers [21].

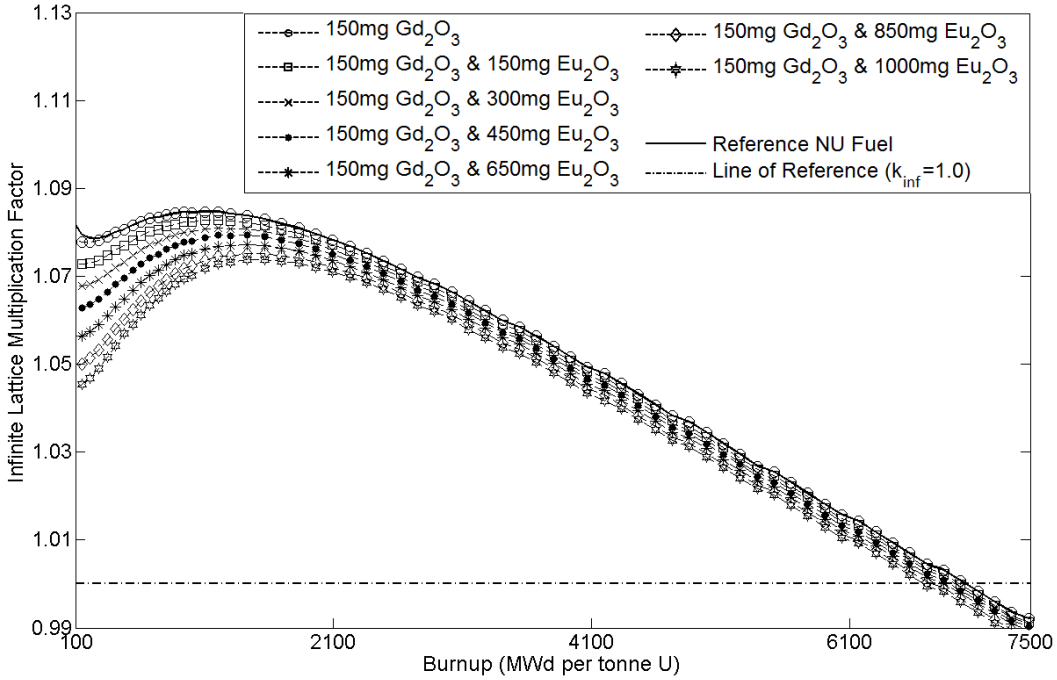

Figure 41. Evolution of the lattice reactivity (k_{inf}) versus burnup between 100 to 7500 MWd (tonneU)$^{-1}$ for CANDU fuels containing burnable absorbers [21].

The simulated generation of fuel operating data using fuels containing BNAs was conducted using a similar methodology to [21], but with a major difference being that the duration of the core-following was extended to 10,000 FPDs as opposed to the 400 FPDs in [21]. The methodology involves the same generation of refuelling history using the regular NU fuel, with all LZCs fixed at a value of 42.5% fill level. As such, the same refuelling history from section 6.4.3 was used. The refuelling history was implemented using the BNA fuel, with the same equilibrium core from section 6.4.3 as the starting point of the core-following. Therefore, a transition core-following from the regular NU fuel to the BNA fuel was simulated, with the full replacement of the original core occurring within approximately 500 FPDs. The resulting trends in the average and maximum linear element powers, as well as the average discharge burnup for each of the radial regions, are presented below in **Figure 42** and **43**. Also, the relative changes in the channel and fuel bundle powers between the two fuel types are listed below in **Table 17**.

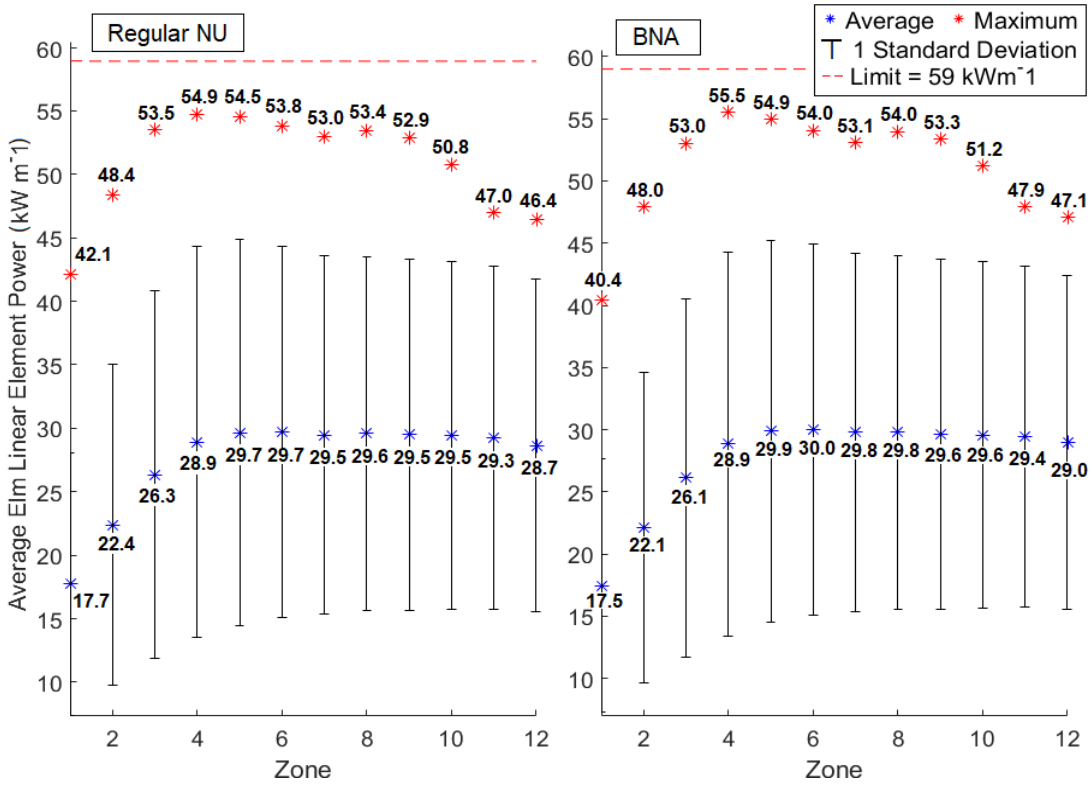

Figure 42. Average and maximum peak linear element power rating of each radial zone for the BNA-transitioned core (right) in comparison to the regular NU fuel core (left).

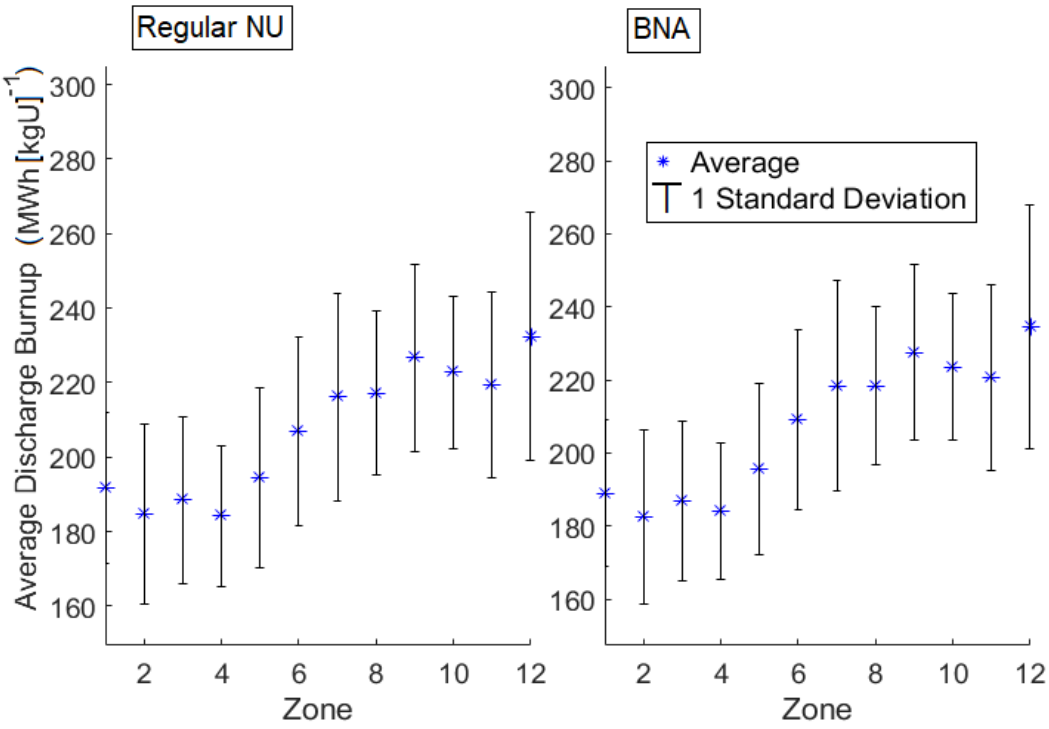

Figure 43. Average discharge fuel burnup for each radial zone for the BNA-transitioned core (right) in comparison to the regular NU fuel core (left).

Table 17. A comparison of peak channel and bundle powers between the regular NU-fuelled (control) core versus the BNA-transitioned core.

Parameters (average/max over core-following duration)	Control Core (Regular NU fuel)	BNA Transitioned Core
Maximum peak channel power	7294 kW	7285 kW
Average peak channel power	6734 kW	6716 kW
Average channel power	5523 kW	5523 kW
Maximum peak bundle power	880 kW	892 kW
Average peak bundle power	824 kW	825 kW
Average bundle power	425 kW	425 kW
Average LZC fill level	42.5%	4%

It should be noted that the preliminary results in **Table 17** indicate that while there is an overall improvement (lower peak powers) in the peak fuel channel powers for the BNA-fuelled core-following, its results exhibit a slightly higher peak power for the fuel bundle powers. This is contrary to the observations from [21], and is in part caused by

the significant difference in the length of the core-following that was conducted for the present study (10,000 FPDs) in comparison to the 400 FPD in [21]. In the case of [21], a significant portion of the duration of the core-following was spent transitioning the originally NU-fuelled core to BNA fuels, during which the LZCs were still largely in transition towards its new equilibrium fill level. When the NU-fuelled core is transition-refuelled using the BNA fuel, the LZC levels slowly decline over time to a negligible, new equilibrium value of approximately 4%. Conversely, a continued refuelling using the NU fuel maintains the LZC levels at approximately 42.5% throughout the entire core-following. The decline of the LZC fill levels in response to transitioning is not caused by a reduction in the overall reactivity imparted by each fresh fuel throughout the course of their in-core life, due to the presence of the BNAs. This is indicated by the steady maintenance of criticality long after the LZC fill levels reach their new equilibrium at 4% (after approximately 300 FPDs). Instead, this is caused by the selective, strategic reduction in fuel reactivity, coinciding exclusively with the fuelling transient and the plutonium peak regions of fuel burnup, which results in significantly smaller refuelling ripples at each instance of refuelling. This improvement in turn results in the spatial control of the LZCs being engaged at a significantly lower level than otherwise required for the regular NU fuel. Therefore, as the core is transitioned to BNA fuels and the LZC fill levels drop, the inherent improvements in transitory, peak fuel powers are exchanged for reductions in the spatial power dampening that is normally provided by the LZCs.

The above phenomenon can be viewed as transition from a finer, continuous spatial power dampening provided by the LZCs to an inherent, discrete spatial power dampening that is built into the fuel in the form of BNAs. This exchange results in the conservation of the safety margins that would otherwise be provided by the LZCs, and the refuelling ripples are inherently suppressed. This is beneficial because it increases the margins to reaching a regional overpower trip, and it provides immediate suppression of refuelling ripples as opposed to the relatively slower action of the LZCs that follow the control error signal derived from the regional power differential. However, the minor

trade-off of this benefit is that the inherent suppression of refuelling ripples by the BNAs is not as smooth or continuous as the power dampening provided by the LZCs. Also, as the LZC fill levels drop, it results in an increase in localized fuel powers that is biased towards the centre of the core, which is most significant axially, but is also observed at a relatively smaller magnitude for the radial direction. The shift in power concentration to the axial centre is demonstrated in **Table 17** by the increase in peak fuel powers (located near axial centres) as opposed to the average fuel powers (takes into account the axial periphery) which remained the same when comparing the BNA-transitioned core-following to the regular NU fuel core. Although less significant than the axial bias, a radial shift in power concentration to the centre is also demonstrated by **Figure 42**, where fuel powers for zones located near the radial centre of the core is relatively greater than the peripheral zones. The cause for this power shift towards the centre is due to the relative proximity of the LZCs' placement near the centre of the core in comparison to the periphery. As shown previously in the calandria cross-sectional diagram in **Figure 19**, the placements of LZCs' guide tubes are biased towards the axial centre of the core. Also, the position of the LZCs sitting within the guide tubes, as shown in **Figure 22**, are slightly biased towards the radial centre of the core, although much less so than the axial bias. Therefore, the transition of the main spatial power dampening from the action of LZCs to the presence of BNAs within fuels drives a bias for power concentration towards the centre of the core. This shift in power density is able to fully manifest if the transition-refuelling is allowed to play out for a sufficiently long period of time (such as 10,000 FPDs) as opposed to the relatively short, 400 FPDs that was demonstrated in [21].

As the core transitions, this eventually results in a power shift towards the axial centre of the core, and a relatively smaller power shift towards the radial centre of the core. As a consequence, the peak fuel powers, which coincide with fuel bundles located near the axial centre of the fuel channel, are further enhanced and become higher for the BNA-transitioned core in comparison to the control NU fuel core. On the other hand, the peak fuel channel powers, which are a blended sum of the fuels within the channel and is

located near the radial centre of the core, demonstrates a reduction in powers due to the suppression of fuelling ripples by the BNAs although there is a slight power shift towards the radial centre. The average values for each channel power and fuel power remain the same between both BNA and the regular fuel, because there is no change to the total power of the reactor. It should be also noted, as shown in **Figure 43**, despite the presence of BNAs, there is negligible impact on the discharge burnup of fuels for all zones, as their short-lived impact on fuel reactivity during the early stages of fuel burnup is compensated by the drop in the LZC fill levels.

The preliminary analysis indicates the presence of BNAs will produce improved channel power margins for the overall core, but also produce peak instances of fuel bundle response levels, especially temperatures, that are slightly higher. The use of BNAs, although observed to cause a slight power density shift towards the central region of the core, also reduces the occurrence of the significantly larger power impulses which are characteristic of regular NU fuels in comparison to the BNA fuel. The inherent reduction of the large power ramps, which is the major cause for fuel failure as indicated previously in Section 5.1 via **Figure 8**, is a significant advantage that is provided by the presence of BNAs. Furthermore, as indicated in [21], the conservation of the LZCs as a reservoir for bulk control and spatial dampening provides an additional layer of margin that is greatly useful from the perspective of safety.

Chapter 7: Results

In this section, the results of the Monte Carlo simulations of the 37-element CANDU fuel's reliability are presented. As there were very large quantities and sizes of relevant data generated, the results were post-processed to provide concise, graphical and tabular representations of their trends. The results are also presented as a comparison against the limit-of-envelope benchmark, comparable results from [20], as well as for regional comparisons between different radial zones of the core.

7.1 Limit-Of-Envelope Benchmark

The LOE benchmark used in this study is the same as the benchmark used in [20], but with higher resolution between burnup for the NOC simulations and time for the 80% ROH break transient simulations. The burnup range used for the benchmark is 0 to 200 $MWh(kg \cdot U)^{-1}$, and the element power is fixed at 55 kWm^{-1}. **Figure 44** shown below illustrates the trends in the resulting response functions for the LOE benchmark simulation. The figure shows that for the LOE case, the NOC centerline temperature first decreases slightly, then increases steadily as the burnup increases toward the discharge value. The initial decrease is most likely caused by the slight improvement in the heat transfer conditions from the fuel pellet surface to the fuel sheath, which is caused by the inward displacement of the sheath from the initial peak. This occurs between 0 to 45 $MWh(kg \cdot U)^{-1}$, and it decreases the magnitude of the pellet-to-sheath gap. The gradual rise in temperature afterwards is caused by a gradual decrease in the thermal conductivity of the fuel pellet with burnup, which occurs due to pellet grain growth and swelling. The LOE fuel sheath temperature, on the other hand, remains relatively constant through the entire burnup range during NOC despite changes in the fuel centerline temperature. This is because although there is significant heat transfer from the pellet surface to the inner surface of the fuel sheath, the sheath outer surface is cooled very effectively by its contact with the coolant, which is at 287°C. The coolant is pressurized and has a very high specific heat capacity; therefore, it is very effective in removing heat from the

sheath. The thickness of the sheath is not very significant relative to the rate of heat transfer to the coolant, therefore the temperature gradient across the sheath (from inner to outer) is steeply biased towards the temperature of the coolant. This causes the average temperature of the sheath to largely follow the temperature of the coolant, and relatively minor changes in the pellet surface temperature do not significantly impact the average temperature of the sheath.

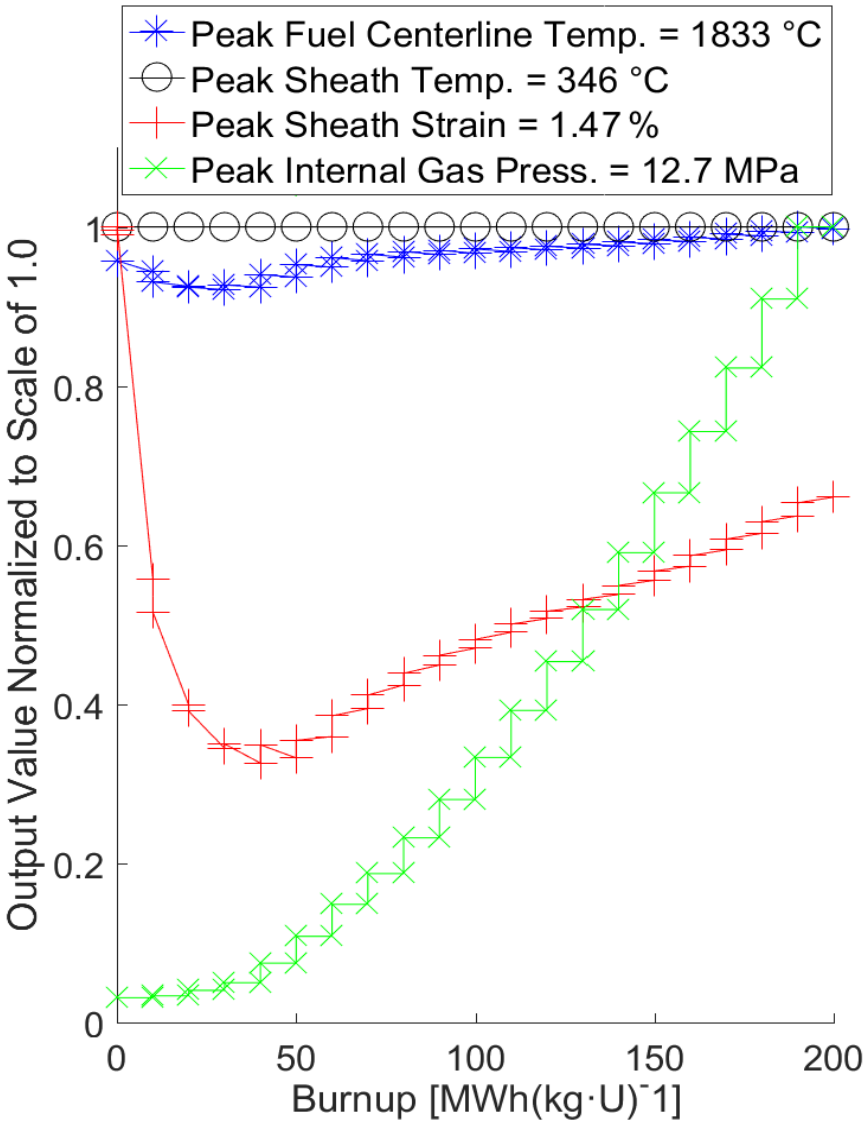

Figure 44. Diagram demonstrating the trend in the four chosen fuel response functions during NOC for the LOE benchmark case. The values are normalized to the highest occurrences of the response function value over the entire range of the burnup.

It can also be seen from **Figure 44** that the LOE internal pressure value during NOC is observed to start at the base fill gas pressure, then climbs with burnup, which is expected as fission gases accumulate inside the sheath element as the burnup increases. The LOE sheath hoop strain, on the other hand, starts at its peak value due to the initial, instantaneous and very large power ramp (from 0 to 55 kWm^{-1}) that the fresh fuel experiences upon its entry into the reactor core. The sheath hoop strain is then shown to decline linearly with burnup, and reaches a V-shaped bottom at approximately 45 $MWh(kg \cdot U)^{-1}$, then begins to rise linearly until discharge. A closer examination of this trend in strain is provided in **Figure 45**, where the total strain is broken down into its plastic and elastic (mechanical) components, as well as the thermal strain, against burnup.

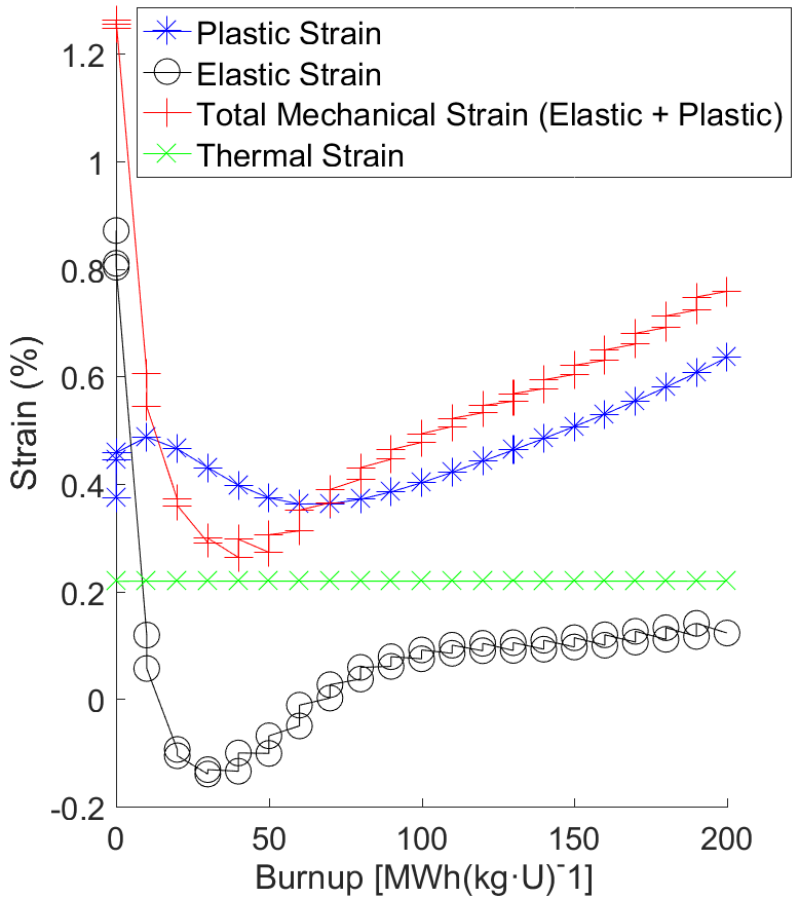

Figure 45. Diagram describing the breakdown of mechanical (elastic + plastic) and thermal strains experienced by the fuel sheath during NOC for the LOE benchmark case (not normalized).

Figure 45 shows that the LOE benchmark fuel for NOC initially experiences a significant peak value of strain upon its entry into the core at 0 burnup, where the plastic strain is 0.38% and the elastic strain is approximately 0.87%, for a combined mechanical strain value of 1.25%. When the thermal strain is also added, this results in the combined total strain value of 1.47%. This value is a very significant magnitude of the total sheath hoop strain in the positive direction, and is primarily driven by the large power ramp of 55 kWm^{-1} that is experienced by the fuel at the start of its power history. The initial, instantaneous power ramp of the fuel results in a sudden and significant thermal expansion of the UO_2 pellet. For large magnitudes of power such as 55 kWm^{-1}, this is expected to cause the fuel pellet to thermally expand to the point of experiencing increased contact with the fuel sheath. This contact, depending on the magnitude of the expansion of the pellet, can cause a significant displacement of the fuel sheath in the positive direction, enough to result in plastic deformation. The above phenomenon occurs as a consequence of the relatively low thermal conductivity of oxide fuel materials such as UO_2. The low conductivity results in a short, transitory period of time where the rate of pellet-to-sheath and then sheath-to-coolant heat transfer is relatively low. Specifically, the rate of propagation of the temperature gradient across the pellet, then into the sheath, does not occur fast enough to immediately establish a significant temperature differential between the sheath inner surface and the surface contacting the coolant (287℃). This means there is no immediate transfer of heat into the coolant before the fuel pellet experiences a significant thermal expansion. However, once the temperature of the fuel sheath inner surface exceeds the coolant temperature, heat transfer into the coolant begins, and the average temperatures of the sheath and the fuel pellet begin to decrease until the overall temperature gradient reaches an equilibrium.

Simultaneously, as the fuel pellet decreases back in size due to the in-reactor sintering (thermal reduction), a significant portion or all of the lost fuel-to-sheath gap may be recovered via the elastic behaviour of the sheath, minus any permanent deformations in the plastic region. The above phenomenon is observed in **Figure 45**,

between 0 to 10 MWh(kg·U)$^{-1}$, where the total mechanical strain declines steeply from the initial peak with a simultaneous decrease of the elastic strain and an increase of the plastic strain. After 10 MWh(kg·U)$^{-1}$, the fuel pellet is likely to have sufficiently decreased in size such that the fuel-to-sheath contact is largely lost, and the tensile property of the sheath causes the fuel to elastically continue returning to its original position, minus the permanent plastic deformation. However, the plastic strain is observed to continue decreasing beyond 10 MWh(kg·U)$^{-1}$, because of the inward creep induced by the high pressure differential between the coolant (10 MPa) and the fuel internal gas pressure. The negative value of the elastic strain, at this point, is indicative of this process.

The inward sheath creep occurs until an exact balance of pressure differential between the coolant and the fuel internal pressure is achieved. The internal pressure rises to match the coolant pressure via the accumulation of fission gases, assisted by the tensile property of the sheath (internal stress), as well as the added pressurization caused by the reduction of the sheath element plenum volume. This can be observed with the increase in burnup, as the elastic strain is seen to reach a V-shaped bottom at approximately 45 MWh(kg·U)$^{-1}$. As the burnup continues to increase beyond this point, the further accumulation of fission gases causes the combination of the fuel internal pressure, tensile strength of the sheath, and the added pressurization due to the previous volume reduction, to overtake the coolant pressure and to reverse the direction of the sheath creep to the positive direction. This causes the elastic strain to start to rise from the V-shaped bottom, reaching the positive strain territory once again, which continues on until discharge. The plastic strain lags behind the elastic strain slightly, because the initial portion of this positive displacement is largely an elastic rebound, and further displacement in the positive direction is required to actually induce a plastic strain. The thermal strain on the other hand, remains constant with burnup, because throughout this entire process the fuel sheath temperature remains very stable with burnup.

As the fuel further accumulates burnup, it is possible for the pellet grain growth and the increases in the porosity of the pellet to cause the pellet to expand sufficiently to once again establish a significant fuel-to-sheath contact. This occurrence introduces an additional mechanism by which the fuel sheath creep will be accelerated in the positive direction. Furthermore, if a fuel pellet that has experienced significant swelling is perturbed with a significant power ramp, the thermal loading can induce another sudden thermal expansion. In this case, there is very little to no margin of fuel-to-sheath gap left, so a larger proportion of the pellet expansion will directly translate to contact displacement of the sheath. It is for the above reason that high burnup fuels are susceptible to failure if introduced to a large power ramp, and this constitutes the main mechanism by which CANDU fuels have failed in the past (shown in **Figure 8**).

Next, the 80% ROH break transient simulated for the LOE benchmark is shown below in **Figure 46**. For the transient case, the centerline temperature is shown to roughly follow the shape of the power impulse, with its peak occurring at around 1.7 seconds. This is coincident to the timing of the power impulse as shown in **Figure 39**. The peaked centerline temperature then declines steadily over time until plateauing at around 30 seconds, which is a consequence of the emergency cooling and the shutdown systems engaging in response to the power transient. The sheath surface temperature, on the other hand, appears to follow a combined shape of both the power and coolant pressure trends, with a delayed peak at approximately 12 seconds, then declining over time due to a decrease in power. Also, the transient sheath temperature is observed to reach high temperatures that are well beyond the temperatures observed during NOC. The internal gas pressure also follows the shape of the power trend closely, but with a slightly delayed peak occurring at approximately 5 seconds, followed by a steady decline that also plateaus at around 30 seconds. The trend in the sheath hoop strain, however, is shown to primarily follow the depressurization of the coolant, which allows the fuel internal pressure to overcome the significantly reduced coolant pressure and therefore displace the sheath element. The sheath is displaced in the outward direction until an

equilibrium between the inside and the outside pressures is re-established. This also provides an explanation for the steady decline of the internal gas pressure, as increases in the element plenum volume due to the sheath displacement results in a proportional depressurization of the element. It should be noted that the power impulse is observed to only cause a relatively small, initial rise in the sheath strain, which coincides with the time of the impulse. This indicates that the majority of the sheath strain progression is driven by the depressurization of the coolant.

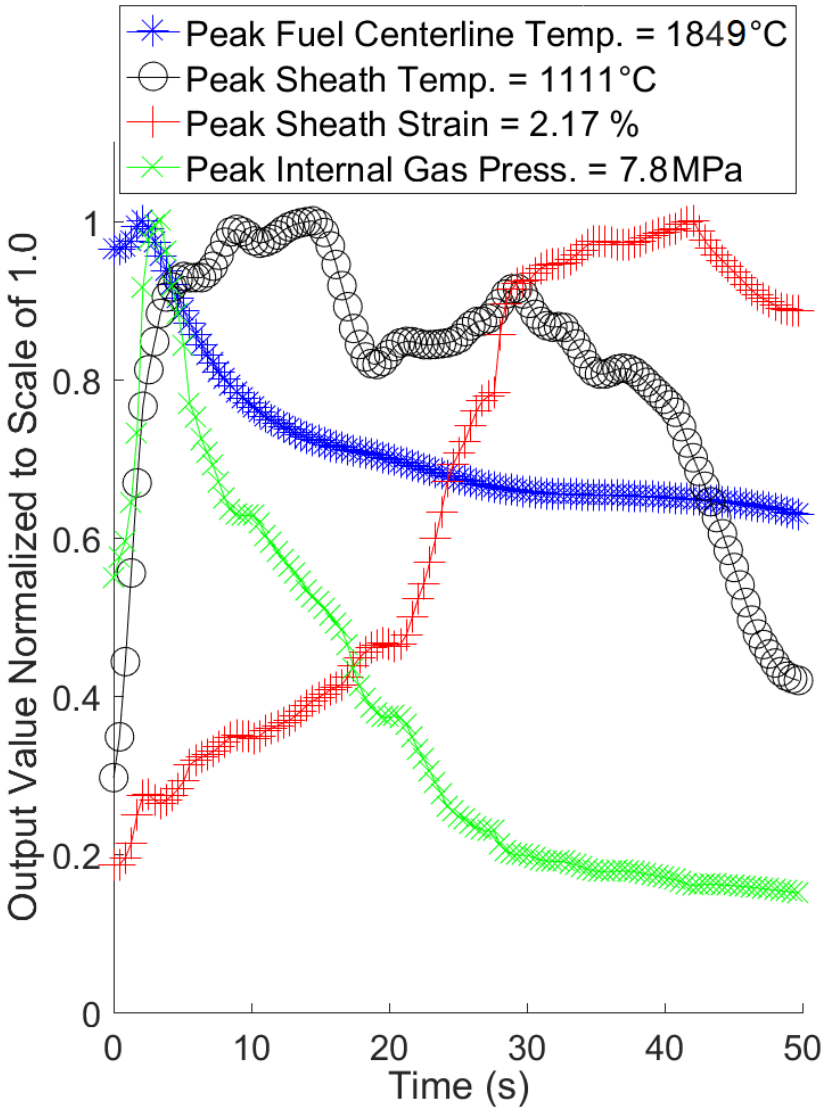

Figure 46. Diagram demonstrating the trend in the four chosen fuel response functions during the 80% ROH break transient scenario for the LOE benchmark case.

7.2 Detailed Analysis of a Fuel History Sample

Before the overall results of the Monte Carlo simulations are presented, a full-range breakdown of the results of the simulation for a randomly sampled fuel bundle is presented as an example. This is done so to provide a more detailed, representative analysis of the four fuel response functions over the full range of the fuel burnup history. As shown previously in **Figure 35**, zone #4 exhibited the highest maximum fuel power among all regions, and along with zone #5, is the most likely region to experience response function values that are closer to the limit criteria. For this reason, zone #4 was selected as the representative region where the random fuel bundle was selected for the detailed review. The specific power history of the example fuel bundle is presented in **Figure 47**. The resulting outcomes of the fuel response functions, during NOC, for the example fuel bundle are presented in **Figure 48**.

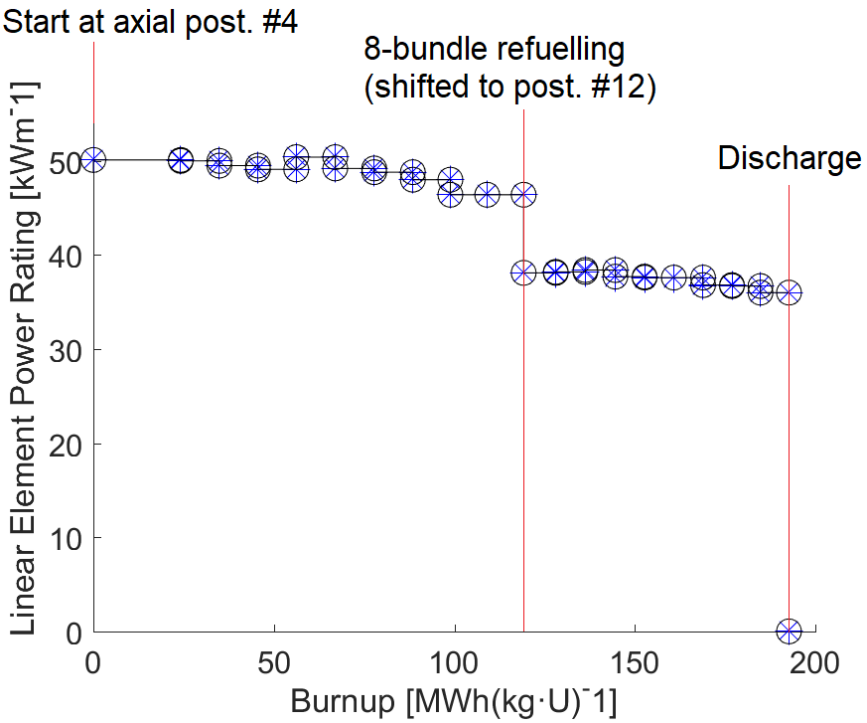

Figure 47. Burnup versus power relationship for the representative fuel simulation sample from zone #4. This particular fuel originates from a fuel channel refuelled using the 8-bundle-shift refuelling mode.

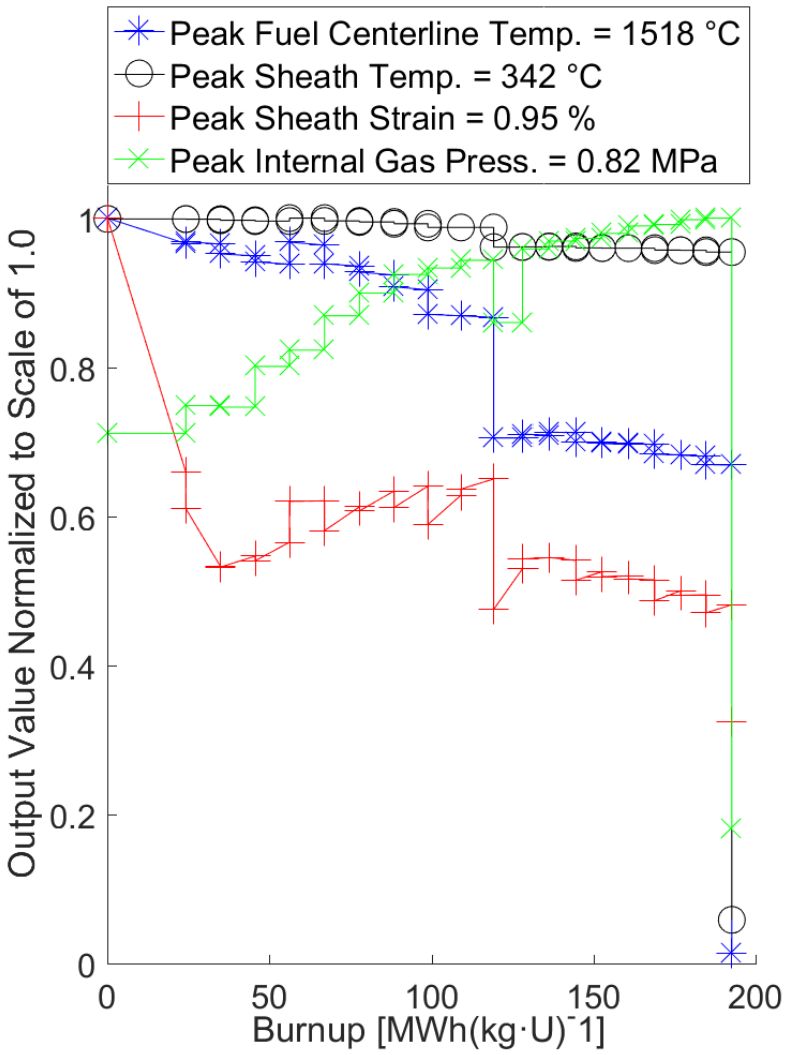

Figure 48. Diagram demonstrating the trend in the four chosen fuel response functions during NOC for the representative fuel simulation sample from zone #4.

It can be observed from **Figure 48** that, with a realistic treatment of the operating input data, the four response functions during NOC behave significantly differently in comparison to the LOE benchmark case shown previously in **Figure 44**, where the power was fixed against burnup. The centerline temperature does not rise over time, but rather peaks at an early stage in fuel burnup, then slightly steps down in power several times during the course of burnup, before significantly dropping in power at 119 $MWh(kg \cdot U)^{-1}$ in a pronounced "square" shape that resembles a step-down function. This observation is the combined result of changes in the fuel element's power rating and the fuel pellet's

thermal conductivity that occurs with the progression of the burnup, plus the transition of the fuel's axial position during its in-core life which significantly affects its power. This is a unique consideration which fully reflects the on-power, axial push-through refuelling methodology used in CANDU reactors, where the shift of fuels can result in significant step-up or step-down in power. A comparison between **Figure 47** and **Figure 48** demonstrates that the major step-down for the linear power curve coincides precisely with the drop in NOC centerline temperature at the burnup value of 119 MWh(kg·U)$^{-1}$. On the other hand, the slight decline in centerline temperature between 0 to 56 MWh(kg·U)$^{-1}$, followed by a very small step-up between 56 to 67 MWh(kg·U)$^{-1}$, coincides with the fuelling transient and the plutonium peak phases in the evolution of fuel reactivity as a function of burnup (described in **Figure 17**). The continuous decreases in the centerline temperature beyond 67 MWh(kg·U)$^{-1}$, and after the axial shift at 119 MWh(kg·U)$^{-1}$, follow the phase in the evolution of fuel reactivity where the fuel power declines linearly due to the accumulation of non-saturating fission products.

The NOC sheath surface temperature also follows a trend similar to the trend of the fuel centerline temperature, but with a less pronounced step-down in temperature following the same drop in power at 119 MWh(kg·U)$^{-1}$. As previously explained for the LOE benchmark case, this is likely due to the fact the sheath surface temperature is most significantly influenced by the temperature of the coolant. The coolant acts as a very strong heat sink for the sheath temperature regardless of significant changes in the rate of heat transfer from the fuel pellet. Nevertheless, it should be noted that the peak sheath temperature for this particular fuel power history is 342℃, which is slightly less than that of the LOE benchmark case, which had a higher value of 346℃. This observation indicates that although the temperature of the fuel sheath is strongly dependent on the temperature of the coolant, the power rating of the fuel element and therefore the fuel pellet surface temperature, does influence the resulting sheath temperature to a lesser degree. In the case of the internal gas pressure, the response appears to correlate to both power and burnup, because the pressure increases proportionally as the burnup rises, but

it also experiences a "square" shaped dip at 119 MWh(kg·U)$^{-1}$ where the element power is stepped down. This is an expected outcome, because fuel burnup drives the generation of fission gases, and therefore the pressure increases with the accumulation of fuel burnup. However, the fuel element power also plays an important role as it affects the rate of reaction and decay mechanisms for fission products that depend on the neutron flux. Therefore, the internal gas pressure closely follows the progression of burnup, but also incorporates the trend of any significant perturbations in the fuel power.

The NOC sheath hoop strain starts at an initial, peaked value of 0.95% for the total strain. This value is significantly less than the 1.48% observed for the LOE benchmark. This difference is caused by the change of 5 kWm^{-1} that exists between this particular fuel bundle power history (50 kWm^{-1}) and that of the LOE benchmark (55 kWm^{-1}), at zero burnup. Nevertheless, an initial power rating of 50 kWm^{-1} is still a very high value with a low probability of occurrence. The large positive mechanical strain indicates that the power ramp has caused a sufficient fuel pellet expansion to induce pellet-to-sheath contact and a subsequent sheath displacement. A further investigation on the impact of the magnitude of the initial fuel power on the initial value of mechanical strain has confirmed that the initial mechanical strain becomes zero when fuel bundles are operated at element powers approximately below 22kWm^{-1}. The exact initial fuel power at which this occurs does vary depending on other manufacturing properties of the fuel bundle, especially the initial fuel-to-clad distance. However, this indicates that low fuel element powers, such as below 22 kWm^{-1}, cannot induce sufficiently high magnitudes of thermal load to cause a meaningful contact displacement in the positive direction. In fact, for low fuel element powers below 20 kWm^{-1}, there is negligible fuel-to-sheath contact in general, and thus immediately experience sheath creep in the negative direction due to the coolant pressure. For very low fuel powers, this is sufficient to cause an overall total strain in the negative direction despite the positive thermal strain. In the case of this particular fuel bundle history, however, the initial power ramp of 0 to 50 kWm^{-1} causes a significant mechanical strain in the positive direction.

Following the initial, positive peak in the mechanical strain, the sheath elastically rebounds towards its original shape, minus the plastic deformation, in the same way as described for the LOE benchmark case. The sheath then creeps in the negative direction until an equilibrium in the internal and external forces is reached. This equilibrium coincides with the V-shaped bottom of strain plot, which in this case occurs at 35 MWh(kg·U)$^{-1}$. After this point, the steady rise in the fuel internal pressure with increasing burnup causes the sheath to slowly creep in the positive direction. The fuel, however, is shifted to a lower-powered axial position at 119 MWh(kg·U)$^{-1}$, which causes an abrupt power ramp-down and therefore an abrupt drop in the mechanical sheath strain. Following this shift, the fuel experiences a series of slow, small decreases in power with increasing burnup, which results in proportional decreases in the fuel internal pressure. This causes the internal and external pressure balance to shift in favour of the coolant once again, which drives the subsequent sheath creep in the negative (inward) direction. A detailed breakdown of the mechanical strains (elastic and plastic), as well as the thermal strain is presented below in **Figure 49**.

Although the change in magnitude is relatively small, the thermal strain does not remain constant in **Figure 49**, but instead follows the trend in fuel power changes that occur with increasing burnup, as well as the refuelling shift which occurs at 119 MWh(kg·U)$^{-1}$. This observation is contrary to that which was observed for the LOE benchmark case in **Figure 45**, where the fuel power was constant with the burnup. However, this is an expected observation, because the sheath thermal strain is affected by the fuel sheath temperature, which in turn is affected by changes in the fuel pellet temperature. The fuel pellet temperature is, of course, affected by the fuel element power rating, which was not fixed in this case. It should also be noted, for this particular fuel history, the initial mechanical strain of 0.73% at zero burnup consists entirely of elastic strain, and there is no plastic strain. For the LOE benchmark case, the initial plastic strain was 0.38% and the elastic strain was 0.87%, for a combined mechanical strain value of 1.25%. The LOE benchmark case likely required slightly higher

mechanical strain than this particular fuel history to cause an immediate plastic strain, as it was operating with a slightly higher sheath temperature. A higher temperature value causes the tensile yield strength of the sheath to become lower and the yield strain to become higher as the alloy becomes more malleable. Nevertheless, this suggests that a mechanical strain value somewhere between 0.73 and 0.87 % is required to immediately cause plastic strain to occur at zero burnup, for a sheath temperature value between 342 to 346 ℃.

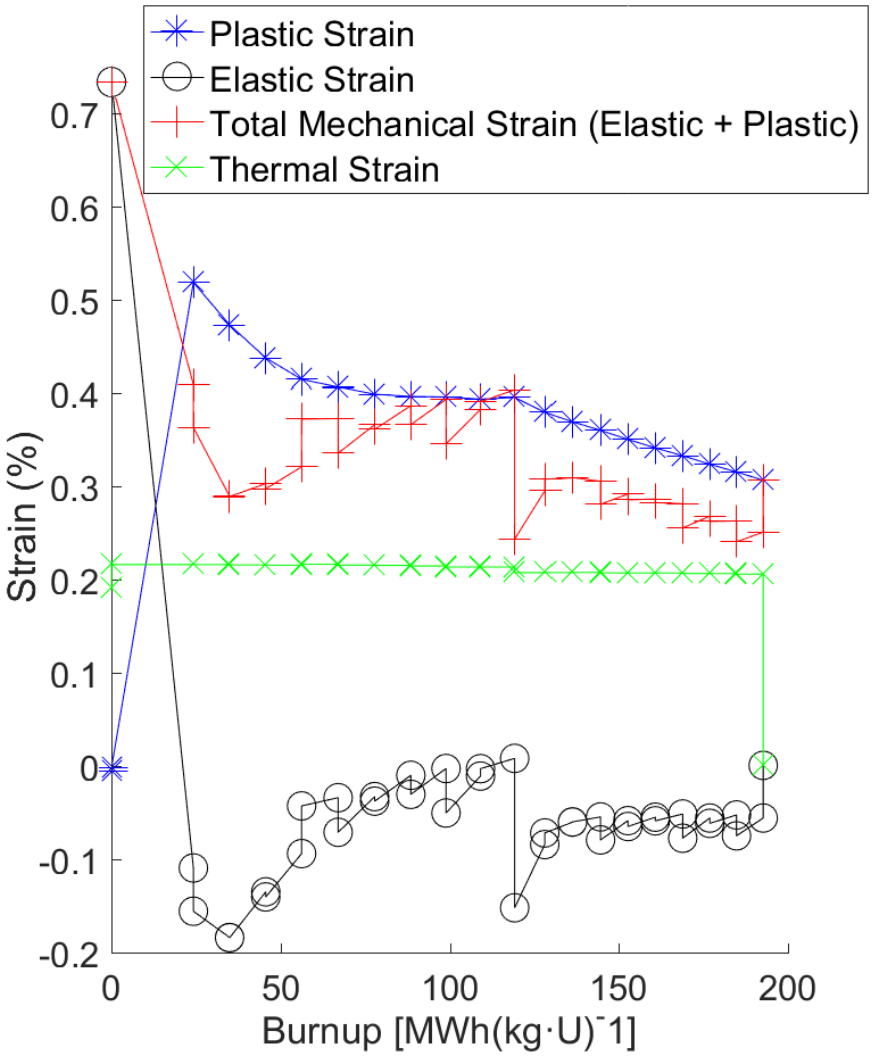

Figure 49. Diagram describing the breakdown of mechanical (elastic + plastic) and thermal strains experienced by the fuel sheath during NOC for the representative fuel simulation sample from zone #4.

Another important observation for the two mechanical strains is that the initial elastic strain value of 0.73% quickly declines to -0.11%, while the plastic strain sharply increases from 0 to 0.52%, between the burnup values of 0 to 24 MWh(kg·U)$^{-1}$. This behaviour was also observed for the LOE benchmark case in **Figure 45** where the plastic strain increased from the initial value of 0.38% to a value of 0.49% by 10 MWh(kg·U)$^{-1}$, whereas the elastic strain decreased from 0.87% to 0.1%. It should be noted that the above conversion of the initial elastic strain to plastic has been observed to occur consistently between 0 to 8 MWh(kg·U)$^{-1}$, but is not always reflected in the output data. This is because the number of burnup steps used for each simulation are limited in order to reduce the computational requirements of the overall analyses. Therefore, smaller burnup steps are typically allocated to major events, such as an axial shift caused by the refuelling, and relatively coarser burnup steps are used throughout the rest. Nevertheless, the above conversion of the elastic strain to plastic is consistently observed for fuels experiencing an initial peak in the positive mechanical strain. This is because the above phenomenon consists of a significant thermal expansion of the fuel pellet followed by a subsequent thermal reduction due to cooling. This results in a large, contact-induced sheath displacement in the outward direction, followed by an inward, elastic return. The plastic portion of the deformation, however, does not return with the elastic rebound and therefore emerges in place of the elastic strain as it decreases.

Next, the 80% ROH break transient scenario, simulated for the representative fuel bundle sample history from zone #4, is shown below in **Figure 50**. It should be noted that the transient scenario in this study is simulated to occur at a burnup value of 50% of the fuel discharge burnup. This selection is very important to the peak power experienced during the transient, and is further discussed in section 7.3.1. The transient simulation indicates that the fuel centerline and sheath temperatures behave similarly to the LOE benchmark in **Figure 46**, but the internal gas pressure and the sheath hoop strain are observed to behave significantly differently. The trend in the fuel centerline temperature for the transient simulation closely resembles the transient trend in the fuel

power shown in **Figure 39**, which was expected. The main difference of this sample fuel in comparison to the fuel centerline temperature observed in the LOE benchmark case is that the magnitude is smaller, as a lower fuel element power was used. The fuel sheath temperature, on the other hand, follows the inverse of the transient trend in the coolant pressure shown in **Figure 39**, but once again with a smaller magnitude overall, due to the lower fuel power that was used in comparison to the LOE benchmark. The internal gas pressure, however, does not peak with the occurrence of the power impulse as the LOE benchmark case did. Instead, it continues to increase steadily in magnitude until peaking and starting to decline at 18 seconds into the transient.

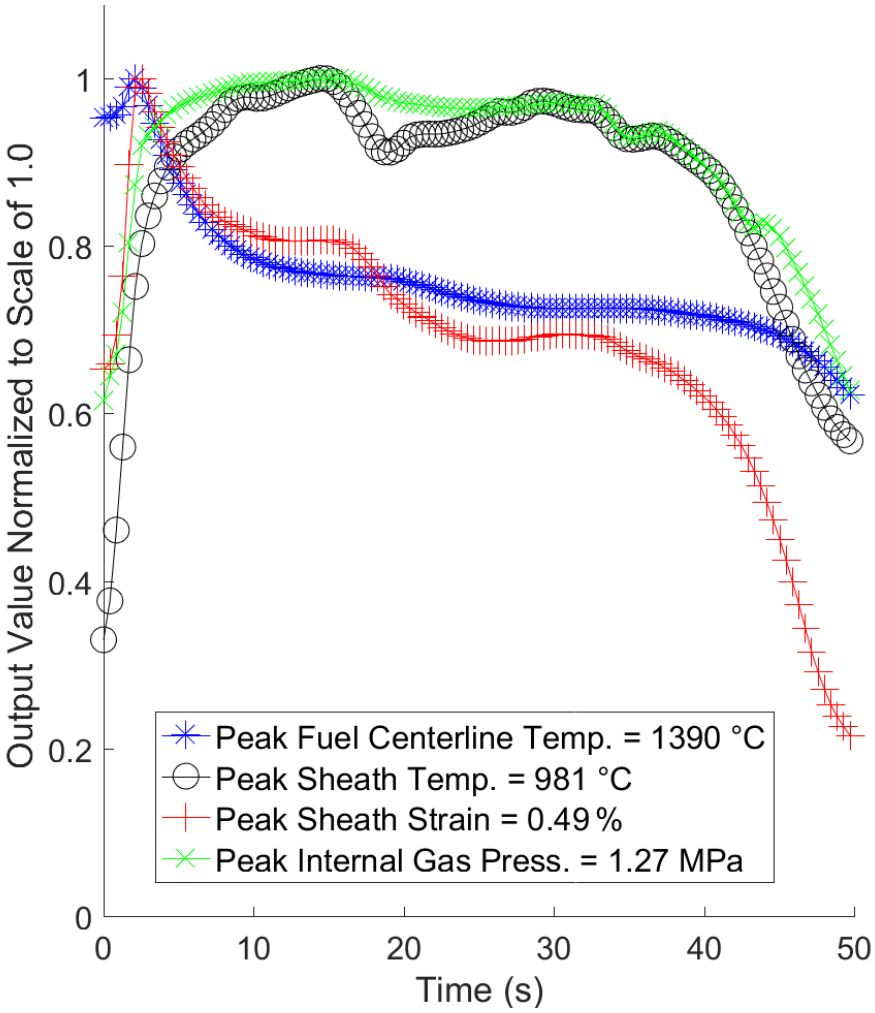

Figure 50. Diagram demonstrating the trend in the four chosen fuel response functions during the 80% ROH break scenario for the fuel simulation sample from zone #4.

The sheath hoop strain, on the other hand, does peak at the same time as the power impulse, but unlike the LOE benchmark case, continues to decline after with time. The above observations for the fuel internal pressure and the sheath hoop strain are related, and are likely due to the magnitude of the peak pressure obtained during the transient being significantly smaller than which was observed for the LOE benchmark case. The peak internal pressure observed during the transient for the sample fuel history is 1.27 MPa, whereas it was 8.25 MPa for the LOE benchmark case. The pressure value peaks, then declines rapidly for the LOE simulation, because the high value of the internal pressure causes the fuel element to expand once the opposing coolant pressure rapidly declines, thereby increasing the element volume and consequently decreasing the internal pressure. This effect is not observed for the sample fuel history, because the fuel element only reaches a peak internal pressure of 1.27 MPa shortly after the power impulse, such that the residual internal pressure following the power decrease is unable to overcome the tensile strength of the sheath and cause a displacement. Moreover, at a peak value of 1.27 MPa, the internal gas pressure does not significantly overcome the external coolant pressure that still maintains a minimum value between 1 to 1.5 MPa after depressurization.

7.3 Regionalized (Radial) Monte Carlo Simulations

The outcomes of the Monte Carlo simulations for both ELESTRES and ELOCA, where fuel data were discretized between 12 radial regions of the core as defined in **Figure 34**, are presented in this section. The results presented here consist of the average occurrence plus the standard deviation of the peak values of response functions observed over the entire duration of the fuel burnup history, for each radial region. The peak value of the response functions was chosen as the performance metric of interest, because it is most likely to coincide with a breach of the limit criteria, or the most significant breach among other instances. Overall, the NOC simulations indicate there are significant increases in the predicted margins to performance limits when more realistic treatment of

manufacturing and operating data are implemented in place of conservative assumptions. This was observed across the board for all output performance parameters that were tracked in this study. The transient simulations using ELOCA also demonstrated an overall improvement in safety margins in comparison to the more conservative benchmarks. However, there were unexpected improvements in some of the response function values for the transient simulations in comparison to the NOC.

7.3.1 Fuel Centerline Temperature

First, the trend in the fuel centerline temperatures for the NOC and the transient simulations, for each region, are shown below in **Figure 51**. It can be observed that the peak centerline temperatures predicted for both NOC and transient conditions indicate reductions in the average fuel centerline temperatures when compared to the control benchmark as well as values adapted from [20]. This improvement is significant, with the smallest relative difference in fuel centerline temperature for the NOC condition being from the highest-powered region of zone #4, which exhibited an average temperature of 1343°C with a standard deviation of 104°C. This is still an improvement of approximately 433°C in comparison to the fuel centerline value of 1776°C from [20], and 490°C in comparison to the LOE benchmark value of 1833°C. Furthermore, the differences between the average fuel centerline temperature values and the limit criteria, for all zones and for both NOC and the transient case, are equal to multiple times the values of their standard deviations. As an example, for zone #4 which is the most limiting region, the limit criteria of 2840°C is 14 standard deviations away from its average peak centerline temperature of 1343°C.

The trend in the peak centerline temperature for both the NOC and the transient simulations appears to strongly follow the trend of the peak element powers for each zone. The central regions of the core exhibit higher fuel centerline temperature values than the periphery, with the peak region being in the vicinity of zone #4. This outcome is

likely driven by the relationship between the fuel pellet temperatures and the volumetric heat generation rate, which is a function of the fuel power. The dominant resemblance in trend between the element power rating and the peak pellet centerline temperature suggests that the difference in the average discharge burnup between each radial region do not impart as significant of an impact on the peak pellet centerline temperatures. However, it should be noted that high burnup fuels do tend to exhibit higher pellet centerline temperatures due to reductions in the heat transfer coefficient of the UO_2 pellet, as it will have become more porous and non-stoichiometric (excess oxygen) [22].

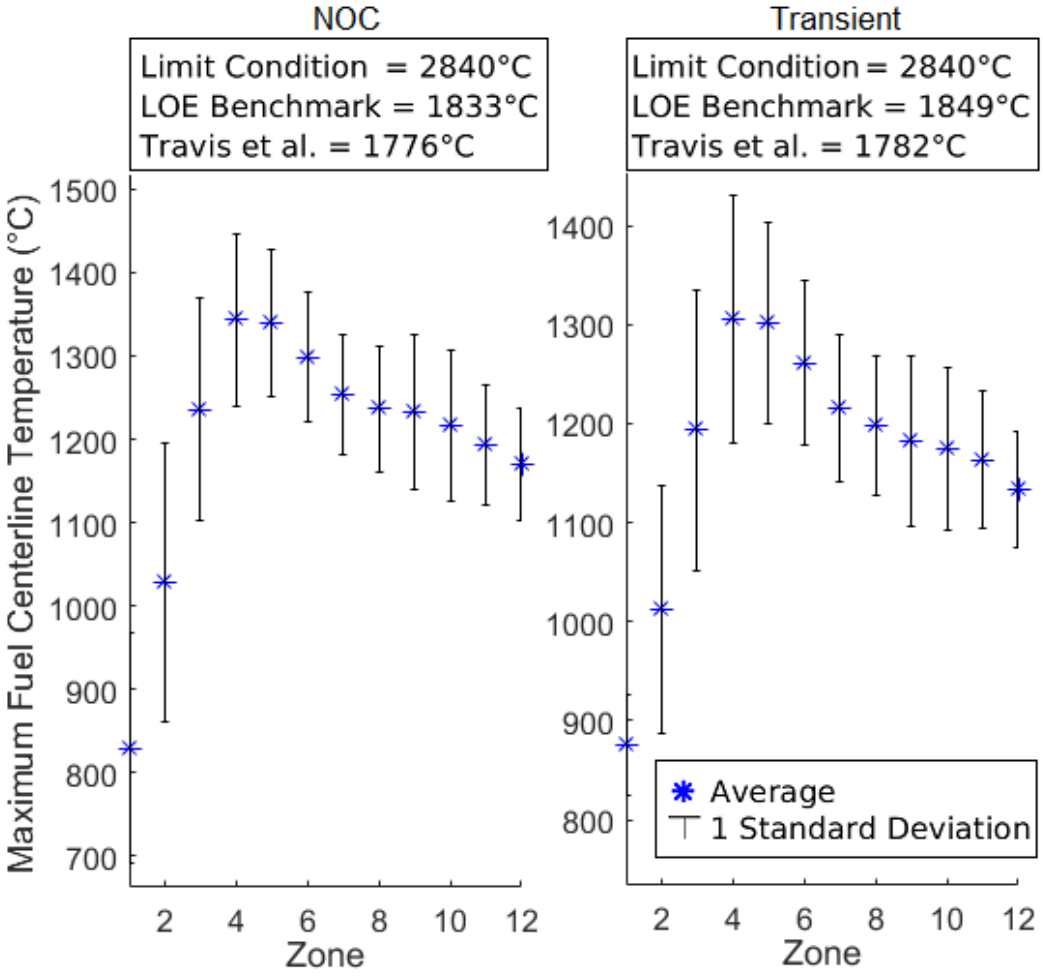

Figure 51. Trend in the maximum fuel centerline temperature during NOC (left) and the 80% ROH break transient case (right), for each radial region.

The comparison between the transient and NOC simulations is interesting, because it indicated some unexpected safety margin improvement observed for the transient simulations in relation to NOC, as shown in **Figure 51**. For example, the peak NOC centerline temperature for zone #4 was 1343℃, whereas the transient equivalent is 1305℃ with a standard deviation of 125℃, which places it 12 standard deviations away from the limit. This observation is contrary to expectations because the transient used in this study emulates an impulse power peaking of 1.93 times the pre-transient power rating, which should result in a significant consumption of safety margins, especially those which relate to the pellet temperatures. This outcome is explained by the fact the element power snapshot, which is produced by ELESTRES to be used as the start of the transient by ELOCA, was set at the burnup value of 50% to the discharge burnup within the NOC fuel power history. This was the default setting for the transient ELOCA model, and was kept with the reasoning that a fuel at the half-way point in its burnup to discharge is a reasonable, average representation of a random fuel bundle to experience the sudden transient condition if one was to occur. However, the selection of the instantaneous burnup at which the transient simulation begins is a critically important consideration that has a significant impact on the outcomes of the transient simulations.

When a fuel is at its halfway point in burnup, it is typically past its peak power not only due to the accumulation of non-saturating fission products, but more significantly due to its likely shift away from the high-power axial location within the channel due to refuelling. This is further demonstrated below in **Figure 52**, where the fractions of discharge burnup at which the peak fuel power occurs, for both the four and eight bundle shift refuelling modes, respectively, are presented. It is observed that for the vast majority of the time, moments of peak powers within the burnup lifetime of fuel bundles occur well before the half-way point in their burnup to discharge, typically near the 20% fraction region. This is caused by the combined effect of the plutonium peaking phenomenon, which occurs around 45 $MWh(kg \cdot U)^{-1}$ and therefore at approximately 24% of discharge burnup for zone #4 as an example, as well as the burnup value at which the refuelling shift to a higher-powered axial location occurs for the particular fuel bundle.

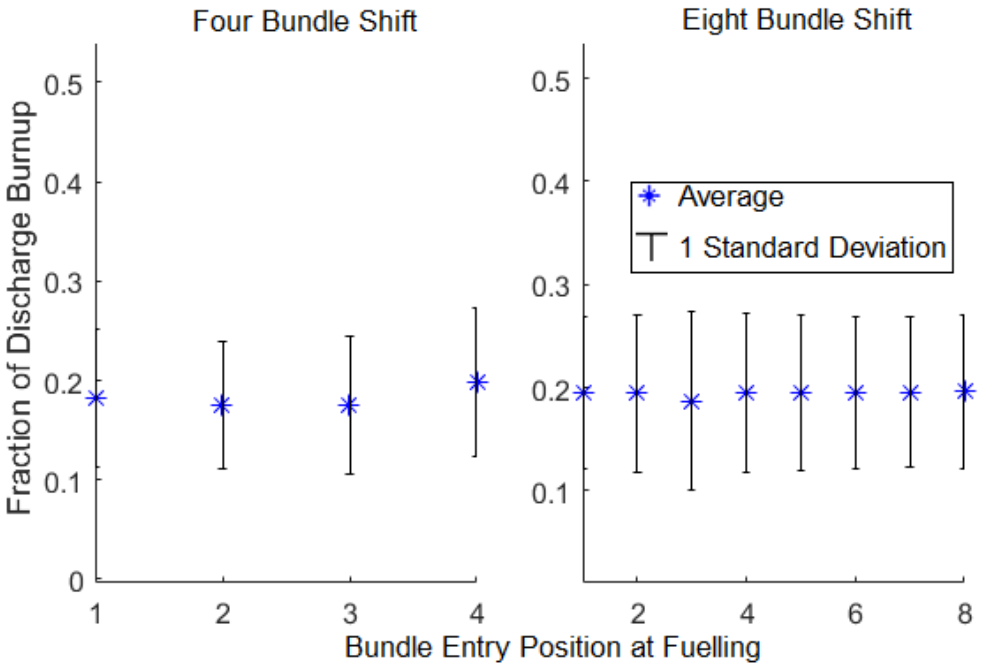

Figure 52. Average fraction of discharge burnup at peak fuel power rating for four (left) and eight (right) bundle shift refuelling modes.

Typically, the timing of the refuelling shift occurs at a relatively low burnup value. This is because when a fuel bundle is located in a low-power axial position, its rate of burnup accumulation is relatively slow. As a result, although irradiation at a low-powered axial position may occupy a significant time period during the in-core lifetime of the fuel, it only accounts for a fraction of its overall accumulation in burnup by the time a refuelling shift occurs. The vast majority of the burnup accumulation occurs when the particular fuel bundle becomes located in a high-powered axial position, whether via consecutive refuelling shifts or via an immediate insertion when first introduced into the core. For example, in the case of the particular fuel history provided in **Figure 47**, because the fuel was immediately inserted into a high-power position, the peak power occurs around 56 MWh(kg·U)$^{-1}$, which is approximately at 29% of the discharge burnup of 193 MWh(kg·U)$^{-1}$. This confirms that although a power impulse of 1.93 times the initial value is imparted by the simulated LOCA, the initial, pre-transient element power snapshot derived from the half-way point to discharge burnup from NOC history is still significantly lower than the NOC peak power that is reached at 18% of discharge burnup.

Moreover, although the power impulse is significant, the increase only starts at 0.4 seconds, peaks at 1.7 seconds, then decreases back down to the initial power level at 2.0 seconds, and continues to decrease to less than a fractional value of 0.15 by 3.0 seconds from the start of the perturbation. The duration of the power peak that is experienced for the transient case is therefore very short-lived, which in comparison to the duration and the magnitudes experienced in the full range of the NOC power histories, is typically less important and thus results in lower peak values for the fuel temperatures. It should be noted that the internal time-step used for ELOCA in this study is 0.2 seconds. Therefore, the progression of the simulated LOCA transient and the occurrence of peak values for the response functions are captured with a sufficient time-resolution [27].

To confirm the impact of pre-transient start-point selection, the transient simulations were recalculated using two additional pre-transient selection points that provide a better coverage of the full range of NOC power history. They consist of the pre-transient starting at the burnup value coincident to the peak fuel power during NOC, and the transient starting right before the bundle discharge. The recalculated transient simulations starting at peak NOC power yielded output parameter values that were closer to limit states than values obtained for NOC, which was the expected outcome not observed in the original transient simulations with half-way burnup as the pre-transient condition. For example, for zone #4, which had an average peak centerline temperature of 1305°C during transient versus 1343°C during NOC, a higher peak centerline temperature of 1444°C was predicted by the recalculated transient simulations using the peak NOC power as the pre-transient condition. This value is still multiple standard deviations away from the limit. Alternatively, when the exact discharge burnup value was used as the pre-transient condition, the initial power was at its lowest, thereby resulting in only 880°C at the peak of the power impulse. This observation indicates that although high-burnup fuels face higher risks of failure due to defect mechanisms influenced by burnup accumulation, they are also much more likely to experience significantly smaller power ramps in response to perturbations.

7.3.2 Fuel Sheath Temperature

Next, the trends in the sheath surface temperature for both NOC and the transient simulation cases, respectively, are shown below in **Figure 53**. Unlike the fuel centerline temperature, a smaller improvement in safety margin was observed for the sheath surface temperatures. For zone #4 as the most limiting example (close to the limit value), there was an improvement of approximately 10°C from the LOE benchmark of the NOC simulations, and approximately 150°C for the transient case. Nevertheless, the trend in the sheath surface temperature in relation to the zones appears to follow a similar trend as the peak linear element ratings per each region. This is an expected outcome considering the dominant relationship between the fuel power and the rate of heat generation.

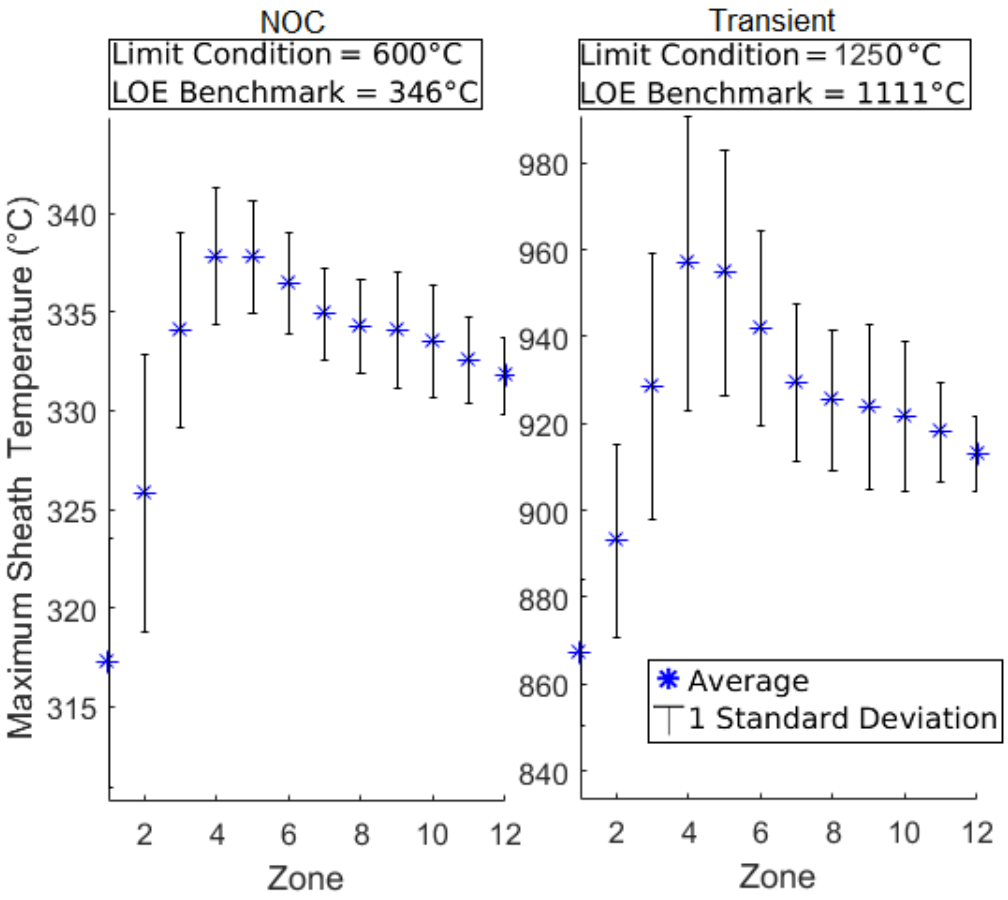

Figure 53. Trend in the peak sheath inner surface temperature during NOC (left) and the peak sheath average temperature for the 80% ROH break transient (right).

For NOC, the limit value for the sheath temperature is many standard deviations away from the average peak values. For example, the average peak temperature value for zone #4, which is 338 ℃, has 1 standard deviation equal to 3.5 ℃, and is therefore 75 standard deviations away from the limit value of 600℃. However, for the transient, the average values consistently exceed 600℃, which is a reasonable observation considering the significant decline in coolant-to-sheath heat transfer coefficient that is caused by the rapid depressurization (further discussed in 7.4). In the case of zone #4, the average peak sheath temperature for the transient simulations was 957℃ with a standard deviation of 34℃, which is still 26 standard deviations below the zircaloy-4 melting limit of 1850℃. The transient sheath surface temperatures were also recalculated using fuel power snapshots derived from different points in the NOC burnup history. For zone #4, the recalculated transient sheath temperature using the pre-transient burnup snapshot at peak fuel power resulted in a value of 994°C. This is significantly higher than predicted by the original calculation using the half-way burnup. On the other hand, the recalculated transient simulations using the exact value of the discharge burnup as the pre-transient condition resulted in 856°C due to the significantly lower initial power condition.

7.3.3 Internal Gas Pressure

Next, the trends in the sheath internal pressure for NOC and transient conditions, respectively, are shown below in **Figure 54**. Similar to the other performance parameters, there is a significant safety margin improvement for the sheath internal pressure during NOC in comparison to the benchmark simulation and values predicted by [20]. The trend of the internal pressure in relation to each zone appears to also closely follow the shape of the trend in peak linear element power rating relative to the zones. The limit condition is multiple standard deviations away from the average values as well, where zone #4, with the average peak value of 0.8 MPa and 1 standard deviation equal to 0.18 MPa, is 51 standard deviations away from the 10 MPa limit. For the internal gas pressure, there was no performance improvement observed for the transient simulations in comparison to the NOC despite using the half-way point in NOC burnup as the pre-

transient snapshot. This is because the internal gas pressure depends not only on the accumulation of burnup, but also on large perturbations of fuel power. For fuel bundles that are input with realistic operating histories, the internal gas pressure does not only increase constantly with the accumulation of burnup, but can instead increase or decrease with perturbations in power.

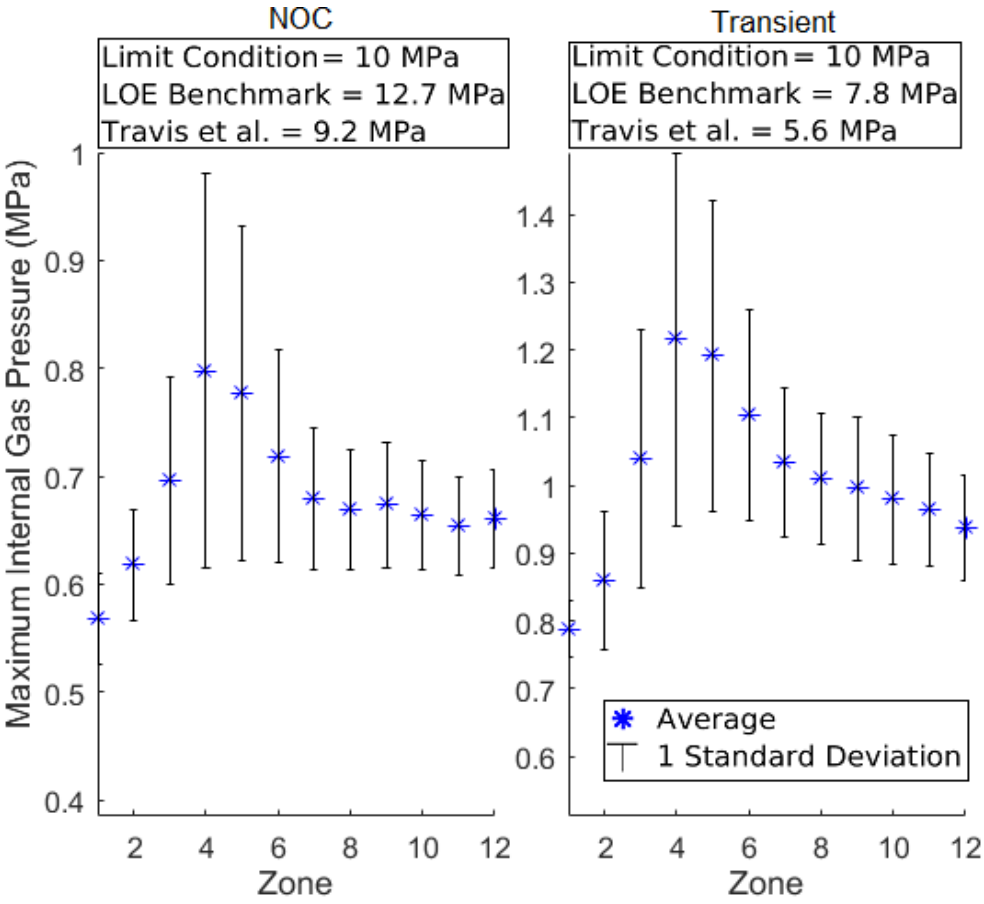

Figure 54. Trend in the maximum internal gas pressure during NOC (left) and 80% ROH break transient (right) for each zone.

As shown previously in **Figure 48** for the example fuel bundle from zone #4, the internal gas pressure achieved at 50% of the discharge burnup during NOC is only slightly smaller (about 10%) in value than the pressure experienced at the discharge burnup. Where a realistic power history is used as input, this small difference of internal pressures between 50% to 100% of the burnup range during NOC applies to the vast

majority of fuel bundles. This is because a large majority of fuel bundles experience a significant step down in power from their peak values prior to discharge, due to a shift in their axial position caused by refuelling. The exception to this is fuel bundles inserted into axial positions greater than #5, in 8-bundle-shift refuelled channels, because they are immediately discharged from the core upon refuelling, rather than being shifted axially. Amplified by the power impulse experienced during the transient, this refuelling shift is sufficient to result in a higher instantaneous value of transient internal pressure than the NOC maximum, even if a slightly lower value of pressure was used as the pre-transient condition. For zone #4, the average peak internal pressure for the transient case was 1.22 MPa with a standard deviation of 0.28 MPa, which places it 31 standard deviations away from the limit value of 10 MPa. For comparison, recalculations using pre-transient power snapshots at different burnup values were also computed. This resulted in different values of peak transient pressures, which as an example for zone #4, yielded a value of 1.25 MPa using the peak NOC power as pre-transient, and 0.9 MPa when the discharge burnup was used as the pre-transient. In consideration of their pre-transient values of internal pressure as well as the fuel power, the above recalculated values of transient pressures compare reasonably to the previous value of 1.22 MPa obtained using the 50% to discharge burnup.

7.3.4 Sheath Hoop Strain

Next, the trends in sheath hoop strain at pellet end for NOC and transient, respectively, are shown below in **Figure 55**. For the maximum sheath hoop strain, significant improvements in margins to limit were observed. For example, the average peak strain value during NOC was 0.50% for zone #4, which is about 0.97% less than the strain predicted for the benchmark case, and 0.85% less than the comparable value reported by [20]. The limit state of 5.00% for temperatures below 1000°C, which applies to all cases within NOC, is also multiple standard deviations away from the average NOC value. The strain value of 0.50% predicted for zone #4, with 1 standard deviation equal to 0.17%, is 26 standard deviations away from this limit.

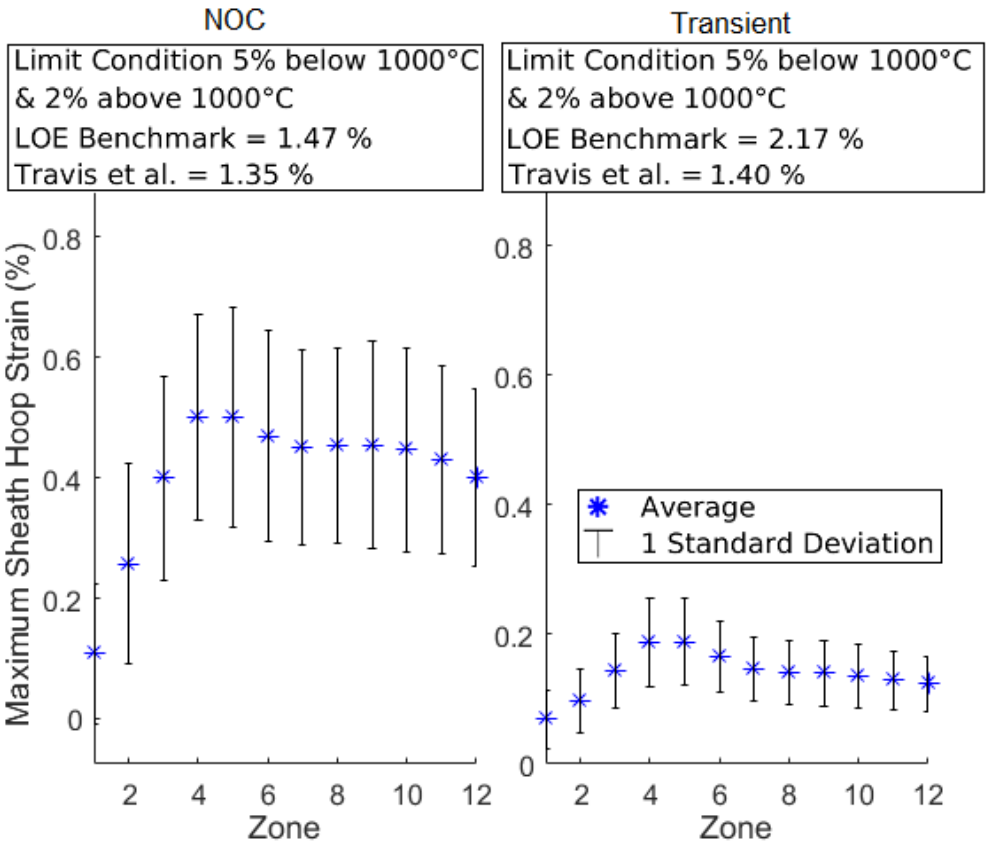

Figure 55. Trend in the maximum sheath hoop strain at pellet end during NOC (left) and 80% ROH break transient (right) for each zone.

For the sheath hoop strain, there were expectations that the trend in strain development would be affected by the average discharge burnup of each zone, with higher burnup zones exhibiting higher peak strain. However, the predicted peak strain values still appear to be mostly influenced by the fuel power, as the trend in strain among zones appears to predominantly follow it (shown in **Figure 42**) as opposed to the burnup. This is such that the highest average value of the peak strain among all zones occurs in zone #4, which has the highest maximum for peak fuel element powers, but with a relatively lower average discharge burnup value of 193 $MWh(kg \cdot U)^{-1}$. On the other hand, the zone with the highest average discharge burnup, which is zone #9 with a value of 225 $MWh(kg \cdot U)^{-1}$, resulted in a relatively smaller value of the average peak strain. This suggests that, on average, the initial, fuel-to-sheath contact displacement that can be induced by the impulsive thermal expansion of the fuel pellet, which is dependent on the

initial power ramp of the fuel at the start of irradiation, is a very significant contributor to the peak value of the total mechanical strain. This occurs because for fuel bundles that experience an impulsive fuel-to-sheath contact displacement (followed by a rebound) at the start of irradiation, the initial strain can often be greater than the maximum strain caused by creep. This is because the progression of creep is a relatively slow process that is capped by the length of the fuel's in-core life. This phenomenon was previously demonstrated in **Figure 48** and **49** for a random fuel bundle sampled from zone #4. To further demonstrate this effect, the probability of occurrence for the impulsive, fuel-to-sheath contact displacement at the start of irradiation was computed for each radial region. This was done via a binary count of whether a contact displacement occurred at the start of irradiation, for all fuels simulated for the radial region, divided by the total number of fuels for the region. The probabilities for each radial region are shown below in **Figure 56**, which indicates a significant value between 0.38 to 0.50 for all zones.

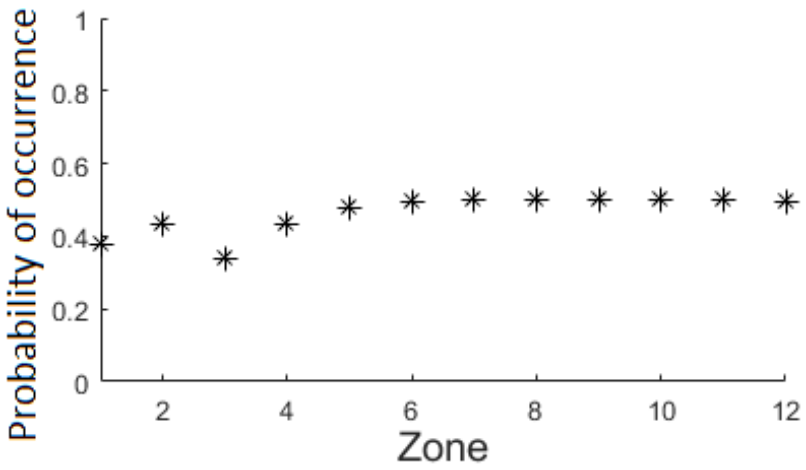

Figure 56. Probability of occurrence for an impulsive sheath displacement due to fuel-to-sheath contact at the start of irradiation.

As the above probabilities were obtained via a binary count, there is no variance associated with their values. Also, zones #1 and #2 are shown to experience higher probabilities than zone #3 despite the lower average powers, because they are refuelled using the 8-bundle-shift refuelling mode as opposed to the rest that are refuelled using the 4-bundle-shift mode. The 8-bundle-shift refuelling mode increases the probability

that a fuel bundle, upon its entry into the core, will be placed in a high-power axial position near the middle of the fuel channel, in comparison to the 4-bundle-shift mode.

Performance improvements between NOC and transient simulations were also observed for the sheath hoop strain, where the average peak strain value observed for the LOCA simulation for zone #4 was 0.19%, which is well below the equivalent NOC value of 0.50%. This was contrary to the expectation, because higher sheath temperatures that were reached during the transient simulations were expected to cause the fuel sheath to become more prone to displacement due to a reduction in its tensile strength. The sheath temperatures observed during transient simulations were in excess of 1000°C for all radial regions except zones #1 and #2, beyond which the strain limit becomes 2.00%. The average peak strain value observed for zone #4, at a value of 0.19% with 1 standard deviation equal to 0.07%, is therefore 26 standard deviations away from the limit value.

The unexpectedly low strain values observed from the transient simulations, in comparison to the NOC, are caused by the selection of the pre-transient, initial strain values that were used for the transient simulations. The pre-transient strain snapshot is carried over from the NOC simulation at a select point in burnup, and the default value used was at 50% burnup to discharge, which is at a relatively low stage of strain progression. Also, the inventory of the fission gases and consequent element internal pressure carried over from the NOC simulation as a pre-transient snapshot is relatively small, especially at the 50% of discharge burnup. The average peak internal pressure value from the NOC simulations was only 0.8 MPa for zone #4. A fraction of this peak pressure value is not sufficient to overcome the tensile strength of the sheath, in addition to the residual coolant pressure value of 1.5 MPa, to impart a significant sheath strain in the positive direction. Also, it should be noted that pellet swelling occurs with fuel burnup, such that a contact can eventually be made with the sheath inner surface. This results in a secondary mechanism, in addition to the internal gas pressure, that can cause deformations of the sheath. The burnup-driven pellet-to-sheath contact typically only occurs at high values of burnup where the pellet has swelled significantly. Therefore, in

the case of the pre-transient snapshot taken at 50% of the discharge burnup, the pellet swelling is likely to have been insufficient to make contact with the sheath inner surface.

To confirm the impact of the pre-transient burnup selection on the predicted sheath strain, the transient simulations were repeated using burnup value coinciding on the peak fuel power, as well as at the discharge burnup. The recalculated average peak sheath strain for the transient simulations using the pre-transient burnup at peak power yielded a value of 0.24% for zone #4, which is not significantly larger than the original average peak strain value of 0.19%. This has likely occurred because although the pre-transient state coinciding on the peak power would significantly increase the strain as a result of higher element power rating, it occurs at a low burnup, and likely coincided with a low value of strain in the positive direction. On the other hand, the recalculated value for the average peak sheath strain for the transient simulations, using the discharge burnup as the pre-transient snapshot, was 0.12% for zone #4. This is a very low value considering the relatively greater accumulation of fission gases and pellet swelling at the pre-transient snapshot, due to the higher value of fuel burnup. The cause behind this observation is due to the fuel element power being very low at the discharge value of the burnup, which ultimately causes the peak strain value observed during the transient to be very small.

7.3.5 Oxide Cracks

In addition to the four response functions relating to temperatures, pressure and strain, the occurrence of oxide cracks was also tracked. ELOCA provides predictions for oxide crack formation by indicating whether or not one has occurred. No figures or tables are presented in this subsection because there was no oxide crack formation observed during all stages of simulation for the 80% ROH break transient scenario. No particular trend could therefore be observed for oxide crack formation in relation to the operating and manufacturing inputs. However, this observation is indicative that for the input parameter ranges at which the 80% ROH break LOCA transient was simulated, there is a negligible risk of oxide crack formation.

7.4 Non-Regionalized Monte Carlo Simulations

The results of the Monte Carlo simulations with randomized selection of fuel bundles from the entire core without regionalization are outlined below in Figures **57** to **80**. Three different graphical representations of the results are presented. First, a histogram with an empirically fit PDF with its 95% Confidence Interval (CI), plus the 95% Prediction Interval (PI) for the population are presented. The bin sizes for the histograms were selected via the Freedman–Diaconis rule [50]. The second diagram represents the empirical CDF fit, as well as the 95% CI of the fit based on its shape parameters. The theoretical fits based on Normal, Log-normal, Exponential, and Weibull distribution types are also represented in the second diagram. The third diagram represents the survival function, also known as the Complementary Cumulative Distribution Function (CCDF), which represents the cumulative probability that the random value of "*x*" will exceed a selected value of "*X*."

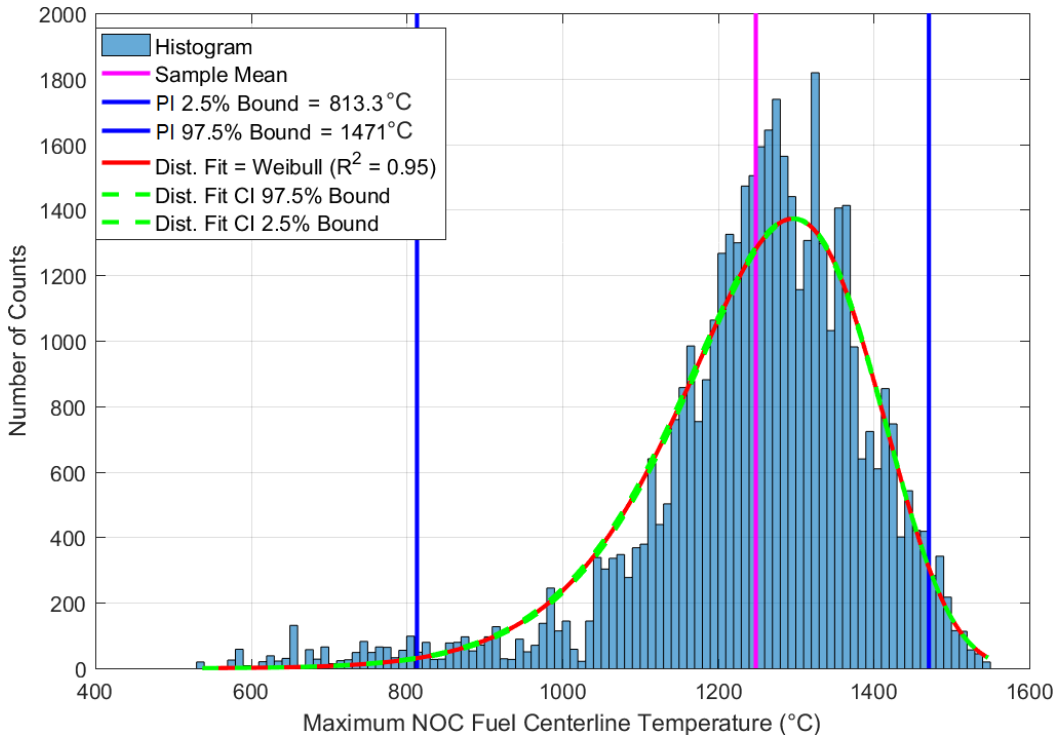

Figure 57. Histogram and empirical PDF fit of NOC Fuel Centerline Temperature with 95% CI.

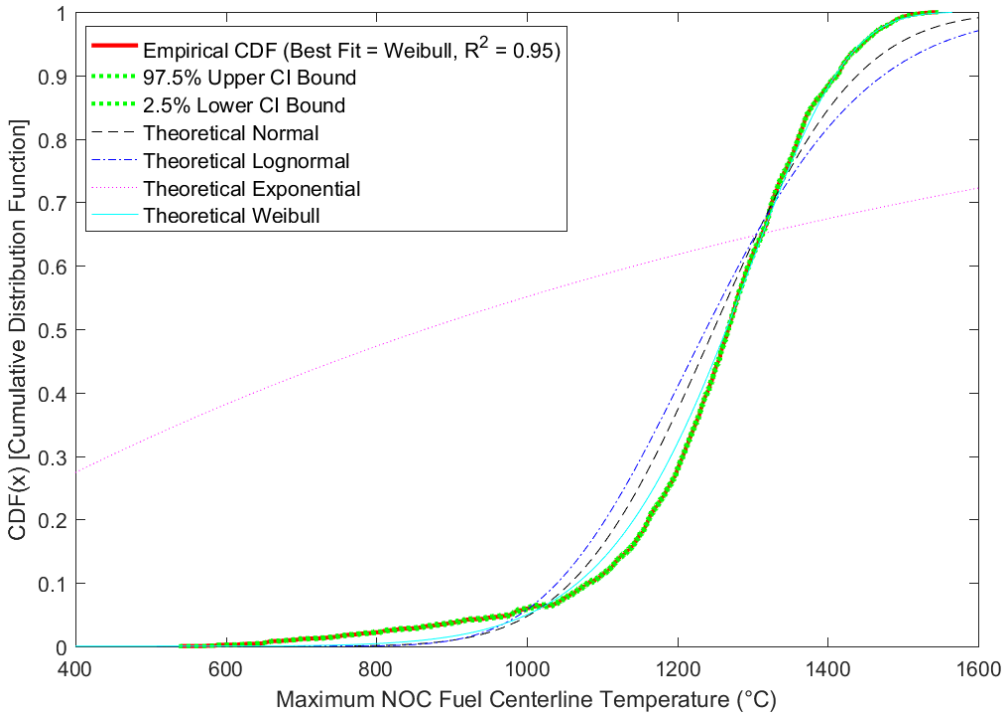

Figure 58. Comparison of empirical CDF fit with 95% CI versus theoretical distribution fits for NOC Fuel Centerline Temperature.

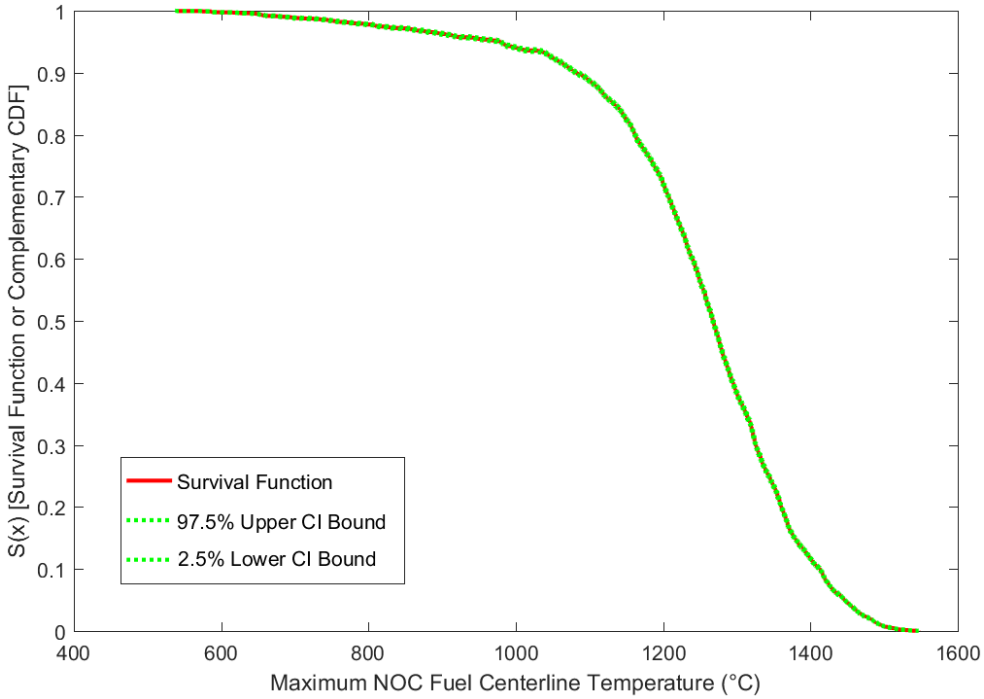

Figure 59. Empirical survivability function fit with 95% CI for NOC Fuel Centerline Temperature.

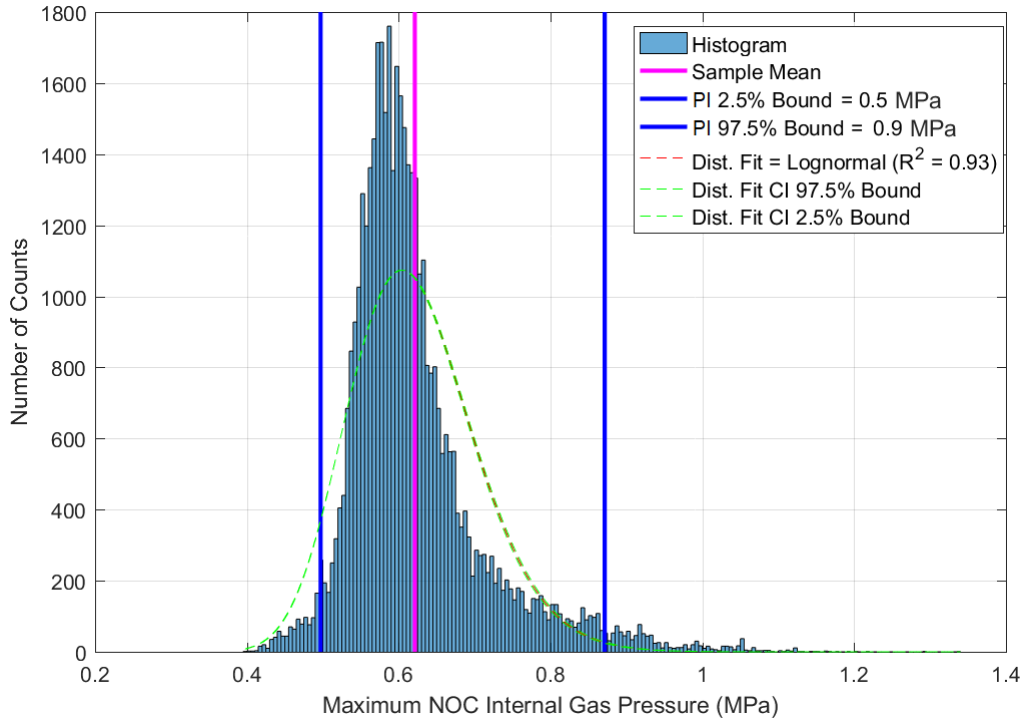

Figure 60. Histogram and empirical PDF fit of NOC Internal Gas Pressure with 95% CI.

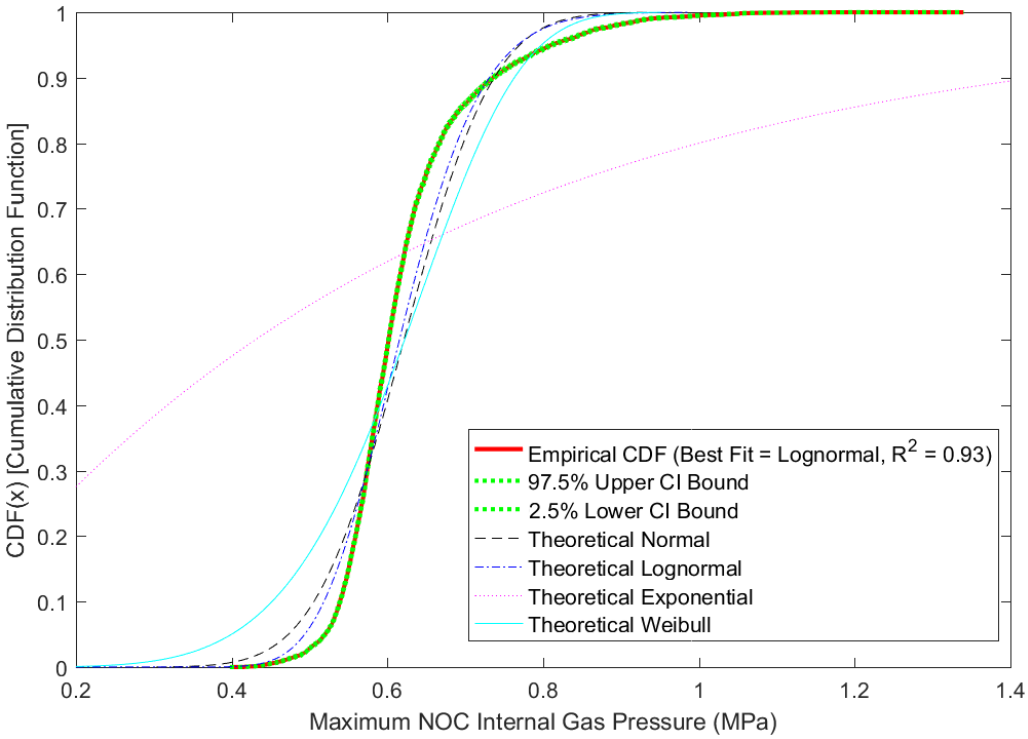

Figure 61. Comparison of empirical CDF fit with 95% CI versus theoretical distribution fits for NOC Internal Gas Pressure.

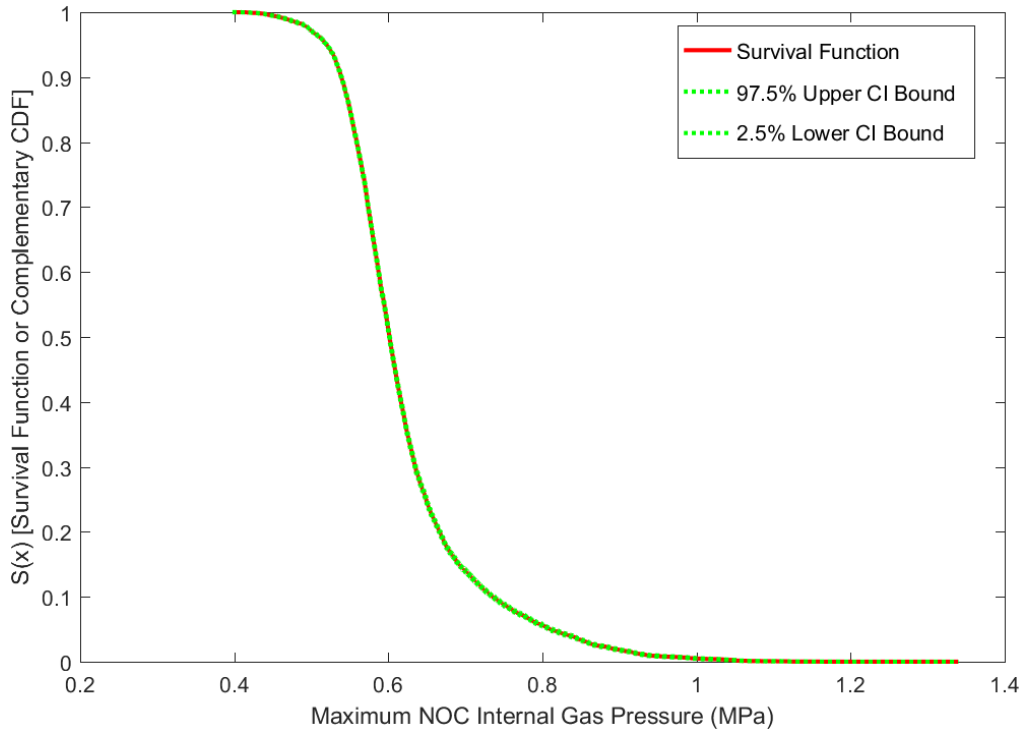

Figure 62. Empirical survivability function fit with 95% CI for NOC Internal Gas Pressure.

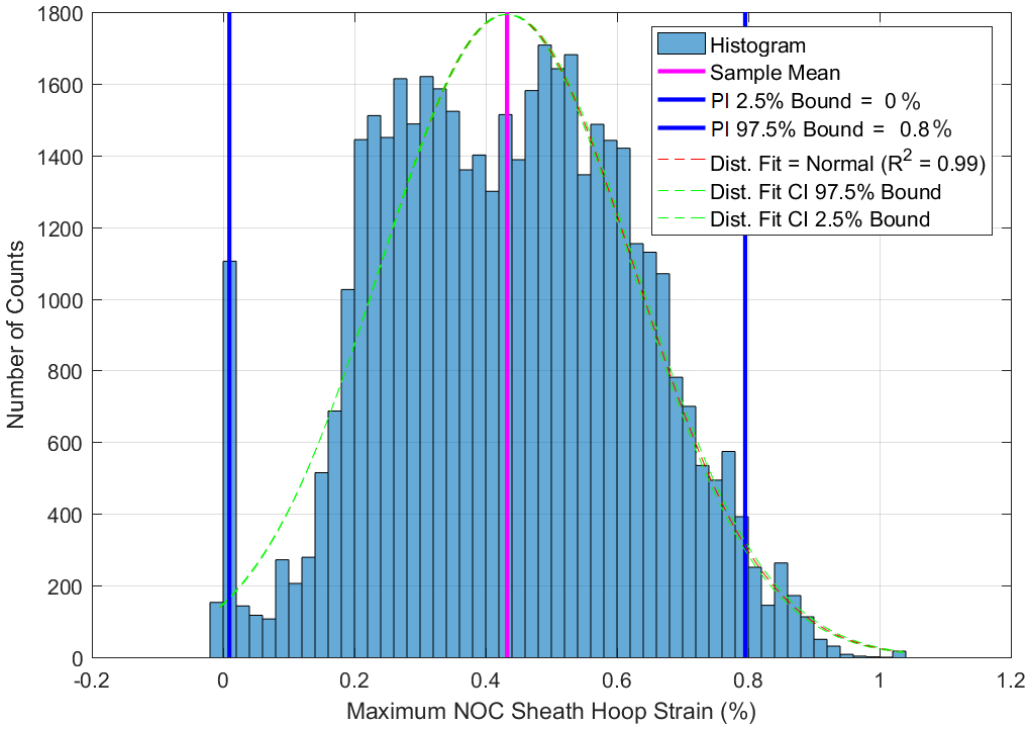

Figure 63. Histogram and empirical PDF fit of NOC Sheath Hoop Strain with 95% CI.

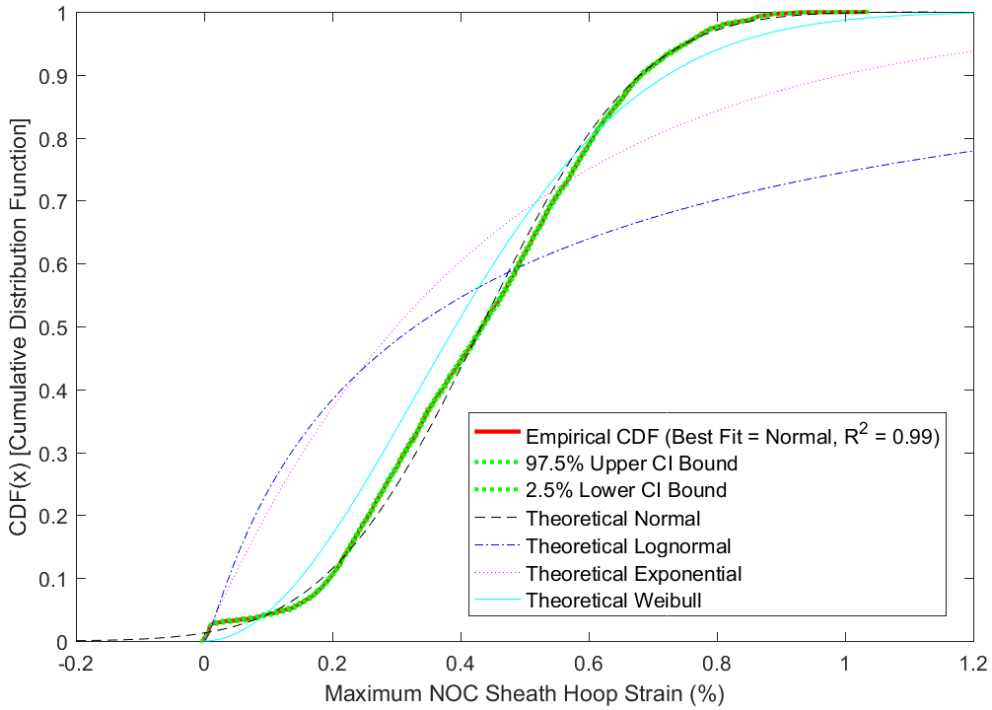

Figure 64. Comparison of empirical CDF fit with 95% CI versus theoretical distribution fits for NOC Sheath Hoop Strain.

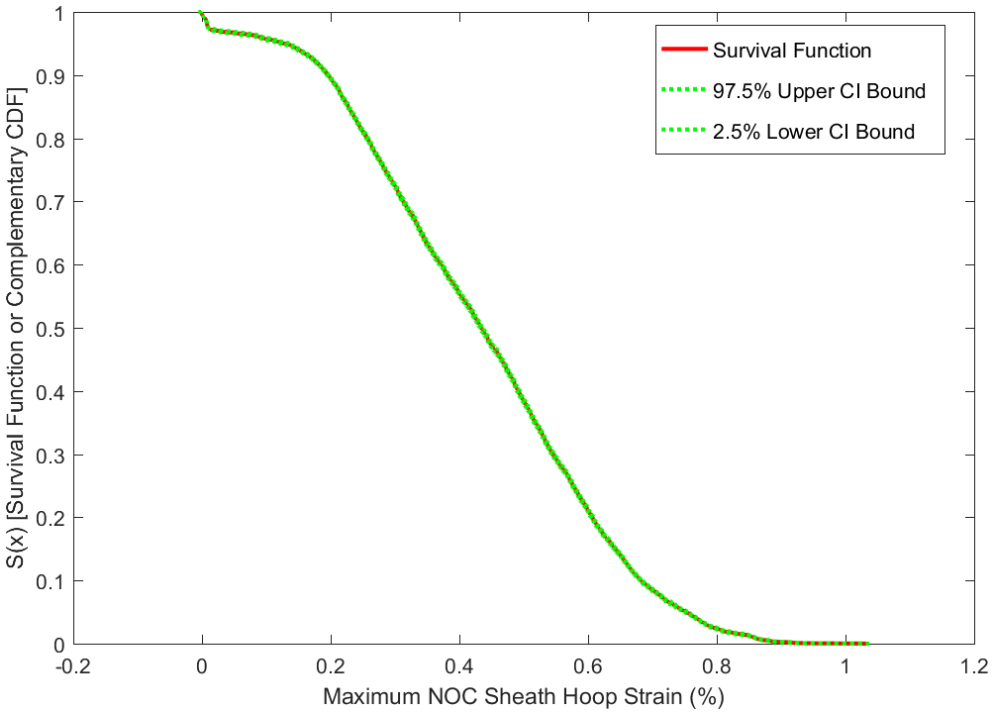

Figure 65. Empirical survivability function fit with 95% CI for NOC Sheath Hoop Strain.

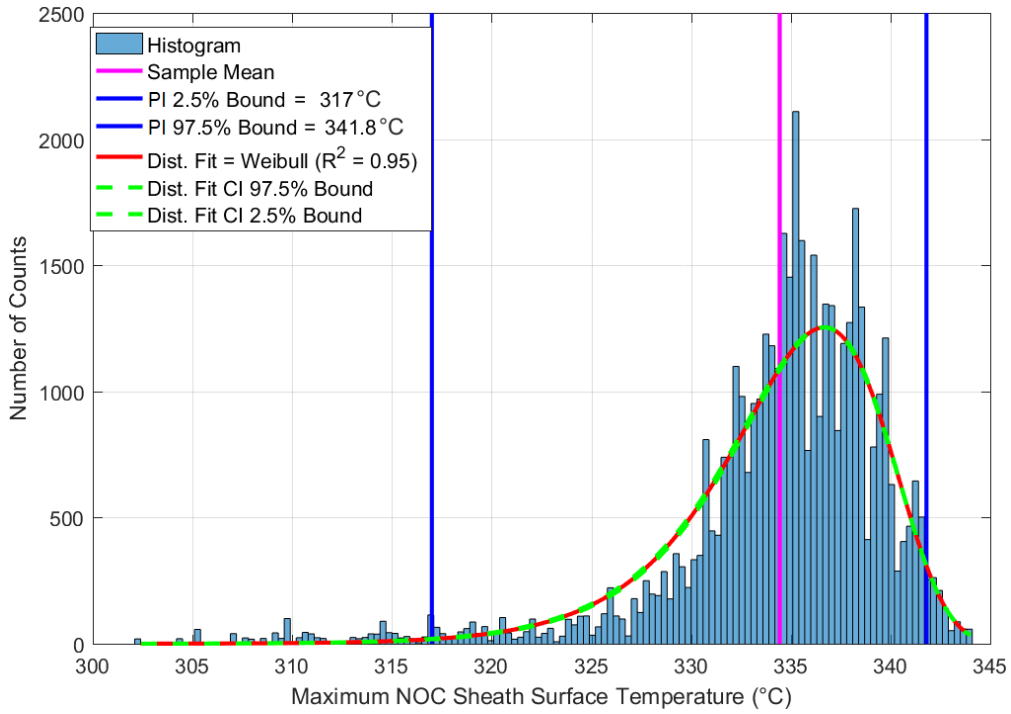

Figure 66. Histogram and empirical PDF fit of NOC Sheath Surface Temperature with 95% CI.

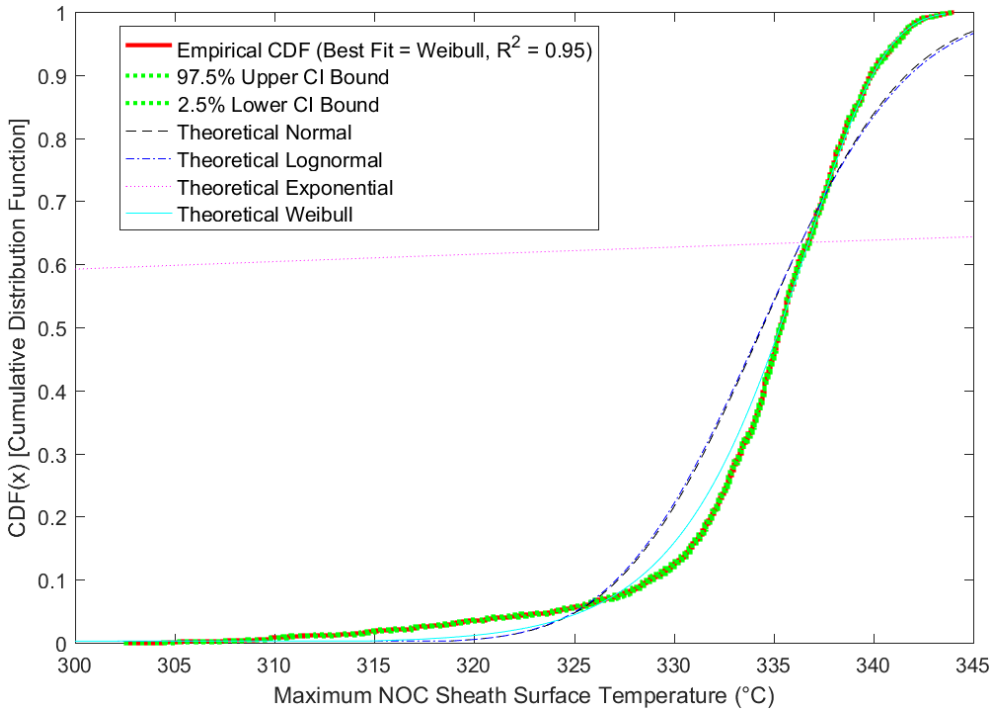

Figure 67. Comparison of empirical CDF fit with 95% CI versus theoretical distribution fits for NOC Sheath Surface Temperature.

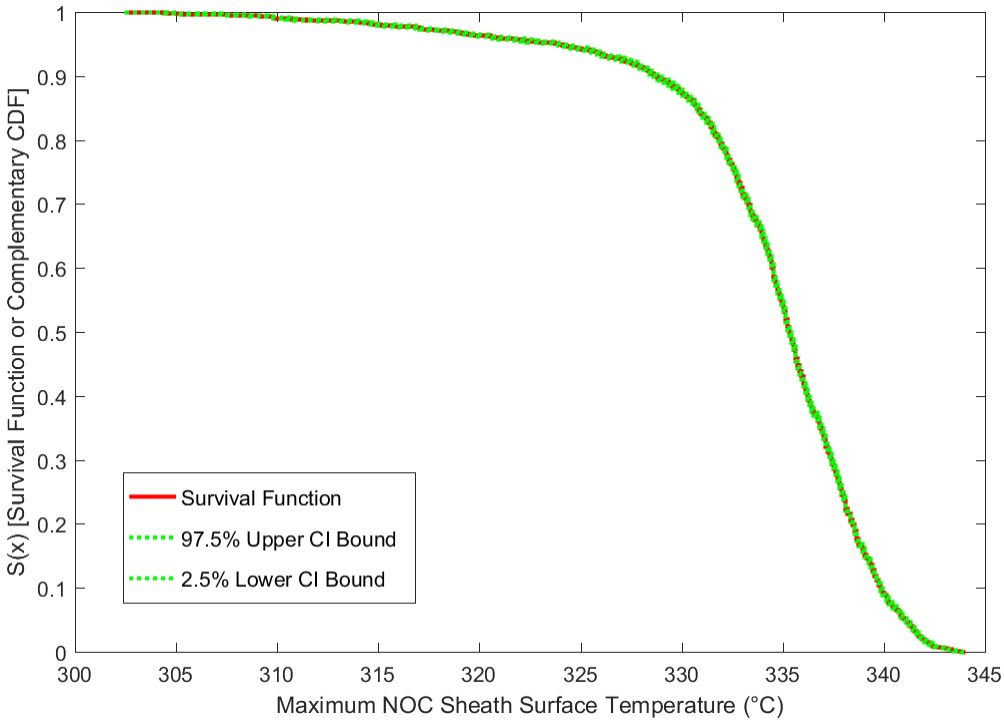

Figure 68. Empirical survivability function fit with 95% CI for NOC Sheath Surface Temperature.

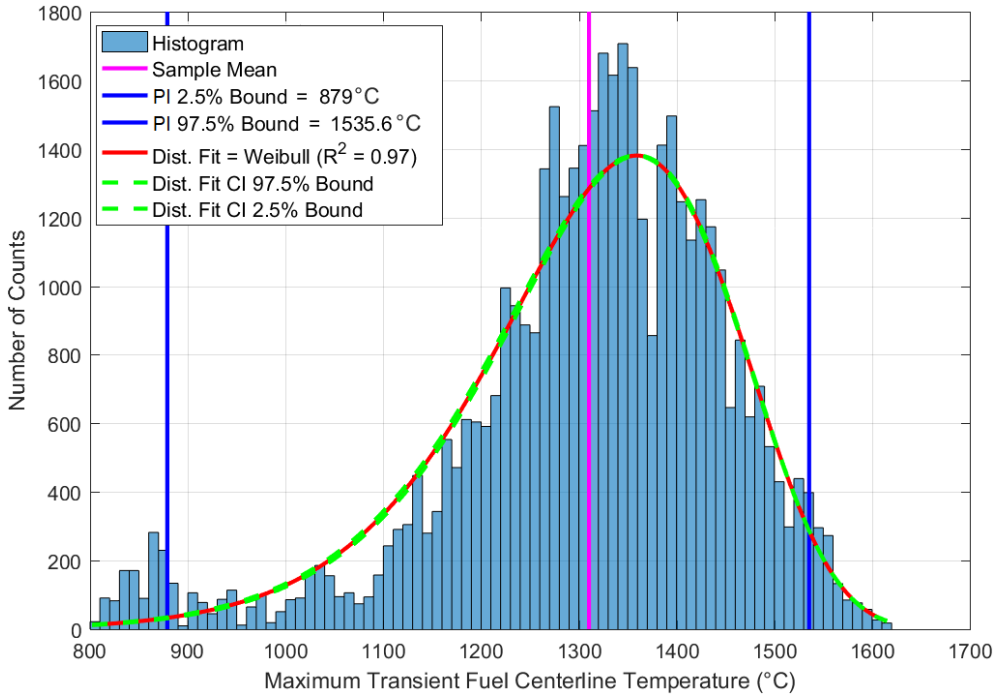

Figure 69. Histogram and empirical PDF fit of the 80% ROH Break LOCA Fuel Centerline Temperature with 95% CI.

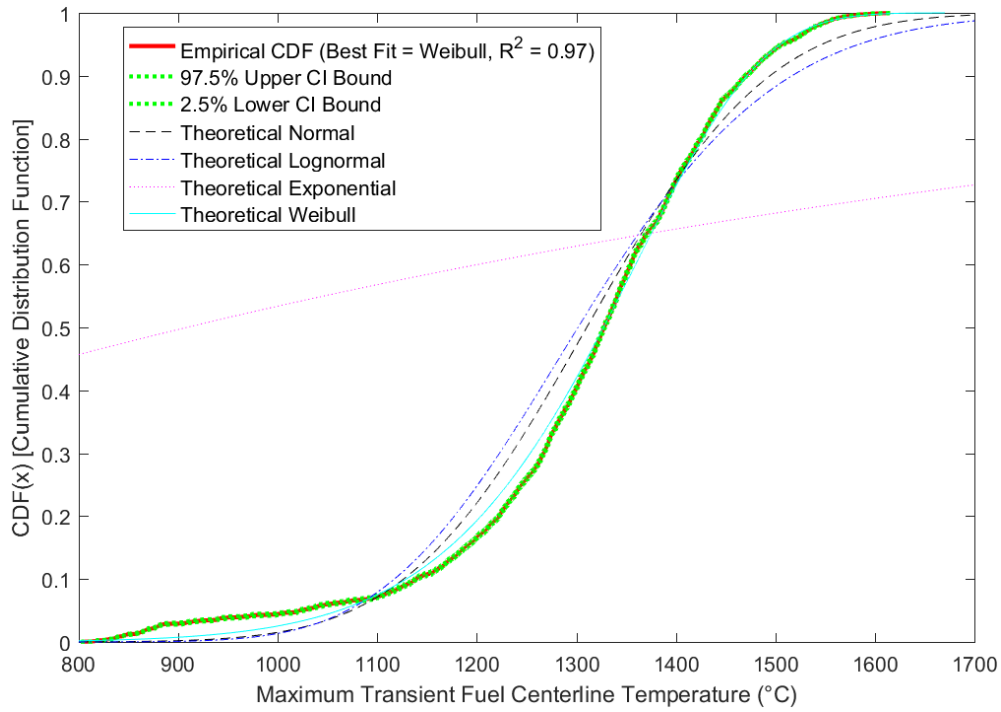

Figure 70. Comparison of empirical CDF fit with 95% CI versus theoretical distribution fits for the 80% ROH Break LOCA Fuel Centerline Temperature.

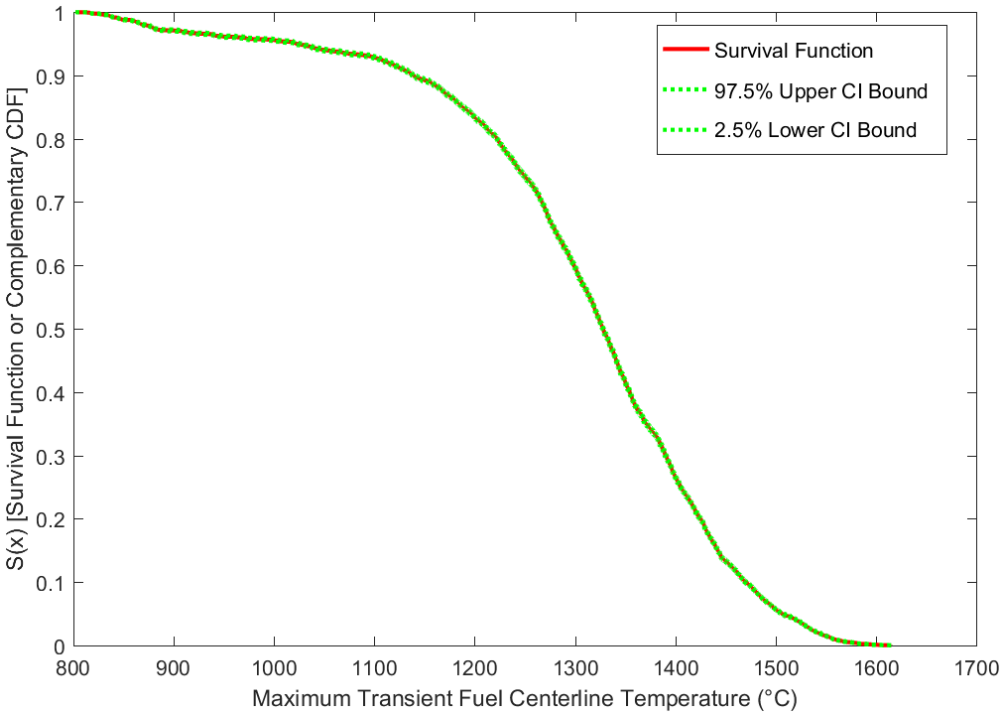

Figure 71. Empirical survivability function fit with 95% CI for the 80% ROH Break LOCA Fuel Centerline Temperature.

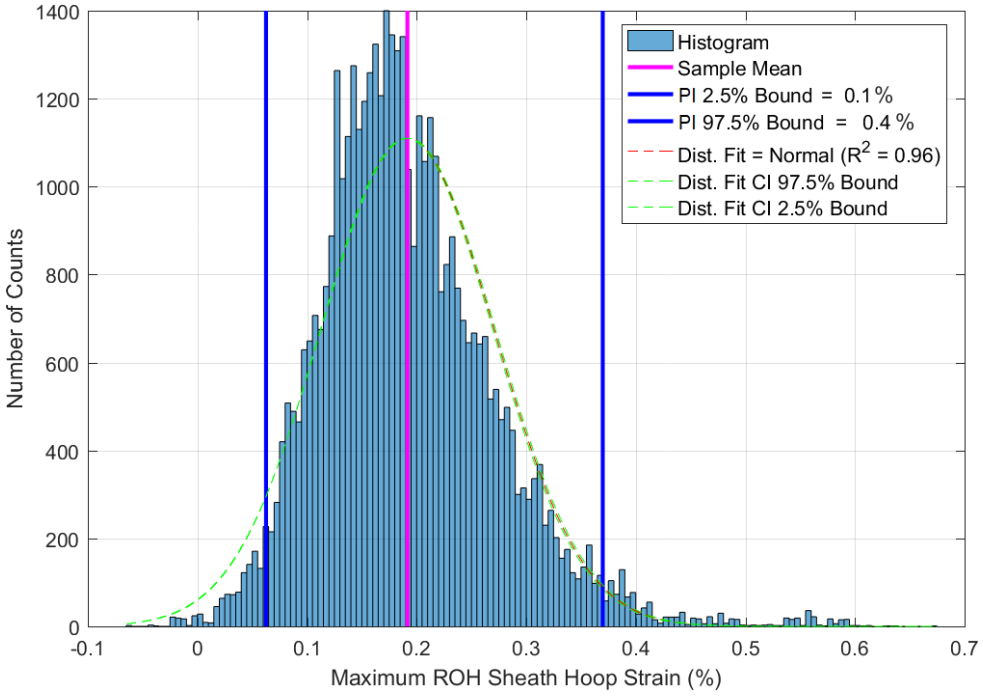

Figure 72. Histogram and empirical PDF fit of the 80% ROH Break LOCA Sheath Hoop Strain with 95% CI.

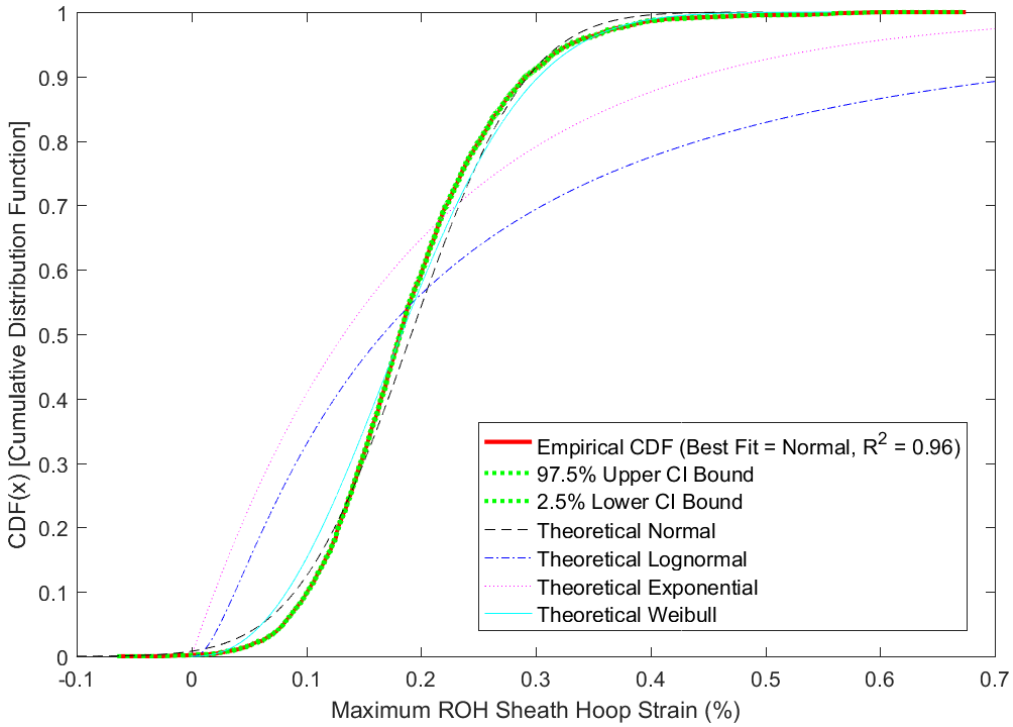

Figure 73. Comparison of empirical CDF fit with 95% CI versus theoretical distribution fits for the 80% ROH Break LOCA Sheath Hoop Strain.

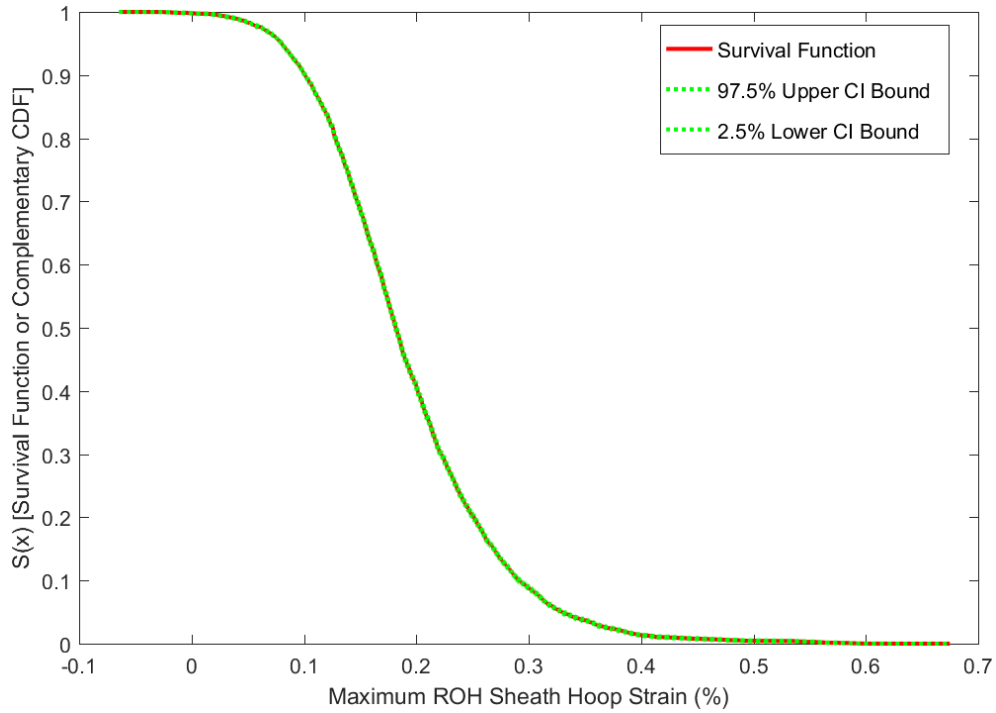

Figure 74. Empirical survivability function fit with 95% CI for the 80% ROH Break LOCA Sheath Hoop Strain.

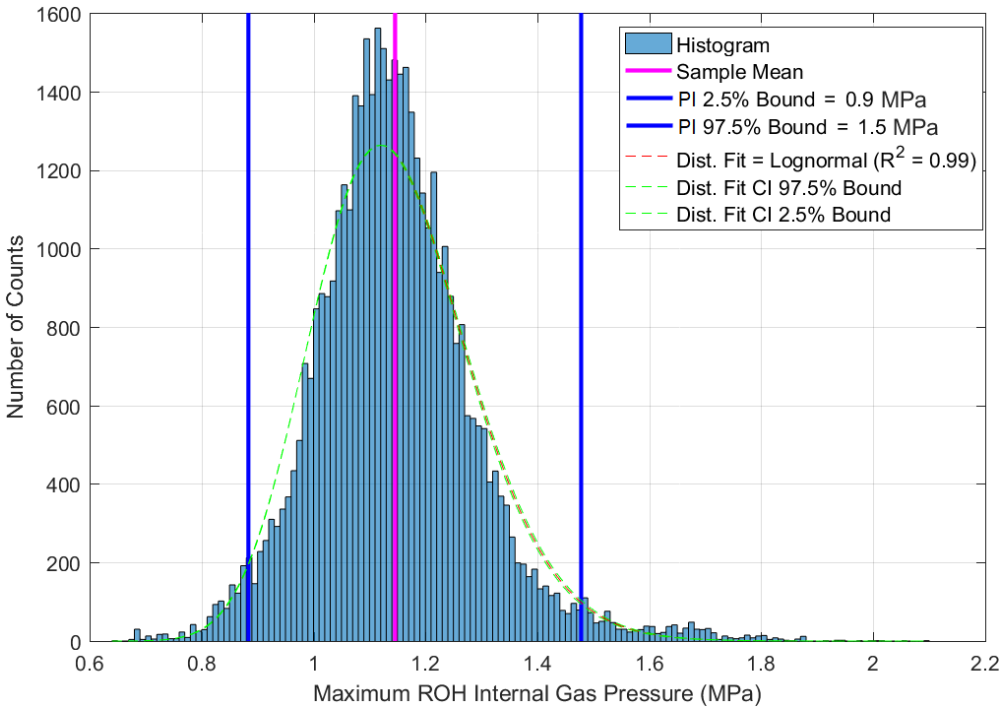

Figure 75. Histogram and empirical PDF fit of the 80% ROH Break LOCA Internal Gas Pressure with 95% CI.

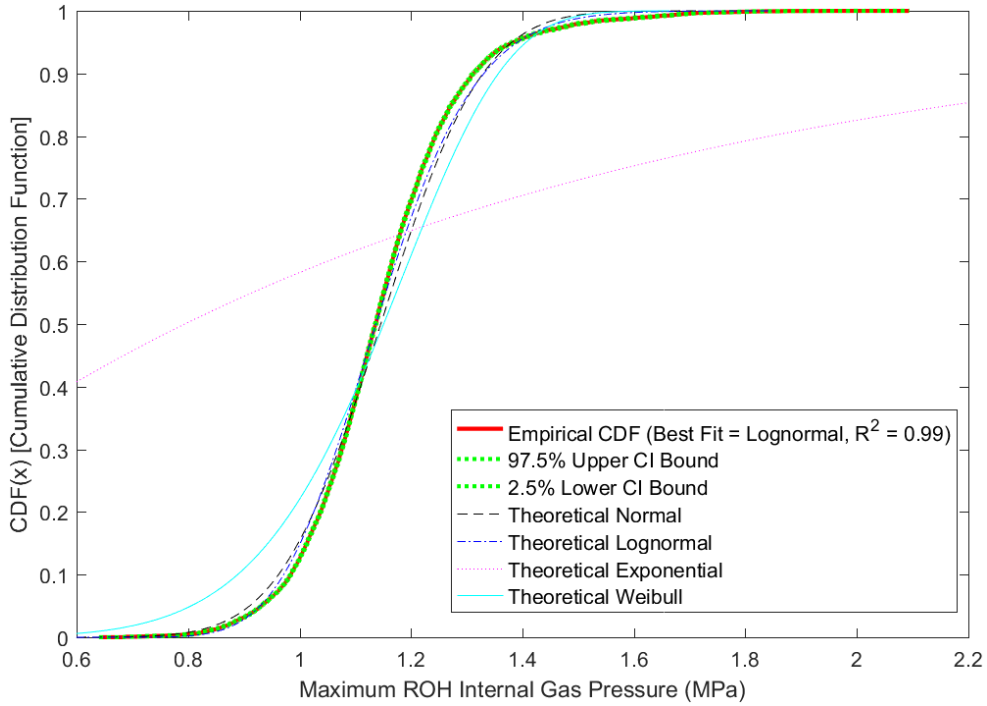

Figure 76. Comparison of empirical CDF fit with 95% CI versus theoretical distribution fits for the 80% ROH Break LOCA Internal Gas Pressure.

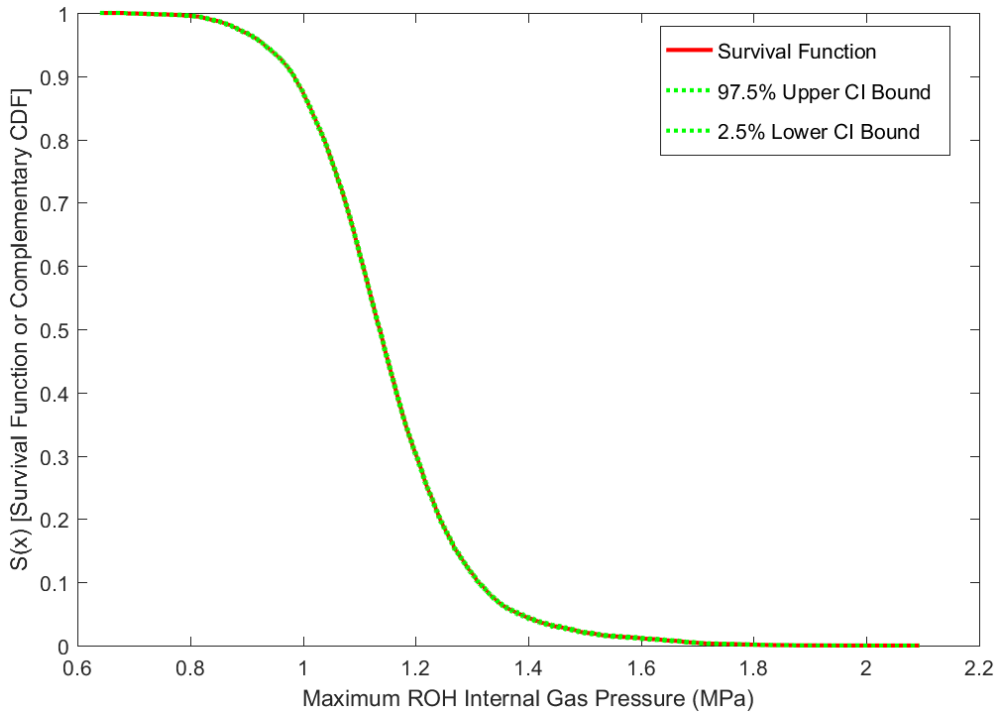

Figure 77. Empirical survivability function fit with 95% CI for the 80% ROH Break LOCA Internal Gas Pressure.

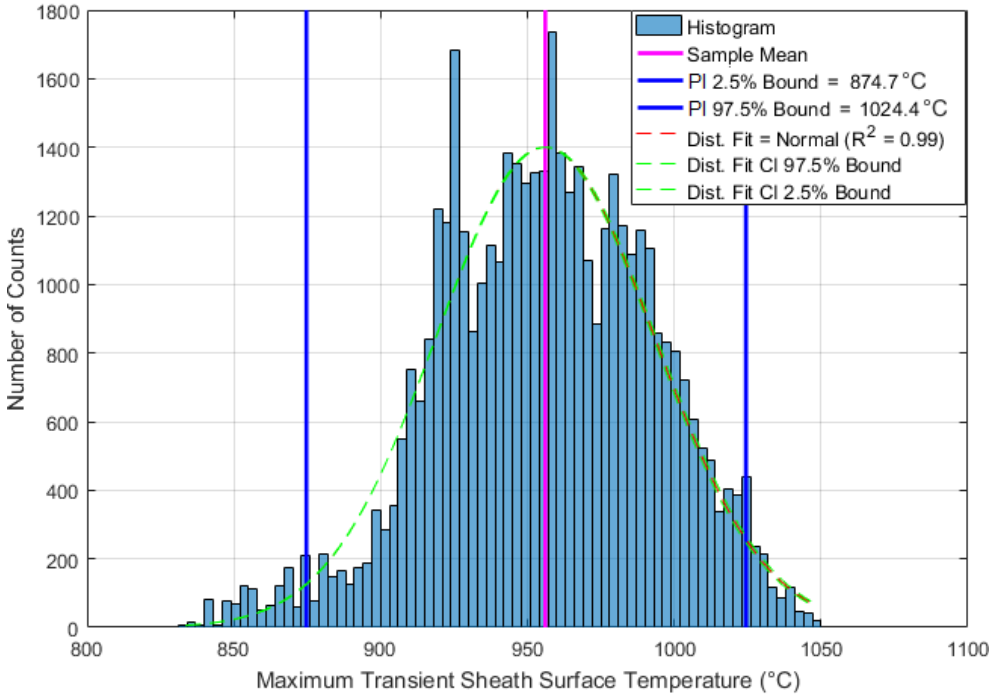

Figure 78. Histogram and empirical PDF fit of the 80% ROH Break LOCA Average Sheath Temperature with 95% CI.

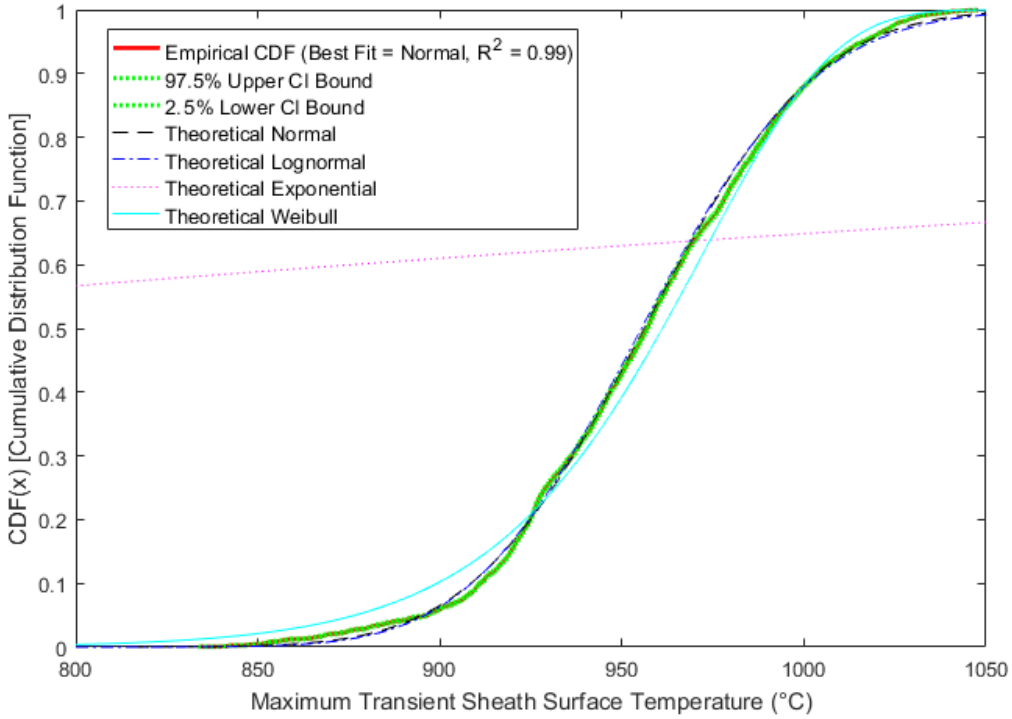

Figure 79. Comparison of empirical CDF fit with 95% CI versus theoretical distribution fits for the 80% ROH Break LOCA Average Sheath Temperature.

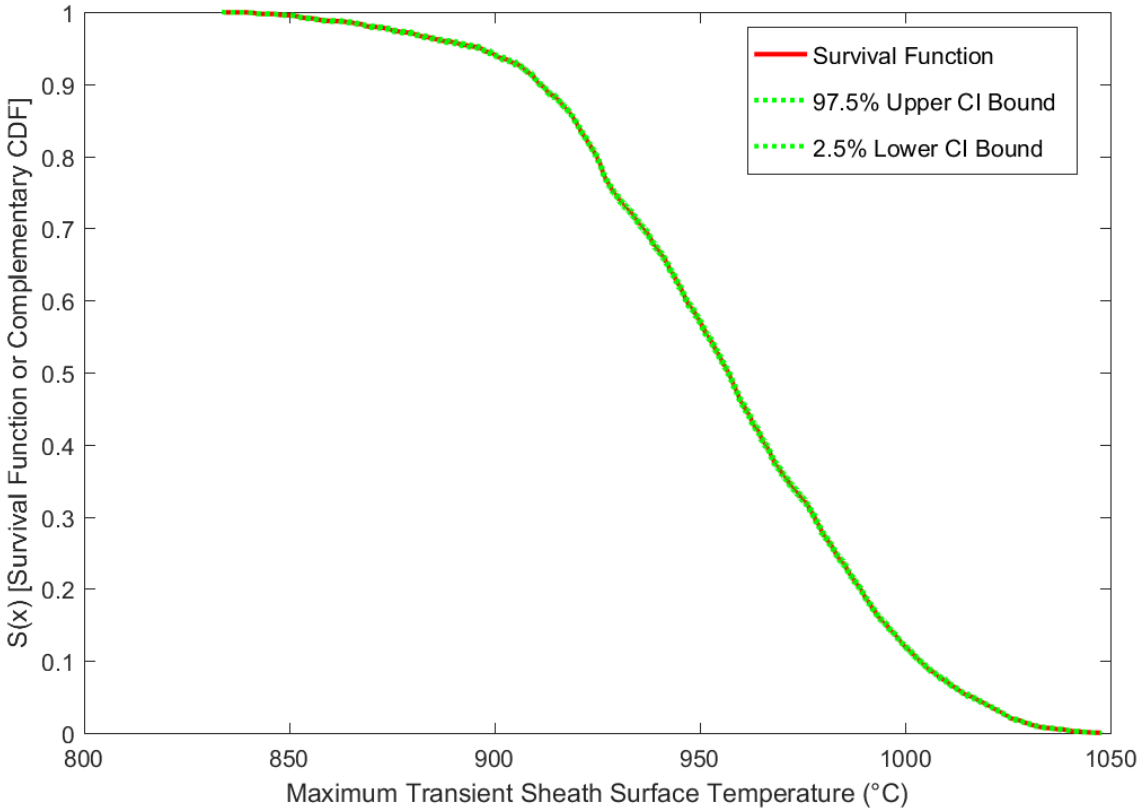

Figure 80. Empirical survivability function fit with 95% CI for the 80% ROH Break LOCA Average Sheath Temperature.

As observed in Figures **57** to **80**, the outcomes of the non-regionalized Monte Carlo simulations are well-described between Normal, Log-normal and Weibull distributions. Each of the distribution fits yield a R^2 value between 0.93 to 0.99, and the comparison between their empirical and theoretical CDF plots provide strong, graphical indications of a good fit. Furthermore, the distribution fits of each response functions based on the estimation of their statistical moments, which are the quantitative measures related to the graphical shape of the distribution function such as the mean or the variance, appear to yield tight CIs. This can be observed in the graphical proximity between the empirical fits and their 95% CI bounds in all three types of the plots presented (histogram, CDF, as well as Survival). The statistical moments of each of the response functions are summarized below in **Table 18**. It should also be noted, there were nil counts of oxide crack formation predicted for the non-regionalized simulations as well.

Table 18. Moments of each response functions with 95% CI.

	Mean			Standard Deviation				
Response Functions	**Mean Lower CI**	**Mean**	**Mean Upper CI**	**STDEV Lower CI**	**STDEV**	**STDEV Upper CI**	**Skew -ness**	**Kurtosis**
NOC Fuel Centerline Temp (°C)	1246	1248	1250	149	150	152	-1.44	3.36
NOC Internal Gas Pressure (MPa)	0.62	0.62	0.62	0.09	0.09	0.09	1.85	5.57
NOC Sheath Hoop Strain (%)	0.43	0.43	0.44	0.19	0.19	0.20	-0.02	-0.49
NOC Sheath Temperature (°C)	334.3	334.4	334.5	5.6	5.7	5.8	-2.02	5.93
Transient Fuel Centerline Temp (°C)	1308	1310	1312	144	145	147	-1.08	1.65
Transient Internal Gas Pressure (MPa)	1.15	1.15	1.15	0.14	0.14	0.15	0.94	3.41
Transient Sheath Hoop Strain (%)	0.19	0.19	0.19	0.08	0.08	0.08	0.74	1.58
Transient Sheath Temperature (°C)	955.4	955.9	956.5	37.1	37.4	37.8	-0.25	-0.11

Next, the Survival (or CCDF) probability of each of the response functions at significant response levels, including the response values at their limit criteria, are summarized below in **Table 19**. All of the survivability response levels at limit criteria for all response functions yield a probability value of zero. The distance between the mean values for each of the response functions in comparison to their limit criteria also yields significantly large values ranging from 8.1 times to the upwards of 101.3 times their respective standard deviations. The above results indicate there is negligible risk of limit criteria being exceeded for the respective response functions, for both NOC and the 80% ROH break LOCA scenario. With regards to the above, it should be noted that 600°C is not used as the limit criteria for the transient scenario. This is because although the limit state of 600°C is important for the commencement of voiding via contact heating of the coolant during NOC, this limit does not apply to LOCA scenarios. When the coolant depressurizes from the original pressure of 10 MPa, 600°C is no longer the temperature of critical heat flux at which voiding occurs. In LOCA conditions, voiding is expected to occur anyways at much lower temperatures, depending on the degree of

the depressurization (voids form at 101.4℃ for atmospheric pressure). Therefore, a more suitable limit criteria to be used in such cases is the zircaloy-4 melting temperature at 1850℃. For the 80% ROH break LOCA scenario, this limit value is 23.9 standard deviations in excess of the mean peak sheath temperature and has nil probability of being exceeded. Thus, a significant margin to the melting temperature failure limit is observed to still exist for the fuel sheath during the 80% ROH break LOCA scenario, although the formation of voids (and dryout) cannot be avoided.

Table 19. Survival (or CCDF) probability of each response functions at various response levels including the limit criteria, plus the number of standard deviations the mean value is away from the limit criteria.

Response Functions	Response Level 1 (Limit Criteria)	Response Level 1 Probability	No. of STDEVs between mean & Limit Criteria	Response Level 2	Response Level 2 Probability	Response Level 3	Response Level 3 Probability
NOC Fuel Centerline Temp [TCC] (℃)	2840℃	0.00	10.6	1400℃	0.12	1200℃	0.71
NOC Internal Gas Pressure [PRES] (MPa)	10 MPa	0.00	101.3	2 MPa	0.00	0.5 MPa	0.97
NOC Sheath Hoop Strain [TSTETHE] (%)	2.00% & 5.00	0.0 & 0.0	8.1 & 23.5	0.50%	0.39	0.20%	0.89
NOC Sheath Temperature [SSTC] (℃)	600℃	0.00	46.6	340℃	0.09	300℃	1.00
Transient Fuel Centerline Temp [CFT] (℃)	2840℃	0.00	10.5	1400℃	0.27	1200℃	0.83
Transient Internal Gas Pressure [PGAS] (MPa)	10 MPa	0.00	61.0	2 MPa	6.00E-04	1.2 MPa	0.32
Transient Sheath Hoop Strain [EQQ] (%)	2.00% & 5.00%	0.0 & 0.0	22.9 & 60.8	0.50%	3.65E-03	0.20%	0.42
Transient Sheath Temperature [TSH] (℃)	1850℃ (limit for LOCA)	0.00	23.9	600℃ (not the limit for LOCA)	1.00	950℃	0.56

7.5 Global Sensitivity Analysis

The results of the global sensitivity analysis of the response functions, for both NOC and the transient simulations, are outlined in relation to each of the input parameters in **Table 20**. A condensed bar graph of their response sensitivities, excluding input parameters with negligible values of sensitivity indices, is also presented in **Figure 81**. The sensitivity indices that are presented are referred to as Sobol indices, which are the product of a method of global sensitivity analysis using decomposition of the variance of the system output into fractional indices that can be attributed to the variance of the input parameters. The Sobol indices method provides the advantage of measuring the sensitivity across the whole input space, and is capable of accounting for non-linear responses, as well as measuring the effect of interactions in non-additive systems.

The results of the global sensitivity analysis demonstrate that the variance in the response functions pertaining to temperatures, such as the fuel centerline (TCC and CFT) and sheath temperatures (SSTC and TSH) for both NOC and the transient, are almost entirely driven by variability in the fuel power data. The input parameters that determine the fuel power history consist of the radial zone, the channel position within the radial zone, as well as the axial position within the channel. The sum of the Sobol sensitivity indices for the above three input parameters exceeds the unity value of 1.0, because they are not mutually exclusive from one another with respect to their effect on fuel power. The three parameters are correlated; thus, a part of their variance is repetitively reflected in the sensitivities of the response functions. Between the three parameters, the radial zone has the greatest impact on the fuel power, followed by the axial start position of the fuel bundle. This is observed because fuel channels within the same radial region exhibit relatively lower variance in fuel power, whereas the variance among different radial regions as well as between different axial positions are relatively greater. To determine the Sobol index of the fuel power history as a consolidated, single input parameter, the indices of all other input parameters unrelated to fuel power are subtracted from 1.0. This yields the remainder of the sensitivity index that is attributable to fuel power.

Table 20. The total Sobol indices for each of the input parameters, in relation to the response functions.

Input Parameters	NOC Fuel Centerline Temp. [TCC] (°C)	NOC Internal Gas Pres. [PRES] (MPa)	NOC Sheath Hoop Strain [TSTETHE] (%)	NOC Sheath Temp. [SSTC] (°C)	Trans. Fuel Centerline Temp [CFT] (°C)	Trans. Internal Gas Pres. [PGAS] (MPa)	Trans. Sheath Hoop Strain [EQQ] (%)	Trans. Sheath Temp. [TSH] (°C)
Pellet Density	4.9E-04	1.5E-03	9.5E-04	0.0E+00	5.4E-04	6.7E-03	3.9E-03	6.0E-04
Stack Length	3.8E-06	1.4E-02	1.7E-06	0.0E+00	4.5E-06	2.1E-05	1.2E-02	7.8E-06
Sheath Length	2.5E-07	6.1E-05	1.3E-08	0.0E+00	9.1E-08	3.1E-06	5.4E-05	2.6E-06
Weld Disp. A	2.2E-08	2.2E-06	1.3E-09	0.0E+00	4.8E-08	2.7E-06	8.8E-07	2.6E-06
Weld Disp. B	3.3E-08	2.4E-06	1.7E-09	0.0E+00	6.2E-08	7.8E-06	9.9E-07	2.6E-06
Sheath Roughness	1.5E-05	1.4E-04	9.5E-06	0.0E+00	1.5E-05	2.8E-05	3.8E-05	2.1E-05
Pellet Roughness	1.9E-04	1.5E-03	1.3E-04	0.0E+00	2.0E-04	1.5E-04	4.6E-04	2.7E-04
Sheath Yld Stress	0.0E+00	0.0E+00	0.0E+00	0.0E+00	0.0E+00	0.0E+00	0.0E+00	0.0E+00
Chamfer Length	9.0E-06	6.8E-02	1.8E-03	0.0E+00	6.9E-04	1.5E-03	2.3E-01	4.9E-04
Chamfer Depth	2.7E-06	6.1E-03	3.2E-06	0.0E+00	2.3E-05	3.7E-05	4.2E-03	1.8E-05
Pellet Dia.	1.9E-06	4.2E-03	1.4E-02	2.2E-06	3.1E-07	1.1E-01	1.1E-02	6.0E-06
Sheath ID	2.7E-06	5.2E-03	1.7E-02	2.4E-05	3.6E-07	1.4E-01	1.3E-02	5.0E-06
Dish Depth	2.4E-06	8.8E-03	5.1E-05	0.0E+00	1.4E-04	5.1E-05	5.8E-02	1.1E-04
Land Width	2.5E-07	1.0E-04	2.2E-06	0.0E+00	1.5E-06	1.3E-05	8.3E-04	5.2E-06
Sheath Thickness	5.1E-06	1.3E-05	2.0E-06	4.3E-04	2.2E-06	4.2E-05	8.6E-05	7.3E-06
He Fraction	7.3E-06	1.9E-04	2.3E-06	0.0E+00	7.5E-06	3.0E-05	3.2E-05	1.5E-05
Pellet Grain Size	1.3E-06	8.2E-02	6.7E-11	0.0E+00	6.5E-06	1.4E-04	2.1E-02	1.2E-05
Fuel Power History (combined)	1.0E+00	8.1E-01	9.7E-01	1.0E+00	1.0E+00	7.4E-01	6.4E-01	1.0E+00
Radial Zone (Power)	9.0E-01	5.8E-01	5.9E-01	9.1E-01	8.9E-01	6.1E-01	5.2E-01	8.4E-01
Channel Selection (Power)	3.3E-01	3.9E-01	3.3E-01	2.9E-01	3.5E-01	5.2E-01	3.2E-01	3.9E-01
Bundle Axial Position (Power)	2.3E-01	3.4E-01	5.9E-01	2.1E-01	2.2E-01	3.6E-01	3.0E-01	2.4E-01

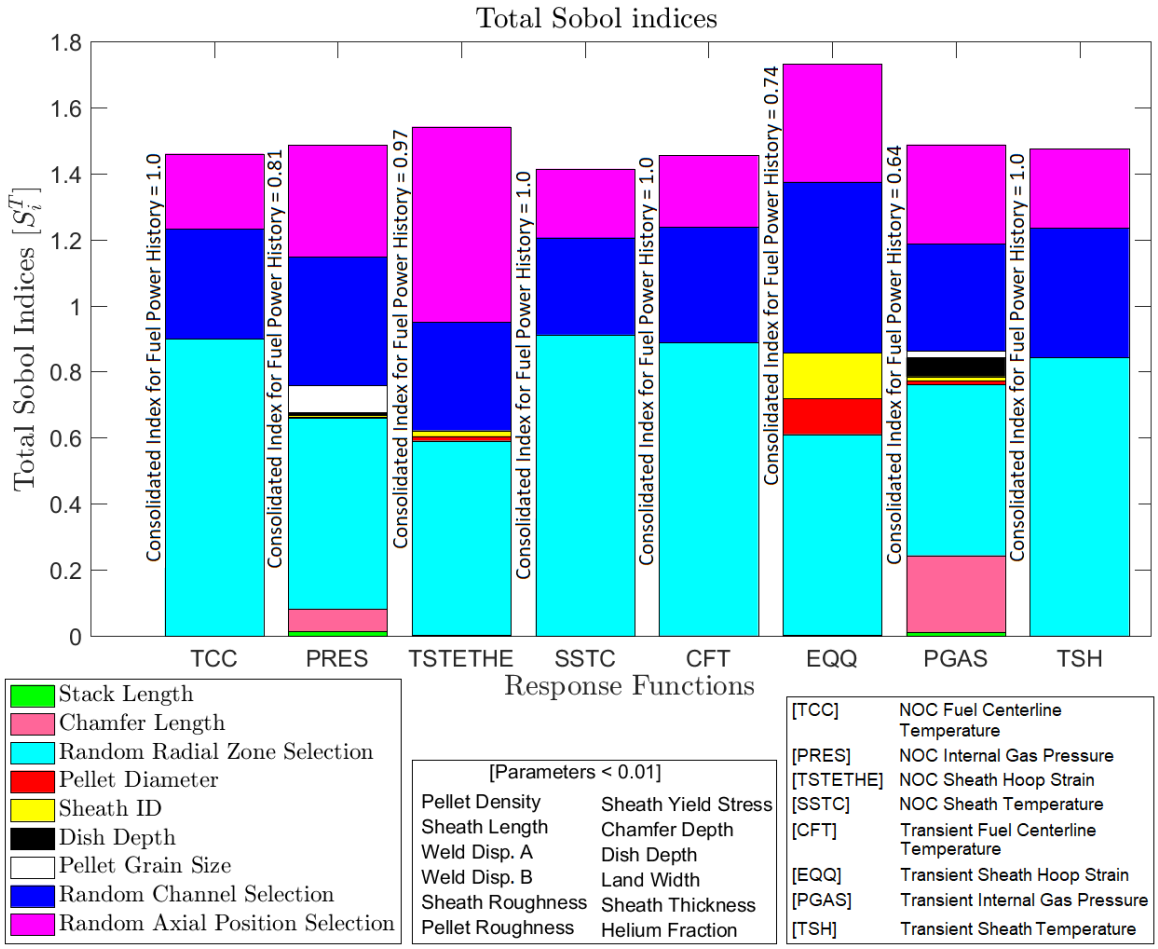

Figure 81. Global sensitivity analyses of each response functions in relation to their respective input parameters.

The variance of the sheath hoop strains (TSTETHE and EQQ) on the other hand, although they are primarily determined by the three parameters affecting the fuel power, appear to also be influenced by the sheath inner diameter and the pellet diameter. Together, the two diameter variables define the pellet-to-sheath gap distance, which critically affects the establishment of the fuel-to-sheath contact. The sensitivity of the sheath hoop strain in association with the two diameter variables therefore suggests that the pellet-to-sheath contact phenomenon is indeed a major driving mechanism for sheath deformation. This mechanism may be of a greater significance than the internal gas pressure, as the internal pressure values experienced during both NOC and the transient are generally slow or insufficient to overcome the external coolant pressure plus the

stiffness of the sheath. Finally, in addition to being primarily influenced by the fuel power history, the internal gas pressures for both NOC and the transient (PRES and PGAS) appear to be sensitive to the chamfer length, the dish depth, the stack length, and the pellet grain size. In the case of the transient simulation, the internal pressure is also additionally sensitive to the pellet and the sheath inner diameters. These are reasonable observations, because the mechanism via which the fission gases are released into the free volume within the fuel element is understood to be significantly influenced by the above six parameters. The pellet grain size affects the migration and release of fission gas bubbles within the fuel pellet to its surface. On the other hand, the chamfer length, the dish depth, the stack length, the pellet diameter and the sheath inner diameter determine the free volume of the element plenum and the design cavity between the pellets, which mitigate pressurization from fission gas buildup.

The observations obtained from **Figure 81** provide an interesting insight in comparison to the findings from [20], shown in **Figure 82**, where the pellet density was the most sensitive factor contributing to the response function variability.

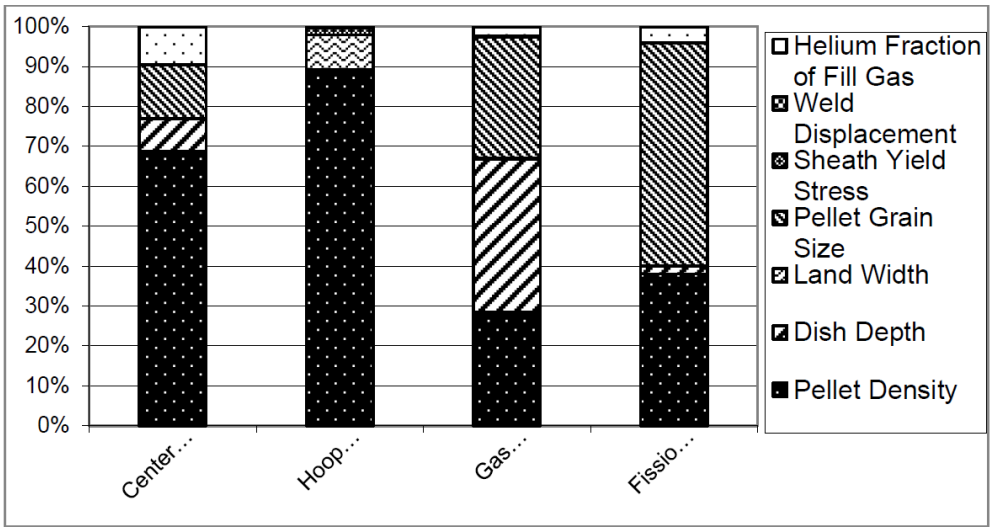

Figure 82. Global sensitivity analyses of each response functions in relation to their respective input parameters adapted from [20].

The results from [20] provide a reasonable observation for sensitivities when the element power is fixed at a constant value, because the pellet density, although quality controlled to a similar level of variability as other manufacturing parameters, is the most significant manufacturing parameter to influence the fuel pellet temperature gradient. This is because the pellet density impacts the heat transfer coefficient of the pellet in a major way. However, the sensitivity analysis produced within this study indicates that the impact of manufacturing variability in pellet density is insignificant in comparison to the impact of variability in fuel power operating data. This suggests that from a sensitivities perspective, the manufacturing quality control of pellet density, along with all other parameters with low index values shown in **Figure 81**, are very tightly grouped and behave closer to a constant value when compared to the fuel power operating data. Furthermore, similar to the current study, response functions' sensitivities to dish depth and pellet grain size were also observed to be of significance in [20]. However, unlike the current study, the pellet diameter and the sheath inner diameter were not reported to be of significance in [20]. A possible explanation for the lack of sensitivity to the pellet and sheath inner diameters in [20] is likely due to its use of a high, fixed value of element power at 55 kWm^{-1}. This would have rendered small variations in the pellet-to-sheath gap distance trivial in comparison to the relatively significant levels of pellet expansion that would have occurred as a result of the high power. With a realistic treatment of the fuel power data in the current study, the fuel-to-sheath gap distance is expected to play a much more significant role on whether a pellet-to-sheath contact is established. This is because the relatively lower fuel power, and hence the burnup rate, would result in relatively lower magnitudes of fuel thermal expansion or swelling, which may or may not establish pellet-to-sheath contact depending on the distance that exists.

7.6 Case Study: Performance of Fuels Containing Burnable Absorbers

The resulting peak response levels for each of the response functions, for the regionalized Monte Carlo simulations using the BNA fuel, are presented in this section. As previously discussed in section 6.8, the transition refuelling of the model core using

the BNA fuel causes the LZC fill levels to decrease to a significantly lower value, which results in a slight shift in the fuel power density of the core towards its central region. This was previously shown in **Figure 42**. The results of the Monte Carlo simulations indicate that this transition in power density has caused slight decreases in the average values of the response functions for the peripheral zones (#1-4) and slight increases for the central regions (#5-12), in comparison to the equivalent results for the regular NU fuel. The magnitudes of the decreases tended to be the greatest towards zone #1, whereas the magnitudes of the increases tended to be greater towards the innermost region in zone #12. Due to this change, zone #5 is the most limiting region with the highest values of fuel response functions for the BNA-transitioned core, as opposed to zone #4 for the regular NU fuel. This is a significant change, because the average fuel element power rating of zone #5 has a tighter statistical variance in comparison to zone #4. The likely cause behind this difference compared to zone #4 is due to its lower rate of refuelling relative to the average burnup. This was demonstrated previously in **Figure 38**. The lower rate of refuelling results in a lower frequency of power perturbations caused by refuelling ripples, and therefore a lower variability in the observed fuel power. Furthermore, the tighter variance of the fuel power as an input parameter impacts the predicted fuel reliability, because it affects the variance of the dependent fuel response outputs. Specifically, this has the effect of causing the safety margins of the fuel response functions to improve significantly in the case of the most limiting region, which is now zone #5. The improvements are in the form of decreased probability of occurrence for the limit conditions, or the number of standard deviations from which the average values are distanced from the limit criteria.

7.6.1 Regionalized Fuel Centerline Temperature

The trend in the fuel centerline temperatures for the BNA-fuelled core, regionalized over the 12 zones, for both the NOC and the transient case, are shown below in **Figure 83**. It can be observed that the regional trend in the magnitudes of the average peak fuel centerline temperature has indeed shifted from the peripheral regions (zones #1

to #4) to the central regions (zones #5 to #12) in comparison to the regular core in **Figure 51**. For zone #5, the average peak centerline temperature during NOC is 1346℃ with a standard deviation of 85℃. This value is slightly higher than the equivalent value observed for the regular NU fuel, which was 1343℃ from zone #4. However, due to the smaller standard deviation associated with the radial region, the margin to the 2840℃ limit for the BNA-fuelled core is equal to 18 standard deviations, as opposed to the 14 standard deviations for the regular core. In the case of the 80% ROH break scenario, the BNA-transitioned core resulted in a fuel centerline temperature value of 1306℃ with a standard deviation of 97℃ for zone #5. This is also slightly higher than the equivalent value for the regular core, which was 1305℃. However, the margin to limit for the BNA-transitioned core is 16 standard deviations away, which has a lower probability of being reached in comparison to the margin of 12 standard deviations for the regular fuel.

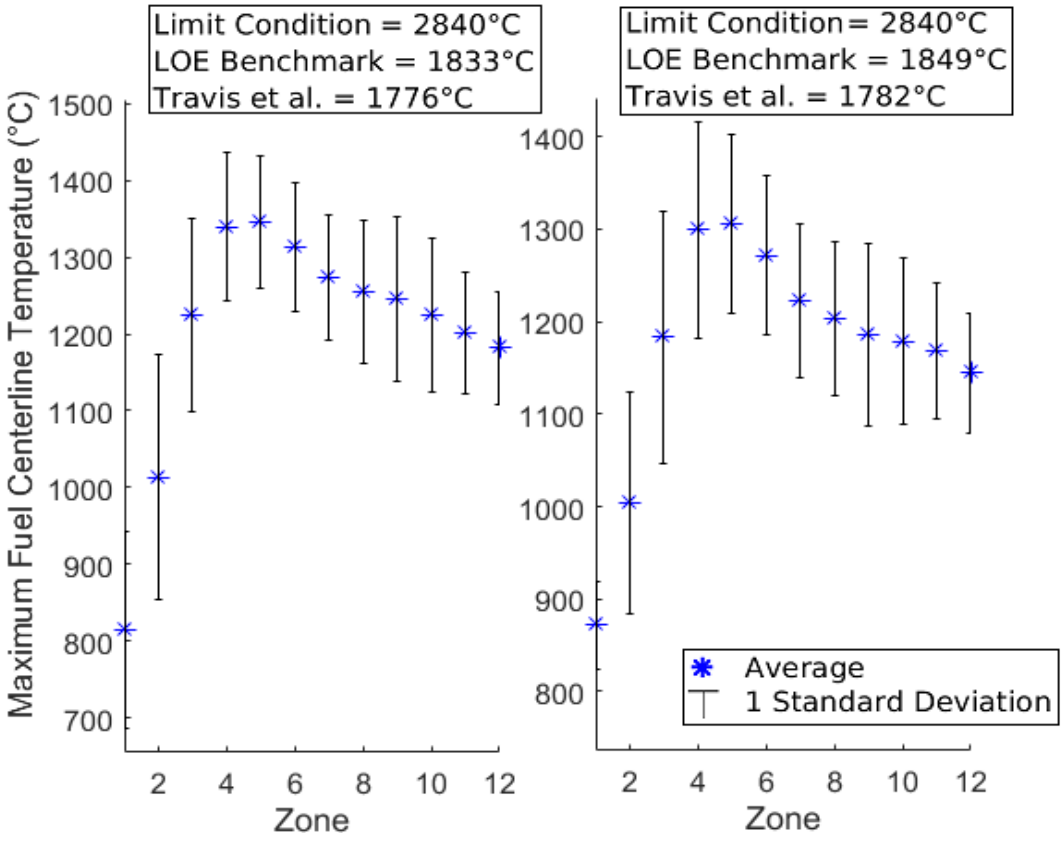

Figure 83. Trend in the maximum fuel centerline temperature during NOC (left) and during the 80% ROH break transient (right), for the BNA fuel.

7.6.2 Regionalized Fuel Sheath Temperature

The trends in the fuel sheath temperature for the BNA-fuelled core, regionalized over the 12 radial zones, for both NOC and the transient case, are shown below in **Figure 84**.

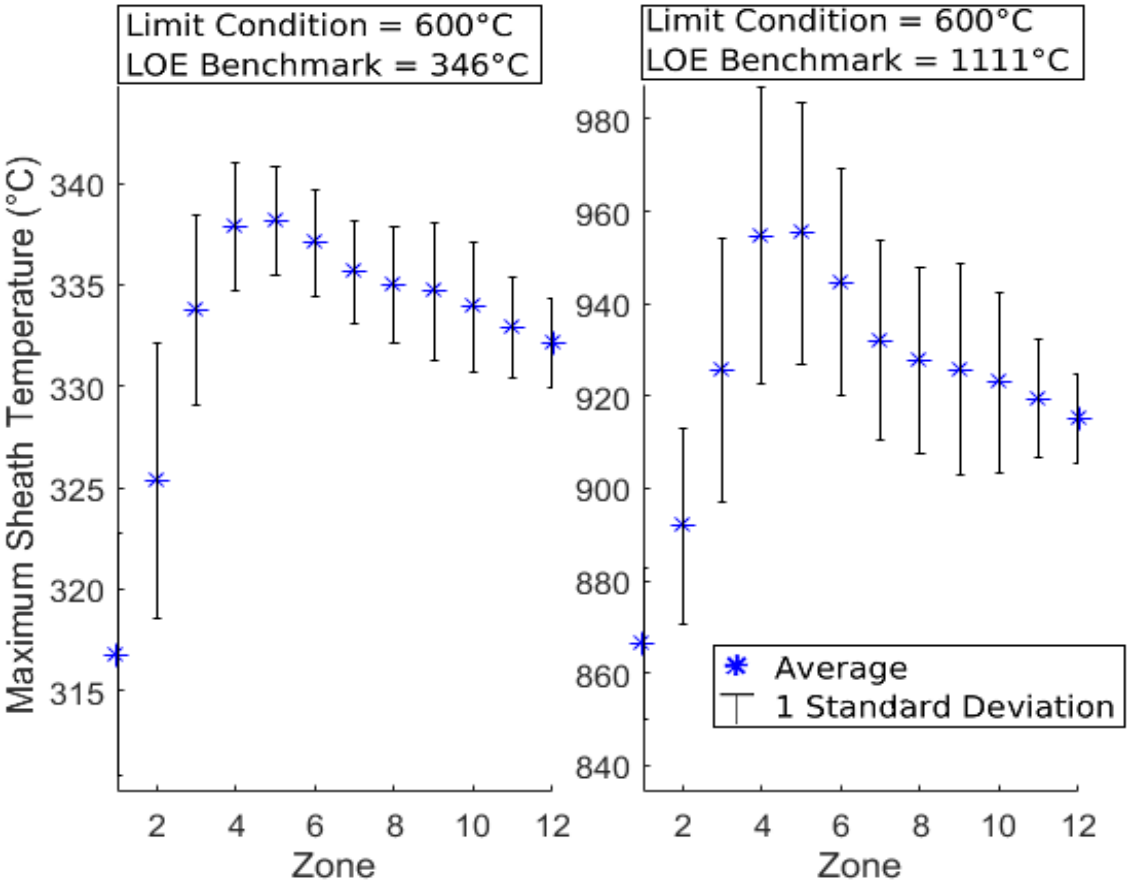

Figure 84. Trend in the peak sheath inner surface temperature during NOC (left) and the peak sheath average temperature for the 80% ROH break case (right), for the BNA fuel.

The regional trend in the magnitude of the sheath temperature is also observed to have shifted from the peripheral regions to the central regions when compared to the regular NU-fuelled core in **Figure 53**. The average peak sheath surface temperature for the BNA fuel during NOC is 338℃ with a standard deviation of 2.7℃ for the limiting

region (zone #5), which is the same value as for the limiting region of the regular NU-fuelled core, but with a smaller standard deviation. This puts the value of the BNA-fuelled core at 97 standard deviations away from the 600℃ limit, in comparison to 75 by the regular NU-fuelled core. In the case of the 80% ROH break scenario, the BNA-transitioned core resulted in an average peak fuel sheath temperature value of 955℃ with a standard deviation of 28℃ for the limiting region. This is slightly lower than the equivalent value for the limiting region of the regular NU fuel core, which was 957℃. The limiting region of the BNA-fuelled core's transient sheath temperature is 32 standard deviations away from the zircaloy-4 melting limit of 1850℃. The limiting region of the regular fuel, on the other hand, is less at 26 standard deviations away from the zircaloy-4 melting limit.

7.6.3 Regionalized Fuel Internal Gas Pressure

The trends in the fuel internal gas pressure for the BNA-fuelled core, regionalized over the 12 radial regions, for both NOC and the transient case, are shown below in **Figure 85**. The regional trend in the magnitudes of the fuel internal pressure is observed to have also shifted from the peripheral regions to the central region of the core when compared to the regular NU-fuelled core in **Figure 54**. The average peak internal pressure for the BNA fuel during NOC is 0.78 MPa with a standard deviation of 0.17% for the limiting region (zone #5). This is less than the value of 0.8 MPa for the limiting region of the regular NU-fuelled core. This puts the value of the BNA-fuelled core at 54 standard deviations away from the 10 MPa limit, in comparison to 51 by the regular NU-fuelled core. In the case of the 80% ROH break scenario, the BNA-fuelled core resulted in an average peak internal pressure value of 1.20 MPa with a standard deviation of 0.23 MPa for zone #5. This is slightly lower than the equivalent for the regular core, which was 1.22 MPa. The margin to limit for the BNA-transitioned core is therefore 38 standard deviations away for the transient case, which has a lower probability of being reached in comparison to the margin of 31 standard deviations for the regular NU core.

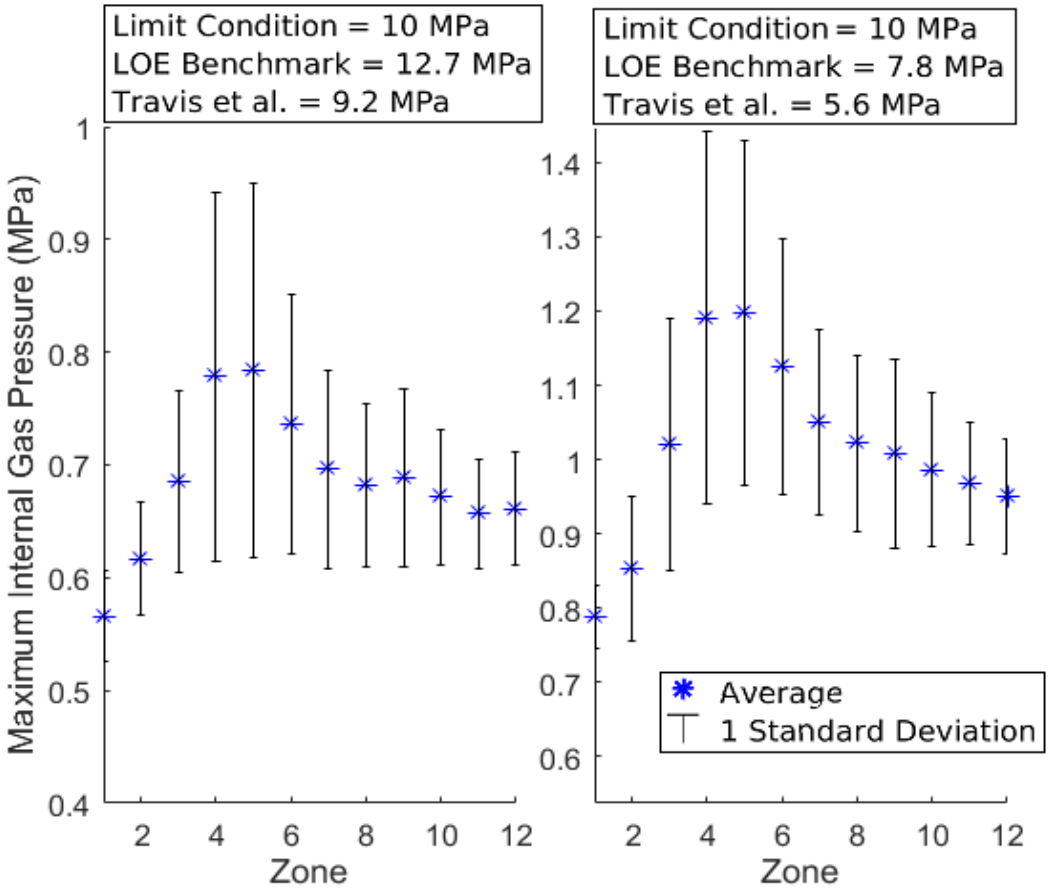

Figure 85. Trend in the maximum fuel internal gas pressure during NOC (left) and during the 80% ROH break transient (right), for the BNA fuel.

7.6.4 Regionalized Fuel Sheath Strain

The trends in the fuel sheath hoop strain for the BNA-fuelled core, regionalized over the 12 radial regions, for both NOC and the transient case, are shown below in **Figure 86**. The regional trend in the magnitude of the fuel sheath hoop strain is observed to have also shifted from the peripheral regions to the central regions when compared to the regular NU-fuelled core in **Figure 55**. The average peak sheath hoop strain for the limiting region (zone #5) of the BNA-fuelled core during NOC is 0.51% with a standard deviation of 0.19%. This value is slightly higher than the average peak value of 0.50% for the limiting region of regular NU-fuelled core, and also has a slightly higher value of standard deviation by comparison. This puts the value of the BNA-fuelled core at 24

standard deviations away from the 5.00% limit, in comparison to 26 for the regular NU-fuelled core. In the case of the 80% ROH break scenario, the BNA-transitioned core resulted in an average peak sheath hoop strain value of 0.19% with a standard deviation of 0.07% for zone #5. This is the same value as the comparable result from the limiting region of the regular NU-fuelled core, and also with the same standard deviation. The margin to limit for both the BNA-transitioned core and the regular NU-fuelled core is therefore 26 standard deviations away from the 2.00% limit for the transient case.

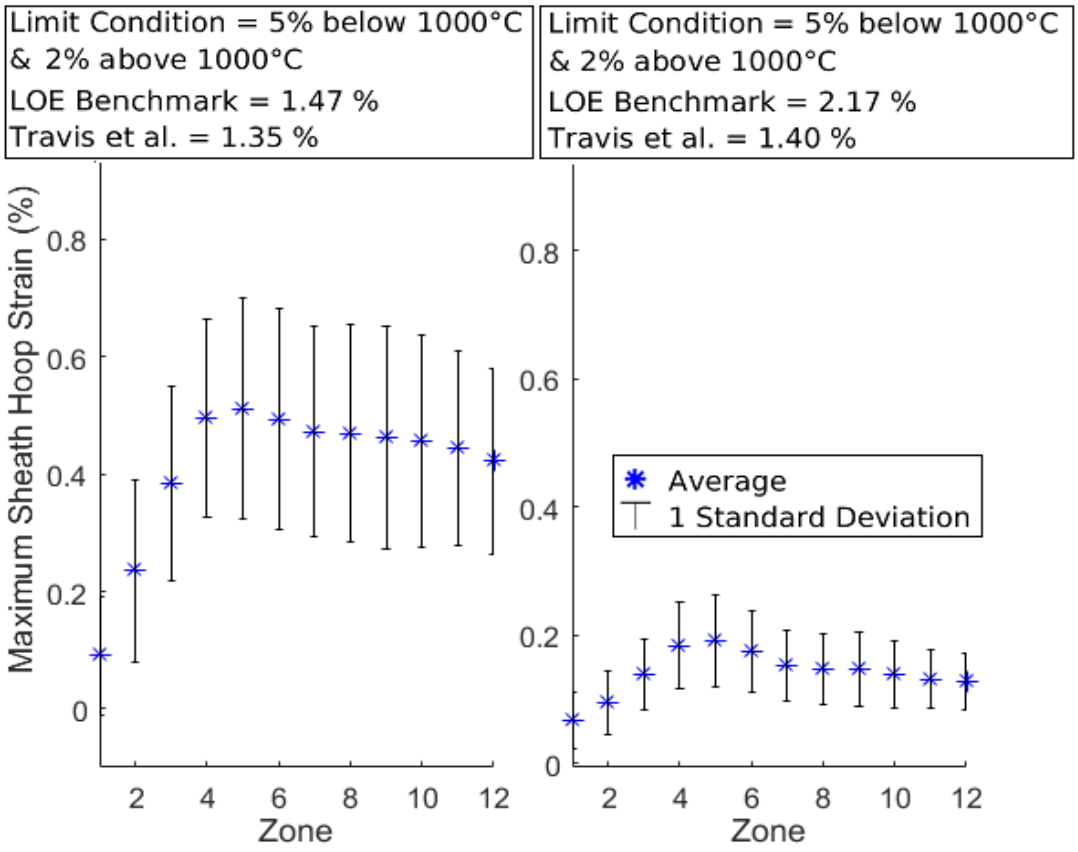

Figure 86. Trend in the maximum fuel sheath hoop strain during NOC (left) and during the 80% ROH break transient (right), for the BNA fuel.

7.6.5 Regionalized Oxide Cracks

For the oxide cracks, just as it was observed for the regular NU-fuelled core, none were predicted to occur at all stages of the transient simulations for all radial regions for

the BNA-transitioned core. The probability of oxide crack formation therefore remains negligible in the case of the BNA fuel as well.

7.6.6 Non-regionalized Response Functions

For the non-regionalized Monte Carlo simulations for the performance of fuels containing BNAs, figures comparable to Figures **57** to **80** are not presented, because graphical trends remain virtually identical between both fuel types, as there are only slight changes in the overall values of the statistical moments. The statistical moments of each of the response functions are summarized below for the BNA-fuelled core in **Table 21**. The survival probability for each of the response functions at significant response levels, including the values at the limit criteria, are summarized in **Table 22**.

Table 21. Moments of each response functions with 95% CI for simulations using the BNA fuel, with the comparative change in value from the equivalent moments for the regular NU-fuelled core shown in brackets.

	Mean			Standard Deviation				
Response Functions	**Mean Lower CI**	**Mean**	**Mean Upper CI**	**STDEV Lower CI**	**STDEV**	**STDEV Upper CI**	**Skewness**	**Kurtosis**
NOC Fuel Centerline Temp. (°C)	1253 (+6.92)	1255 (+7.01)	1257 (+7.10)	155 (+6.11)	156 (+6.17)	158 (+6.23)	-1.40	2.95
NOC Internal Gas Pressure (MPa)	0.63 (+0.01)	0.63 (+0.01)	0.63 (+0.01)	0.10 (0.00)	0.10 (0.00)	0.10 (0.00)	1.79	5.19
NOC Sheath Hoop Strain (%)	0.44 (+0.01)	0.44 (+0.01)	0.44 (+0.01)	0.20 (+0.01)	0.21 (+0.01)	0.21 (+0.01)	0.09	-0.46
NOC Sheath Temperature (°C)	334.7 (+0.41)	334.8 (+0.41)	334.9 (+0.41)	5.8 (+0.19)	5.9 (+0.19)	6.0 (+0.19)	-1.99	5.42
Transient Fuel Centerline Temp. (°C)	1316 (+8.80)	1319 (+8.89)	1321 (+8.97)	150 (+5.96)	151 (+6.02)	153 (+6.08)	-1.11	1.48
Transient Internal Gas Pressure (MPa)	1.16 (+0.02)	1.17 (+0.02)	1.17 (+0.02)	0.16 (+0.02)	0.16 (+0.02)	0.16 (+0.02)	0.99	2.96
Transient Sheath Hoop Strain (%)	0.19 (0.00)	0.19 (0.00)	0.19 (0.00)	0.08 (0.00)	0.08 (0.00)	0.08 (0.00)	0.51	0.68
Transient Sheath Temperature (°C)	959.2 (+3.78)	959.7 (+3.80)	960.2 (+3.83)	38.8 (+1.63)	39.2 (+1.65)	39.5 (+1.67)	-0.35	-0.22

Table 22. Survival (or CCDF) probability of each response functions for simulations using the BNA fuel at various response levels, plus the distance of the mean value from the limit criteria as a multiple of the standard deviation, and the comparative change in value from the equivalent moments for the regular NU-fuelled core in brackets.

Response Function	Response Level 1 (Limit Criteria)	Response Level 1 Probability	No. of STDEVs between mean & Limit Criteria	Response Level 2	Response Level 2 Probability	Response Level 3	Response Level 3 Probability
NOC Fuel Centerline Temp. (°C)	2840°C	0.00 (no change)	10.1 (-0.46)	1400°C	0.14 (+0.03)	1200°C	0.72 (+0.01)
NOC Internal Gas Pressure (MPa)	10 MPa	0.00 (no change)	97.5 (-3.74)	2 MPa	0.00 (no change)	0.5 MPa	0.97 (+ less than 0.01)
NOC Sheath Hoop Strain (%)	2.00% & 5.00	0.0 & 0.0 (no change)	7.5 & 22.1 (-0.51 & -1.42)	0.50%	0.40 (+0.01)	0.20%	0.88 (-0.01)
NOC Sheath Temp. (°C)	600°C	0.00 (no change)	45.0 (-1.57)	340°C	0.12 (+0.03)	300°C	1.00 (no change)
Transient Fuel Centerline Temp. (°C)	2840°C	0.00 (no change)	10.1 (-0.48)	1400°C	0.32 (+0.05)	1200°C	0.83 (+ less than 0.01)
Transient Internal Gas Pressure (MPa)	10 MPa	0.00 (no change)	54.5 (-6.54)	2 MPa	1.40E-03 (+ less than 0.01)	1.2 MPa	0.37 (+0.05)
Transient Sheath Hoop Strain (%)	2.00% & 5.00%	0.0 & 0.0 (no change)	23.1 & 61.5 (+0.24 & +0.63)	0.50%	1.05E-03 (+ less than 0.01)	0.20%	0.42 (+0.01)
Transient Sheath Temp. (°C)	1850°C (limit for LOCA)	0.00 (no change)	22.7 (-1.15)	600°C (not the limit for LOCA)	1.00 (no change)	950°C	0.61 (+0.05)

It can be observed from **Table 21** and **22** that there are very small differences in the mean and mean confidence intervals of each response function between the regular core and the BNA-fuelled core. Also, there are very marginal changes in the size of the standard deviations and their associated confidence intervals as well. The changes in the mean values tended to be small, positive differences for the temperature-related response

functions. However, the pressure and sheath hoop strain values resulted in negligible changes to their statistical moments. Overall, the results indicate that the presence of BNAs and the consequent reduction of average LZC levels (to approximately 4%) does not impart a meaningful change to the response functions investigated in this study. A further verification of this was conducted via a global sensitivity analysis using random sampling of simulated operating data from both the regular NU fuel and the BNA fuel with equal weight, with all other input treatments remaining the same as previous. The variance-based decomposition of the random samples resulted in the following Sobol indices shown in **Figure 87**.

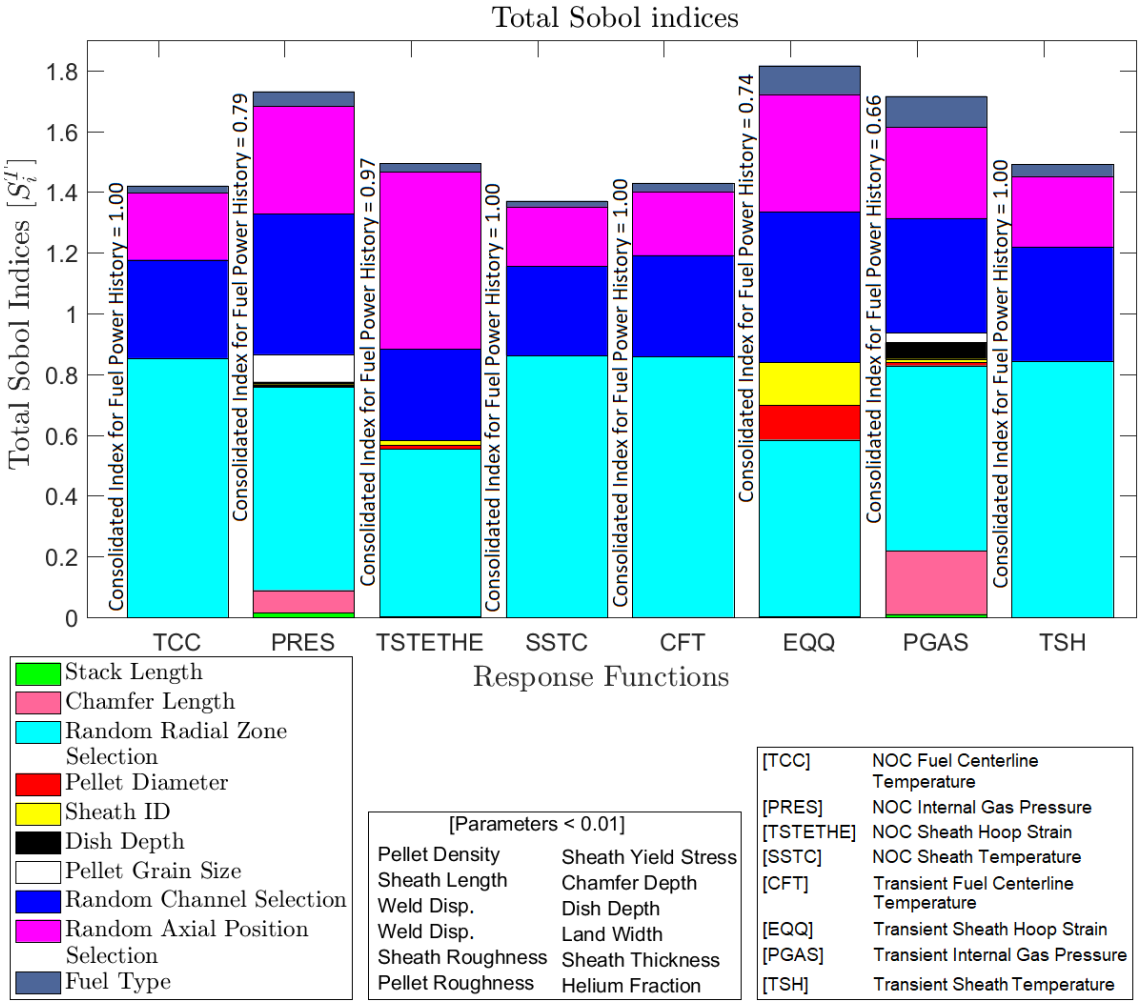

Figure 87. Global sensitivity analyses for case study using random simulated fuel operating data from both regular NU fuel and BNA fuel.

The results of **Figure 87** indicate that the output response functions exhibit slight sensitivities towards the use of the two different fuel types, shown in the grey colour. This is because the difference between the regular NU fuel and its BNA-doped counterpart does impact the fuel power history that is fed into the fuel performance codes. However, this impact is relatively minor compared to the other operating inputs such as the radial zone selection, the random channel selection, as well as the bundle start position selection. It should nevertheless be noted that the sensitivity index for the fuel type selection is still similar or greater in magnitude than many of the manufacturing input parameters, depending on the output response function type. The above observation further confirms the relatively greater magnitude to which response functions exhibit sensitivities to input parameters relating to the fuel power history. Furthermore, this suggests that changes to the operating condition of the fuel, such as fuel design changes, changes to refuelling modes, as well as changes in fuel management strategies can significantly impact the outcome of the fuel safety analysis.

Chapter 8: Discussion

8.1 Regionalized (radial) Monte Carlo Experiment

The outcomes of the regionalized Monte Carlo simulations of fuel performance shown in **Figure 51** to **55** demonstrated that there is a significant margin of safety between the average fuel response levels and their limit criteria. As predicted by the regional trends in fuel power previously shown in **Figure 35**, zone #4 was observed to be the most limiting radial region with response levels closest to the limit criteria. Nevertheless, the average NOC response levels for zone #4 were all found to reside between 14 to 75 standard deviations away from their respective limit criteria. It should be noted that for a Normally distributed (or approximately Normal) dataset, the values residing within 3 standard deviations of the population mean account for approximately 99.7% of the dataset.

For the 80% ROH break LOCA transient, the average response levels of fuel sheath temperature and internal gas pressure were higher than the average values observed for the NOC simulation. However, the average response values of fuel centerline temperature and the sheath hoop strain were observed to be lower for the transient simulation in comparison to the NOC. As discussed previously in section 7.3, this is caused by the selection of the pre-transient snapshot state of the fuel being set at the 50% fractional value of burnup to the discharge value. As such, the pre-transient snapshot does not correspond to the initial peak sheath strain that occurs at zero burnup, as well as the peak fuel power that typically occurs at around 20% fractional value of the discharge burnup. This results in the peak transient values of sheath strain and fuel centerline temperature being less than the NOC peak values despite the impulsive amplification in power experienced during the LOCA. On the other hand, the peak transient values of the internal pressure still exceed those of the NOC. This is because the internal gas pressure remains relatively significant throughout its entire burnup range as the accumulation of fission gas continues to sustain the internal pressure despite

declines in fuel power due to the burnup of the fuel or refuelling shifts. Lastly, the fuel sheath temperature also experiences a significantly higher average value for the transient simulation than NOC, regardless of the pre-transient snapshot of the fuel power. This is, of course, because of the significant depressurization of the coolant and the consequent reduction in its heat transfer coefficient. Nevertheless, the average response levels for the transient simulations were well below their respective limit criteria by between 12 to 31 standard deviations. Also, there was nil occurrence of oxide crack formation for all of the radial regions during the transient simulations.

8.2 Non-regionalized Monte Carlo Experiment

The non-regionalized Monte Carlo simulations further demonstrated the presence of significant safety margins for all response functions when considering the entire core without regional discretization. The results shown in **Figure 57** to **80** consist of the histogram and the PDF fit of the response function output data, as well as both the empirical and the theoretical CDF fits for various distribution types, and the best fit survivability function with a 95% CI for each of the response functions. The probabilities of the limit criteria being exceeded for all response functions, for both NOC and the transient case, were zero, with each limit criteria residing 8.1 to 101.3 standard deviations away from their respective mean response levels. The probability of oxide crack formation during the transient case was also observed to be zero, as nil occurrence of oxide crack formation was observed at all iterations of the simulation. Further descriptions of response levels and their associated probabilities, as well as statistical moments of each response function were outlined in **Table 18** and **19**.

8.3 Global Sensitivity Analysis

A global sensitivity analysis using a variance-based decomposition was computed for the non-regionalized Monte Carlo simulations. The results of the analysis, expressed

in terms of the total Sobol indices, were outlined in **Table 20** and **Figure 81**. The global sensitivity analysis provided a novel demonstration of the hierarchy of fuel response sensitivities to each of its input parameters. It also confirmed that, as expected, the variability of fuel powers imparts the greatest influence on the variance of the response functions. Of the three parameters governing the fuel powers, it was determined that the variability in the selection of the radial region resulted in the greatest variance of the response functions, which was the expected outcome. Also, because the three input parameters pertinent to the fuel power history are statistically correlated to one another, the total sum of their indices was observed to exceed 1.0. This is the main reason why the total Sobol indices were used for this study, because it allows the sum of the indices to exceed the unity value of 1.0 when input variables are correlated to one another. The total Sobol indices were further processed by computing the consolidated Sobol index value for the fuel power history by subtracting all parameters unrelated to fuel power (manufacturing parameters) from the unity value of 1.0. This of course assumes that all other (manufacturing) parameters possessing relevant values of Sobol indices are independent variables. Otherwise, the sum of the total Sobol indices will not be equal to the unity value of 1.0 even with consolidation of the three inputs that determine the fuel power history. It should be noted, this assumption is not fundamentally true as some parameters such as pellet density and grain size are likely to be partially correlated as they are both affected by some shared processes during manufacturing. However, the impact of their correlation on the overall sensitivities of the output response functions are relatively insignificant in comparison to the three fuel power input parameters. Therefore, the above assumption reasonably holds true in this case, and can be used to provide a normalized (to the unity value of 1.0) assessment of the sensitivity indices.

In addition to the input parameters relating to fuel power, the pellet and sheath inner diameters were also found to impart some variance on the response function for the sheath hoop strain. This suggests that the pellet-to-sheath gap value, which influences the pellet-to-sheath contact pressure, has a significant role in the displacement of the fuel

sheath. This was contrary to [20] where Sobol indices for the pellet and sheath inner diameters were considered to be negligible, which is likely due to their use of unrealistically high linear element power value that may have guaranteed pellet-to-sheath contact regardless of the size of the pellet-to-sheath gap. Furthermore, the internal pressure response function, in addition to being greatly affected by the fuel power history, was also sensitive to the variance of the chamfer length, the dish depth, the stack length, the pellet grain size, as well as the pellet and sheath inner diameters. This observation is attributed to the fuel plenum free volume that is determined as a function of the geometrical parameters of the fuel and the sheath, as well as the impact that pellet grain size has on the transport of fission gases from within the pellet to the pellet gap boundary.

8.4 Case Study: Performance of Fuels Containing Burnable Absorbers

The case study for the implementation of the BEPU framework developed in this study was demonstrated for the resulting fuel reliability from the transition refuelling of a regular NU-fuelled core with a BNA-doped fuel. The case study provided a very useful demonstration of the potential application of the method framework via an analysis that is uniquely in-depth in terms of the model and code integration. The analysis incorporates both the modelling of the modified fuel design, the simulation of large quantities of fuel operating data based on the new fuel design, plus the Monte Carlo simulation of its reliability. This covers almost the full range of the impact analysis for the design change, as it includes the lattice level neutronics analysis, the in-core neutronics analysis, plus the in-core thermal-mechanical fuel reliability analysis for both NOC and a transient case. The one missing major component to the method framework is the thermal-hydraulics analysis of the design change. However, in the case of the BNA-doping, which does not change the geometry or the heat transfer characteristics of the fuel and sheath, this analysis is not the most important. The results of the case study were outlined in **Figure 83** to **86** for simulations regionalized per each radial zone, and **Table 21** and **22** for the non-regionalized, full-core simulations.

From the perspective of the most limiting radial region, the presence of the BNAs shifts power away from zone #4, which is the region of peak fuel power for the control core (NU-fuel), to zone #5 where there is a relatively lower variance in fuel power. The resulting fuel response functions for the limiting region demonstrate an increase in the safety margins to the limit criteria in comparison to the control core. This is with the exception of the sheath hoop strain during NOC for which there was a slight decrease in the margin, and for the sheath hoop strain during the transient simulation where there was no change in the margin. As discussed previously, this is most likely due to zone #5 having a higher average discharge burnup than zone #4. Alternatively, from the perspective of the non-regionalized, full-core simulation, the BNA-transitioned core yielded margins to limits that were slightly smaller (worse) in comparison to the control core. The sheath hoop strain during the transient simulation was once again an exception to this, for which there was no change to the margin. The cause behind the difference in the safety margin change observed between the limiting region case and the full-core simulation is due to the limiting region case being a unique situation where the variance of the response functions decreased significantly for the BNA-fuelled core.

It should also be noted, the relative changes in the mean values of the response functions for the total-core simulations were negligible, with average values of changes for each response function ranging between -0.49% to +1.62%. The changes in the values of standard deviations, on the other hand, ranged between -1.3% to +12.8%. However, the relatively high percentage changes for the standard deviations of some response functions, and for some of the mean values to a lesser degree, are not necessarily significant because the response functions that account for them have very small output values to begin with. An example of this is the transient sheath hoop strain, for which the output value is very often less than 1.0, and the value of its standard deviation is an even smaller fraction. This is such that any small changes may appear over-exasperated as a significant percentage differential.

Overall, the results of the case study indicate that negligible changes in the safety margins ensue from the transition-refuelling of the model core using the BNA-doped fuel. However, a notable potential safety advantage is observed in having shifted power away from the previously limiting region of zone #4 with the higher variance, to zone #5 which has a lower variance. It should also be noted that the above observations are made in spite of the significant reduction of the average LZC fill levels to a new equilibrium value of approximately 4%, as opposed to the previous average value of 42.5% in the case of the control core. This level of preservation of the LZCs is, of course, a significant improvement in the safety margins for the overall core with respect to regional overpower protection. The overall impact to the discharge burnup of the fuel due to the presence of the BNAs was also observed to be negligible, most likely due to the neutron savings provided by the reduction of the LZC fill levels which counterbalanced the parasitic loss of neutrons to the BNAs.

8.5 Limitations and Validation of Research

8.5.1 Limitations of Research

In the case of the stochastic (aleatory) uncertainty, its quantification requires the characterization of the input uncertainties, followed by the forward propagation of these uncertainties via the computational model, and performing statistical assessments on the resulting responses. Naturally, the quality of the stochastic uncertainty quantification is limited by the quality by which the input uncertainties are initially characterized. When pursuing the assessment via a Monte Carlo method, the characterizations of input uncertainties are well-propagated in the output response functions, assuming a suitable sampling method is utilized. The deterministic (epistemic) uncertainty, on the other hand, is difficult to assess via a probabilistic approach, as they consist of systemic biases that impart an absolute (non-random) error on the output response. Moreover, deterministic uncertainty is difficult to quantify *a priori* to the identification and the quantification of

the specific, systemic bias. As such, this study is primarily focused on the quantification of the stochastic uncertainty, and it provides assessments of deterministic uncertainty in a qualitative manner using benchmarks wherever possible.

In this study, input variables relating to the manufacturing parameters were defined via statistical distributions derived from measurement data obtained from Cameco Fuel Manufacturing Inc. For these parameters the effect of stochastic uncertainty is well-captured by the statistical fits that were used to drive the Monte Carlo random sampling method for the uncertainty quantification. This means that the stochastic uncertainties of the manufacturing inputs are very well reflected in the stochastic uncertainty of the response functions via error propagation. However, the error of the goodness-of-fit for each of the manufacturing inputs is not propagated forward via the computational model, which results in a systemic bias that is a source of deterministic uncertainty. The value of this uncertainty could be approximated by computing the average error between the real manufacturing data and the value predicted by the fitted distribution, then computing the error it would impart on the response functions. This, of course, would need to be computed as a combined effect of all input parameters for each of the response functions. At this time, the estimation of the above particular deterministic error is yet to be completed, but it is planned to be addressed in the future refinement of the current project. However, as the distributions used to model each of the manufacturing variables demonstrate very good fits, both graphically and by the coefficient of determination, the resulting error is expected to be very small.

On the other hand, the stochastic error associated with the initial characterization of input uncertainties for the operating data is of significant limitation for this study, as it is based on a random selection of simulated fuel power history. The stochastic error, characterizable via the random variability of the fuel power data, is therefore fundamentally biased due to the fuel management strategy used for the refuelling algorithm. The refuelling strategy used in this study is expected to differ in some

unknown (proprietary) ways from the actual implementations used at nuclear power generating stations. For the non-regionalized Monte Carlo simulations, another source of deterministic uncertainty is the quality of the distribution fit that describes the refuelling density between radial regions. The regional refuelling density variable has a very good fit to the Normal distribution as previously shown in **Figure 38**, but for the same reason as the manufacturing inputs, there is inevitably some deterministic error that results from the non-perfect quality of the fit. Also, the random selection of a fuel channel within a radial region and a bundle axial position within a channel were assumed to both follow a uniform random distribution. However, this assumption is not perfectly correct for the random selection of a fuel channel from a radial region. This is because the locations of the guide-tube end-weights within the core, which induce a slight flux suppression in their vicinity, are biased towards the bottom side of the core [21]. Therefore, there is a slight bias in the refuelling frequency towards the top side of the core, where there is slightly less parasitic absorption of neutrons. The deterministic uncertainty resulting from the goodness-of-fit for the distributions that describe the random selection of a fuel history can also be estimated by determining the average error it produces in the response functions. However, this is yet to be pursued for the current study as its quantification alone is not very meaningful without the quantification of the much larger, fundamental biases associated with the way in which the fuel power history data are generated.

The fuel history data used in this study were generated via core-following using the principles of conventional CANDU fuel management, with lattice data from WIMS-AECL, reactivity devices from DRAGON and core neutron diffusion calculations using RFSP. Due to the means by which they are produced, the fuel history data are subject to the fundamental, deterministic uncertainty associated with the code, the model definition within the code, as well as the quality of the refuelling algorithm that was used for the core-following. The impact of these uncertainties on the error of the output response functions is difficult to estimate, as most of the systemic biases are code-to-experiment discrepancies due to fundamental modelling issues that are yet to be understood, or are

unavailable due to proprietary reasons. Therefore, these uncertainties are not quantified as a part of this study. Nevertheless, it should be noted that the RFSP code is an industry standard toolset that has been validated against power reactor measurements as described in [47], as well as via multiple studies using core snapshots extrapolated from FINCH data, such as described in [51]. Multiple FINCH are distributed across the CANDU core, such that their measurements can be used to extrapolate the flux distribution (via relative flux-mapping) of the entire core, which is how the power of the CANDU reactor is tracked real-time while on-power.

Among all potential sources of deterministic uncertainty affecting the response functions tracked in this study, the biases associated with the core model, the fuel simulation codes, or the refuelling algorithm are expected to be more significant than biases associated with the manufacturing processes or measurements. This is suggested by the relatively larger variance exhibited by the fuel power data in comparison to the manufacturing variables. Furthermore, this is also suggested by the relatively high sensitivity indices of the fuel power input parameters in comparison to the relatively small sensitivity indices observed for the manufacturing inputs. Therefore, efforts to improve the current methodology should take particular focus towards improving the accuracy of the fuel history data for a better statistical representation of the real fuel operating data.

Although they are not assessed as part of uncertainty quantification (stochastic) in relation to the propagation of error from inputs, the ELESTRES and ELOCA codes are also subject to systemic biases within their design, model specifications, or assumptions on boundary conditions. A literature review on the validation of the ELESTRES and ELOCA codes in [52], [53] and [54] does demonstrate good accuracy between the above two codes in relation to various Post-Irradiation Examination (PIE) data for both NOC samples as well as data from LOCA experiments. Furthermore, an examination of the statistical moments of both NOC and the transient simulations against values published

in literature confirms that the range of fuel response levels observed in this study are within the expected range of values for CANDU fuels for their given conditions [11].

8.5.2 Method Validation

For the present study, the quality of the simulated core data was benchmarked via comparison to two full-core snapshots obtained from the Darlington nuclear generating station's cores, which are extrapolated from the actual FINCH channel measurements. The above assessment provided indication that the simulated data are a reasonable representation of the actual core data in terms of both the distribution of the power densities and magnitudes [3]. The average relative difference between the fuel bundle powers of all 6240 fuel lattices of Darlington snapshot #1, compared to all 40,000 simulated core snapshots from this study, was 11% with a standard deviation of 14%. The comparison to Darlington snapshot #2 also yielded an average differential of 11% with a standard deviation of 13%.

The majority of differences between the Darlington core snapshots and the simulated core snapshots were concentrated in the peripheral regions of the core, with the differences in the central regions being significantly smaller. It should be noted that a control comparison between random simulated snapshots yielded a mean difference of approximately 4%, and a 4% standard deviation. These values account for the variability in the simulated core snapshot data against time, which is driven by the perpetual propagation of the refuelling ripples and changes in the burnup distribution. The above comparison indicates that there is some difference between the fuel power distributions of the Darlington snapshot data and the simulated snapshots that are beyond just the average difference that one random snapshot would exhibit in comparison to another random snapshot. Nevertheless, the simulated core data are assessed to provide a reasonable representation of realistic core-operating data, and it may be seamlessly

replaced if real core snapshot data were to be made available in a sufficiently large sample size.

The design of the computer analysis developed for the current study cannot be extensively validated against measured data, as experimental and PIE data were available in only limited, statistically non-significant quantities, and/or there was a lack of sufficient detail in the cataloguing of pre-irradiation specifications for the examined fuels. An independent cross-code benchmark or code-to-experiment benchmark was not directly pursued in this study, because the literature review yielded a closely relevant benchmark case in [11]. The ELESTRES and ELOCA code-to-experiment data benchmark reported by [11] incorporates all of the same PIE data that were available for this study. This includes seven fuel sample PIE data for NOC conditions from Atomic Energy Canada Limited (AECL), as well as the FIO-131 experiment data for simulated LOCA on an instrumented fuel element sample A10H [11]. The benchmark case in [11] provided indication that there is a good agreement between the PIE measurement data and the predictions yielded by ELESTRES and ELOCA. The report from [11] also provided a cross-code benchmark for ELESTRES and ELOCA against the novel Fuel And Sheath modelling Tool (FAST) code. This assessment provided a benchmark indication that there is strong agreement between the predictions made by ELESTRES and ELOCA in comparison to the FAST code.

To perform a full experimental validation of the overall methodology, a significant database of real fuel PIE measurement data covering a wide range of fuel operating conditions, for both NOC and as a pre-transient snapshot, with realistic statistical distributions is necessary. This would first require a sufficiently large sample of fully-catalogued fuel data including a pre-irradiation account of fuel manufacturing specifications, as well as the tracking of power and burnup history within instrumented channels or experimental reactors, followed by post-irradiation examination data to obtain a distribution fit with a tight confidence interval. This would allow an

experimental validation of the statistical moments for the NOC simulations. Secondly, to account for the 80% ROH break LOCA simulation, a sufficiently large number of simulated coolant depressurization experiments, with full cataloguing of pre-irradiation, as well as pre-transient data, followed by post-irradiation examination would be required to the same effect. An experimental validation for the LOCA simulation to the above level of detail would be prohibitively expensive to pursue. On the other hand, the NOC validation can be partially achieved at the post-irradiation examination level if an extensive data collection effort at the power generating station level is implemented with full cataloguing of pre-irradiation measurement data, as well as FINCH data and post-irradiation data for randomly selected fuels. This is however, also prohibitively expensive as a means to generate a sufficiently large sample size, as it is expensive to take full PIE measurements of irradiated fuels, such that it is typically only done so for confirmed defective fuels. A more realistic strategy for the validation of the fuel reliability analysis, for both NOC and transient conditions, would be to generate a limited range of benchmarking validation cases as opposed to building a statistically significant database of experimental or catalogued data.

Chapter 9: Conclusion

This study has developed a method framework for determining the reliability of CANDU fuels during both NOC and transient conditions based on the *best-estimate plus uncertainty* approach. The method framework incorporates the current industry standard toolset codes for fuel performance in both NOC and transient conditions to simulate the major fuel performance response functions considered within the study. The simulation framework is augmented by a realistic input treatment using statistical inference of manufacturing data, as well as simulated fuel power histories using industry toolset codes for lattice, device and core neutron diffusion modelling. Furthermore, the method framework implements uncertainty quantification by propagating the characterized input uncertainty via a Monte Carlo random sampling method.

The results of the study yielded realistic values of statistical moments and response levels for all four response functions, for both the NOC and an 80% ROH break LOCA scenario. The response functions included fuel pellet centerline temperature, fuel sheath temperature, internal gas pressure, and fuel sheath strain. In addition to the four response functions, the probability of the oxide crack formation was also tracked within the study, for which nil occurrences were predicted. The range of response for these values compared reasonably to their known range of values found in literature and industry reports, with any differences being reasonably attributable to the realistic fuel power histories used in the study [11,52,53,54]. Overall, the study demonstrated the achievement of the WANO zero fuel defect criterion by the 37-element CANDU fuel, for the four fuel response functions plus the oxide crack formation tracked in the study. This was demonstrated for both NOC and the transient simulations for each of the response functions, as nil probabilities were predicted for the occurrence of their limit conditions. Furthermore, the study demonstrated the existence of significantly larger safety margins for the four response functions, for both NOC and the 80% ROH break LOCA, in comparison to a generic and conservative benchmark analysis, as well as the comparable

findings reported by [20]. It should also be noted, the results of this study in the form of the probability for the occurrence of a fuel defect, can be directly adapted as the rate of defect occurrence for the level 1 PSA as outlined by REGDOC-2.4.2 [15]. The results of this study are therefore of significant utility to the industrial stakeholders of CANDU technology. More specifically, they provide a pathway for the industry to shift away from utilizing Bayesian probabilistic adaptations of past experience, and towards a multiphysics approach augmented by statistical treatment of inputs. This is a significantly advantageous development for the industry, as probabilistic adaptations of past experience are limited by their nature of typically being indirect, subjective, unique or non-standardized observations of past fuel defects.

A global sensitivity analysis based on a variance-based decomposition was also conducted with the Monte Carlo simulations of fuel performance. The results of the analysis confirmed that the response functions assessed within this study are the most sensitive to the fuel power history data, and to a much lesser extent, to parameters that determine the pellet-to-sheath radial gap, as well as the pellet grain size, and additional geometrical parameters that determine the void volume of the element plenum. The geometrical parameters important to the void volume include the radial pellet-to-sheath gap, the chamfer length, and the dish depth, plus the stack length which is dependent on the axial pellet-to-sheath gap and the pellet-to-pellet gap. All other remaining input parameters were found to be negligible in their influence on the variance of the output response functions. The confirmation of this hierarchy is highly useful for industrial application, as it provides a statistical basis for the optimization of manufacturing processes as well as operating practices to selectively optimize the performance of the CANDU fuel via its most important variables. In addition to the sensitivity analysis, an application case study on the reliability analysis of the 37-element fuel following a design change was also conducted. The modified fuel design consisted of burnable absorber doping within the CANLUB layer of the fuel, using 150 mg of GdO_2 and 300 mg of EuO_2. The case study demonstrated there are no significant drawbacks in the

safety margins of the four fuel response functions, for both NOC and the transient simulations. Simultaneously, it was demonstrated that the margins for regional overpower mitigation provided by the LZCs were conserved as a result of the transition-refuelling using the BNA-doped fuel.

In summary, the current study developed a method framework that incorporates a uniquely large scope of physics codes, models, statistical toolsets and data, and successfully implemented it as a proof-of-concept for the *best-estimate plus uncertainty* analysis of CANDU fuel reliability. This study was the first of its kind for implementing the *best-estimate plus uncertainty* approach for the probabilistic analysis of nuclear fuel reliability for both NOC and LOCA scenarios, and furthermore it is the first of its kind to be implemented for the 37-element CANDU fuel. In addition, the applicability of the method framework was demonstrated via the reliability case analysis involving a fuel design change which imparts a significant impact on the in-core neutronics of the fuel. The method framework operates within the MATLAB^{TM} numerical computing environment that is interfaced with the DAKOTA statistical toolset, which provides seamless code-coupling and execution of the computer experiment from a single work environment. The above design of the method framework easily allows the replacement of codes, data, as well as sampling and post-processing methods for future improvements or adaptive application.

Chapter 10: Recommendations

As illustrated by the case study on the effects of BNA-doping on fuel reliability using the current method framework, the application of the *best-estimate plus uncertainty* method is highly relevant and especially useful in the cases of comparative analyses where absolute accuracy of the statistical moments is less important. The research and development towards implementing engineering changes to the fuel design has traditionally been a popular means of improving margins and mitigating aging within the CANDU industry. For this reason, the current methodology is a highly applicable framework by which preliminary studies on the downstream effects of fuel design or process changes can be conducted with relative ease and a high level of realism. Moreover, with further refinement, the current method framework is capable of providing a strong advantage in terms of accuracy, or act as an alternative benchmark against the current, conventional practice of formulating the level 1 PSA initiating event rates.

To support future applications, the advancement of the present method framework should be pursued in the way of improving the uncertainty characterization of manufacturing inputs, as well as the random selection of fuel histories. This can be accomplished by increasing the statistical significance of the input database via accumulating more sample measurements, as well as by improving the quality of the measurements themselves. Also, although the current study has made significant advancements in removing unrealistic, conservative assumptions in its input treatment, there are still some input parameters that were treated with conservative, arbitrary assumptions. Some significant examples include the conversion of the fuel bundle power history data to the fuel linear element power data, for which the most limiting, outer annulus of the fuel was used, as well as arbitrary assumptions made for the pellet and sheath roughness, plus the chamfer variables. Furthermore, if obtainable in sufficiently large, statistically significant quantities, the actual core-tracking data obtained via flux-

mapping from FINCH data should be used as the fuel power history input instead of the simulated core-following data. A cross-code validation using the Fuel And Sheath modelling Tool (FAST) code, for both NOC and transient conditions, should also be conducted as an extension of the method validation.

Additionally, in consideration of the case study resulting in a successful transition from LZC-based suppression of refuelling ripples to an inherent, embedded BNA-based suppression, a further exploration on the application of the BNA-doped fuel should be pursued. In particular, it should be noted from the results of the NOC simulations that the moment at which a fuel bundle experiences its most significant thermal-mechanical impulse-loading during its in-core life is when the fuel first enters the core. This occurs as the freshly inserted fuel instantaneously transitions from its prior out-of-core, storage state and begins to generate large magnitudes of heat that is released via fission reaction. As discussed above in section 5.1 and **Figure 8**, the most significant cause for fuel defects is the exposures to large power ramps. Among all the power steps that a fuel experiences in its in-core life cycle, the initial fuelling transient generally poses as the greatest power ramp (as shown in **Figure 47**), and the presence of the BNAs allows a significant proportion of this impulsive power loading to be mitigated without any device response-time delay. Building on the use of BNAs as a means to mitigate the fuelling transient, the application may be taken further to "over-suppress" the initial reactivity of the fuel beyond the levelling of the fuelling transient, such that the initial power ramp is further reduced for both the inserted fuel, as well as all other fuels in its vicinity that would also experience a ramp in power. If this could be implemented without sacrificing the useful reactivity of the fuel over the course of its entire in-core life, then it could significantly reduce the level of fuel sheath strain or fuel pellet thermal damage (cracking) with negligible impact on the required refuelling rate.

References

[1] Canadian Nuclear Safety Commission, 2014, Deterministic Safety Analysis, Regulatory Document, REGDOC-2.4.1.

[2] Koh, H., Magee, L., 2006, A functional approach for studying technological progress: Application to information technology, 2006 Technological Forecasting & Social Change, vol. 73, 1061–1083.

[3] OPG Darlington Nuclear Generating Station Web Site: https://www.opg.com/generating-power/nuclear/stations/darlington-nuclear/

[4] OPG Pickering Nuclear Generating Station Web Site: https://www.opg.com/generating-power/nuclear/stations/pickering-nuclear

[5] Bruce Power Nuclear Generating Station Web Site: https://www.brucepower.com/about-us/history/

[6] New Brunswick Power Corporation, Point Lepreau Nuclear Generating Station Web Site: https://www.nbpower.com/en/about-us/divisions/nuclear

[7] Garland, J., 2014, The Essential CANDU: a textbook on the CANDU nuclear power plant technology, Prologue: CANDU in Context, University Network of Excellence in Nuclear Engineering, pg 13-24.

[8] Chaplin, R., 2014, The Essential CANDU: a textbook on the CANDU nuclear power plant technology, Chapter 2: Genealogy of CANDU Reactors, Chapter 8: Nuclear Plant Systems, and Chapter 9: Plant Operation, University Network of Excellence in Nuclear Engineering, pg 59-107, 623-681 and 681-751.

[9] Tayal, M., Gacesa, M., 2014, The Essential CANDU: a textbook on the CANDU nuclear power plant technology, Chapter 17: Fuel and Chapter 18: Fuel Cycles, University Network of Excellence in Nuclear Engineering, pg 1351-1479.

[10] Song, W., and Manzer, A.M., 2005, CANDU Fuel Performance, Shanghai Nuclear Engineering Design & Research Institute, Atomic Energy of Canada Limited.

[11] Prudil, A., 2013, FAST: A Fuel And Sheath Modelling Tool for CANDU Reactor Fuel, Thesis Manuscript, Royal Military College of Canada.

[12] International Atomic Energy Agency, 2008, Best Estimate Safety Analysis for Nuclear Power Plants: Uncertainty Evaluation, IAEA Safety Reports Series, No 52, pp 1-162.

[13] Ivanov, E., Dubois, F., Sargeni, A., Bruna, G.B., 2018, Best estimate plus uncertainty (BEPU), why is it still not widely used, Proceedings of 2018 ANS international conference on BEPU methods.

[14] International Atomic Energy Agency, 2003, Safety margins of operating reactors: Analysis of uncertainties and implications for decision making, Technical Document, IAEA-TECDOC-1332.

[15] Canadian Nuclear Safety Commission, 2014, Probabilistic Safety Assessment (PSA) for Nuclear Power Plants, Regulatory Document, CNSC-REGDOC-2.4.2.

[16] International Atomic Energy Agency, 2014, Development and Application of Level 1 Probabilistic Safety Assessment for Nuclear Power Plants, IAEA Safety Standard, SSG-4.

[17] International Atomic Energy Agency, 2014, Development and Application of Level 2 Probabilistic Safety Assessment for Nuclear Power Plants, IAEA Safety Standard, SSG-3.

[18] Rouben, B., 1999, Fuel Management in CANDU, CANDU Fuel Management Course, Atomic Energy of Canada Ltd.

[19] World Association of Nuclear Operators, 2017, Performance Indicators, Program Description Document.

[20] Cunning, T.A., Chan, P.K., Pandey, M.D., 2017, An Examination of CANDU Fuel Performance Margins Derived from a Statistical Assessment of Industrial Manufacturing Data, Nuclear Technology, MS# NT13-126.

[21] Song, J., Chan, P., Bonin, H., Paquette, S., 2017, Fuelling study of a CANDU reactor using fuels containing burnable neutron absorbers, Nuclear Technology, vol. 195, issue 3, pages 310-328, DOI: 10.13182/NT16-1

[22] Chan, P.K., Livingstone, S., 2013, CC533 Nuclear Fuel Engineering, Course notes, Royal Military College of Canada, Kingston, Ontario.

[23] International Atomic Energy Association, 2010, Review of Fuel Failures in Water Cooled Reactors, IAEA Nuclear Energy Series NF-T-2.1, STI/PUB/1445 978-92-0-102610-1, page 32.

[24] Lewis, B.J., Thompson, W.J., Kleczek, M.R., Shaheen, K., Juhas, M., Iglesias, F.C., 2011, Modelling of iodine-induced stress corrosion cracking in CANDU fuel, Journal of Nuclear Materials, vol. 408, issue 3, pages 209-223, DOI: 10.1016/j.jnucmat.2010.10.063.

[25] MacDonald, R.D., Lewis, B.J., Manzer, A.M., Truant, P.T., 1990, Detecting, Locating, and Identifying Failed Fuel in Canadian Power Reactors, AECL-9714, Atomic Energy Canada Limited.

[26] Chassie, G.G., 2006. ELESTRES-IST 1.2 Theory Manual, 153-113370-STM-001. Atomic Energy of Canada Limited.

[27] Caswell, D.J., Williams, A.F., and Richmond, W.R., 2005, “ELOCA 2.2 User’s Manual,” 153-113400-UM-001, Atomic Energy of Canada Limited.

[28] Harvey, M.R., Teter, A.R., and Legget, 1969, R.L., Fabrication of Oxide Nuclear Fuel Pellets, The DOW Chemical Company, US Atomic Energy Commission Contract AT(29-1)-1106, Golden, Colorado, retrieved January 2021 from https://www.osti.gov/servlets/purl/4776353.

[29] Nichita, E., and Rouben, B., 2014, The Essential CANDU: a textbook on the CANDU nuclear power plant technology, Chapter 5 Reactor Dynamics, University Network of Excellence in Nuclear Engineering, pg 217-265.

[30] Hepburn, G.A., 2014, The Essential CANDU: a textbook on the CANDU nuclear power plant technology, Chapter 10 Instrumentation and Control, University Network of Excellence in Nuclear Engineering, pg 751-798.

[31] Canadian Nuclear Safety Commission, 2017, CNSC-LCH-PR-13.01/2025-R002: Darlington Nuclear Generating Station Nuclear Power Reactor Operating License, Canadian Nuclear Safety Commission License Conditions Handbook, License No. PROL-13.01/2025.

[32] Shen, W., and Doyle, F., 2015, CANDU Safety R&D Status, Challenges, and Prospects in Canada, Science and Technology of Nuclear Installations, Volume 2015.

[33] Tezel, H., Christodoulou, N., and Mesmous, N, 2010, Assessment of the Impact of Aging on the Performance of CANDU Special Safety and Safety Related Systems; Safety Analysis Perspective, Canadian Nuclear Safety Commission.

[34] Pandey., M.D., Jyrkama, M.I., 2015, CIVE 601 Engineering Risk and Reliability Course Notes, University of Waterloo.

[35] Sun., A and Tayal, M., 2010, Technical Basis for ACR-1000 Fuel Acceptance Criteria, Proceedings of 11th International Conference on CANDU Fuel, Canadian Nuclear Society.

[36] D'Auria, F., Giorgio, G., 2019, Best Estimate Plus Uncertainty Approach in Nuclear Reactor Safety and Licensing: Brief History and Elements after Licensing, Nuclear Technology and Radiation Protection, vol. 34, no. 3, pg 299-312, DOI: 10.2298/NTRP190413022D.

[37] Cameco Corporation Web Site: http://www.cameco.com.

[38] The MathWorks Inc, MATLAB version 8.1.0.604, 2013, Natick, Massachusetts, United States.

[39] Pajo, L., 2001, UO_2 Fuel Pellet Impurities, Pellet Surface Roughness And n(^{18}O)/n(^{16}O) Ratios Applied to Nuclear Forensic Science, University of Helsinki, retrieved January 20, 2020 from https://helda.helsinki.fi/bitstream/handle/10138/21067/uo2fuelp.pdf?sequence=1

[40] Barberis, P., Mardon, J.P., Rebeyrolle, V., and Aubin, J.L., 2010, Method of Manufacturing A Fuel Cladding Tube For A Nuclear Reactor And A Tube Obtained Thereby, US 7738620 B2, United States Patent and Trademark Office,

retrieved January 8, 2020 from https://patentimages.storage.googleapis.com/94/fe/1c/e0133379a2bb83/US7738620.pdf

[41] Akhiani, H., 2015, Zircaloy-4 And Incoloy 800H/Ht Alloys For The Current And Future Nuclear Fuel Claddings, University of Saskatchewan, retrieved January 2, 2020 from https://harvest.usask.ca/handle/10388/ETD-2015-01-1885.

[42] Palleck, S.J., Sejnoha, R., and Wong, B.J., 1997, Bundle Uranium Content And Performance Of Candu Fuel, Proceedings of 5th International Conference on CANDU Fuel, Missisauga, Ontario, Canada, retrieved December 20, 2019 from https://inis.iaea.org/search/search.aspx?orig_q=RN:31006133.

[43] Jonkmans, G., 2006, WIMS-AECL Version 3.1 User's Manual, ISTP-05-5115, CANDU Owners Group Inc.

[44] Chan, P.K., Paquette, S., and Bonin, H.W., 2015, Variation of Burnable Neutron Absorbers in Heavy Water-Moderated Fuel Lattice: A Potential to Improve CANDU Reactor Operating Margins, Journal of Nuclear Technology, vol. 191, issue 1, DOI: 10.13182/NT14-67.

[45] Shen, W., 2002, CANDU Three-Dimensional Neutron Transport Calculations with DRAGON, Atomic Energy of Canada Limited.

[46] Schwanke, P., 2006. RFSP-IST Version REL_3-04: Users' Manual, SQAD-06-5054, 153-117360-UM-002. CANDU Owners Group Inc.

[47] Ovanes, M., Jenkins, D.A., Ardeshiri, F., Mao, A.C., Shad, M., Sissaoui, T., and Chow, H.C., 2001, Validation of the RFSP-IST Code Against Power-Reactor Measurements, Atomic Energy of Canada Limited, retrieved February 20, 2020 from http://pbadupws.nrc.gov/docs/ML0236/ML023600327.pdf.

[48] Pierce, D., 2017, Mitigation of End-flux Peaking in CANDU Fuel Bundles Using Neutron Absorbers, Royal Military College of Canada, Masters Thesis, RMC-CCE-CC504-15-3, Kingston, ON, Canada. retrieved January 12, 2020 from https://espace.rmc.ca/bitstream/11264/1361/1/MastersThesis_DPierce.pdf.

[49] Adams, B., Ebeida, M., Eldred, M., Geraci, G., Jakeman, J., Maupin, K., Monschke, J., Stephens, A., Swiler, L., Vigil, D., and Wildey, T., 2018, Dakota, A Multilevel Parallel Object-orientated Framework for Design Optimization, Parameter Estimation, Uncertainty Quantification and Sensitivity Analysis: Version 6.9 Theory Manual, Sandia National Laboratories, SAND2014-4253, Albuquerque, New Mexico, USA.

[50] Freeman, D., Diaconis, P., 1981, On the histogram as a density estimator: L2 theory, Probability Theory and Related Fields, vol 57(4), pg. 453-476, DOI:10.1007/BF01025868.

[51] LeRoy, G., Sullivan, A., 2017, Improvements in RFSP prediction capability for spatial control in Darlington reactors, Proceedings of 37th Annual CNS conference, Toronto, Canada.

[52] Sim, K.S., Chassie, G.G., Xu, Z., Tayal, M., Westbye, C., 2001, Progress in qualifying ELESTRES-IST 1.0 code: verification and interim results of validation, Proceedings of 7th international conference on CANDU fuel, Toronto, Canada.

[53] Hallgrimson, K., Tayal, M., Wong, B., and Aboud, R., 1992, Recent validation of the ELESTRES code, Proceedings of 3rd international conference on CANDU fuel, Toronto, Canada.

[54] Walker, J.R., De Vaal, J.W., Arimescu, V.I., McGrady, T.G., and Wong, C., 1992. Use of ELOCA.Mk5 to calculate transient fission product release from CANDU fuel elements, IAEA Report Number: AECL--10591, Atomic Energy of Canada Limited, Chalk River, ON, Canada, 27 pages. Free download from: https://inis.iaea.org/collection/NCLCollectionStore/_Public/23/059/23059652.pdf?r=1&r=1.

Appendix A

WIMS-AECL (accessed via WIMS-UTIL) IST code inputs for 37-element CANDU fuel lattice burnup calculation & conversion into RFSP fuel table

Input File:

-

```
@cleanup
@wims3
PRELUDE
*
Title "fuel_2g DNGS with 2 group WIMS-Corrected Bundle Specifications"
* Corrections introduced (December 2009):
* 1- Change the inner ring pitch radius to 1.4885 cm
* 2- Change the fuel density to 10.5057 g/cc
*
Sequence Pij
Cell Cluster
*
lines  0.       4.9800    100  7
lines  4.9800  14.2876    223  1
*
symmetry -12 0d 30d
*
ANNULUS #   0.98  Coolant
ANNULUS #   1.32  Coolant
ANNULUS #   1.65  Coolant
ANNULUS #   1.98  Coolant
ANNULUS #   2.32  Coolant
ANNULUS #   2.65  Coolant
ANNULUS #   2.98  Coolant
ANNULUS #   3.32  Coolant
ANNULUS #   3.65  Coolant
ANNULUS #   3.98  Coolant
ANNULUS #   4.31  Coolant
ANNULUS #   4.65  Coolant
ANNULUS #   4.98  Coolant
ANNULUS #   5.150 Coolant2
*
ANNULUS #   5.1689  PT
ANNULUS #   5.6007 PT
ANNULUS #   6.44780 Gap
ANNULUS #   6.58750 CT
*
ANNULUS #   6.94 Moder
ANNULUS #   7.29 Moder
ANNULUS #   7.65 Moder
ANNULUS #   8.00 Moder
ANNULUS #   8.35 Moder
ANNULUS #   8.71 Moder
```

```
ANNULUS #   9.06 Moder
ANNULUS #   9.41 Moder
ANNULUS #   9.77 Moder
ANNULUS #  10.12 Moder
ANNULUS #  10.47 Moder
ANNULUS #  10.82 Moder
ANNULUS #  11.18 Moder
ANNULUS #  11.53 Moder
ANNULUS #  11.88 Moder
ANNULUS #  12.24 Moder
ANNULUS #  12.59 Moder
ANNULUS #  12.94 Moder
ANNULUS #  13.30 Moder
ANNULUS #  13.65 Moder
ANNULUS #  14.00 Moder
ANNULUS #  14.2876 Moder
NPIJAN #
Polygon # 4 Moder 14.2876
*
Array # 1 1 0 0
Rodsub # #    .429709 Fuel1 90d Fuel1 270d
Rodsub # #    .609000 Fuel1 90d Fuel1 270d
Rodsub # #    .609600 Clad1
Rodsub # #    .650460 Clad
*
Array # 1 6  1.48850 0
Rodsub # #    .429709 Fuel2 90d Fuel2 270d
Rodsub # #    .609000 Fuel2 90d Fuel2 270d
Rodsub # #    .609600 Clad1
Rodsub # #    .650460 Clad
*
Array # 1 12 2.87550 15d
Rodsub # #    .429709 Fuel3 90d Fuel3 270d
Rodsub # #    .609000 Fuel3 90d Fuel3 270d
Rodsub # #    .609600 Clad1
Rodsub # #    .650460 Clad
*
Array # 1 18 4.33050 0
Rodsub # #    .429709 Fuel4 90d Fuel4 270d
Rodsub # #    .609000 Fuel4 90d Fuel4 270d
Rodsub # #    .609600 Clad1
Rodsub # #    .650460 Clad
*
Power 8   12757.75 0.05 1 0.0001
Buckling 1.0e-4 1.0e-4 1.0e-5 1.0e-5
*
newres   4  .1  -12  0d  30d 4 0.3 6 0.01 1 0
*
TOLERANCE 1E-6
*
FEWGROUPS 4 8 12 16 20 22 24 26 28 31 35 39 41 $
44 47 50 53 56 59 62 65 67 69 71 73 75 77 79 $
81 83 85 87 89 * 33 groups
```

```
*
SUPPRESS 1 1 1 1 1  1 1 1 1 1  1 1 1 -1 1 -1
*
Water    Coolant  0.8189  561.66 CO         $
         DD2O=99.11
Water    Coolant2  0.8189  561.66 CO         $
         DD2O=99.11
Water    Water1  0  339.16 MO               $
         DD2O=99.97
Material Boron 1.08699 339.16 MO            $
         b10=198.255                        $
         b11=889.899
Mixture Moder Water1 1 Boron 0 339.16 MO    $
* md=1.08579
noburn moder
*
MATERIAL PT 6.5500  530.00 MO               $
         NB93=2.58                          $
         FE54=0.00266589864                 $
         FE56=0.042976786                   $
         FE57=0.00100160658                 $
         FE58=0.000135886544                $
         CR50=0.000337568856                $
         CR52=0.006769656                   $
         CR53=0.000782319888                $
         CR54=0.000198430992                $
         NI58=0.002481955                   $
         NI60=0.00098154                    $
         NI64=3.6505e-05                    $
         ZR90=49.344300082                  $
         ZR91=10.880521806                  $
         ZR92=16.813671028                  $
         ZR94=17.410197266                  $
         ZR96=2.8645910062                  $
         B10=.00002431
*
MATERIAL Gap 0.001293 350.00 MO             $
         C=27.11                            $
         O16=72.89
* CO2 in gap
MATERIAL CT 6.5500 330.00  MO               $
         FE54=0.00769338                    $
         FE56=0.1240245                     $
         FE57=0.002890485                   $
         FE58=0.000392148                   $
         NI58=0.03900215                    $
         NI60=0.0154242                     $
         NI64=0.00057365                    $
         CR50=0.0041737                     $
         CR52=0.0837                        $
         CR53=0.0096726                     $
         CR54=0.0024534                     $
         ZR90=49.798482681                  $
```

```
         ZR91=10.980670023                  $
         ZR92=16.968430074                  $
         ZR94=17.570446953                  $
         ZR96=2.8909577271                  $
         B10=.00005962
*
* Format 2 is used where relative weight
* fractions are specified for materials
MATERIAL Fuel1 10.6630 1200.00 FU           $
         O16=13.439472                     $
         U234=0.005408                     $
         U235=0.710971                     $
         U238=99.283620                     $
         TH232=0.000000                    $
*
MATERIAL Fuel2 = Fuel1
MATERIAL Fuel3 = Fuel1
MATERIAL Fuel4 = Fuel1
*
MATERIAL Clad 6.5500  600.00  CL            $
         ZR90=49.784791791                  $
         ZR91=10.977651153                  $
         ZR92=16.963765014                  $
         ZR94=17.565616383                  $
         ZR96=2.8901629281                  $
         FE54=0.01196748                    $
         FE56=0.192927                      $
         FE57=0.00449631                    $
         FE58=0.000610008                   $
         CR50=0.0041737                     $
         CR52=0.0837                        $
         CR53=0.0096726                     $
         CR54=0.0024534                     $
         NI58=0.00496391                    $
         NI60=0.00196308                    $
         NI64=7.301e-05                     $
         B10=.00005962
Mixture Endreg Clad=0.3774 Coolant=0.5480 561.66 -Cool
* cd=0.810
*
MATERIAL Clad1 6.39180 600.00  CL           $
         ZR90=49.78490820950                $
         ZR91=10.97767682352                $
         ZR92=16.963804682662                $
         ZR94=17.565657459052                $
         ZR96=2.890169686558                $
         FE54=0.011967507985                $
         FE56=0.192927451147                $
         FE57=0.004496320514                $
         FE58=0.000610009426                $
         CR50=0.004173709760                $
         CR52=0.083700195727                $
         CR53=0.009672622619                $
```

```
         CR54=0.002453405737                $
         NI58=0.004963921608                $
         NI60=0.001963084590                $
         NI64=0.000073010171                $
         B10=0.000059620140                $
         B11=0.000000000000                $
         EU151=0.000000000                $
         EU153=0.000000000                $
         GD152=0.000000000                $
         GD154=0.000000000                $
         GD155=0.000000000                $
         GD156=0.000000000                $
         GD157=0.000000000                $
         GD158=0.000000000                $
         GD160=0.000000000                $
         SM144=0.000000000                $
         SM147=0.000000000                $
         SM148=0.000000000                $
         SM149=0.000000000                $
         SM150=0.000000000                $
         SM152=0.000000000                $
         SM154=0.000000000                $
         O16=0.000000000                $
* Clad1 is the variable clad layer where neutron absorbers will be
inserted later
*
Begin
*
Benoist
Buckling 1.0e-4 1.0e-4
Beeone 1
Leakage -6
* note that last value should equal coolant annulus number to uncrept
P.T. I.R.
ENDcap endreg .0289473 -1 1.152 14
Print -2 -2 1 1   1 0
Reaction u235=0 u238=0 pu239=0 pu241=0 i135=0 xe135=0 NP239=0 Pu240=0
Pu241=0 Pu242=0 I135=0 SM149=0
Partition 65 89 * 2 groups
CELLAV
*
Material 0
Begin
Power 8 -1 0.2 1
begin
begin
Power 8 -1 0.25 1
begin
begin
Power 8 -1 0.4 1
begin
begin
Power 8 -1 0.6 1
```

```
begin
begin
Power 8 -1 1 1
begin
begin
Power 8 -1 2 1
begin
begin
Power 8 -1 2 2
begin
begin
Power 8 -1 2 3
begin
begin
Power 8 -1 2 4
Begin
Begin
Power 8 -1 2 4
Begin
Begin
Power 8 -1 3 3
Begin
Begin
Power 8 -1 4 3
Begin
Begin
Power 8 -1 4 4
Begin
Begin
Power 8 -1 4 5
Begin
Begin
Power 8 -1 4 5
Begin
Begin
Power 8 -1 4 5
Begin
Begin
Power 8 -1 4 5
Begin
Begin
Power 8 -1 4 5
Begin
Begin
Power 8 -1 4 5
Begin
Begin
Power 8 -1 4 5
Begin
Begin
Power 8 -1 4 5
Begin
Begin
```

```
Power 8 -1 4 5
Begin
Begin
Power 8 -1 4 5
Begin
Begin
Power 8 -1 4 5
Begin
Begin
Power 8 -1 4 5
Begin
Begin
Power 8 -1 4 5
Begin
Begin
Power 8 -1 4 5
Begin
Begin
Power 8 -1 4 5
Begin
Begin
Power 8 -1 4 5
Begin
Begin
Power 8 -1 4 5
Begin
Begin
Power 8 -1 4 5
Begin
Begin
Power 8 -1 4 5
Begin
Begin
Power 8 -1 4 5
Begin
Begin
Power 8 -1 4 5
Begin
Begin
Power 8 -1 4 5
Begin
Begin
Power 8 -1 4 5
Begin
Begin
Power 8 -1 4 5
Begin
```

```
Begin
Power 8 -1 4 5
Begin
Begin
Power 8 -1 4 5
Begin
Begin
Power 8 -1 4 5
Begin
Begin
@end
@microburn wimsutilinput temp1
@end
@condens temp1 temp2
21 33
@end
@wrfsp temp2
boc
lcell 49.53
vcell 40442.76
reference
xenon LIB7
twoGroup
@end
```

-

Appendix B

ELESTRES Input File

```
-----------------------------------------------------------------------------------------------------------
-
ELESTRES-IST 1.2.0.1
* (has to start with ELESTRES-IST 1.2.0.1)
   8   2
* (Inp #8, num of info records following present record, case ID #, blank)
*Reference Input Template
*Prepared by Jason Jaeho Song
   1  30   12.230    0.175        1        0   10.450      0.0    484.0
* (Inp #1, # of pell, pell OD, dish depth, land width, cent hole dia, pell density, porosity fract, stack length)
   2  37     0.12    0.050    0.390   911.20        0        0      0.8
* (Inp #2, # elem, axi clear, diam clear, sheat wall thic, fill gas vol, plenum void, transduc cavity, He vol frac)
   3   0
* (Inp #3, sheat mat code, sheat Youngs Mod, blank, sheat coeff therm exp, sheat therme cond, blank)
   4   1              50.0      0.5      0.8
* (Inp #4, has CANLUB?, blank, film heat tx coef btw sheat n cool, sheat inside surf rough, pell surf rough,
blank)
   5   0    560.0    10.00                    5.0     0.71
* (Inp #5, distr of axi clear btwn stack n endcap, cool temp, cool pres, neutr invers diff length, therm to fiss pwr
*  ratio, pellet grain siz, U235 enrich, diffusion coeff multiplier)
* (Inp #6 is NOT USED)
   7
* (Inp #7, total # of circum groovs, groov width, groov depth, flux detector dia, blank)
   9   1    -20.0
* (Inp #9, output option indicator, Y-th calculation indication, further values of Y-th calc for printing)
  11   2    0.004    0.650    0.144    400.0
* (Inp #11, num dishes per pellet, axi clear length btw adj pell, pell chamf dept, pell chamf lengt, sheat axi
*  yield str, ramp time or ramp rate)
  10  20
* (Inp #10, total # of pwr history, scaling factor elem lin power, blank)
            55.0       10
            55.0       20
            55.0       30
            55.0       40
            55.0       50
            55.0       60
            55.0       70
            55.0       80
            55.0       90
            55.0      100
            55.0      110
            55.0      120
            55.0      130
            55.0      140
            55.0      150
            55.0      160
            55.0      170
            55.0      180
            55.0      190
            55.0      200
```

0
* (blank, trigger option to store, element lin pwr, burnup at lin pwr step, cool temp, cool press, sheat to cool
* heat tx coeff, plenum void, ramp rate or ramp time)

-

ELESTRES TAPE4 Output File

-

CREATED 2020/01/16 at 03:37:37.6 FOR CASE:*Reference Input Template

BURNUP	POWER	PRES	PSTYS(1)	STEYS(1)	PSTYS(NAX)	STEYS(NAX)	TCC	TSC	HTCOUTTGO	PERGS	GAP(1)
6.69E-05	1.74E+01	3.66E-01	-2.20E-03	-1.83E-01	-2.20E-03	-1.83E-01	6.08E+02	3.15E+02	4.98E+01	0.00E+00	0.00E+00	1.59E-02
1.07E-03	1.74E+01	3.66E-01	-5.20E-03	-1.83E-01	-5.20E-03	-1.83E-01	6.08E+02	3.15E+02	5.13E+01	1.98E-09	2.76E-07	1.57E-02
1.51E-03	4.82E+01	6.27E-01	-5.41E-03	1.54E-01	-2.66E-03	6.41E-01	1.46E+03	3.57E+02	7.34E+01	1.98E-09	2.76E-07	0.00E+00
2.43E+01	4.82E+01	6.27E-01	8.84E-02	-1.81E-01	4.48E-01	-1.81E-01	1.41E+03	3.58E+02	6.91E+01	6.35E+01	3.89E-01	2.45E-03
2.43E+01	4.71E+01	5.66E-01	8.84E-02	-1.82E-01	4.48E-01	-1.82E-01	1.38E+03	3.58E+02	6.23E+01	6.35E+01	3.89E-01	5.61E-03
3.33E+01	4.71E+01	5.66E-01	1.44E-02	-1.82E-01	4.09E-01	-1.82E-01	1.38E+03	3.59E+02	6.16E+01	1.15E+02	5.13E-01	6.11E-03
3.33E+01	4.83E+01	5.85E-01	1.44E-02	-1.82E-01	4.09E-01	-1.82E-01	1.42E+03	3.61E+02	6.01E+01	1.15E+02	5.13E-01	4.54E-03
4.24E+01	4.83E+01	5.85E-01	-4.09E-02	-1.81E-01	3.70E-01	-1.81E-01	1.41E+03	3.61E+02	6.00E+01	2.10E+02	7.39E-01	2.11E-03
4.24E+01	4.96E+01	6.67E-01	-4.09E-02	-1.53E-01	3.70E-01	-1.81E-01	1.45E+03	3.63E+02	5.93E+01	2.10E+02	7.39E-01	0.00E+00
5.16E+01	4.96E+01	6.67E-01	-5.96E-02	-8.23E-02	3.44E-01	-1.21E-01	1.45E+03	3.63E+02	5.94E+01	3.90E+02	1.13E+00	0.00E+00
5.16E+01	4.85E+01	6.78E-01	-5.96E-02	-1.10E-01	3.44E-01	-1.64E-01	1.42E+03	3.64E+02	5.37E+01	3.90E+02	1.13E+00	0.00E+00
6.08E+01	4.85E+01	6.78E-01	-7.74E-02	-8.01E-02	3.20E-01	-1.15E-01	1.41E+03	3.64E+02	5.36E+01	5.12E+02	1.26E+00	0.00E+00
6.08E+01	4.86E+01	7.05E-01	-7.74E-02	-7.60E-02	3.20E-01	-1.08E-01	1.42E+03	3.65E+02	5.05E+01	5.12E+02	1.26E+00	0.00E+00
7.00E+01	4.86E+01	7.05E-01	-9.06E-02	-6.26E-02	3.03E-01	-8.10E-02	1.41E+03	3.65E+02	5.06E+01	6.43E+02	1.37E+00	0.00E+00
7.00E+01	4.90E+01	7.46E-01	-9.06E-02	-5.10E-02	3.03E-01	-6.25E-02	1.43E+03	3.68E+02	4.76E+01	6.43E+02	1.37E+00	0.00E+00
7.91E+01	4.90E+01	7.46E-01	-9.96E-02	-4.46E-02	2.94E-01	-4.64E-02	1.42E+03	3.68E+02	4.76E+01	8.01E+02	1.51E+00	0.00E+00
7.91E+01	4.66E+01	7.79E-01	-9.96E-02	-9.70E-02	2.94E-01	-1.26E-01	1.35E+03	3.66E+02	4.34E+01	8.01E+02	1.51E+00	0.00E+00
8.81E+01	4.66E+01	7.79E-01	-1.10E-01	-5.11E-02	2.83E-01	-5.64E-02	1.34E+03	3.66E+02	4.32E+01	8.58E+02	1.45E+00	0.00E+00
8.81E+01	4.59E+01	7.82E-01	-1.10E-01	-6.53E-02	2.83E-01	-7.78E-02	1.32E+03	3.66E+02	4.25E+01	8.58E+02	1.45E+00	0.00E+00
9.69E+01	4.59E+01	7.82E-01	-1.19E-01	-4.62E-02	2.74E-01	-4.61E-02	1.32E+03	3.66E+02	4.25E+01	8.99E+02	1.38E+00	0.00E+00
9.69E+01	4.66E+01	8.01E-01	-1.19E-01	-3.01E-02	2.74E-01	-2.21E-02	1.34E+03	3.67E+02	4.23E+01	8.99E+02	1.38E+00	0.00E+00
1.06E+02	4.66E+01	8.01E-01	-1.24E-01	-2.79E-02	2.70E-01	-1.93E-02	1.33E+03	3.67E+02	4.23E+01	9.54E+02	1.35E+00	0.00E+00
1.06E+02	4.55E+01	8.15E-01	-1.24E-01	-5.24E-02	2.70E-01	-5.68E-02	1.30E+03	3.66E+02	4.10E+01	9.54E+02	1.35E+00	0.00E+00
1.14E+02	4.55E+01	8.15E-01	-1.30E-01	-3.40E-02	2.65E-01	-2.89E-02	1.30E+03	3.66E+02	4.10E+01	9.89E+02	1.29E+00	0.00E+00
1.14E+02	3.47E+01	7.00E-01	-1.30E-01	-1.25E-01	2.65E-01	-1.65E-01	9.86E+02	3.49E+02	3.76E+01	9.89E+02	1.29E+00	0.00E+00
1.22E+02	3.47E+01	7.00E-01	-1.45E-01	-8.73E-02	2.48E-01	-1.06E-01	9.85E+02	3.49E+02	3.76E+01	1.01E+03	1.24E+00	0.00E+00
1.22E+02	3.47E+01	7.02E-01	-1.45E-01	-9.54E-02	2.48E-01	-1.18E-01	9.85E+02	3.49E+02	3.80E+01	1.01E+03	1.24E+00	0.00E+00
1.29E+02	3.47E+01	7.02E-01	-1.57E-01	-8.51E-02	2.34E-01	-1.03E-01	9.84E+02	3.49E+02	3.81E+01	1.02E+03	1.18E+00	0.00E+00
1.29E+02	3.54E+01	7.13E-01	-1.57E-01	-7.89E-02	2.34E-01	-9.42E-02	1.00E+03	3.50E+02	3.84E+01	1.02E+03	1.18E+00	0.00E+00
1.35E+02	3.54E+01	7.13E-01	-1.69E-01	-8.11E-02	2.21E-01	-9.71E-02	1.00E+03	3.50E+02	3.84E+01	1.02E+03	1.12E+00	0.00E+00
1.35E+02	3.58E+01	7.26E-01	-1.69E-01	-7.84E-02	2.21E-01	-9.35E-02	1.01E+03	3.51E+02	3.84E+01	1.02E+03	1.12E+00	0.00E+00
1.42E+02	3.58E+01	7.26E-01	-1.80E-01	-7.83E-02	2.08E-01	-9.13E-02	1.01E+03	3.51E+02	3.85E+01	1.02E+03	1.07E+00	0.00E+00
1.42E+02	3.56E+01	7.33E-01	-1.80E-01	-8.58E-02	2.08E-01	-1.03E-01	1.01E+03	3.50E+02	3.83E+01	1.02E+03	1.07E+00	0.00E+00
1.49E+02	3.56E+01	7.33E-01	-1.91E-01	-7.72E-02	1.96E-01	-8.82E-02	1.01E+03	3.50E+02	3.83E+01	1.02E+03	1.03E+00	0.00E+00
1.49E+02	3.41E+01	7.26E-01	-1.91E-01	-1.09E-01	1.96E-01	-1.36E-01	9.67E+02	3.48E+02	3.78E+01	1.02E+03	1.03E+00	0.00E+00
1.55E+02	3.41E+01	7.26E-01	-2.02E-01	-7.96E-02	1.84E-01	-8.91E-02	9.66E+02	3.48E+02	3.77E+01	1.03E+03	9.85E-01	0.00E+00
1.55E+02	3.43E+01	7.28E-01	-2.02E-01	-8.33E-02	1.84E-01	-9.51E-02	9.72E+02	3.48E+02	3.82E+01	1.03E+03	9.85E-01	0.00E+00
1.62E+02	3.43E+01	7.28E-01	-2.13E-01	-8.02E-02	1.72E-01	-9.16E-02	9.70E+02	3.48E+02	3.82E+01	1.03E+03	9.49E-01	0.00E+00
1.62E+02	3.30E+01	7.24E-01	-2.13E-01	-1.07E-01	1.72E-01	-1.32E-01	9.38E+02	3.46E+02	3.77E+01	1.03E+03	9.49E-01	0.00E+00
1.68E+02	3.30E+01	7.24E-01	-2.24E-01	-8.27E-02	1.61E-01	-9.28E-02	9.37E+02	3.46E+02	3.76E+01	1.03E+03	9.15E-01	0.00E+00
1.68E+02	1.00E-06	1.35E-01	-2.24E-01	5.24E-04	1.61E-01	5.24E-04	2.00E+01	2.00E+01	1.90E+01	1.03E+03	9.15E-01	3.79E-02
1.68E+02	1.00E-06	1.35E-01	-2.24E-01	5.04E-04	1.61E-01	5.04E-04	2.00E+01	2.00E+01	1.85E+01	1.03E+03	9.15E-01	3.92E-02

SSTC	TVD	ORP(NAX)	ORP(1)	GRSSC	GRSSG	(TSTM+THE)	(TSTE+THE)	RADP	AXDP	AVTEMPC	TSTE	TSTM
3.06E+02	1.64E+00	6.14E+00	6.14E+00	0.00E+00	0.00E+00	7.57E-03	7.57E-03	3.49E+01	3.14E+01	4.60E+02	-1.85E-01	-1.85E-01
3.06E+02	1.63E+00	6.14E+00	6.14E+00	4.29E-11	9.39E-12	4.59E-03	4.59E-03	3.49E+01	3.14E+01	4.60E+02	-1.88E-01	-1.88E-01
3.40E+02	9.63E-01	6.20E+00	6.17E+00	4.28E-11	9.38E-12	3.64E-01	8.54E-01	9.77E+01	4.44E+01	8.44E+02	6.39E-01	1.48E-01
3.40E+02	9.88E-01	6.18E+00	6.16E+00	1.38E+00	3.02E-01	1.23E-01	4.82E-01	7.46E+01	3.55E+01	8.27E+02	2.67E-01	-9.25E-02
3.39E+02	1.10E+00	6.17E+00	6.15E+00	1.38E+00	3.02E-01	1.21E-01	4.80E-01	6.95E+01	3.37E+01	8.16E+02	2.65E-01	-9.37E-02
3.39E+02	1.17E+00	6.17E+00	6.15E+00	2.49E+00	5.45E-01	4.63E-02	4.41E-01	6.34E+01	2.95E+01	8.14E+02	2.26E-01	-1.68E-01
3.40E+02	1.10E+00	6.17E+00	6.15E+00	2.49E+00	5.45E-01	4.77E-02	4.42E-01	6.58E+01	3.07E+01	8.31E+02	2.27E-01	-1.68E-01
3.40E+02	1.09E+00	6.17E+00	6.15E+00	4.56E+00	1.00E+00	-6.86E-03	4.04E-01	6.40E+01	2.76E+01	8.29E+02	1.89E-01	-2.22E-01
3.41E+02	1.02E+00	6.18E+00	6.15E+00	4.56E+00	9.99E-01	2.19E-02	4.06E-01	6.95E+01	2.90E+01	8.47E+02	1.90E-01	-1.94E-01
3.41E+02	1.09E+00	6.18E+00	6.16E+00	8.45E+00	1.85E+00	7.43E-02	4.39E-01	7.20E+01	2.72E+01	8.46E+02	2.23E-01	-1.42E-01
3.40E+02	1.10E+00	6.17E+00	6.15E+00	8.45E+00	1.85E+00	4.58E-02	3.96E-01	6.94E+01	2.61E+01	8.32E+02	1.80E-01	-1.70E-01
3.40E+02	1.13E+00	6.18E+00	6.15E+00	1.11E+01	2.43E+00	5.79E-02	4.20E-01	7.09E+01	2.54E+01	8.30E+02	2.05E-01	-1.57E-01

3.40E+02	1.13E+00	6.18E+00	6.15E+00	1.11E+01	2.43E+00	6.20E-02	4.27E-01	7.13E+01	2.56E+01	8.33E+02	2.11E-01	-1.53E-01
3.40E+02	1.14E+00	6.18E+00	6.15E+00	1.39E+01	3.06E+00	6.22E-02	4.37E-01	7.19E+01	2.52E+01	8.31E+02	2.22E-01	-1.53E-01
3.41E+02	1.13E+00	6.18E+00	6.16E+00	1.39E+01	3.06E+00	7.41E-02	4.56E-01	7.31E+01	2.58E+01	8.39E+02	2.40E-01	-1.42E-01
3.41E+02	1.13E+00	6.18E+00	6.15E+00	1.74E+01	3.80E+00	7.15E-02	4.63E-01	7.35E+01	2.58E+01	8.37E+02	2.47E-01	-1.44E-01
3.38E+02	1.16E+00	6.17E+00	6.15E+00	1.74E+01	3.80E+00	1.73E-02	3.81E-01	6.85E+01	2.35E+01	8.05E+02	1.67E-01	-1.97E-01
3.38E+02	1.17E+00	6.18E+00	6.15E+00	1.86E+01	4.08E+00	5.30E-02	4.40E-01	7.21E+01	2.44E+01	8.03E+02	2.26E-01	-1.61E-01
3.37E+02	1.18E+00	6.18E+00	6.15E+00	1.86E+01	4.08E+00	3.83E-02	4.18E-01	7.08E+01	2.38E+01	7.94E+02	2.05E-01	-1.75E-01
3.37E+02	1.18E+00	6.18E+00	6.15E+00	1.95E+01	4.27E+00	4.86E-02	4.41E-01	7.22E+01	2.45E+01	7.92E+02	2.28E-01	-1.65E-01
3.38E+02	1.17E+00	6.18E+00	6.15E+00	1.95E+01	4.27E+00	6.52E-02	4.66E-01	7.37E+01	2.52E+01	8.02E+02	2.52E-01	-1.49E-01
3.38E+02	1.16E+00	6.18E+00	6.15E+00	2.07E+01	4.53E+00	6.22E-02	4.65E-01	7.37E+01	2.58E+01	8.01E+02	2.51E-01	-1.52E-01
3.37E+02	1.18E+00	6.18E+00	6.15E+00	2.07E+01	4.53E+00	3.69E-02	4.27E-01	7.13E+01	2.48E+01	7.86E+02	2.14E-01	-1.76E-01
3.37E+02	1.17E+00	6.18E+00	6.15E+00	2.14E+01	4.70E+00	4.89E-02	4.49E-01	7.27E+01	2.57E+01	7.85E+02	2.36E-01	-1.64E-01
3.25E+02	1.39E+00	6.17E+00	6.15E+00	2.14E+01	4.70E+00	-5.05E-02	3.05E-01	6.38E+01	1.81E+01	6.46E+02	1.00E-01	-2.56E-01
3.25E+02	1.40E+00	6.17E+00	6.15E+00	2.20E+01	4.81E+00	-2.69E-02	3.48E-01	6.64E+01	1.86E+01	6.45E+02	1.42E-01	-2.32E-01
3.25E+02	1.40E+00	6.17E+00	6.15E+00	2.20E+01	4.81E+00	-3.50E-02	3.36E-01	6.57E+01	1.85E+01	6.45E+02	1.30E-01	-2.40E-01
3.25E+02	1.39E+00	6.17E+00	6.15E+00	2.20E+01	4.82E+00	-3.70E-02	3.36E-01	6.57E+01	1.88E+01	6.45E+02	1.31E-01	-2.42E-01
3.26E+02	1.37E+00	6.17E+00	6.15E+00	2.20E+01	4.82E+00	-3.02E-02	3.46E-01	6.63E+01	1.93E+01	6.53E+02	1.40E-01	-2.36E-01
3.26E+02	1.36E+00	6.17E+00	6.15E+00	2.21E+01	4.83E+00	-4.43E-02	3.29E-01	6.53E+01	1.96E+01	6.53E+02	1.23E-01	-2.50E-01
3.26E+02	1.35E+00	6.17E+00	6.15E+00	2.21E+01	4.83E+00	-4.13E-02	3.33E-01	6.55E+01	1.98E+01	6.58E+02	1.27E-01	-2.47E-01
3.26E+02	1.34E+00	6.17E+00	6.15E+00	2.21E+01	4.85E+00	-5.22E-02	3.23E-01	6.49E+01	2.01E+01	6.57E+02	1.17E-01	-2.58E-01
3.26E+02	1.34E+00	6.17E+00	6.15E+00	2.21E+01	4.85E+00	-5.99E-02	3.11E-01	6.42E+01	1.99E+01	6.55E+02	1.05E-01	-2.66E-01
3.26E+02	1.33E+00	6.17E+00	6.15E+00	2.22E+01	4.86E+00	-6.23E-02	3.14E-01	6.43E+01	2.02E+01	6.55E+02	1.08E-01	-2.68E-01
3.25E+02	1.35E+00	6.17E+00	6.14E+00	2.22E+01	4.86E+00	-9.48E-02	2.65E-01	6.13E+01	1.90E+01	6.37E+02	6.06E-02	-3.00E-01
3.25E+02	1.36E+00	6.17E+00	6.15E+00	2.23E+01	4.88E+00	-7.67E-02	3.00E-01	6.35E+01	1.95E+01	6.37E+02	9.53E-02	-2.82E-01
3.25E+02	1.35E+00	6.17E+00	6.15E+00	2.23E+01	4.88E+00	-8.02E-02	2.94E-01	6.31E+01	1.96E+01	6.39E+02	8.93E-02	-2.85E-01
3.25E+02	1.34E+00	6.17E+00	6.15E+00	2.23E+01	4.89E+00	-8.80E-02	2.86E-01	6.26E+01	1.99E+01	6.39E+02	8.08E-02	-2.93E-01
3.23E+02	1.36E+00	6.17E+00	6.14E+00	2.23E+01	4.89E+00	-1.16E-01	2.44E-01	6.00E+01	1.88E+01	6.24E+02	4.00E-02	-3.20E-01
3.23E+02	1.37E+00	6.17E+00	6.14E+00	2.24E+01	4.91E+00	-1.03E-01	2.72E-01	6.17E+01	1.92E+01	6.24E+02	6.77E-02	-3.07E-01
2.00E+01	7.26E+00	6.11E+00	6.10E+00	2.24E+01	4.92E+00	-2.23E-01	1.61E-01	1.23E+00	-2.25E+01	2.00E+01	1.61E-01	-2.23E-01
2.00E+01	7.33E+00	6.10E+00	6.10E+00	2.24E+01	4.92E+00	-2.23E-01	1.61E-01	-1.28E+00	-2.28E+01	2.00E+01	1.61E-01	-2.23E-01

BURNUP = Element Burnup (MW.h/kg U)
POWER = Element Linear Power (kW/m)
PRES = Internal Gas Pressure (MPa)
PSTYS(1) = Plastic Hoop Strain at the Pellet Midplane Location (%)
STEYS(1) = Elastic Hoop Strain at the Pellet Midplane Location (%)
PSTYS(NAX) = Plastic Hoop Strain at the Pellet End (circumferential ridge) Location (%)
STEYS(NAX) = Elastic Hoop Strain at the Pellet End (circumferential ridge) Location (%)
TCC = Fuel Pellet Centre Temperature (C)
TSC = Fuel Pellet Surface Temperature (C)
HTCOUT = Pellet-Sheath Heat Transfer Coeff.(kW/m2K)
TGO = Fission Gas Release Volume (cm3)
PERGS = Percent Fission Gas Release (%)
GAP(1) = Radial Gap (mm)
SSTC = Sheath Temperature at the Inside Surface (C)
TVD = Total Internal Free Voidage (mm3/K)

ORP(NAX) = Fuel Radius at Pellet End (Ridge) (mm)
ORP(1) = Fuel Radius at the Pellet Midplane (mm)
GRSSC = Fission Gas Release Concentration at the Sheath Inside Surface (P.atoms/mm2)
GRSSG = Fission Gas Release Concentration at the Sheath Inside Surface (ug/mm2)
(TSTM+THE) = Total Sheath Hoop Strain at the Pellet Midplane Location (%)
(TSTE+THE) = Total Sheath Hoop Strain at the Pellet End Location (%)
AXDP = Pellet Axial Displacement at the Ridge (um)

RADP = Pellet Radial Displacement at the Ridge (um)
AVTEMC = Fuel Pellet Volume-Average Temperature (C)
TSTE = Mechanical Sheath Hoop Strain at the Pellet
End Location (%)
TSTM = Mechanical Sheath Hoop Strain at the Pellet
Midplane Location (%)

-

Appendix C

ELOCA Input File

```
----------------------------------------------------------------------------------------------------------------
-
MK4S (coolant history will be read from this .inp file)
   1                                    (Group 2)
   1.0000              1                (Group 3)
                                        (Group 4)
STANDARD 37-ELEMENT FUEL OUTER ELEMENT: 80% ROH BREAK (ex3_1_f_td_ist) (Group 5)
 0 0 3 0 0 5 0 0 0       1.0      2.0          (Group 6)
 0 0-2   0    1.e-6      1.0     1.00 1        (Group 7)
FROM_DATA                           (Start of FROM_SFD Oxidation Model Options)
COMP_OUT      1.0E+0
SMOOTH
LIMIT_O2
BREAKAWAY
LIMIT_INERT
END_MODELS                          (End of FROM_SFD Oxidation Model Options)
       1   0.5E-06  0.50E-06    1.0E-6  2.3E-03(Initial thickness of each FROM region)
END_FROM
   0.0000   10.0000    560.00   50.0000 100000.0        1      (Group 8 – coolant data vs. time)
   1.0039    9.6793    584.82    1.7672 100000.0        1
   2.0205    9.3334    708.91    0.4539 100000.0        1
   3.0371    8.4875    890.42    0.2576 100000.0        1
   4.0731    7.6413   1016.43    0.4512 100000.0        1
   5.1114    6.7950   1026.43    0.6563 100000.0        1
   6.1325    5.9500   1038.93    0.7659 100000.0        1
   7.1543    5.7000   1058.42    0.6250 100000.0        1
   8.1842    5.4500   1078.98    0.3211 100000.0        1
   9.1932    5.2000   1087.87    0.5606 100000.0        1
  10.2041    5.0500   1081.76    0.7407 100000.0        1
  12.2654    4.6250   1094.11    0.4443 100000.0        1
  14.4540    4.2000   1080.22    0.3813 100000.0        1
  16.5221    3.7750   1032.49    0.9883 100000.0        1
  18.0635    3.3500    998.55    1.5089 100000.0        1
  20.1156    2.7167   1148.22    2.1619 100000.0        1
  22.1540    2.0833   1135.67    1.9604 100000.0        1
  24.2026    1.4500   1150.22    1.5430 100000.0        1
  26.2208    1.4666   1191.56    1.2806 100000.0        1
  28.2331    1.4833    925.78    0.0866 100000.0        1
  30.2402    1.5000   1101.11    0.6132 100000.0        1
  32.2504    1.4967    899.11    0.2134 100000.0        1
  34.2583    1.4939   1013.56    0.9645 100000.0        1
  36.2619    1.4900   1023.56    0.4701 100000.0        1
  38.2648    1.4629   1018.15    0.8775 100000.0        1
  40.2701    1.4357    999.11    1.0649 100000.0        1
  42.2848    1.4085    952.43    1.8052 100000.0        1
  44.2950    1.3814    843.16    2.0170 100000.0        1
  46.3050    1.3543    712.91    1.9614 100000.0        1
  48.3189    1.3271    648.97    1.8976 100000.0        1
  49.8259    1.3000    633.71    1.6697 100000.0        1
```

0.00	1.00	0.93	(power multiple factor vs. time)
0.20	1.00	0.93	
0.40	1.02	0.931	
0.60	1.10	1.023	
0.80	1.16	1.079	
1.00	1.23	1.144	
1.20	1.40	1.302	
1.40	1.68	1.562	
1.60	1.90	1.767	
1.70	1.93	1.795	
1.80	1.30	1.209	
2.00	1.30	1.209	
2.50	0.30	0.279	
3.00	0.150	0.14	
4.00	0.130	0.12	
6.00	0.100	0.09	
8.00	0.090	0.075	
10.00	0.080	0.065	
20.00	0.064	0.05	
40.00	0.052	0.04	
60.00	0.046	0.035	

-

ELOCA mod_ex3_1_f_td_ist (80% ROH example) Output File

-

TIME (s)	SEGMT	PWCX (MPa)	TCOOL (K)	HSC (W/m2.K)	PNORM	CFT (K)	AFT (K)	SFT (K)	TSH (K)	VOVT (m3/K)	HRTE (K/s)	PGAS (MPa)
0.00E+00	1	1.00E+01	5.60E+02	5.00E+04	1.00E+00	1.58E+03	1.06E+03	6.35E+02	5.97E+02	6.87E-10	0.00E+00	9.23E-01
4.25E-01	1	9.86E+00	5.71E+02	1.21E+04	1.03E+00	1.59E+03	1.06E+03	6.69E+02	6.41E+02	6.44E-10	1.54E+02	9.84E-01
8.50E-01	1	9.73E+00	5.81E+02	2.95E+03	1.18E+00	1.59E+03	1.09E+03	7.41E+02	7.23E+02	6.15E-10	2.69E+02	1.03E+00
1.28E+00	1	9.59E+00	6.18E+02	1.23E+03	1.50E+00	1.60E+03	1.13E+03	8.31E+02	8.20E+02	5.64E-10	2.24E+02	1.12E+00
1.70E+00	1	9.44E+00	6.70E+02	6.97E+02	1.93E+00	1.63E+03	1.20E+03	9.31E+02	9.21E+02	4.94E-10	2.50E+02	1.28E+00
2.13E+00	1	9.25E+00	7.28E+02	4.28E+02	9.01E-01	1.65E+03	1.24E+03	1.01E+03	1.01E+03	4.56E-10	1.61E+02	1.39E+00
2.55E+00	1	8.89E+00	8.03E+02	3.38E+02	2.80E-01	1.63E+03	1.26E+03	1.06E+03	1.06E+03	4.43E-10	8.76E+01	1.43E+00
2.98E+00	1	8.54E+00	8.79E+02	2.67E+02	1.55E-01	1.61E+03	1.26E+03	1.09E+03	1.09E+03	4.35E-10	6.67E+01	1.46E+00
3.40E+00	1	8.19E+00	9.35E+02	3.13E+02	1.42E-01	1.58E+03	1.27E+03	1.11E+03	1.11E+03	4.29E-10	4.93E+01	1.48E+00
3.83E+00	1	7.84E+00	9.86E+02	3.95E+02	1.33E-01	1.55E+03	1.27E+03	1.13E+03	1.13E+03	4.42E-10	1.88E+00	1.43E+00
4.25E+00	1	7.50E+00	1.02E+03	4.81E+02	1.26E-01	1.52E+03	1.27E+03	1.15E+03	1.15E+03	4.61E-10	3.11E+01	1.38E+00
4.68E+00	1	7.15E+00	1.02E+03	5.61E+02	1.19E-01	1.50E+03	1.27E+03	1.16E+03	1.16E+03	4.76E-10	1.18E+01	1.33E+00
5.10E+00	1	6.80E+00	1.03E+03	6.54E+02	1.13E-01	1.48E+03	1.28E+03	1.17E+03	1.17E+03	4.89E-10	1.94E+01	1.30E+00
5.53E+00	1	6.45E+00	1.03E+03	6.99E+02	1.06E-01	1.46E+03	1.28E+03	1.18E+03	1.17E+03	5.01E-10	1.82E+01	1.27E+00
5.95E+00	1	6.10E+00	1.04E+03	7.45E+02	1.01E-01	1.44E+03	1.28E+03	1.18E+03	1.18E+03	5.09E-10	1.06E+01	1.25E+00
6.38E+00	1	5.89E+00	1.04E+03	7.30E+02	9.80E-02	1.43E+03	1.28E+03	1.19E+03	1.18E+03	5.17E-10	-6.99E+00	1.23E+00
6.80E+00	1	5.79E+00	1.05E+03	6.71E+02	9.59E-02	1.42E+03	1.28E+03	1.19E+03	1.19E+03	5.27E-10	1.83E+01	1.21E+00
7.23E+00	1	5.68E+00	1.06E+03	5.97E+02	9.38E-02	1.40E+03	1.28E+03	1.20E+03	1.20E+03	5.34E-10	1.54E+01	1.19E+00
7.65E+00	1	5.58E+00	1.07E+03	4.54E+02	9.17E-02	1.39E+03	1.28E+03	1.21E+03	1.20E+03	5.45E-10	2.20E+01	1.16E+00
8.08E+00	1	5.48E+00	1.08E+03	3.45E+02	8.96E-02	1.39E+03	1.28E+03	1.21E+03	1.21E+03	5.52E-10	-2.71E+01	1.15E+00
8.50E+00	1	5.37E+00	1.08E+03	3.82E+02	8.74E-02	1.38E+03	1.28E+03	1.22E+03	1.22E+03	5.61E-10	2.01E+01	1.13E+00
8.93E+00	1	5.27E+00	1.09E+03	4.83E+02	8.52E-02	1.37E+03	1.28E+03	1.23E+03	1.23E+03	5.67E-10	7.71E+00	1.12E+00
9.35E+00	1	5.18E+00	1.09E+03	5.85E+02	8.31E-02	1.36E+03	1.28E+03	1.23E+03	1.23E+03	5.71E-10	2.79E+00	1.11E+00
9.78E+00	1	5.11E+00	1.08E+03	6.58E+02	8.11E-02	1.36E+03	1.28E+03	1.23E+03	1.23E+03	5.71E-10	-6.09E-01	1.11E+00
1.02E+01	1	5.05E+00	1.08E+03	7.40E+02	7.96E-02	1.36E+03	1.28E+03	1.23E+03	1.23E+03	5.72E-10	-3.76E+00	1.11E+00
1.06E+01	1	4.96E+00	1.08E+03	6.67E+02	7.89E-02	1.35E+03	1.28E+03	1.23E+03	1.23E+03	5.73E-10	3.02E+00	1.11E+00
1.11E+01	1	4.88E+00	1.09E+03	6.01E+02	7.81E-02	1.35E+03	1.28E+03	1.23E+03	1.23E+03	5.76E-10	5.74E+00	1.10E+00
1.15E+01	1	4.79E+00	1.09E+03	5.40E+02	7.74E-02	1.35E+03	1.28E+03	1.23E+03	1.23E+03	5.80E-10	7.00E+00	1.10E+00
1.19E+01	1	4.70E+00	1.09E+03	4.86E+02	7.67E-02	1.34E+03	1.28E+03	1.24E+03	1.24E+03	5.82E-10	8.26E+00	1.09E+00
1.23E+01	1	4.61E+00	1.09E+03	4.42E+02	7.60E-02	1.34E+03	1.28E+03	1.24E+03	1.24E+03	5.86E-10	6.94E+00	1.08E+00
1.28E+01	1	4.53E+00	1.09E+03	4.30E+02	7.52E-02	1.34E+03	1.29E+03	1.24E+03	1.24E+03	5.88E-10	6.45E+00	1.08E+00
1.32E+01	1	4.45E+00	1.09E+03	4.17E+02	7.45E-02	1.34E+03	1.29E+03	1.25E+03	1.24E+03	5.91E-10	5.37E+00	1.07E+00
1.36E+01	1	4.37E+00	1.09E+03	4.05E+02	7.38E-02	1.34E+03	1.29E+03	1.25E+03	1.25E+03	5.92E-10	4.84E+00	1.07E+00
1.40E+01	1	4.28E+00	1.08E+03	3.93E+02	7.31E-02	1.33E+03	1.29E+03	1.25E+03	1.25E+03	5.94E-10	4.44E+00	1.07E+00
1.45E+01	1	4.20E+00	1.08E+03	3.81E+02	7.24E-02	1.33E+03	1.29E+03	1.25E+03	1.25E+03	5.95E-10	4.12E+00	1.07E+00
1.49E+01	1	4.11E+00	1.07E+03	4.63E+02	7.18E-02	1.33E+03	1.29E+03	1.25E+03	1.25E+03	5.95E-10	-3.76E+00	1.07E+00
1.53E+01	1	4.03E+00	1.06E+03	5.63E+02	7.11E-02	1.33E+03	1.29E+03	1.25E+03	1.25E+03	5.93E-10	-1.02E+01	1.07E+00
1.57E+01	1	3.94E+00	1.05E+03	6.85E+02	7.04E-02	1.33E+03	1.29E+03	1.24E+03	1.24E+03	5.89E-10	-1.70E+01	1.07E+00
1.62E+01	1	3.85E+00	1.04E+03	8.33E+02	6.97E-02	1.33E+03	1.29E+03	1.24E+03	1.23E+03	5.83E-10	-2.58E+01	1.09E+00
1.66E+01	1	3.76E+00	1.03E+03	1.00E+03	6.91E-02	1.33E+03	1.28E+03	1.22E+03	1.22E+03	5.76E-10	-2.89E+01	1.10E+00
1.70E+01	1	3.64E+00	1.02E+03	1.13E+03	6.84E-02	1.33E+03	1.28E+03	1.21E+03	1.21E+03	5.69E-10	-2.23E+01	1.11E+00
1.74E+01	1	3.53E+00	1.01E+03	1.27E+03	6.78E-02	1.33E+03	1.28E+03	1.20E+03	1.20E+03	5.61E-10	-3.28E+01	1.13E+00
1.79E+01	1	3.41E+00	1.00E+03	1.42E+03	6.71E-02	1.33E+03	1.27E+03	1.19E+03	1.18E+03	5.53E-10	-3.46E+01	1.15E+00
1.83E+01	1	3.28E+00	1.01E+03	1.57E+03	6.65E-02	1.33E+03	1.26E+03	1.18E+03	1.17E+03	5.47E-10	-1.52E+01	1.16E+00
1.87E+01	1	3.15E+00	1.04E+03	1.69E+03	6.59E-02	1.33E+03	1.26E+03	1.17E+03	1.17E+03	5.46E-10	-1.04E+01	1.16E+00
1.91E+01	1	3.02E+00	1.08E+03	1.82E+03	6.53E-02	1.33E+03	1.25E+03	1.17E+03	1.17E+03	5.50E-10	4.71E+00	1.16E+00
1.96E+01	1	2.89E+00	1.11E+03	1.96E+03	6.46E-02	1.33E+03	1.25E+03	1.17E+03	1.17E+03	5.57E-10	2.03E+01	1.14E+00
2.00E+01	1	2.76E+00	1.14E+03	2.11E+03	6.40E-02	1.32E+03	1.25E+03	1.18E+03	1.18E+03	5.66E-10	2.17E+01	1.12E+00
2.04E+01	1	2.63E+00	1.15E+03	2.13E+03	6.37E-02	1.32E+03	1.25E+03	1.19E+03	1.18E+03	5.75E-10	1.28E+01	1.10E+00
2.08E+01	1	2.50E+00	1.14E+03	2.09E+03	6.35E-02	1.32E+03	1.25E+03	1.19E+03	1.19E+03	5.80E-10	-4.13E+00	1.09E+00
2.13E+01	1	2.36E+00	1.14E+03	2.05E+03	6.32E-02	1.32E+03	1.25E+03	1.19E+03	1.19E+03	5.84E-10	6.42E+00	1.09E+00
2.17E+01	1	2.23E+00	1.14E+03	2.01E+03	6.29E-02	1.31E+03	1.25E+03	1.19E+03	1.19E+03	5.87E-10	6.15E-01	1.08E+00
2.21E+01	1	2.10E+00	1.14E+03	1.97E+03	6.26E-02	1.31E+03	1.24E+03	1.19E+03	1.19E+03	5.90E-10	-1.46E+00	1.08E+00
2.25E+01	1	1.97E+00	1.14E+03	1.88E+03	6.23E-02	1.31E+03	1.24E+03	1.19E+03	1.19E+03	5.93E-10	1.65E+00	1.07E+00
2.30E+01	1	1.84E+00	1.14E+03	1.79E+03	6.21E-02	1.30E+03	1.24E+03	1.19E+03	1.19E+03	5.96E-10	8.88E+00	1.07E+00
2.34E+01	1	1.71E+00	1.14E+03	1.70E+03	6.18E-02	1.30E+03	1.24E+03	1.19E+03	1.19E+03	5.99E-10	3.62E+00	1.06E+00
2.38E+01	1	1.57E+00	1.15E+03	1.62E+03	6.15E-02	1.30E+03	1.24E+03	1.19E+03	1.19E+03	6.02E-10	1.34E+01	1.05E+00
2.42E+01	1	1.45E+00	1.15E+03	1.54E+03	6.13E-02	1.30E+03	1.24E+03	1.20E+03	1.19E+03	6.06E-10	9.74E+00	1.05E+00
2.47E+01	1	1.45E+00	1.16E+03	1.48E+03	6.10E-02	1.29E+03	1.24E+03	1.20E+03	1.20E+03	6.09E-10	1.05E+01	1.04E+00
2.51E+01	1	1.46E+00	1.17E+03	1.42E+03	6.07E-02	1.29E+03	1.24E+03	1.20E+03	1.20E+03	6.14E-10	8.77E+00	1.04E+00
2.55E+01	1	1.46E+00	1.18E+03	1.37E+03	6.04E-02	1.29E+03	1.24E+03	1.21E+03	1.21E+03	6.18E-10	1.02E+01	1.03E+00
2.59E+01	1	1.46E+00	1.19E+03	1.32E+03	6.02E-02	1.29E+03	1.24E+03	1.21E+03	1.21E+03	6.22E-10	1.64E+01	1.02E+00
2.64E+01	1	1.47E+00	1.17E+03	1.08E+03	5.99E-02	1.29E+03	1.24E+03	1.22E+03	1.21E+03	6.25E-10	6.77E+00	1.01E+00
2.68E+01	1	1.47E+00	1.12E+03	6.10E+02	5.97E-02	1.28E+03	1.25E+03	1.21E+03	1.21E+03	6.25E-10	-1.94E+00	1.01E+00
2.72E+01	1	1.47E+00	1.06E+03	3.45E+02	5.94E-02	1.28E+03	1.25E+03	1.21E+03	1.21E+03	6.24E-10	2.17E+00	1.01E+00
2.76E+01	1	1.48E+00	1.01E+03	1.95E+02	5.91E-02	1.28E+03	1.25E+03	1.22E+03	1.21E+03	6.26E-10	1.42E+01	1.01E+00
2.81E+01	1	1.48E+00	9.50E+02	1.11E+02	5.89E-02	1.28E+03	1.25E+03	1.22E+03	1.22E+03	6.29E-10	1.23E+01	1.01E+00
2.85E+01	1	1.49E+00	9.47E+02	1.10E+02	5.86E-02	1.28E+03	1.25E+03	1.22E+03	1.22E+03	6.32E-10	8.30E+00	1.00E+00
2.89E+01	1	1.49E+00	9.84E+02	1.66E+02	5.84E-02	1.28E+03	1.25E+03	1.23E+03	1.23E+03	6.33E-10	2.71E+00	1.00E+00
2.93E+01	1	1.49E+00	1.02E+03	2.51E+02	5.81E-02	1.28E+03	1.25E+03	1.23E+03	1.23E+03	6.33E-10	-2.50E+00	1.00E+00
2.98E+01	1	1.50E+00	1.06E+03	3.80E+02	5.78E-02	1.28E+03	1.25E+03	1.23E+03	1.22E+03	6.31E-10	-4.40E+00	1.00E+00
3.02E+01	1	1.50E+00	1.10E+03	5.75E+02	5.76E-02	1.28E+03	1.25E+03	1.22E+03	1.22E+03	6.30E-10	-6.31E+00	1.01E+00
3.06E+01	1	1.50E+00	1.06E+03	5.08E+02	5.73E-02	1.28E+03	1.25E+03	1.22E+03	1.22E+03	6.27E-10	-6.50E+00	1.01E+00
3.10E+01	1	1.50E+00	1.02E+03	4.06E+02	5.71E-02	1.28E+03	1.25E+03	1.22E+03	1.22E+03	6.25E-10	-4.64E+00	1.01E+00
3.15E+01	1	1.50E+00	9.80E+02	3.25E+02	5.68E-02	1.28E+03	1.25E+03	1.22E+03	1.22E+03	6.23E-10	-9.84E+00	1.02E+00
3.19E+01	1	1.50E+00	9.37E+02	2.60E+02	5.66E-02	1.28E+03	1.25E+03	1.22E+03	1.22E+03	6.23E-10	-3.27E+00	1.02E+00

3.23E+01	1	1.50E+00	9.02E+02	2.22E+02	5.63E-02	1.28E+03	1.25E+03	1.22E+03	1.22E+03	6.23E-10	3.55E-01	1.02E+00
3.27E+01	1	1.50E+00	9.26E+02	3.05E+02	5.61E-02	1.28E+03	1.25E+03	1.22E+03	1.21E+03	6.22E-10	-1.22E+01	1.02E+00
3.32E+01	1	1.50E+00	9.50E+02	4.19E+02	5.58E-02	1.28E+03	1.25E+03	1.21E+03	1.21E+03	6.19E-10	-2.24E+01	1.02E+00
3.36E+01	1	1.49E+00	9.75E+02	5.77E+02	5.56E-02	1.28E+03	1.25E+03	1.21E+03	1.20E+03	6.18E-10	-2.42E+01	1.03E+00
3.40E+01	1	1.49E+00	9.99E+02	7.94E+02	5.53E-02	1.28E+03	1.24E+03	1.20E+03	1.19E+03	6.17E-10	-2.55E+01	1.03E+00
3.44E+01	1	1.49E+00	1.01E+03	9.09E+02	5.51E-02	1.28E+03	1.24E+03	1.19E+03	1.19E+03	6.16E-10	-2.01E+01	1.03E+00
3.49E+01	1	1.49E+00	1.02E+03	7.80E+02	5.49E-02	1.28E+03	1.24E+03	1.18E+03	1.18E+03	6.13E-10	-6.56E+00	1.03E+00
3.53E+01	1	1.49E+00	1.02E+03	6.70E+02	5.46E-02	1.28E+03	1.24E+03	1.18E+03	1.18E+03	6.11E-10	-6.91E-01	1.04E+00
3.57E+01	1	1.49E+00	1.02E+03	5.75E+02	5.44E-02	1.28E+03	1.23E+03	1.18E+03	1.18E+03	6.09E-10	6.20E+00	1.04E+00
3.61E+01	1	1.49E+00	1.02E+03	4.94E+02	5.41E-02	1.28E+03	1.23E+03	1.19E+03	1.18E+03	6.08E-10	5.19E+00	1.04E+00
3.66E+01	1	1.49E+00	1.02E+03	5.14E+02	5.39E-02	1.28E+03	1.23E+03	1.19E+03	1.19E+03	6.11E-10	2.55E+00	1.04E+00
3.70E+01	1	1.48E+00	1.02E+03	5.87E+02	5.37E-02	1.28E+03	1.23E+03	1.19E+03	1.18E+03	6.12E-10	-7.50E+00	1.04E+00
3.74E+01	1	1.47E+00	1.02E+03	6.70E+02	5.34E-02	1.28E+03	1.23E+03	1.18E+03	1.18E+03	6.12E-10	-6.57E+00	1.04E+00
3.78E+01	1	1.47E+00	1.02E+03	7.65E+02	5.32E-02	1.27E+03	1.23E+03	1.18E+03	1.18E+03	6.11E-10	-1.63E+01	1.04E+00
3.83E+01	1	1.46E+00	1.02E+03	8.73E+02	5.30E-02	1.27E+03	1.23E+03	1.17E+03	1.17E+03	6.11E-10	-1.58E+01	1.04E+00
3.87E+01	1	1.46E+00	1.01E+03	9.13E+02	5.27E-02	1.27E+03	1.22E+03	1.17E+03	1.17E+03	6.11E-10	-1.48E+01	1.04E+00
3.91E+01	1	1.45E+00	1.01E+03	9.51E+02	5.25E-02	1.27E+03	1.22E+03	1.16E+03	1.16E+03	6.11E-10	-1.53E+01	1.04E+00
3.95E+01	1	1.45E+00	1.01E+03	9.91E+02	5.23E-02	1.27E+03	1.22E+03	1.16E+03	1.16E+03	6.11E-10	-1.50E+01	1.04E+00
4.00E+01	1	1.44E+00	1.00E+03	1.03E+03	5.20E-02	1.27E+03	1.21E+03	1.15E+03	1.15E+03	6.11E-10	-1.48E+01	1.04E+00
4.04E+01	1	1.43E+00	9.97E+02	1.09E+03	5.19E-02	1.27E+03	1.21E+03	1.15E+03	1.15E+03	6.11E-10	-1.90E+01	1.04E+00
4.08E+01	1	1.43E+00	9.87E+02	1.22E+03	5.17E-02	1.26E+03	1.21E+03	1.14E+03	1.14E+03	6.12E-10	-2.27E+01	1.04E+00
4.12E+01	1	1.42E+00	9.77E+02	1.37E+03	5.16E-02	1.26E+03	1.20E+03	1.13E+03	1.13E+03	6.13E-10	-2.65E+01	1.03E+00
4.17E+01	1	1.42E+00	9.67E+02	1.53E+03	5.15E-02	1.26E+03	1.20E+03	1.12E+03	1.12E+03	6.14E-10	-2.52E+01	1.03E+00
4.21E+01	1	1.41E+00	9.57E+02	1.71E+03	5.13E-02	1.26E+03	1.19E+03	1.11E+03	1.10E+03	6.16E-10	-3.19E+01	1.03E+00
4.25E+01	1	1.41E+00	9.41E+02	1.83E+03	5.12E-02	1.26E+03	1.18E+03	1.09E+03	1.09E+03	6.17E-10	-3.48E+01	1.03E+00
4.29E+01	1	1.40E+00	9.18E+02	1.87E+03	5.11E-02	1.25E+03	1.18E+03	1.08E+03	1.07E+03	6.48E-10	-7.01E+01	9.89E-01
4.34E+01	1	1.39E+00	8.95E+02	1.91E+03	5.09E-02	1.25E+03	1.17E+03	1.06E+03	1.06E+03	6.14E-10	-3.86E+01	1.03E+00
4.38E+01	1	1.39E+00	8.71E+02	1.96E+03	5.08E-02	1.25E+03	1.16E+03	1.05E+03	1.04E+03	6.03E-10	-4.05E+01	1.05E+00
4.42E+01	1	1.38E+00	8.48E+02	2.01E+03	5.07E-02	1.24E+03	1.15E+03	1.03E+03	1.02E+03	5.96E-10	-4.20E+01	1.06E+00
4.46E+01	1	1.38E+00	8.22E+02	2.01E+03	5.05E-02	1.24E+03	1.14E+03	1.01E+03	1.00E+03	5.93E-10	-4.29E+01	1.07E+00
4.51E+01	1	1.37E+00	7.94E+02	2.00E+03	5.04E-02	1.23E+03	1.12E+03	9.95E+02	9.86E+02	5.94E-10	-4.42E+01	1.07E+00
4.55E+01	1	1.37E+00	7.67E+02	1.98E+03	5.03E-02	1.23E+03	1.11E+03	9.77E+02	9.66E+02	6.05E-10	-4.65E+01	1.05E+00
4.59E+01	1	1.36E+00	7.39E+02	1.97E+03	5.02E-02	1.22E+03	1.10E+03	9.59E+02	9.47E+02	6.18E-10	-4.67E+01	1.03E+00
4.63E+01	1	1.35E+00	7.12E+02	1.96E+03	5.00E-02	1.22E+03	1.09E+03	9.41E+02	9.27E+02	6.32E-10	-4.63E+01	1.00E+00
4.68E+01	1	1.35E+00	6.99E+02	1.95E+03	4.99E-02	1.21E+03	1.07E+03	9.25E+02	9.09E+02	6.49E-10	-3.82E+01	9.78E-01
4.72E+01	1	1.34E+00	6.85E+02	1.93E+03	4.98E-02	1.20E+03	1.06E+03	9.11E+02	8.94E+02	6.68E-10	-3.52E+01	9.51E-01
4.76E+01	1	1.34E+00	6.72E+02	1.92E+03	4.96E-02	1.19E+03	1.05E+03	8.97E+02	8.79E+02	6.87E-10	-3.36E+01	9.24E-01
4.80E+01	1	1.33E+00	6.58E+02	1.91E+03	4.95E-02	1.18E+03	1.03E+03	8.84E+02	8.65E+02	7.08E-10	-3.23E+01	8.98E-01
4.85E+01	1	1.32E+00	6.48E+02	1.88E+03	4.94E-02	1.17E+03	1.02E+03	8.72E+02	8.52E+02	7.29E-10	-3.07E+01	8.71E-01
4.89E+01	1	1.32E+00	6.43E+02	1.81E+03	4.92E-02	1.16E+03	1.01E+03	8.62E+02	8.43E+02	7.52E-10	-2.02E+01	8.45E-01
4.93E+01	1	1.31E+00	6.39E+02	1.75E+03	4.91E-02	1.15E+03	9.95E+02	8.54E+02	8.35E+02	7.76E-10	-1.87E+01	8.19E-01
4.97E+01	1	1.30E+00	6.35E+02	1.68E+03	4.90E-02	1.14E+03	9.83E+02	8.48E+02	8.28E+02	8.00E-10	-1.56E+01	7.95E-01

HFS (W/m2.K)	SQQ (%)	EQQ (%)	RATE (1/s)	MIDP	GAP (m)	INTP (MPa)	AXIG (m)	PCAX (MPa)	EQP (%)	EQT (%)	OX (m)	FW
4.98E+04	-1.32E+01	-1.44E-01	0.00E+00	0.00E+00	0.00E+00	8.25E+00	6.34E-04	0.00E+00	-3.58E-01	2.06E-01	5.00E-07	9.99E-01
5.30E+04	-2.35E+01	-1.40E-01	5.40E-11	0.00E+00	0.00E+00	7.40E+00	4.23E-04	0.00E+00	-3.58E-01	2.24E-01	5.00E-07	1.00E+00
5.57E+04	-5.05E+01	-1.23E-01	1.08E-09	0.00E+00	0.00E+00	5.52E+00	5.20E-04	0.00E+00	-3.58E-01	2.79E-01	5.00E-07	1.00E+00
5.91E+04	-6.69E+01	-8.80E-02	-3.20E-07	0.00E+00	0.00E+00	4.26E+00	4.16E-04	0.00E+00	-3.58E-01	3.44E-01	5.00E-07	1.00E+00
6.45E+04	-6.31E+01	-2.21E-02	-1.18E-05	0.00E+00	0.00E+00	4.20E+00	1.22E-04	0.00E+00	-3.58E-01	4.12E-01	5.00E-07	1.00E+00
7.07E+04	-6.14E+01	2.34E-02	-1.15E-04	0.00E+00	0.00E+00	4.00E+00	0.00E+00	9.22E-01	-3.60E-01	4.69E-01	5.00E-07	1.00E+00
7.92E+04	-3.54E+01	2.87E-02	-1.02E-03	0.00E+00	0.00E+00	5.24E+00	0.00E+00	3.67E+00	-4.21E-01	5.03E-01	5.00E-07	1.00E+00
8.85E+04	-2.42E+00	1.98E-02	-4.05E-08	0.00E+00	0.00E+00	6.93E+00	0.00E+00	6.80E+00	-4.40E-01	4.64E-01	2.27E-06	1.00E+00
9.46E+04	1.12E+01	9.53E-03	-2.57E-04	0.00E+00	0.00E+00	7.42E+00	0.00E+00	9.42E+00	-4.43E-01	4.41E-01	1.67E-06	1.00E+00
9.32E+04	1.70E+01	2.01E-02	1.10E-03	0.00E+00	0.00E+00	7.49E+00	0.00E+00	8.61E+00	-4.31E-01	4.25E-01	1.81E-06	1.00E+00
9.69E+04	1.14E+01	3.87E-02	8.04E-04	0.00E+00	0.00E+00	6.84E+00	0.00E+00	7.59E+00	-3.89E-01	4.10E-01	2.07E-06	1.00E+00
9.70E+04	7.86E+00	5.35E-02	5.33E-04	0.00E+00	0.00E+00	6.32E+00	0.00E+00	6.85E+00	-3.57E-01	3.98E-01	2.06E-06	1.00E+00
9.68E+04	5.88E+00	6.48E-02	3.94E-04	0.00E+00	0.00E+00	5.88E+00	0.00E+00	6.28E+00	-3.34E-01	3.90E-01	2.15E-06	1.00E+00
9.66E+04	4.77E+00	7.38E-02	3.40E-04	0.00E+00	0.00E+00	5.48E+00	0.00E+00	5.81E+00	-3.17E-01	3.83E-01	2.28E-06	1.00E+00
9.60E+04	2.84E+00	7.96E-02	1.87E-04	0.00E+00	0.00E+00	5.04E+00	0.00E+00	5.24E+00	-3.03E-01	3.78E-01	2.62E-06	1.00E+00
9.61E+04	2.08E+00	8.50E-02	1.35E-04	0.00E+00	0.00E+00	4.80E+00	0.00E+00	4.95E+00	-2.92E-01	3.74E-01	2.73E-06	1.00E+00
9.77E+04	2.88E+00	9.28E-02	2.83E-04	0.00E+00	0.00E+00	4.76E+00	0.00E+00	4.95E+00	-2.80E-01	3.68E-01	2.84E-06	1.00E+00
9.88E+04	1.86E+00	9.92E-02	2.05E-04	0.00E+00	0.00E+00	4.61E+00	0.00E+00	4.75E+00	-2.66E-01	3.62E-01	3.23E-06	1.00E+00
1.01E+05	2.44E+00	1.10E-01	4.26E-04	0.00E+00	0.00E+00	4.57E+00	0.00E+00	4.73E+00	-2.49E-01	3.55E-01	3.29E-06	1.00E+00
1.04E+05	1.02E+00	1.18E-01	1.74E-04	0.00E+00	0.00E+00	4.40E+00	0.00E+00	4.48E+00	-2.30E-01	3.46E-01	3.38E-06	1.00E+00
1.05E+05	8.52E-01	1.27E-01	1.57E-04	0.00E+00	0.00E+00	4.30E+00	0.00E+00	4.36E+00	-2.13E-01	3.38E-01	3.48E-06	1.00E+00
1.07E+05	6.98E-01	1.33E-01	7.74E-05	0.00E+00	0.00E+00	4.19E+00	0.00E+00	4.25E+00	-2.02E-01	3.34E-01	3.62E-06	1.00E+00
1.10E+05	1.12E+00	1.37E-01	7.66E-05	0.00E+00	0.00E+00	4.13E+00	0.00E+00	4.24E+00	-1.97E-01	3.32E-01	3.77E-06	1.00E+00
1.09E+05	3.31E-01	1.37E-01	9.40E-06	0.00E+00	0.00E+00	4.03E+00	0.00E+00	4.06E+00	-1.96E-01	3.32E-01	3.92E-06	1.00E+00
1.09E+05	-5.23E-01	1.36E-01	-2.34E-05	0.00E+00	0.00E+00	3.91E+00	0.00E+00	3.93E+00	-1.96E-01	3.33E-01	4.09E-06	1.00E+00
1.08E+05	3.10E-01	1.36E-01	3.28E-06	0.00E+00	0.00E+00	3.88E+00	0.00E+00	3.91E+00	-1.97E-01	3.33E-01	4.27E-06	1.00E+00
1.08E+05	1.53E+00	1.39E-01	4.80E-05	0.00E+00	0.00E+00	3.87E+00	0.00E+00	3.97E+00	-1.95E-01	3.31E-01	4.56E-06	1.00E+00
1.09E+05	2.47E+00	1.42E-01	1.11E-04	0.00E+00	0.00E+00	3.85E+00	0.00E+00	4.00E+00	-1.90E-01	3.28E-01	4.78E-06	1.00E+00
1.10E+05	2.60E+00	1.45E-01	1.21E-04	0.00E+00	0.00E+00	3.77E+00	0.00E+00	3.94E+00	-1.84E-01	3.25E-01	4.96E-06	1.00E+00
1.12E+05	2.83E+00	1.49E-01	1.44E-04	0.00E+00	0.00E+00	3.71E+00	0.00E+00	3.89E+00	-1.77E-01	3.22E-01	5.14E-06	1.00E+00
1.12E+05	2.54E+00	1.53E-01	1.09E-04	0.00E+00	0.00E+00	3.61E+00	0.00E+00	3.79E+00	-1.71E-01	3.19E-01	5.32E-06	1.00E+00
1.13E+05	2.61E+00	1.56E-01	1.12E-04	0.00E+00	0.00E+00	3.54E+00	0.00E+00	3.72E+00	-1.65E-01	3.17E-01	5.47E-06	1.00E+00
1.13E+05	2.41E+00	1.58E-01	8.83E-05	0.00E+00	0.00E+00	3.45E+00	0.00E+00	3.62E+00	-1.61E-01	3.15E-01	5.61E-06	1.00E+00
1.14E+05	2.30E+00	1.60E-01	7.68E-05	0.00E+00	0.00E+00	3.36E+00	0.00E+00	3.52E+00	-1.57E-01	3.13E-01	5.74E-06	1.00E+00
1.14E+05	2.26E+00	1.62E-01	7.30E-05	0.00E+00	0.00E+00	3.28E+00	0.00E+00	3.44E+00	-1.53E-01	3.11E-01	5.86E-06	1.00E+00
1.13E+05	1.24E+00	1.63E-01	1.98E-05	0.00E+00	0.00E+00	3.13E+00	0.00E+00	3.24E+00	-1.51E-01	3.12E-01	5.97E-06	1.00E+00
1.10E+05	-1.46E+00	1.60E-01	-3.30E-05	0.00E+00	0.00E+00	2.87E+00	0.00E+00	2.86E+00	-1.52E-01	3.15E-01	6.10E-06	1.00E+00
1.05E+05	-4.47E+00	1.54E-01	-2.26E-04	0.00E+00	0.00E+00	2.58E+00	0.00E+00	2.37E+00	-1.57E-01	3.20E-01	6.23E-06	1.00E+00
1.01E+05	-5.93E+00	1.46E-01	-4.34E-04	0.00E+00	0.00E+00	2.39E+00	0.00E+00	2.05E+00	-1.72E-01	3.28E-01	6.36E-06	1.00E+00
9.69E+04	-6.23E+00	1.33E-01	-5.73E-04	0.00E+00	0.00E+00	2.27E+00	0.00E+00	1.88E+00	-1.94E-01	3.39E-01	6.49E-06	1.00E+00
9.31E+04	-5.66E+00	1.21E-01	-5.09E-04	0.00E+00	0.00E+00	2.17E+00	0.00E+00	1.79E+00	-2.19E-01	3.49E-01	6.61E-06	1.00E+00
8.96E+04	-5.95E+00	1.06E-01	-6.21E-04	0.00E+00	0.00E+00	2.02E+00	0.00E+00	1.62E+00	-2.45E-01	3.61E-01	6.71E-06	1.00E+00
8.64E+04	-5.92E+00	8.99E-02	-7.19E-04	0.00E+00	0.00E+00	1.89E+00	0.00E+00	1.49E+00	-2.74E-01	3.74E-01	6.81E-06	1.00E+00
8.40E+04	-3.96E+00	7.58E-02	-4.40E-04	0.00E+00	0.00E+00	1.88E+00	0.00E+00	1.57E+00	-3.04E-01	3.86E-01	7.09E-06	1.00E+00
8.35E+04	-2.31E+00	6.80E-02	-1.78E-04	0.00E+00	0.00E+00	1.85E+00	0.00E+00	1.64E+00	-3.19E-01	3.91E-01	7.23E-06	1.00E+00
8.32E+04	-6.58E-01	6.68E-02	-3.27E-05	0.00E+00	0.00E+00	1.82E+00	0.00E+00	1.78E+00	-3.23E-01	3.91E-01	7.32E-06	1.00E+00
8.16E+04	1.35E+00	7.00E-02	6.25E-05	0.00E+00	0.00E+00	1.83E+00	0.00E+00	1.86E+00	-3.20E-01	3.88E-01	7.38E-06	1.00E+00
8.47E+04	4.62E+00	7.57E-02	2.19E-04	0.00E+00	0.00E+00	1.93E+00	0.00E+00	2.13E+00	-3.13E-01	3.81E-01	7.40E-06	1.00E+00
8.56E+04	5.78E+00	8.29E-02	2.74E-04	0.00E+00	0.00E+00	1.89E+00	0.00E+00	2.21E+00	-3.01E-01	3.74E-01	7.43E-06	1.00E+00
8.47E+04	4.33E+00	8.61E-02	1.51E-04	0.00E+00	0.00E+00	1.67E+00	0.00E+00	1.96E+00	-2.93E-01	3.72E-01	7.70E-06	1.00E+00
8.37E+04	3.33E+00	8.75E-02	9.03E-05	0.00E+00	0.00E+00	1.49E+00	0.00E+00	1.71E+00	-2.89E-01	3.71E-01	7.75E-06	1.00E+00
8.28E+04	2.37E+00	8.79E-02	4.68E-05	0.00E+00	0.00E+00	1.30E+00	0.00E+00	1.47E+00	-2.86E-01	3.70E-01	7.80E-06	1.00E+00
8.12E+04	1.54E+00	8.78E-02	2.05E-05	0.00E+00	0.00E+00	1.12E+00	0.00E+00	1.23E+00	-2.85E-01	3.71E-01	7.84E-06	1.00E+00
8.05E+04	1.48E+00	8.83E-02	2.04E-05	0.00E+00	0.00E+00	9.89E-01	0.00E+00	1.07E+00	-2.84E-01	3.70E-01	7.88E-06	1.00E+00
7.96E+04	2.10E+00	8.96E-02	4.07E-05	0.00E+00	0.00E+00	9.03E-01	0.00E+00	1.01E+00	-2.83E-01	3.69E-01	7.92E-06	1.00E+00
7.94E+04	2.59E+00	9.13E-02	6.11E-05	0.00E+00	0.00E+00	8.07E-01	0.00E+00	9.43E-01	-2.81E-01	3.68E-01	7.95E-06	1.00E+00
7.83E+04	3.12E+00	9.34E-02	8.67E-05	0.00E+00	0.00E+00	7.16E-01	0.00E+00	8.97E-01	-2.78E-01	3.66E-01	7.98E-06	1.00E+00
7.75E+04	3.38E+00	9.57E-02	1.04E-04	0.00E+00	0.00E+00	6.15E-01	0.00E+00	8.23E-01	-2.73E-01	3.63E-01	8.01E-06	1.00E+00
7.80E+04	3.82E+00	9.89E-02	1.41E-04	0.00E+00	0.00E+00	6.51E-01	0.00E+00	8.85E-01	-2.68E-01	3.61E-01	8.04E-06	1.00E+00
7.85E+04	4.08E+00	1.03E-01	1.81E-04	0.00E+00	0.00E+00	6.77E-01	0.00E+00	9.34E-01	-2.61E-01	3.57E-01	8.08E-06	1.00E+00
7.86E+04	4.08E+00	1.08E-01	2.16E-04	0.00E+00	0.00E+00	6.88E-01	0.00E+00	9.54E-01	-2.53E-01	3.54E-01	8.11E-06	1.00E+00

7.86E+04	3.63E+00	1.13E-01	2.16E-04	0.00E+00	0.00E+00	6.72E-01	0.00E+00	9.21E-01	-2.43E-01	3.49E-01	8.14E-06	1.00E+00
7.87E+04	2.77E+00	1.17E-01	1.59E-04	0.00E+00	0.00E+00	6.28E-01	0.00E+00	8.32E-01	-2.33E-01	3.46E-01	8.17E-06	1.00E+00
7.81E+04	8.55E-01	1.16E-01	1.56E-05	0.00E+00	0.00E+00	5.11E-01	0.00E+00	6.22E-01	-2.31E-01	3.46E-01	8.22E-06	1.00E+00
7.79E+04	5.64E-01	1.16E-01	8.63E-06	0.00E+00	0.00E+00	4.96E-01	0.00E+00	5.58E-01	-2.31E-01	3.46E-01	8.27E-06	1.00E+00
7.83E+04	1.60E+00	1.19E-01	5.21E-05	0.00E+00	0.00E+00	5.66E-01	0.00E+00	6.76E-01	-2.29E-01	3.45E-01	8.32E-06	1.00E+00
7.96E+04	2.96E+00	1.23E-01	1.62E-04	0.00E+00	0.00E+00	6.59E-01	0.00E+00	8.46E-01	-2.23E-01	3.41E-01	8.36E-06	1.00E+00
8.04E+04	3.17E+00	1.28E-01	2.12E-04	0.00E+00	0.00E+00	6.81E-01	0.00E+00	8.95E-01	-2.14E-01	3.37E-01	8.39E-06	1.00E+00
7.98E+04	1.75E+00	1.30E-01	8.19E-05	0.00E+00	0.00E+00	5.99E-01	0.00E+00	7.31E-01	-2.08E-01	3.35E-01	8.44E-06	1.00E+00
8.00E+04	9.06E-01	1.31E-01	2.43E-05	0.00E+00	0.00E+00	5.49E-01	0.00E+00	6.31E-01	-2.05E-01	3.35E-01	8.50E-06	1.00E+00
7.98E+04	5.63E-02	1.30E-01	-3.90E-06	0.00E+00	0.00E+00	4.97E-01	0.00E+00	5.40E-01	-2.05E-01	3.35E-01	8.56E-06	1.00E+00
7.83E+04	-1.22E+00	1.29E-01	-2.90E-05	0.00E+00	0.00E+00	4.17E-01	0.00E+00	3.90E-01	-2.06E-01	3.37E-01	8.63E-06	1.00E+00
7.64E+04	-2.82E+00	1.26E-01	-8.92E-05	0.00E+00	0.00E+00	3.13E-01	0.00E+00	1.80E-01	-2.09E-01	3.40E-01	8.70E-06	1.00E+00
7.56E+04	-3.04E+00	1.23E-01	-9.44E-05	0.00E+00	0.00E+00	2.95E-01	0.00E+00	1.24E-01	-2.13E-01	3.42E-01	8.76E-06	1.00E+00
7.53E+04	-3.04E+00	1.21E-01	-8.84E-05	0.00E+00	0.00E+00	2.91E-01	0.00E+00	9.55E-02	-2.17E-01	3.43E-01	8.83E-06	1.00E+00
7.58E+04	-2.47E+00	1.20E-01	-5.73E-05	0.00E+00	0.00E+00	3.25E-01	0.00E+00	1.47E-01	-2.19E-01	3.44E-01	8.89E-06	1.00E+00
7.65E+04	-1.76E+00	1.20E-01	-2.89E-05	0.00E+00	0.00E+00	3.68E-01	0.00E+00	2.25E-01	-2.21E-01	3.44E-01	8.95E-06	1.00E+00
7.60E+04	-2.31E+00	1.19E-01	-5.09E-05	0.00E+00	0.00E+00	3.32E-01	0.00E+00	1.75E-01	-2.23E-01	3.45E-01	9.01E-06	1.00E+00
7.33E+04	-4.14E+00	1.15E-01	-1.62E-04	0.00E+00	0.00E+00	2.12E-01	0.00E+00	0.00E+00	-2.27E-01	3.49E-01	9.08E-06	1.00E+00
7.12E+04	-5.34E+00	1.07E-01	-3.30E-04	0.00E+00	0.00E+00	1.33E-01	3.41E-05	0.00E+00	-2.38E-01	3.56E-01	9.14E-06	1.00E+00
7.03E+04	-5.52E+00	9.81E-02	-4.53E-04	0.00E+00	0.00E+00	1.19E-01	8.15E-05	0.00E+00	-2.55E-01	3.64E-01	9.21E-06	1.00E+00
7.04E+04	-4.62E+00	8.82E-02	-4.03E-04	0.00E+00	0.00E+00	1.73E-01	1.27E-04	0.00E+00	-2.76E-01	3.72E-01	9.29E-06	1.00E+00
7.16E+04	-3.12E+00	8.28E-02	-1.67E-04	0.00E+00	0.00E+00	2.64E-01	1.23E-04	0.00E+00	-2.88E-01	3.75E-01	9.35E-06	1.00E+00
7.25E+04	-2.23E+00	8.15E-02	-4.33E-05	0.00E+00	0.00E+00	3.16E-01	8.70E-05	0.00E+00	-2.92E-01	3.76E-01	9.43E-06	1.00E+00
7.29E+04	-1.66E+00	8.22E-02	1.51E-05	0.00E+00	0.00E+00	3.47E-01	3.88E-05	0.00E+00	-2.92E-01	3.75E-01	9.53E-06	1.00E+00
7.32E+04	-8.86E-01	8.36E-02	3.91E-05	0.00E+00	0.00E+00	3.92E-01	0.00E+00	6.38E-02	-2.90E-01	3.74E-01	9.62E-06	1.00E+00
7.42E+04	2.23E-01	8.48E-02	2.13E-05	0.00E+00	0.00E+00	4.61E-01	0.00E+00	3.41E-01	-2.89E-01	3.73E-01	9.69E-06	1.00E+00
7.39E+04	-8.47E-01	8.36E-02	-8.29E-06	0.00E+00	0.00E+00	3.91E-01	0.00E+00	2.81E-01	-2.89E-01	3.73E-01	9.76E-06	1.00E+00
7.27E+04	-2.57E+00	8.04E-02	-8.29E-05	0.00E+00	0.00E+00	2.77E-01	0.00E+00	1.02E-01	-2.91E-01	3.75E-01	9.84E-06	1.00E+00
7.08E+04	-3.74E+00	7.62E-02	-1.79E-04	0.00E+00	0.00E+00	1.96E-01	1.37E-06	0.00E+00	-2.97E-01	3.79E-01	1.01E-05	1.00E+00
6.99E+04	-4.11E+00	7.03E-02	-2.56E-04	0.00E+00	0.00E+00	1.67E-01	2.04E-05	0.00E+00	-3.07E-01	3.84E-01	1.02E-05	1.00E+00
6.96E+04	-3.94E+00	6.41E-02	-2.69E-04	0.00E+00	0.00E+00	1.72E-01	4.10E-05	0.00E+00	-3.19E-01	3.90E-01	1.03E-05	1.00E+00
6.95E+04	-3.63E+00	5.80E-02	-2.53E-04	0.00E+00	0.00E+00	1.85E-01	5.84E-05	0.00E+00	-3.31E-01	3.95E-01	1.03E-05	1.00E+00
6.93E+04	-3.47E+00	5.17E-02	-2.52E-04	0.00E+00	0.00E+00	1.90E-01	7.36E-05	0.00E+00	-3.42E-01	4.00E-01	1.04E-05	1.00E+00
6.91E+04	-3.37E+00	4.53E-02	-2.58E-04	0.00E+00	0.00E+00	1.91E-01	8.76E-05	0.00E+00	-3.54E-01	4.05E-01	1.04E-05	1.00E+00
6.88E+04	-3.25E+00	3.91E-02	-2.62E-04	0.00E+00	0.00E+00	1.93E-01	1.02E-04	0.00E+00	-3.66E-01	4.10E-01	1.05E-05	1.00E+00
6.80E+04	-3.72E+00	3.00E-02	-4.01E-04	0.00E+00	0.00E+00	1.58E-01	1.32E-04	0.00E+00	-3.82E-01	4.18E-01	1.06E-05	1.00E+00
6.74E+04	-3.78E+00	1.92E-02	-4.96E-04	0.00E+00	0.00E+00	1.50E-01	1.76E-04	0.00E+00	-4.02E-01	4.27E-01	1.06E-05	1.00E+00
6.68E+04	-3.18E+00	7.96E-03	-4.15E-04	0.00E+00	0.00E+00	1.84E-01	2.26E-04	0.00E+00	-4.25E-01	4.38E-01	1.07E-05	1.00E+00
6.62E+04	-3.51E+00	-6.89E-03	-5.95E-04	0.00E+00	0.00E+00	1.61E-01	2.90E-04	0.00E+00	-4.52E-01	4.51E-01	1.09E-05	1.00E+00
6.54E+04	-3.01E+00	-2.13E-02	-4.84E-04	0.00E+00	0.00E+00	1.89E-01	3.53E-04	0.00E+00	-4.81E-01	4.64E-01	1.19E-05	1.00E+00
3.58E+04	-6.36E+00	-1.17E-02	-1.72E-03	0.00E+00	1.55E-06	0.00E+00	4.36E-04	0.00E+00	-5.14E-01	5.13E-01	4.67E-06	1.00E+00
6.44E+04	-1.86E+00	-5.50E-02	-1.06E-04	0.00E+00	0.00E+00	2.46E-01	4.16E-04	0.00E+00	-5.56E-01	5.03E-01	4.67E-06	1.00E+00
6.35E+04	-1.97E+00	-7.36E-02	-1.52E-04	0.00E+00	0.00E+00	2.15E-01	3.54E-04	0.00E+00	-5.63E-01	4.91E-01	1.40E-06	1.00E+00
6.26E+04	-2.01E+00	-9.25E-02	-1.42E-04	0.00E+00	0.00E+00	1.93E-01	3.24E-04	0.00E+00	-5.70E-01	4.80E-01	1.40E-06	1.00E+00
6.17E+04	-2.26E+00	-1.12E-01	-1.60E-04	0.00E+00	0.00E+00	1.65E-01	3.23E-04	0.00E+00	-5.77E-01	4.67E-01	1.40E-06	1.00E+00
5.97E+04	-4.82E+00	-1.32E-01	-1.42E-07	0.00E+00	0.00E+00	2.13E-04	3.62E-04	0.00E+00	-5.80E-01	4.55E-01	1.40E-06	1.00E+00
4.99E+04	-5.04E+00	-1.45E-01	-1.23E-07	0.00E+00	4.08E-07	0.00E+00	4.07E-04	0.00E+00	-5.80E-01	4.42E-01	1.40E-06	1.00E+00
4.30E+04	-5.28E+00	-1.59E-01	-1.06E-07	0.00E+00	8.10E-07	0.00E+00	4.54E-04	0.00E+00	-5.80E-01	4.29E-01	1.40E-06	1.00E+00
3.76E+04	-5.54E+00	-1.72E-01	-9.08E-08	0.00E+00	1.21E-06	0.00E+00	5.01E-04	0.00E+00	-5.80E-01	4.16E-01	1.40E-06	1.00E+00
3.34E+04	-5.86E+00	-1.84E-01	-2.91E-08	0.00E+00	1.59E-06	0.00E+00	5.54E-04	0.00E+00	-5.80E-01	4.04E-01	1.40E-06	1.00E+00
3.03E+04	-6.20E+00	-1.95E-01	-1.89E-08	0.00E+00	1.93E-06	0.00E+00	6.05E-04	0.00E+00	-5.80E-01	3.93E-01	1.40E-06	1.00E+00
2.79E+04	-6.53E+00	-2.05E-01	-1.24E-08	0.00E+00	2.24E-06	0.00E+00	6.54E-04	0.00E+00	-5.80E-01	3.84E-01	1.40E-06	1.00E+00
2.60E+04	-6.85E+00	-2.15E-01	-8.12E-09	0.00E+00	2.53E-06	0.00E+00	7.00E-04	0.00E+00	-5.80E-01	3.74E-01	1.40E-06	1.00E+00
2.41E+04	-7.19E+00	-2.24E-01	-5.28E-09	0.00E+00	2.81E-06	0.00E+00	7.45E-04	0.00E+00	-5.80E-01	3.66E-01	1.40E-06	1.00E+00
2.28E+04	-7.47E+00	-2.30E-01	-3.92E-09	0.00E+00	3.07E-06	0.00E+00	7.93E-04	0.00E+00	-5.80E-01	3.59E-01	1.40E-06	1.00E+00
2.17E+04	-7.77E+00	-2.36E-01	-3.07E-09	0.00E+00	3.29E-06	0.00E+00	8.36E-04	0.00E+00	-5.80E-01	3.54E-01	1.40E-06	1.00E+00
2.08E+04	-8.02E+00	-2.41E-01	-2.49E-09	0.00E+00	3.48E-06	0.00E+00	8.74E-04	0.00E+00	-5.80E-01	3.49E-01	1.40E-06	1.00E+00

SIGIR (MPa)	ATHERM (%)	PROB	SUMCP (kJ/kg)	NCRAC	EPC	ZRO2 (m)	AZR (m)	FECS	FSC
1.21E+02	0.00E+00	0.00E+00	2.25E+05	0	0.00E+00	5.00E-07	0.00E+00	0.00E+00	0.00E+00
1.21E+02	0.00E+00	0.00E+00	2.27E+05	0	0.00E+00	5.00E-07	0.00E+00	0.00E+00	0.00E+00
1.22E+02	0.00E+00	0.00E+00	2.34E+05	0	0.00E+00	5.00E-07	0.00E+00	0.00E+00	0.00E+00
1.22E+02	0.00E+00	0.00E+00	2.47E+05	0	0.00E+00	5.00E-07	0.00E+00	0.00E+00	0.00E+00
1.21E+02	0.00E+00	0.00E+00	2.68E+05	0	0.00E+00	5.00E-07	0.00E+00	0.00E+00	0.00E+00
4.03E+01	-1.77E-39	0.00E+00	2.84E+05	0	0.00E+00	5.00E-07	0.00E+00	0.00E+00	0.00E+00
1.56E+00	-1.18E-28	0.00E+00	2.89E+05	0	0.00E+00	5.00E-07	0.00E+00	0.00E+00	0.00E+00
2.01E+00	-1.18E-28	0.00E+00	2.90E+05	0	0.00E+00	5.00E-07	1.77E-06	0.00E+00	0.00E+00
2.08E+00	-1.18E-28	0.00E+00	2.91E+05	0	0.00E+00	5.00E-07	1.17E-06	0.00E+00	0.00E+00
2.64E+00	-1.18E-28	0.00E+00	2.91E+05	0	0.00E+00	5.00E-07	1.31E-06	0.00E+00	0.00E+00
2.74E+00	-1.18E-28	0.00E+00	2.92E+05	0	0.00E+00	5.06E-07	1.57E-06	0.00E+00	0.00E+00
2.77E+00	-1.18E-28	0.00E+00	2.93E+05	0	0.00E+00	6.01E-07	1.46E-06	0.00E+00	0.00E+00
2.77E+00	-1.18E-28	0.00E+00	2.93E+05	0	0.00E+00	6.97E-07	1.45E-06	0.00E+00	0.00E+00
2.75E+00	-1.18E-28	0.00E+00	2.93E+05	0	0.00E+00	7.94E-07	1.49E-06	0.00E+00	0.00E+00
2.72E+00	-1.18E-28	0.00E+00	2.93E+05	0	0.00E+00	8.89E-07	1.73E-06	0.00E+00	0.00E+00
2.69E+00	-1.18E-28	0.00E+00	2.93E+05	0	0.00E+00	9.82E-07	1.75E-06	0.00E+00	0.00E+00
2.66E+00	-1.18E-28	0.00E+00	2.93E+05	0	0.00E+00	1.07E-06	1.76E-06	0.00E+00	0.00E+00
2.61E+00	-1.18E-28	0.00E+00	2.93E+05	0	0.00E+00	1.17E-06	2.06E-06	0.00E+00	0.00E+00
2.56E+00	-1.18E-28	0.00E+00	2.94E+05	0	0.00E+00	1.27E-06	2.02E-06	0.00E+00	0.00E+00
2.48E+00	-1.18E-28	0.00E+00	2.94E+05	0	0.00E+00	1.38E-06	2.00E-06	0.00E+00	0.00E+00
2.37E+00	-1.18E-28	0.00E+00	2.95E+05	0	0.00E+00	1.49E-06	2.00E-06	0.00E+00	0.00E+00
2.26E+00	-1.18E-28	0.00E+00	2.95E+05	0	0.00E+00	1.61E-06	2.01E-06	0.00E+00	0.00E+00
2.19E+00	-1.18E-28	0.00E+00	2.95E+05	0	0.00E+00	1.73E-06	2.04E-06	0.00E+00	0.00E+00
2.09E+00	-1.18E-28	0.00E+00	2.96E+05	0	0.00E+00	1.84E-06	2.08E-06	0.00E+00	0.00E+00
2.08E+00	-1.18E-28	0.00E+00	2.95E+05	0	0.00E+00	1.94E-06	2.14E-06	0.00E+00	0.00E+00
2.05E+00	-1.18E-28	0.00E+00	2.95E+05	0	0.00E+00	2.04E-06	2.23E-06	0.00E+00	0.00E+00
2.03E+00	-1.18E-28	0.00E+00	2.95E+05	0	0.00E+00	2.14E-06	2.42E-06	0.00E+00	0.00E+00
2.01E+00	-1.18E-28	0.00E+00	2.96E+05	0	0.00E+00	2.23E-06	2.55E-06	0.00E+00	0.00E+00
1.95E+00	-1.18E-28	0.00E+00	2.96E+05	0	0.00E+00	2.32E-06	2.64E-06	0.00E+00	0.00E+00
1.91E+00	-1.18E-28	0.00E+00	2.96E+05	0	0.00E+00	2.41E-06	2.73E-06	0.00E+00	0.00E+00
1.85E+00	-1.18E-28	0.00E+00	2.96E+05	0	0.00E+00	2.50E-06	2.82E-06	0.00E+00	0.00E+00
1.82E+00	-1.18E-28	0.00E+00	2.96E+05	0	0.00E+00	2.59E-06	2.88E-06	0.00E+00	0.00E+00
1.78E+00	-1.18E-28	0.00E+00	2.97E+05	0	0.00E+00	2.68E-06	2.93E-06	0.00E+00	0.00E+00
1.75E+00	-1.18E-28	0.00E+00	2.97E+05	0	0.00E+00	2.77E-06	2.96E-06	0.00E+00	0.00E+00
1.72E+00	-1.18E-28	0.00E+00	2.97E+05	0	0.00E+00	2.86E-06	3.00E-06	0.00E+00	0.00E+00
1.71E+00	-1.18E-28	0.00E+00	2.97E+05	0	0.00E+00	2.94E-06	3.03E-06	0.00E+00	0.00E+00
1.70E+00	-1.18E-28	0.00E+00	2.97E+05	0	0.00E+00	3.03E-06	3.07E-06	0.00E+00	0.00E+00
1.66E+00	-1.18E-28	0.00E+00	2.97E+05	0	0.00E+00	3.11E-06	3.12E-06	0.00E+00	0.00E+00
1.73E+00	-1.18E-28	0.00E+00	2.97E+05	0	0.00E+00	3.17E-06	3.19E-06	0.00E+00	0.00E+00
2.00E+00	-1.18E-28	0.00E+00	2.96E+05	0	0.00E+00	3.23E-06	3.26E-06	0.00E+00	0.00E+00
2.28E+00	-1.18E-28	0.00E+00	2.94E+05	0	0.00E+00	3.28E-06	3.32E-06	0.00E+00	0.00E+00
2.62E+00	-1.18E-28	0.00E+00	2.93E+05	0	0.00E+00	3.32E-06	3.39E-06	0.00E+00	0.00E+00
3.24E+00	-1.18E-28	0.00E+00	2.91E+05	0	0.00E+00	3.36E-06	3.46E-06	0.00E+00	0.00E+00
4.21E+00	-1.18E-28	0.00E+00	2.89E+05	0	0.00E+00	3.38E-06	3.72E-06	0.00E+00	0.00E+00
4.90E+00	-1.18E-28	0.00E+00	2.87E+05	0	0.00E+00	3.39E-06	3.84E-06	0.00E+00	0.00E+00
5.16E+00	-1.18E-28	0.00E+00	2.86E+05	0	0.00E+00	3.41E-06	3.91E-06	0.00E+00	0.00E+00
5.11E+00	-1.18E-28	0.00E+00	2.85E+05	0	0.00E+00	3.43E-06	3.95E-06	0.00E+00	0.00E+00

4.92E+00	-1.18E-28	0.00E+00	2.84E+05	0	0.00E+00	3.44E-06	3.96E-06	0.00E+00	0.00E+00
4.76E+00	-1.18E-28	0.00E+00	2.84E+05	0	0.00E+00	3.46E-06	3.97E-06	0.00E+00	0.00E+00
4.67E+00	-1.18E-28	0.00E+00	2.84E+05	0	0.00E+00	3.49E-06	4.21E-06	0.00E+00	0.00E+00
4.64E+00	-1.18E-28	0.00E+00	2.84E+05	0	0.00E+00	3.51E-06	4.24E-06	0.00E+00	0.00E+00
4.64E+00	-1.18E-28	0.00E+00	2.83E+05	0	0.00E+00	3.54E-06	4.26E-06	0.00E+00	0.00E+00
4.63E+00	-1.18E-28	0.00E+00	2.83E+05	0	0.00E+00	3.57E-06	4.27E-06	0.00E+00	0.00E+00
4.62E+00	-1.18E-28	0.00E+00	2.83E+05	0	0.00E+00	3.59E-06	4.29E-06	0.00E+00	0.00E+00
4.62E+00	-1.18E-28	0.00E+00	2.82E+05	0	0.00E+00	3.62E-06	4.30E-06	0.00E+00	0.00E+00
4.63E+00	-1.18E-28	0.00E+00	2.82E+05	0	0.00E+00	3.65E-06	4.30E-06	0.00E+00	0.00E+00
4.65E+00	-1.18E-28	0.00E+00	2.82E+05	0	0.00E+00	3.67E-06	4.31E-06	0.00E+00	0.00E+00
4.65E+00	-1.18E-28	0.00E+00	2.82E+05	0	0.00E+00	3.70E-06	4.31E-06	0.00E+00	0.00E+00
4.66E+00	-1.18E-28	0.00E+00	2.82E+05	0	0.00E+00	3.73E-06	4.31E-06	0.00E+00	0.00E+00
4.64E+00	-1.18E-28	0.00E+00	2.82E+05	0	0.00E+00	3.76E-06	4.31E-06	0.00E+00	0.00E+00
4.59E+00	-1.18E-28	0.00E+00	2.82E+05	0	0.00E+00	3.80E-06	4.31E-06	0.00E+00	0.00E+00
4.46E+00	-1.18E-28	0.00E+00	2.83E+05	0	0.00E+00	3.83E-06	4.31E-06	0.00E+00	0.00E+00
4.29E+00	-1.18E-28	0.00E+00	2.83E+05	0	0.00E+00	3.86E-06	4.31E-06	0.00E+00	0.00E+00
4.14E+00	-1.18E-28	0.00E+00	2.83E+05	0	0.00E+00	3.90E-06	4.32E-06	0.00E+00	0.00E+00
3.98E+00	-1.18E-28	0.00E+00	2.83E+05	0	0.00E+00	3.94E-06	4.33E-06	0.00E+00	0.00E+00
3.89E+00	-1.18E-28	0.00E+00	2.83E+05	0	0.00E+00	3.97E-06	4.34E-06	0.00E+00	0.00E+00
3.80E+00	-1.18E-28	0.00E+00	2.84E+05	0	0.00E+00	4.01E-06	4.35E-06	0.00E+00	0.00E+00
3.65E+00	-1.18E-28	0.00E+00	2.84E+05	0	0.00E+00	4.04E-06	4.35E-06	0.00E+00	0.00E+00
3.41E+00	-1.18E-28	0.00E+00	2.85E+05	0	0.00E+00	4.08E-06	4.36E-06	0.00E+00	0.00E+00
3.22E+00	-1.18E-28	0.00E+00	2.85E+05	0	0.00E+00	4.12E-06	4.37E-06	0.00E+00	0.00E+00
3.10E+00	-1.18E-28	0.00E+00	2.85E+05	0	0.00E+00	4.17E-06	4.39E-06	0.00E+00	0.00E+00
3.04E+00	-1.18E-28	0.00E+00	2.85E+05	0	0.00E+00	4.21E-06	4.42E-06	0.00E+00	0.00E+00
3.00E+00	-1.18E-28	0.00E+00	2.85E+05	0	0.00E+00	4.25E-06	4.45E-06	0.00E+00	0.00E+00
2.97E+00	-1.18E-28	0.00E+00	2.85E+05	0	0.00E+00	4.29E-06	4.47E-06	0.00E+00	0.00E+00
2.92E+00	-1.18E-28	0.00E+00	2.85E+05	0	0.00E+00	4.33E-06	4.50E-06	0.00E+00	0.00E+00
2.90E+00	-1.18E-28	0.00E+00	2.85E+05	0	0.00E+00	4.36E-06	4.53E-06	0.00E+00	0.00E+00
2.89E+00	-1.18E-28	0.00E+00	2.85E+05	0	0.00E+00	4.40E-06	4.55E-06	0.00E+00	0.00E+00
2.88E+00	-1.18E-28	0.00E+00	2.85E+05	0	0.00E+00	4.43E-06	4.58E-06	0.00E+00	0.00E+00
2.81E+00	-1.18E-28	0.00E+00	2.84E+05	0	0.00E+00	4.46E-06	4.61E-06	0.00E+00	0.00E+00
2.55E+00	-1.18E-28	0.00E+00	2.84E+05	0	0.00E+00	4.46E-06	4.67E-06	0.00E+00	0.00E+00
2.55E+00	-1.18E-28	0.00E+00	2.83E+05	0	0.00E+00	4.49E-06	4.72E-06	0.00E+00	0.00E+00
3.13E+00	-1.18E-28	0.00E+00	2.82E+05	0	0.00E+00	4.51E-06	4.78E-06	0.00E+00	0.00E+00
3.69E+00	-1.18E-28	0.00E+00	2.81E+05	0	0.00E+00	4.53E-06	4.82E-06	0.00E+00	0.00E+00
3.95E+00	-1.18E-28	0.00E+00	2.80E+05	0	0.00E+00	4.55E-06	4.88E-06	0.00E+00	0.00E+00
4.03E+00	-1.18E-28	0.00E+00	2.80E+05	0	0.00E+00	4.57E-06	4.97E-06	0.00E+00	0.00E+00
3.97E+00	-1.18E-28	0.00E+00	2.79E+05	0	0.00E+00	4.58E-06	5.04E-06	0.00E+00	0.00E+00
3.88E+00	-1.18E-28	0.00E+00	2.79E+05	0	0.00E+00	4.60E-06	5.09E-06	0.00E+00	0.00E+00
3.78E+00	-1.18E-28	0.00E+00	2.79E+05	0	0.00E+00	4.62E-06	5.14E-06	0.00E+00	0.00E+00
3.74E+00	-1.18E-28	0.00E+00	2.78E+05	0	0.00E+00	4.64E-06	5.21E-06	0.00E+00	0.00E+00
3.77E+00	-1.18E-28	0.00E+00	2.78E+05	0	0.00E+00	4.65E-06	5.43E-06	0.00E+00	0.00E+00
3.97E+00	-1.18E-28	0.00E+00	2.77E+05	0	0.00E+00	4.67E-06	5.51E-06	0.00E+00	0.00E+00
4.33E+00	-1.18E-28	0.00E+00	2.76E+05	0	0.00E+00	4.67E-06	5.59E-06	0.00E+00	0.00E+00
4.78E+00	-1.18E-28	0.00E+00	2.75E+05	0	0.00E+00	4.67E-06	5.66E-06	0.00E+00	0.00E+00
5.24E+00	-1.18E-28	0.00E+00	2.74E+05	0	0.00E+00	4.67E-06	5.71E-06	0.00E+00	0.00E+00
5.72E+00	-1.18E-28	0.00E+00	2.73E+05	0	0.00E+00	4.67E-06	5.77E-06	0.00E+00	0.00E+00
6.28E+00	-1.18E-28	0.00E+00	2.72E+05	0	0.00E+00	4.67E-06	5.82E-06	0.00E+00	0.00E+00
6.91E+00	-1.18E-28	0.00E+00	2.71E+05	0	0.00E+00	4.67E-06	5.88E-06	0.00E+00	0.00E+00
7.84E+00	-1.18E-28	0.00E+00	2.69E+05	0	0.00E+00	4.67E-06	5.97E-06	0.00E+00	0.00E+00
9.16E+00	-1.18E-28	0.00E+00	2.67E+05	0	0.00E+00	4.67E-06	6.07E-06	0.00E+00	0.00E+00
1.07E+01	-1.18E-28	0.00E+00	2.65E+05	0	0.00E+00	4.67E-06	6.21E-06	0.00E+00	0.00E+00
1.28E+01	-1.18E-28	0.00E+00	2.63E+05	0	0.00E+00	4.67E-06	7.21E-06	0.00E+00	0.00E+00
1.50E+01	-1.18E-28	0.00E+00	2.61E+05	0	0.00E+00	4.67E-06	0.00E+00	0.00E+00	0.00E+00
1.73E+01	-1.18E-28	0.00E+00	2.58E+05	0	0.00E+00	4.67E-06	0.00E+00	0.00E+00	0.00E+00
1.93E+01	-1.18E-28	0.00E+00	2.55E+05	0	0.00E+00	1.40E-06	0.00E+00	0.00E+00	0.00E+00
2.09E+01	-1.18E-28	0.00E+00	2.52E+05	0	0.00E+00	1.40E-06	0.00E+00	0.00E+00	0.00E+00
2.20E+01	-1.18E-28	0.00E+00	2.48E+05	0	0.00E+00	1.40E-06	0.00E+00	0.00E+00	0.00E+00
2.24E+01	-1.18E-28	0.00E+00	2.44E+05	0	0.00E+00	1.40E-06	0.00E+00	0.00E+00	0.00E+00
2.24E+01	-1.18E-28	0.00E+00	2.41E+05	0	0.00E+00	1.40E-06	0.00E+00	0.00E+00	0.00E+00
2.24E+01	-1.18E-28	0.00E+00	2.36E+05	0	0.00E+00	1.40E-06	0.00E+00	0.00E+00	0.00E+00
2.24E+01	-1.18E-28	0.00E+00	2.32E+05	0	0.00E+00	1.40E-06	0.00E+00	0.00E+00	0.00E+00
2.24E+01	-1.18E-28	0.00E+00	2.28E+05	0	0.00E+00	1.40E-06	0.00E+00	0.00E+00	0.00E+00
2.24E+01	-1.18E-28	0.00E+00	2.24E+05	0	0.00E+00	1.40E-06	0.00E+00	0.00E+00	0.00E+00
2.23E+01	-1.18E-28	0.00E+00	2.19E+05	0	0.00E+00	1.40E-06	0.00E+00	0.00E+00	0.00E+00
2.23E+01	-1.18E-28	0.00E+00	2.15E+05	0	0.00E+00	1.40E-06	0.00E+00	0.00E+00	0.00E+00
2.23E+01	-1.18E-28	0.00E+00	2.11E+05	0	0.00E+00	1.40E-06	0.00E+00	0.00E+00	0.00E+00
2.23E+01	-1.18E-28	0.00E+00	2.07E+05	0	0.00E+00	1.40E-06	0.00E+00	0.00E+00	0.00E+00
2.23E+01	-1.18E-28	0.00E+00	2.03E+05	0	0.00E+00	1.40E-06	0.00E+00	0.00E+00	0.00E+00
2.23E+01	-1.18E-28	0.00E+00	2.00E+05	0	0.00E+00	1.40E-06	0.00E+00	0.00E+00	0.00E+00

The output in the .csv files is contained in a single table with the following headings:
TIME - current time (s)
SEGMT - segment number
PWCX - current value of coolant pressure (MPa)
TCOOL - coolant temperature (K)
HSC - sheath-to-coolant heat transfer coefficient (W/(m^2K))
PNORM - average normalized power
CFT - centreline fuel temperature (K)
AFT - area-average fuel temperature (K)
SFT - fuel surface temperature (K)
TSH - average sheath temperature (K)
VOVT - gas storage volume (m^3/K)
HRTE - sheath heating rate (K/s)

PGAS - internal gas pressure (MPa)
HFS - fuel-to-sheath heat transfer coefficient (W/(m^2K))
SQQ - engineering sheath hoop stress (%)
EQQ - true sheath hoop strain (%)
RATE - generalized sheath hoop strain rate (1/s)
MIDP - midpoints of axial segments, (as specified by the user in the input file)
GAP - sheath-fuel radial gap (m)
INTP - radial fuel-to-sheath interfacial contact pressure (MPa)
AXIG - segmented axial gap (m)
PCAX - pellet-to-pellet axial interface pressure (MPa)
EQP - true plastic hoop strain (%)
EQT - sheath diametral thermal expansion (%)
OX - thickness of the ⟨-Zr(O)+ZrO_2 layer (m)
FW - fraction of sheath wall carrying load
SIGIR - internal stress in the sheath (MPa)
ATHERM - athermal dislocation glide strain in sheath (%)
PROB - probability of beryllium braze assisted cracking in the sheath
SUMCP - average stored energy in the fuel (J/kg)
NCRAC - number of oxide cracks
EPC - percent strain in first crack
ZRO_2 - oxide layer thickness (m)
AZR - oxygen stabilized ⟨-Zr layer thickness (m)
FECS - ratio of sheath strain under first oxide crack to average engineering plastic strain
FSC - fraction of sheath circumference cracked (%)
